



HAL
open science

Size effects on all-optical helicity-independent switching in magnetic materials

Danny Petty Gweha Nyoma

► **To cite this version:**

Danny Petty Gweha Nyoma. Size effects on all-optical helicity-independent switching in magnetic materials. Physics [physics]. Université de Lorraine, 2023. English. NNT : 2023LORR0035 . tel-04353845

HAL Id: tel-04353845

<https://hal.univ-lorraine.fr/tel-04353845>

Submitted on 19 Dec 2023

HAL is a multi-disciplinary open access archive for the deposit and dissemination of scientific research documents, whether they are published or not. The documents may come from teaching and research institutions in France or abroad, or from public or private research centers.

L'archive ouverte pluridisciplinaire **HAL**, est destinée au dépôt et à la diffusion de documents scientifiques de niveau recherche, publiés ou non, émanant des établissements d'enseignement et de recherche français ou étrangers, des laboratoires publics ou privés.



**UNIVERSITÉ
DE LORRAINE**

**BIBLIOTHÈQUES
UNIVERSITAIRES**

AVERTISSEMENT

Ce document est le fruit d'un long travail approuvé par le jury de soutenance et mis à disposition de l'ensemble de la communauté universitaire élargie.

Il est soumis à la propriété intellectuelle de l'auteur. Ceci implique une obligation de citation et de référencement lors de l'utilisation de ce document.

D'autre part, toute contrefaçon, plagiat, reproduction illicite encourt une poursuite pénale.

Contact bibliothèque : ddoc-theses-contact@univ-lorraine.fr
(Cette adresse ne permet pas de contacter les auteurs)

LIENS

Code de la Propriété Intellectuelle. articles L 122. 4

Code de la Propriété Intellectuelle. articles L 335.2- L 335.10

http://www.cfcopies.com/V2/leg/leg_droi.php

<http://www.culture.gouv.fr/culture/infos-pratiques/droits/protection.htm>

Size effects on all-optical helicity-independent switching in magnetic materials

THÈSE

présentée et soutenue publiquement le 05 Avril 2023

pour l'obtention du

Doctorat de l'Université de Lorraine

(en Physique)

par

Danny Petty Gweha Nyoma

Composition du jury

<i>Président :</i>	Nicolas Rougemaille	Université Grenoble Alpes
<i>Rapporteurs :</i>	Christine Boeglin	Université de Strasbourg
	Liliana Buda-Prejbeanu	Université Grenoble Alpes
<i>Examineurs :</i>	Stanislas Rohart	Université Paris-Saclay
	Stéphane Mangin	Université de Lorraine
<i>Invité :</i>	Eric Fullerton	University of California - San Diego
<i>Directeur de thèse :</i>	François Montaigne	Université de Lorraine

Institut Jean-Lamour - UMR 7198 - Université de Lorraine

Département de Physique de la Matière et des Matériaux

Nanomagnétisme et Electronique de spin

Mis en page avec la classe thesul.

Résumé

Au cours des quinze dernières années, le retournement tout optique à impulsion unique a été principalement observé et étudié dans des films minces à base de métaux de transition et de Gd, avec un grand potentiel pour permettre de nouvelles applications de stockage de données, de mémoire, de logique magnétique rapide et économe en énergie. Pour se rapprocher de la nanotechnologie ou de la microtechnologie, il faut concevoir d'autres matériaux contenant peu ou pas de terres rares et réduire latéralement la taille des échantillons.

Dans ce travail, nous démontrons expérimentalement le retournement tout optique de l'aimantation des disques de GdFeCo pour des diamètres allant de 3 μm à 400 nm en utilisant des impulsions laser de 35 femtoseconde polarisées linéairement. Deux différents états magnétiques sont observés en fonction de la fluence laser : soit un renversement déterministe de l'aimantation des disques, soit des disques orientés de façon aléatoire. Nous rapportons que les fluences requises pour observer ses deux états magnétiques présentent un comportement non monotone avec le diamètre du disque, et que les plus petits disques nécessitent la fluence seuil la plus faible pour obtenir un retournement tout optique indépendant de l'hélicité avec une seule impulsion. Une évolution différente des fluences seuils pour les deux phénomènes est observée en fonction de la taille du disque.

Ensuite, nous démontrons qu'en partant d'une bicouche Co/Pt avec une forte anisotropie perpendiculaire, le saupoudrage de Gd à l'interface est suffisant pour induire un retournement tout optique bien définie avec une seule impulsion. Une analyse minutieuse de l'impact de l'interface Gd/Co et de la composition de l'alliage GdCo sur le renversement tout optique est présenté. La démonstration qu'une très petite quantité de Gd est nécessaire pour provoquer le retournement de l'aimantation d'une couche ferromagnétique ouvre non seulement de nouvelles possibilités d'application, mais remet également en question la description théorique du mécanisme de retournement tout optique.

Enfin, nous présentons une étude systématique du renversement de l'aimantation des disques de Pt/Co/Pt saupoudrés de Gd dont le diamètre varie de 1.5 μm à 400 nm avec des impulsions laser à polarisation linéaire de 35 fs. En faisant varier le nombre d'impulsions, il apparaît que la seule probabilité de retournement peut décrire le comportement du renversement de l'aimantation. La variation de cette probabilité est mesurée avec précision dans la gamme de 90% à 99,99%. De plus, la probabilité de retournement se dégrade lorsque le di-

amètre des disques est réduit. La variation "exponentielle" de cette probabilité de retournement avec le diamètre du disque ne peut pas être expliquée par des effets thermiques spécifiques. Au contraire, un processus de renversement hautement non-uniforme avec une faible probabilité de retournement microscopique explique nos données expérimentales. Un modèle probabiliste simple, analogue au théorème du jury de Condorcet est proposé et comparé aux simulations micro-magnétiques.

Mots-clés: Renversement de l'aimantation, effets de taille, impulsions laser femtoseconde, retournement tout optique.

Abstract

In the last fifteen years single pulse all-optical switching has mainly been observed and studied in Transition Metal- Gd based thin film with high potential for enabling new application for energy efficient and fast magnetic data storage, memory, and logic. To move closer to nano or micro technologies, other materials with no or less rare-earth need to be engineered and lateral sample size must be reduced.

In this work, we experimentally demonstrate single pulse toggle switching of the magnetization of GdFeCo disks with perpendicular to film plane anisotropy which diameter ranges from 3 μm to 400 nm using 35 fs linearly polarized laser pulses. Two different magnetic states are observed depending on the laser fluence: either deterministic switching of the disks magnetization or randomly oriented disk. We report that the fluence required to observe both magnetic states show a non-monotonic behavior with disk diameter, and that the smallest disks require the lowest minimum fluence for achieving single pulse all-optical helicity-independent switching. Different evolution of the fluence thresholds for both phenomenon as a function of the disk size is observed and discussed.

Then, we demonstrate that starting with a Co/Pt bilayer showing strong perpendicular anisotropy, Gd dusting at the interface is sufficient to induce well define single pulse all optical switching. A careful analysis of the impact of the Gd/Co interface and the CoGd alloy composition on all optical switching is presented. The demonstration that very little amount of Gd is needed to induce the magnetization reversal of a ferromagnetic layer not only open new possibility for application, but it also questions theoretical description of the toggle switching mechanism.

Finally, we present a systematic study of the magnetization reversal for Gd-dusted Pt/Co/Pt ferromagnet disks whose diameter ranges from 1.5 μm to 400 nm with 35 fs linear polarization laser pulses. By varying the number of pulses, it appears that a single toggle switching probability can describe the behavior. The variation of this switching probability is precisely measured in a range from 90% to 99.99%. The switching probability degrades as the diameter of the disks is reduced. The "exponential" variation of the switching probability with the disk diameter size cannot be explained by specific thermal effects. On the other hand, a highly non uniform switching process with a weak microscopic switching probability explains our experimental data. A simple probabilistic model, analog to Condorcet's jury theorem is proposed and compared to micromagnetic simulations.

Keywords: Magnetization reversal, size effects, femtosecond laser pulses, all-optical switching.

Acknowledgments

This section concludes my research adventure of the last three years. It is with great pleasure that I thank all those who participated in this work.

I would like firstly to greatly thank my Ph.D. supervisor François Montaigne. Initially, for giving me the opportunity to work in the field of AOS at nanoscale and helping me with all aspects of life as a foreign Ph.D. student. For example, you supported me a lot for the nanofabrication and for the establishment of my residence permit in France (10 years). Secondly, by imparting to me many values such as integrity, rigor, humility, and honesty which I am sure will help me to become a good researcher.

Secondly, I would like to thank Stéphane Mangin, the head of the Nano-magnetism and spintronic team (101 team). In 2018, during my master's degree, you helped me to understand the basics of magnetism and spintronics as a teacher. Then you continued to give me advice throughout my doctoral years. Finally, at the end of my work, you assisted me again to write my scientific papers.

I greatly thank Michel Hehn and Daniel Lacour for three main reasons. First of all, you were the first members of the 101 team to give me the opportunity to be part of this family of nano-magnetism and spintronics, since you were my two supervisors during my final year internship. Secondly, I greatly appreciated working with you with all the discussions we had. I also enjoyed your constructive feedbacks and suggestions on my work. Finally, the accomplishment of my work would not have been possible without your experimental participation. Indeed, if I need to thank Michel Hehn for the growing of the full film and wedge samples, I would also like to underline the availability of Daniel Lacour to carry out Magnetic Force Microscopy (MFM) measurements. I hope we can still work together in the future.

I also thank Grégory Malinowski, Julius Hohlfeld and Jon Gorchon for discussions, explanations about experimental and theoretical aspects of my work inside or outside the laser room. In fact, in the course of my work, both of you have taught me a lot about different ultrafast dynamic settings, different possible configurations of the laser table or even possible future projects based on my Ph.D. results. In addition, I also enjoyed our informal discussions which always made my hundreds of hours in the laser room more enjoyable. I would like to thank other permanent members of the 101 teams for the discussions: Stéphane ANDRIEU, Olivier COPIE, Thomas HAUET (Thank for the SQUID measurements of the sample used in Chapter 5), Sébastien PETIT-WATELOT, and Juan-Carlos ROJAS-SANCHEZ.

I also want to express my gratitude to all the members of my Ph.D. jury for reading my manuscript, for the commentaries inside my manuscript and during the Ph. D defense, for all

the questions. I could have during my Ph.D. defense. I am especially grateful to Christine Boeglin and Liliana Buda-Prejbeanu to accept reviewing this PhD book. I hope we can meet again in the future at conferences and/or seminars.

In order to carry out this work, I used many experimental methods during which I collaborated with many PhD students and post-docs. In this paragraph, I would like to thank some of them. Firstly, I would like to highlight the importance of what I call the MOKE user team: Junta IGARASHI, Remy QUENTIN, Wei ZHANG, Wei Jiaqi, Boyu Zhang, Maxime VERGES and Tianxun HUANG (each of you are now doctor). Individually or in team, I really learned a lot of you at the beginning of my work and even at the end. Thank you, dear colleagues. Secondly, I would like to thank a second list of new Doctors: Aitoukaci Kosseila and Massouras Maryam. It is the MFM user team!!!! As the MOKE user team, I really appreciated all the advice you gave me at the beginning of my Ph.D., when I started to probe nanostructures after the excitation of a laser pulse. I would like to thanks other PhD students turned friends for the discussions and the nice work atmosphere: Héloïse, Valentin, Eva, Anna, Zongxia, Jun-Xiao LIN, Yi PENG and Yann LE GUEN. More Generally, I would like to thank the Nano-magnetism and Spintronics team for the great atmosphere inside the team (in formal and less formal discussions).

Finally, due to my PhD project, I have no choice but to thank 03 Competence Centre (CC) present at the Institut Jean Lamour: Micro and Nanotechnology CC for the good atmosphere inside the cleaning room, which allowed me to perform nanofabrication described in chapter 2. Magnetism and Cryogenics CC for allowing magnetic characterization of samples presented in the last three chapter of this manuscript. Microscopies, Microwaves and Metallography CC for all the structural, physical, and chemical characterization of the sample of the chapter 5. Moreover, all of this could not have been possible without the efforts of the administrative staff at Institut Jean Lamour which I also thank a lot.

Since a Ph.D. cannot be realize without a good environment. I would like to thank other people that are not from 101 team but gave me lovely vibes and unlimited moral support. I would like to thanks Bodry TEGOMO, Victor PALIN and Alix VALDENNAIRE for all our scientific discussions or informal conversions that we had within laboratory or outside (restaurants, houses, classroom, phones. etc). Consider our five years relationships (since master), it was really nice to spend all this time with you my friends. I hope we will keep in touch in the future. In addition, it was a pleasure for me to share some week-end, parties, sports sessions, PlayStation games, or free time with all the student coming from the convention between Dschang and Lorraine University (Fresnelle, Wilfrid, Calvin, Abel, Nadine, Loveline, Daniel, Sama, Claude, Ebenezer, Guy, . . . etc.). I also greatly appreciated the motivation that I always obtained for my

previous master supervisor in Cameroon Nguenang Jean Pierre and from Daniel Malterre the head of the master of condenser matter and nanotechnology (thank you to have gave me this opportunity to continue my dream). Finally, I would like to thank all my office members (Krupali, Ulrich, Marnix, Spenser, Jeremy) for the good atmosphere with shared moments of music/foods/drinks/happiness.

I can't end this section of thanks without mentioning the great support of my family: I am very grateful to my mother (Hello Ma Rachel, this manuscript is dedicated to you), to my father (Daniel), to all my siblings (Patrick, Laura, Dimitri, and Daryl), to my girlfriend (Carelle, I hope we can continue to build our life together my precious), to my former classmates turned siblings (Julio, Edgar and Abem), to all the Montemont family (especially Nyango and her husband for allowing me to spend my first two years in France in their house). I would also like to thank those of you who were able to attend my defense, it was on Wednesday, but you were there just for me.

Je ne peux pas terminer cette section de remerciements sans mentionner le grand soutien de ma famille: Je suis très reconnaissant à ma mère (Coucou Ma Rachel, ce manuscrit t'est dédié), à mon père (Daniel), à tous mes frères et sœurs (Patrick, Laura, Dimitri, et Daryl), à ma petite amie (Carelle, j'espère que nous pourrons continuer à construire notre vie ensemble ma précieuse), à mes anciens camarades de classe devenus des frères (Julio, Edgar et Abem), à toute la famille Montemont (en particulier Nyango et son mari pour m'avoir permis de passer mes deux premières années en France dans leur maison). Je voudrais aussi remercier ceux d'entre vous qui ont pu assister à ma soutenance, c'était un mercredi, mais vous étiez là juste pour moi.

Contents

Introduction	1
1 State of art	3
1.1 Laser induced dynamics in metals	4
1.1.1 Ultrafast demagnetization in Ni film	4
1.1.2 Mechanism involved in the ultrafast magnetization dynamics	5
1.2 All Optical switching in ferrimagnet	12
1.2.1 AO-HDS in ferrimagnetic materials	12
1.2.2 AO-HIS in ferrimagnetic materials	14
1.2.3 AO-HIS in synthetic ferrimagnetic materials	17
1.3 All Optical switching in ferromagnet thin films and multilayers	21
1.3.1 MP-AOHDS in CoPt multilayers	21
1.3.2 Domain wall helicity dependent switching in CoPt trilayers and multilayers	23
1.3.3 State diagram of AOS	25
1.3.4 Mechanism of all-optical switching	26
1.4 All-Optical magnetization switching mediated by spin transport: spin valve structure	33
1.4.1 Spin current induced AOS in ferromagnetic layer	33
1.4.2 Influence of the ferromagnetic Curie temperature	34
1.5 All Optical switching in magnetic micro and nanostructures	36
1.5.1 Highly efficient AOS in GdFeCo	36
1.5.2 Nanoscale sub-100 picosecond AOS in GdFeCo	38
1.5.3 AOS in nanostructure of GdCo	40

CONTENTS

1.6	Goals and outline of the thesis	41
2	Experimental methods	43
2.1	Full film deposition and nanofabrication	43
2.1.1	Full film deposition	43
2.1.2	Nanofabrication	44
2.2	Magneto-optical and magnetic characterization	51
2.2.1	MOKE magnetometry	52
2.2.2	MOKE microscopy with femtosecond laser pulse excitation	53
2.2.3	Magnetic Force microscopy	57
3	Size effect on GdFeCo ferrimagnetic alloy	67
3.1	Introduction	67
3.2	From 10 μm to 3 μm disk diameter	68
3.2.1	Characteristics of the full film	68
3.2.2	AO-HIS in GdFeCo microdisks	70
3.2.3	Limitations	76
3.3	From 3 μm to 400 nm disk diameter	77
3.3.1	Characteristics of the full film	77
3.3.2	AO-HIS of GdFeCo disks	78
3.4	Summary	94
4	Gd effect on Pt/Co/Pt ferromagnet	95
4.1	Introduction	95
4.2	Single thermal pulse induced AOS in Pt/Co/Gd(wedge)/Pt full film	96
4.2.1	Design of the wedge sample	96
4.2.2	Conversion of the Gd position to Gd thickness	96
4.2.3	Magnetic characterization	98
4.2.4	AO-HIS experiments	99
4.3	Single thermal pulse induced AOS in Pt/Gd(wedge)/Co/Pt full film	107
4.3.1	Design of the wedge sample	107

4.3.2	Structural and magnetic characterization	108
4.3.3	AO-HIS experiments	112
4.4	Single thermal pulse induced AOS in Pt/CoGd(wedge)/Pt full film	116
4.4.1	Design of the wedge sample	116
4.4.2	Extraction of the Gd (Co) concentration	117
4.4.3	Magnetic characterization	118
4.4.4	State diagram of Pt/CoGd (wedge)/Pt full film	119
4.5	Summary and discussion	121
5	Size effect on Gd-dusted Pt/Co/Pt ferromagnet	123
5.1	Introduction	123
5.2	Structural, magnetic and all optical switching	124
5.2.1	Structural properties	124
5.2.2	Magnetic characterizations	126
5.2.3	AOS properties	127
5.3	AO-HIS in nanostructures at femtosecond pulse duration	129
5.3.1	Design of the patterned sample	129
5.3.2	Single shot AO-HIS	130
5.3.3	AO-HIS as a function of the number of pulses	131
5.4	Modeling of all-optical switching in nanostructures	138
5.4.1	Thermal activation	138
5.4.2	Analytical and micromagnetic simulations approach	139
5.5	AO-HIS in nanostructures at picosecond pulse duration	141
5.5.1	Single shot AO-HIS	141
5.5.2	AO-HIS as a function of the number of pulses and light polarization	142
5.5.3	Preliminary quantitative analysis	144
5.6	Summary	147
	Conclusion and perspectives	149

CONTENTS

A	Details of the quantitative analysis	153
A.1	Magnetization and switching probability	153
A.2	switching probability and thermal activation	155
Bibliography		157
Résumé de la thèse		173

List of Figures

1.1	Variation of the Normalized transient remanent longitudinal MOKE signal with the delay Δt between the laser pump and the probe of a Ni(20 nm)/MgF ₂ (100 nm) film for a laser pump fluence of 7 mJ/cm^2 . Figure taken from ³²	5
1.2	(a) Three temperature model represented by 3 baths in interactions. (b) Variation of the three temperatures baths after the excitation by a femtosecond laser pulse (Delay Time above 0 ps).Figure taken from ³²	7
1.3	Evolution of the magnetic moment $M(t)$ with time after one laser pulse excitation for the case (a) without spin-orbit coupling (upper panel), (a) without laser field (lower panel) and (b) with the presence of both spin-orbit coupling and the laser field for various laser intensity of $I(u.a) = 0.03$ (long-dashed line), 0.3 (dot-dashed line) and 1.5 (solid line). Inset: exponential trends of $M(I)$ with the laser intensity field I . Figure taken from ⁴⁶	8
1.4	Illustration of the M3TM with an Elliot-Yafet mechanism inducing (a) ultrafast demagnetization and (b) thermalization of the electrons bath after emission or absorption of phonons.	10
1.5	Evolution of the electron temperature T_e (red curve), phonon temperature T_p (blue curve) and the magnetization (green curve) as a function of time. These variations are obtained after using the microscopic three-temperature model and showed two different demagnetization behaviors in ferromagnetic materials. Figure taken from ¹⁹	11
1.6	Magneto-optical images showing a) initial magnetic state before irradiation of laser on the surface and b) MP-AOHDS in Gd ₂₂ Fe _{76.6} Co _{3.4} induced by sweeping the laser over the sample with left circular (σ^-), right circular (σ^+) and Linear (L) polarization. The light (dark) contrast represents magnetic domain with the magnetization pointing “up” (“down”). Figure taken from ³⁴	13

LIST OF FIGURES

- 1.7 XMCD measurement of the magnetization dynamic of the Gd and Fe sublattice obtained after the irradiation of a femtosecond laser pulse for (a) a short-time scale and (b) a long-time scale. Figure taken from¹. 15
- 1.8 (a) Inverted Heusler (XA) crystal unit cell of typical MRG film. (b) Magneto-optical images of $\text{Mn}_2\text{Ru}_{1.0}\text{Ga}$ full film obtained after the action of five consecutive single laser pulse of 200 fs. The dark grey (light grey) area represents the out of plane magnetization of the Mn(4c) sublattice pointing “up” (“down”) as represented by the circled dot (cross). Every single femtosecond pulse with a fluence of 11.6 mJ/cm^2 and a spot diameter of $100 \mu\text{m}$ linearly polarized illuminates the same circular region of the full film and reverses the magnetization within it. The length of the scale bar is $50 \mu\text{m}$. Figure taken from¹⁵. 17
- 1.9 (a) VSM-SQUID measurement of the magnetic moment per unit area as a function of the temperature. $T_{\text{com}} = 120 \text{ K}$ represents an AF exchange interaction between the Co and Gd layers. Inset: Polar MOKE measurement performed at RT. The square hysteresis loop with 100% remanence confirms a well-defined PMA. (b) AOS experiments were realized for two opposite initial saturation directions. The numbered areas (dotted circles) correspond to the spots where the structure was irradiated by the laser, where the labels indicate the number of pulses each spot is exposed to. All measurements were performed on Pt(4nm)/Co(1nm)/Gd(3nm) stack. Figure taken from⁷. 18
- 1.10 Variation of the laser pulse energy P_0 with (a) the Co concentration x for $\text{Gd}_{1-x}\text{Co}_x$, and (b) the number of Co monolayers in a Co/Gd bilayer. The dark-blue areas indicate that the Co magnetization is reversed after the relaxation (c) and the light-blue areas indicate the exhibition of a transient ferromagnetic state but followed by the relaxation of the magnetization back to its initial direction (d). The white areas indicate the absence of a transient ferromagnetic state, then the magnetization relaxes to its initial direction (e), (f) and the gray areas indicate that the maximum of the phonon temperature is above the Curie temperature. The dashed line in (a) corresponds to the compensation point and the inset in both (a) and (b) present the modeled system with the exchange parameters. (g) Magnetization dynamic in a 5 Co / 3 Gd bilayer for a fixed energy $P_0 = 55 \times 10^8 \text{ J/m}^{-3}$. The inset present the time at which the magnetization of each Co monolayer is reversed for a 14 Co / 3 Gd system for a fixed energy $P_0 = 65 \times 10^8 \text{ J/m}^{-3}$. Figure taken from²³. 20

<p>1.11 Magneto-optical response in a zero applied magnetic field of [Co (0.4 nm)/Pt (0.7 nm)]_N multilayers at various laser polarization (A) N = 8, (B) N = 5 and (C) N = 3. For each image, the laser is circularly polarized (σ^+ or σ^-) or linearly polarized (L). For (A) - (C), the laser beam was scanned over a region of the sample with two opposite magnetic domains showing a black/white contrast in the images. Figure taken from⁸².</p>	22
<p>1.12 (a), (b) Variation of the normalized Hall voltage on the Pt/Co/Pt Hall cross as a function of the number of pulses and the laser polarization: (a) polarization-independent demagnetization over a duration of 1 ms and (b) polarization-dependent magnetization reversal under 120 ms. (c) Magneto-optical image of Pt (4.5 nm)/Co (0.6 nm)/Pt (4.5 nm) after excitation by a single femtosecond laser pulse. For both directions of magnetization saturation (M^+ and M^-), thermal demagnetization is observed with circular (σ^+ and σ^-) and linear (π) polarizations. Figure taken from⁶⁹.</p>	23
<p>1.13 (a) Magneto-optical images of domain wall motion in Pt(5 nm)/[Co(0.4 nm)/Pt(0.7 nm)]₃/Pt(2 nm) induced by 2 ps laser pulses with left (σ^-) and right-circular (σ^+) polarization with a fluence per pulse of 0.04 mJ/cm². The white star and N represent the center of the beam spot and the number of laser pulses, respectively. The dotted line shows the initial position of the domain wall before the laser irradiation.(b) Variation of the DWD with degree of ellipticity. the Figure taken from⁸⁴.</p>	24
<p>1.14 (a) Magnetic state diagram of Glass/Ta (3 nm)/Pt(3 nm)/[Co(0.6 nm)/Pt(0.7 nm)]/Pt(3 nm) using circular LASER polarization as a function of fluence, pulse duration and LASER spot diameter (84 μm for the triangle, 104 μm for the square, and 168 μm for the circle). (b) Variation of the normalized Hall voltage as a function of time, giving the dynamics of the Co/Pt magnetization. The sample, initially having a saturated magnetization, is excited by a polarization pulse of σ^+ (red), σ^- (blue) and π (black). Figure taken from⁸⁷.</p>	26

LIST OF FIGURES

- 1.15 (a) Computed probability of a single grain switching over a range of laser fluences in a zero field and with a constant external field ± 1 T. The lines show a fit to the data. (b) Evolution of the net magnetization after a series of multiple pulses over a range of laser fluences and MCD ratio in a zero field. The solid, dashed and dotted lines represent the net magnetization after 100, 1000 and infinite laser pulses, respectively. (c) Simulations when sweeping the laser with a constant speed and a peak fluence of 20 mJ/cm^2 on a granular structure for different applied fields. A MCD of $\Delta = \pm 2 \%$ is used to model the laser polarization and each grain is switched following the probabilities given in Eq 1.10. Figure taken from⁸⁹. 29
- 1.16 (a) Illustration of the IFE for normal incidence light with right (σ^+) and left (σ^-) circular polarization, generating an effective magnetic field δH^+ and δH^- , respectively. (b) Reproduction of the magnetization profile after single-laser pulse irradiation on $[\text{Co} (0.4 \text{ nm})/\text{Pt}(0.7\text{nm})]_3$ and obtained from M3TM simulations. A multi-domain state is observed in the center and a single switched domain is clearly visible in the rim of the laser spot. Figure taken from^{99,103}. 32
- 1.17 (a) Variation of the normalized MOKE (θ_K) with the magnetic field (H) applied out of plane. The reversal which appears at low magnetic field is assigned to the GdFeCo reversal and is represented by the red and blue open symbols. (b) four magnetic configurations obtained consecutively by using high or low pulses energy. Figure taken from¹¹. 34
- 1.18 (a) MOKE images obtained after exposure of 1 then 2, 3, and 4 fs-laser pulses starting from a $P+$ initial state. (b) Threshold fluences for: the only GdFeCo magnetization switching, AOS of both GdFeCo and the ferromagnetic layers, and multidomain states plotted as a function of the FM layer Curie temperature T_C . (c) Experimental (calculation) variation of $F_{\text{multi}} - F_{\text{both}}$ as a function of T_C represented with closed (opened) symbols. Figure taken from¹². 35

1.19	(a) pump-probe dynamics for a fixed pump beam fluence of 1.9 ± 0.2 mJ/cm ² for various structures size. (b) Variation of the fluence to achieve 100% demagnetization, all optical switching, and the damage with the structure dimension. Inset: Experimental conditions reproducing in scale the dimensions of pump and probe beams. (c) Absorbed energy profiles of the electric field intensity taken at the center of the structures. (d) Normalized simulated energy distribution as a function of the structure size (red squares), compared to the expected behavior in the absence of interference effects (blue circles. Figure taken from ¹¹¹	37
1.20	Time resolved XMCD PEEM imaging as a function of the incident laser fluence F and for an angle between the planar component of the laser wave vector \mathbf{k} with an edge equal to (a) 0^0 and (d) 45^0 . Absorption profile A obtained from the FDTD simulations for the (c) 0^0 and the (f) 45^0 incoming laser direction. Threshold Fluence F_{th} patterns obtained from the XMCD time-resolved experiments for the (b) 0^0 and the (e) 45^0 incoming laser direction. The experimental observations and simulations were carried out inside $5 \mu\text{m} \times 5 \mu\text{m}$ GdFeCo microstructures. Scale bar 5 nm. Figure taken from ¹¹²	39
1.21	(a) Single shot experiment performed with a laser MOKE for dot diameter of 500 nm. Irradiation of 10 consecutive pulses causes the magnetization state to alternate up and down, demonstrating a toggle switching behavior. (b) Variation of the time taken for the magnetization to cross a 75% switching threshold with different dot diameters. The inset shows an extended view of the dot at the nanoscale. Figure taken from ⁶	41
2.1	(a) Structure of the $\text{Gd}_{24}(\text{FeCo})_{76}$ (20 nm) sample and (b) of the tri-layer Pt (3 nm)/Co (0.7 nm)/Pt (3.7 nm) doped with a small amount of Gd at the bottom Co/Pt interface.	44
2.2	electron beam lithography process used in this thesis to realize periodic magnetic structures.	45
2.3	(a) Picture of the Raith150-TWO station for the exposure of electrosensitive resist, installed in the cleanroom of the Jean Lamour Institute. (b) Schematic representation of e-beam lithography. Figure taken from ¹²³	47
2.4	Design of the sample. (a) Illustration of the 8 different writing fields and (b) the case of D equal to 400 nm. For each dot diameter D , an area of size $100 \mu\text{m} \times 100 \mu\text{m}$ is filled with (c) equally spaced disks with a fixed spacing d equal to 300 nm.	47

LIST OF FIGURES

2.5	Evolution of the etching process with time.	49
2.6	Etching of the Gd-doped Pt/Co/Pt trilayer. The increase of the Ta signal marks approximately the end of the operation.	50
2.7	SEM image showing (a) an overview of GdFeCo magnetic dot arrays for all dot sizes and (b) the good agreement of the lattice pitch and the dot diameter in the case of 400 nm of dot diameter.	51
2.8	In situ picture of the MOKE magnetometry setup used in all this work.	52
2.9	Kerr imaging set-up used for magneto-optical characterization of magnetic configuration of patterned or full film samples. The orange color of the LED light has been used for the purpose of representation	54
2.10	Magneto-optical images of Pt(3.7 nm)/Gd/Co(0.7 nm)/Pt(3 nm) full film obtained after the action of (a) zero, (b) one, and (c) two consecutives single laser pulse. The light grey (dark grey) area represents the out of plane magnetization of the film “down” (“up”) as represented by the circled cross. The length of the scale bar is 40 μm	55
2.11	Magneto-optical images obtained after the action of (a)((c)) one and (b)((d)) two consecutives single laser pulse for 400 nm periodic magnetic disks of $\text{Gd}_{24}(\text{FeCo})_{76}(20 \text{ nm})$ (Pt(3.7 nm)/Gd/Co(0.7 nm)/Pt(3 nm)).	56
2.12	MFP3D Asylum Research magnetic force microscope of type “ORIGIN+” used in this work.	57
2.13	Principle of detection of the vibration of the cantilever.	58
2.14	(a) MFM mapping and corresponding (b) AFM of a 1 μm diameter disks array after exposure to a single laser pulse.	60
2.15	(a) MFM mapping and corresponding (b) AFM of a 1 μm diameter dot array obtained after grayscale conversion.	61
2.16	(a) AFM binarized images and (b) graphic representation of the position of disks extracted from AFM image. The size of the displayed red and green circles is completely arbitrary.	62
2.17	Histogram of the average pixel P of each identified dot corresponding to the grayscale MFM image.	63
2.18	MFM images with (a) red circles on unswitched (or unexposed) disks and (b) green circles on switched disks.	64
2.19	(a) Numerical image of the 1 μm Pt/Gd/Co/Pt dot array obtained using the corresponding (b) MFM image. The blue circles represent switched disks.	64

3.1	(a) Structure of the $\text{Gd}_{23}(\text{FeCo})_{77}$ (20 nm) sample and corresponding (b) hysteresis loop measurement with the applied field out of plane.	69
3.2	Magneto-optical images of Pt(5 nm)/ $\text{Gd}_{23}(\text{FeCo})_{77}$ (20 nm)/Pt(5 nm) full film obtained after the action of four consecutive single laser pulse. Every single femtosecond pulse with a fluence of 19.1 mJ/cm^2 and a spot diameter of 50 μm linearly polarized illuminates the same circular region of the full film and reverses the magnetization within it. The length of the scale bar is 20 μm	70
3.3	(a) Optical images of Pt(5 nm)/ $\text{Gd}_{23}(\text{FeCo})_{77}$ (20 nm)/Pt(5 nm) disk of size 10 μm and 30 μm of period, obtained after microfabrication. (b) Hysteresis loop of all the studied disk arrays with the applied field out of plane.	71
3.4	Magneto-optical images of magnetic disks made of $\text{Gd}_{23}(\text{FeCo})_{77}$ (20 nm) obtained after the action of consecutive 35 fs linearly polarized laser pulses. Initial single domain of disks with magnetizations “down” (“up”) are represented by the cross (disk). Each laser pulse with a given fluence irradiates the same region of the patterned structure. The scale of the image can be easily related to the diameter of the microstructures and is equal to 40 μm in all the MOKE images.	72
3.5	Magneto-optical images of magnetic disks made of $\text{Gd}_{23}(\text{FeCo})_{77}$ (20 nm) obtained after the action of consecutive 35 fs linearly polarized laser pulses. Initial single domain of disks with magnetizations “down” (“up”) are represented by the cross (disk). Each laser pulse with a fluence of 24, 25 and 22 mJ/cm^2 irradiates the same region of the patterned 5, 4 and 3 μm structure, respectively. The scale of the image can be easily related to the diameter of the microstructures and is equal to 40 μm in all the MOKE images.	74
3.6	Slow domain dynamic observed after the irradiation of 6 μm disks by a single pulse Linearly polarized. The red circle in (a), (b) and (c) represents the structure of interest when we initially applied a magnetic field in the downward direction. The green circle in (d), (e) represents the structure of interest when we initially applied a magnetic field in the upward direction.	75
3.7	Two AOS experiments performed with the yellow circle representing the laser center at (a) the center of a 8 μm disk and (b) approximately the isobarycenter of the three exposed 8 μm disks. Every single femtosecond pulse with a fluence of 17 mJ/cm^2 and a spot diameter of 50 μm linearly polarized illuminates the same circular region of the patterned array.	77

LIST OF FIGURES

3.8	(a) Hysteresis loop measurement and (b) AOS experiment performed on the $\text{Gd}_{24}(\text{FeCo})_{76}(20 \text{ nm})$ sample. Every single femtosecond pulse linearly polarized with a pulse energy of 15.5 mJ/cm^2 illuminates the same circular region of the full film. The laser beam diameter is around $70 \mu\text{m}$	78
3.9	Magneto-optical images of magnetic disks made of $\text{Gd}_{24}(\text{FeCo})_{76}(20 \text{ nm})$ obtained after the action of one 35 fs linearly polarized pulse and then a second pulse separated by 1 s. Initial single domain of disks with magnetizations “down” (“up”) are represented by the cross (dot). For (b)-(i) ((j)-(q)) the dark grey (light grey) area represents magnetization of disks pointing “up” (“down”). Each laser pulse with an energy of μJ irradiates the same circular region of the patterned structure and reverses the magnetization within it. The length of the scale bar is $20 \mu\text{m}$	80
3.10	Magneto-optical images of $\text{Gd}_{24}(\text{FeCo})_{76}(20 \text{ nm})$ magnetic disks obtained after a single 35 fs laser pulse, linearly polarized. Depending on the pulse energy and the disk diameter, we observe three different magnetic states: (c)-(h) light grey area for no switching at low pulse energy, (a)-(b) homogenous dark grey area for AO-HIS at medium energy and (m) non-homogenous dark grey area for randomly oriented disks at the center of the laser spot for high pulse energy.	81
3.11	Manual determination of the (a) switching and (b) random diameters on MOKE images.	82
3.12	Magneto-optical images of magnetic disks of $\text{Gd}_{24}(\text{FeCo})_{76}(20 \text{ nm})$ obtained after the action of two consecutives 35 fs laser pulses, linearly polarized. Depending on the pulse energy and the disk size, we observe three different magnetic states: light grey area for no switching at low pulse energy, homogenous dark grey area for switching at medium energy and non-homogenous dark grey area for randomly oriented disks at the center of the laser spot for high pulse energy.	83
3.13	Square of the switching diameter as a function of the logarithm of the pulse energy for disk diameter equal to $3 \mu\text{m}$, $2 \mu\text{m}$, $1.5 \mu\text{m}$, $1.2 \mu\text{m}$, $1 \mu\text{m}$, 800 nm , 600 nm , and 400 nm	85
3.14	Laser beam spatial profile plotted (black curve) and fitted with a gaussian distribution (red curve). The inset shows the optical image taken with a CCD camera.	85
3.15	Square of the switching (in blue) and random (in red) diameter as a function of the logarithm of the fluence for all the disks size.	86

3.16 AO-HIS state diagram of $\text{Gd}_{24}(\text{FeCo})_{76}$ (20 nm) disks. Threshold fluencies for switching (F_{sw}) and random state (F_{ra}) as function of disk diameter depicted in blue and red disks, respectively. The FWHM of the laser is around $68.4 \mu\text{m}$. . .	87
3.17 (a) Variation of the filling factor divided by the calculated absorbance as a function of the diameter of disk. (b) Absorption profiles in the smaller magnetic disks leading to the formation of standing waves due to light confinement. (c) Absorption profiles in the bigger magnetic disks.	89
3.18 Evolution of the fluence ratio F_{ra}/F_{sw} as function of disk diameter.	90
3.19 Magneto-optical images of 400 nm $\text{Gd}_{24}(\text{FeCo})_{76}$ (20 nm) disks obtained after the action of a single 35 fs laser pulse, linearly polarized. Depending on the pulse energy and the disk diameter, we observe two different magnetic states: light grey area for no switching and homogenous dark grey area for switching. The diameter of the laser beam is around $75 \mu\text{m}$	91
3.20 Threshold switching fluence on 400 nm $\text{Gd}_{24}(\text{FeCo})_{76}$ (20 nm) disks as a function of the period. The closer disks need less energy to cause AOS and the non-monotonic behavior of F_{sw} highlights the importance of the specific light absorption in nanostructures.	91
3.21 Magneto-optical images of $\text{Gd}_{24}(\text{FeCo})_{76}$ (20 nm) magnetic disks obtained after a single laser pulse, linearly polarized at $16 \text{ mJ}/\text{cm}^2$ of fluence. Depending on the pulse duration and the disk diameter, we observe two different magnetic states: homogenous dark grey area for AO-HIS and non-homogenous dark grey area for randomly oriented disks. The green rectangle is a particular case at $1 \mu\text{m}$ of disk diameter.	92
3.22 Magneto-optical images of $\text{Gd}_{24}(\text{FeCo})_{76}$ (20 nm) magnetic $1 \mu\text{m}$ disks obtained after a single laser pulse, linearly polarized at $16 \text{ mJ}/\text{cm}^2$ of fluence. The augmentation of the pulse duration causes the degradation of the switching state indicated by the increase in the unswitched disks within the exposed area. . . .	94
4.1 Illustration of the four samples needed to form two Gd-wedge. In the middle of the wedge, the thickness of Gd is 0.14 nm and 0.5 nm for the right and left figure, respectively. The yellow and orange mark on the surface of the sample were used to identify the thinner and thicker Gd layer side of each wedge, respectively. The total length of each wedge is 50 mm.	97

LIST OF FIGURES

4.2	(a) Illustration of the two samples needed to form Cu-wedge. At the middle of the wedge, the thickness of Cu is 200 nm. The yellow and orange mark on the surface of the sample were used to identify the thinner and thicker Cu layer side of the wedge, respectively. (b) Evolution of the Cu thickness across the total wedge length. The red line is the linear fit of the experimental data.	98
4.3	Representation of (top) the thinner and (bottom) the thicker Gd-wedge with the thickness value of Gd for the extremity of each wedge.	99
4.4	(a) Out of plane hysteresis loop for Pt/Co/Gd (0.06-0.77 nm) stack at t_{Gd} equal to 0.2 nm (black curve) and 0.7 nm (red curve). Both curves show a strong PMA and demonstrate that the entire Gd-wedge is Co-dominant. (b) Variation of the coercive field with Gd thickness. A maximum of H_c appears at t_{Gd} equal to 0.4 nm.	100
4.5	Magneto-optical images obtained after exposure of consecutive femtosecond pulses with 1 Hz (inside black rectangle) and 5 kHz (inside blue rectangle) of rate repetition in different regions of Pt/Co/Gd (0.06-0.77 nm) stack. We distinguished 5 types of magnetic behavior after the excitation of our wedge sample in single-pulse mode: No switching (not showed), multidomain state, demagnetization in the center of the laser spot, switching regime, and perfect toggle switching (PTS) behavior. The length of both laser diameter (FWHM) and scale bar is respectively 72 μm and 40 μm for all the MOKE measurements and images.	101
4.6	Magneto-optical images obtained after exposure of consecutive femtosecond pulses with 1 Hz of rate repetition in different regions of Pt/Co/Gd(0.07-0.19 nm) stack. The transition from the multidomain state to the switching state is achieved at t_{Gd} equal to 0.19 nm (inside light red rectangle). The length of both laser diameter (FWHM) and scale bar is respectively 72 μm and 40 μm for all the MOKE measurements and images. All incident laser pulses have the same fluence of 4.7 mJ/cm^2	102
4.7	Magneto-optical images obtained after exposure of 10 consecutive femtosecond pulses with (a) 1 Hz and (b) 5 kHz of rate repetition in Pt/Co/Gd (0.21 nm) stack. The switching state is maintained for low pulse frequency and disappears at high frequency. These two AOS experiments highlight the slow domain dynamic proper to the switching regime. The length of both laser diameter (FWHM) and scale bar is respectively 72 μm and 40 μm for all the MOKE measurements and images. All incident laser pulses have the same fluence of 5 mJ/cm^2	104

4.8	AO-HIS state diagram realized on Pt/Co/Gd (0.06-0.77 nm) stack. Magnetization behavior as a function of the Gd thickness t_{Gd} , and the laser fluence F , for Linearly polarized static beam with 70 μm of laser diameter. The dark blue circle (light blue triangle) and the light green square (dark green star) represent respectfully the switching fluence F_{Switch} and the demagnetization fluence F_{Demag} within switching (perfect toggle switching) regime. The black open disk represents the beginning of the multidomain state and the pulse duration is 35 fs for all measurements.	105
4.9	(a) Illustration of the local antiferromagnetic coupling between the magnetization of Co and Gd layer near the Co/Gd interface. (b) Evolution of the ratio F_{Demag}/F_{Switch} with the Gd thickness above 0.4 nm. The dashed line represents the average of all the ratio value in this range of thickness.	107
4.10	Representation of the four samples needed to form two bottom Gd-wedges. In the middle of the wedge, the thickness of Gd is 0.14 nm and 0.5 nm for the right and left figures, respectively. The yellow and orange mark on the surface of the sample were used to identify the thinner and thicker Gd layer side of each wedge, respectively. The total length of each wedge is 50 mm.	108
4.11	Structural characterization of the Glass/ Ta(3 nm)/Pt(3.7 nm)/Gd(0.1 nm)/Co(0.7 nm)/Pt(3 nm) stack.(a) HRTEM micrograph showing the Ta layer (green rectangle), Pt layer (blue rectangle), and Co layer (red rectangle). (b) Intensity depth profile of Pt, Co and Gd using Energy-dispersive X-ray spectroscopy (EDXS) measurement performed along the orange arrow in (a), proving the higher diffusion of Co atoms within the top Pt layer compared to the bottom one and showing the position of the Gd majority atoms after the deposition process. (c) Sketch of the heterostructure.	109
4.12	Structural characterization of the Ta(3)/Pt(3.7)/Gd(2)/Co(2)/Pt(3) (thickness in nm) stack. (a) and (b) illustrate the HAADF-STEM images of the layered structure. While (c) show the corresponding BF-STEM image of (b). (d) EELS-STEM map depicting the elemental distribution of the Gd (green), and Co (red) layers. These STEM measurements confirm that the Gd is mainly present into bottom Pt/Co interface during the deposition process of the Pt/Gd (0.06-0.77 nm)/Co/Pt stack.	111

LIST OF FIGURES

- 4.13 Hysteresis loop for Pt/Gd/Co/Pt stack at t_{Gd} equal to 0.07 nm (black curve) and 0.3 nm (red curve). In plane magnetization has been observed within for a Gd thickness of 0.3 nm. While out of plane has been performed for 0.07 nm. 112
- 4.14 AO-HIS state diagram realized on Pt/Gd (0.06-0.3 nm) Co/Pt stack. Magnetization behavior as a function of the Gd thickness t_{Gd} , and the laser fluence F , for Linearly polarized static beam with 60 μm of laser diameter. The dark blue circle (light blue triangle) and the light green square (dark green star) represent respectfully the switching fluence F_{Switch} and the demagnetization fluence F_{Demag} within switching (perfect toggle switching) regime. The pulse duration is 35 fs for all measurements. 113
- 4.15 AO-HIS state diagram realized on Pt/Gd/Co/Pt. Variation of the fluence and the pulse duration for t_{Gd} equal to 0.07 nm (left) and 0.21 nm (right). The dark blue circle (light blue triangle) and the light green square (dark green star) represent respectfully the switching fluence F_{Switch} and the demagnetization fluence F_{Demag} within switching (perfect toggle switching) regime. These magnetic state diagrams were established by performing linear fits to delineate the switching region with no switching and Demagnetization region. The incident laser pulse is linearly polarized and the laser diameter is 60 μm 115
- 4.16 Illustration of the two samples needed to form the CoGd-wedge. In the middle of the wedge, the thickness of CoGd alloy is 0.8 nm and the composition is $\text{Co}_{90}\text{Gd}_{10}$. The red and black mark on the surface of the sample were used to identify the region of the wedge where we have more Co and Gd, respectively. The total length of each wedge is 50 mm. 117
- 4.17 Evolution of the (a) Gd(Co) concentration and (b) the thickness of the CoGd alloy as a fonction of the CoGd-wedge position. 118
- 4.18 (a) Hysteresis loop for Pt/CoGd(wedge)/Pt stack for $\text{Co}_{93}\text{Gd}_7$ (red curve) and $\text{Co}_{75}\text{Gd}_{25}$ (black curve). Both curves show a Co-dominant stack with an OOP magnetization. (b) Evolution of the coercive field with the Gd concentration. . . 119

<p>4.19 AO HIS state diagram realized on Pt/CoGd (wedge)/Pt full film. Magnetization behavior as a function of the Gd concentration, and the laser fluence F, for Linearly polarized static beam with 70 μm of laser diameter. The dark blue circle (light blue triangle) and the light green square (dark green star) represent respectfully the switching fluence F_{Switch} and the demagnetization fluence F_{Demag} within switching (perfect toggle switching) regime. The pulse duration is 35 fs for all measurements.</p>	120
<p>5.1 Characterization of the Glass/Ta(3nm)/Pt(3.7 nm) /Gd/Co(0.7nm)/Pt(3nm) stack. (a) HRTEM micrograph with the FFT electron diffraction pattern of the Ta layer (green rectangle), lower Pt layer (dark blue rectangle), upper Pt layer (light blue rectangle) and all Pt/Gd/Co/Pt layers (red rectangle). The crystallographic [111] direction remains unchanged despite the presence of a small amount of Gd in the bottom Pt/Co interface. (b) Intensity depth profile of Pt, Co and Gd using Energy-dispersive X-ray spectroscopy (EDXS) measurement performed along the orange arrow in (a). (c) Sketch of the heterostructure.</p>	125
<p>5.2 Characterization of the Glass/Ta (3 nm)/Pt (3.7 nm)/Gd/Co (0.7 nm)/Pt (3 nm) stack. (a) and (b) illustrate the HAADF-STEM images of the layered structure. While (c) show the corresponding BF-STEM image of (b). (d) EELS-STEM map depicting the elemental distribution of the stack: Ta (green), Pt (blue), and Co (red). The absence of Gd in (a), (b), (c), and (d) is due to the Gd thickness below the spatial resolution limit of the STEM.</p>	126
<p>5.3 Out of plane hysteresis loop for Glass/Ta (3 nm)/Pt (3.7 nm)/Gd/Co (0.7 nm)/Pt (3 nm) stack performed through (a) MOKE magnetometry and (b) Vibrating Sample Magnetometer. All the measurements have been realized at room temperature.</p>	127

LIST OF FIGURES

- 5.4 Magneto-optical images of Pt(3.7 nm)/Gd/Co(0.7 nm)/Pt(3 nm) full film obtained after the action of five consecutive single laser pulse of 35 fs. The dark grey (light grey) area represents the out of plane magnetization of the film pointing “up” (“down”) as represented by the circled disk (cross). Every single femtosecond pulse with a fluence of 11.9 mJ/cm^2 illuminates the same circular region of the full film and reverses the magnetization within it. b) AO-HIS state diagram realized by Varying the fluence and the pulse duration. The dark blue circle and light green square represent respectfully the threshold switching fluence F_{Switch} and the demagnetization fluence F_{Demag} within switching state. These magnetic state diagrams were established by performing linear fits to delineate the switching region with no switching and multidomain state region. c) Size evolution of the switched domain with the pulse duration at a fixed fluence of 11.9 mJ/cm^2 . d) Multidomain state obtained after the action of a single pulse at 4 ps of pulse duration with two different laser pulse fluence. In all the AOS experiments, the incident laser pulse is linearly polarized, and the laser diameter is $80 \mu\text{m}$. The length of the scale bar is $40 \mu\text{m}$ 129
- 5.5 Magneto-optical images of magnetic disks made of Pt(3.7 nm)/Gd/Co(0.7 nm)/Pt(3 nm) obtained after the action of (a-h) a single and (i-p) two consecutive 35 fs linearly polarized laser pulses. For (a)-(h) ((i)-(p)) the light grey (dark grey) area represents magnetization of disks pointing “down” (“up”). Each laser pulse with a fluence of 9.2 mJ/cm^2 irradiates different array of the patterned structure. 131
- 5.6 Magneto-optical images of magnetic disks made of Pt (3.7 nm)/Gd/Co (0.7 nm)/Pt (3 nm) obtained after the action of 1, 2, 3, 599 and 600 consecutive 35 fs linearly polarized laser pulses. The light grey (dark grey) area represents magnetization of disks pointing “down” (“up”). Each laser pulse with a fluence of 9.2 mJ/cm^2 irradiates different array of the patterned structure. 132
- 5.7 MFM mapping of $1 \mu\text{m}$, 800 nm , 600 nm , and 400 nm diameter disks array after exposure to a single laser pulse. The dark contrast corresponds to the reversed disks. The field of view is $80 \mu\text{m}$ for all MFM images. 133
- 5.8 MFM mapping of 800 nm diameter disks array after exposure to 1, 2, 3, 599 and 600 consecutive laser pulses. The dark contrast corresponds to the reversed disks. The field of view is $80 \mu\text{m}$ for all MFM images. 134

5.9 Radial profile of a AOS experiment realized by integrating on (a) different circular rings thickness, and on (b) constant number of disks. (c) mixed approach of (a) and (b).	135
5.10 Radial switching profiles of magnetic disks made of Pt (3.7 nm)/Gd/Co (0.7 nm)/Pt (3 nm) obtained after the action of 1 (black curves), 2 (red curves), 3 (green curves), 599 (blue curves) and 600 (magenta curves) consecutive 35 fs linearly polarized laser pulses.	136
5.11 Variation of the toggle switching probability with the disk diameter in Pt (3.7 nm)/Gd/Co (0.7 nm)/Pt (3 nm) heterostructure.	137
5.12 Variation of the energy barrier ΔE with the disk diameter in Pt (3.7 nm)/Gd/Co (0.7 nm)/Pt (3 nm) heterostructure.	139
5.13 Evolution of the toggle switching (black disks) compared with (a) a simple probabilistic model analog to Condorcet’s jury theorem represented by the red curves for η' equal to -0.013 and -0.02, and (b) micromagnetic simulations represented by the blue curve for η' equal to -0.04.	140
5.14 Magneto-optical images of Pt (3.7 nm)/Gd/Co (0.7 nm)/Pt (3 nm) full film obtained after the action of two consecutive single laser pulse of (a) 2 ps and (b) 2.5 ps. The dark grey (light grey) area represents the out of plane magnetization of the film pointing “up” (“down”) as represented by the circled disk (cross). The AOS experiments were performed for a fluence range from 10.7 to 16 mJ/cm ² and an inhomogeneous switching domains are observed. The length of the scale bar is 40 μ m and the laser beam diameter is 70 μ m.	142
5.15 MFM mapping of 1 μ m diameter disks array after exposure to 1, 2 and 600 consecutive laser picosecond pulses with the circularly left (blue circle), right (red circle) and linearly (green arrow) polarized light. The light contrast corresponds to the reversed disks. The field of view is 80 μ m for all MFM images.	143
5.16 Radial switching profiles of magnetic 1 μ m disks made of Pt (3.7 nm)/Gd/Co (0.7 nm)/Pt (3 nm) obtained after the action of 1, 2 and 600 consecutive picoseconds pulses with the circularly left (blue curves), right (red curves) and linearly (green curves) polarized light.	145
5.17 Radial switching profiles of magnetic disks from 1 μ m to 400 nm made of Pt (3.7 nm)/Gd/Co (0.7 nm)/Pt (3 nm) obtained after the action of 1, 2 and 600 consecutive picoseconds pulses with the circularly left, right and linearly polarized light.	146

LIST OF FIGURES

5.18	Evolution of the average magnetization m of 1 μm to 400 nm disks made of Pt (3.7 nm)/Gd/Co (0.7 nm)/Pt (3 nm) obtained after the action of 1, 2 and 600 consecutive picoseconds pulses with the circularly left, right and linearly polarized light.	147
A.1	View of the switching probability	154
1	Principal résultat de ce travail. a) Images magnéto-optiques du film continu de Pt(3.7 nm)/Gd/Co(0.7 nm)/Pt(3 nm) obtenues après l'action de cinq impulsions laser uniques consécutives de 35 fs. La zone gris foncé (gris clair) représente l'aimantation hors plan du film pointant "vers le haut" ("vers le bas") comme représenté par le point (croix) encerclé. Chaque impulsion femtoseconde unique avec une fluence de 11.9 mJ/cm^2 illumine la même région circulaire du film et retourne l'aimantation à l'intérieur. b) Diagramme d'état AO-HIS réalisé en faisant varier la fluence et la durée de l'impulsion. Le cercle bleu foncé et le carré vert clair représentent respectivement la fluence seuil de retournement et la fluence de démagnétisation. c) Croquis de l'empilement des couches minces.	178

List of Tables

1.1	Different IFE model to explain all optical switching in magnetic materials. . . .	31
4.1	Summary of Δ limit values in the switching and PTS regime for thinner and thicker Gd.	115
4.2	Deposit parameters value.	118

Introduction

The possibility to manipulate magnetization deterministically with a single femtosecond laser pulse under no applied field has attracted great attention for application on high-speed and energy-efficient magnetic data storage, memories, and logic. In 2011, the first observation of ultra-fast single pulse all optical helicity independent switching (AO-HIS) was reported¹. Since then, AO-HIS has been achieved in various ferrimagnetic Gd based sample such as $Gd_x(FeCo)_{1-x}$ thin amorphous films¹⁻⁵, Gd_xCo_{1-x} thin amorphous films⁶, Gd/Co multilayers⁷ and $Gd_{1-x-y}Tb_yCo_x$ alloys^{8,9}. Moreover, in 2016, by taking advantage of the exchange coupling between a Co/Pt multilayer and GdFeCo, it has been demonstrated the switching of the Co/Pt magnetization induced by a single femtosecond laser pulse¹⁰. Two years later (2018), AO-HIS has also been reported in more complex heterostructure such as $Gd_x(FeCo)_{1-x}$ based spin valves¹¹. Investigations of single thermal AOS in spin valves for different magnetic materials remains a major area of interest for the research community, as the physics is rich in these complex structures¹²⁻¹⁴. In 2020, the first observation of AO-HIS mechanism without Gd has been reported for two types of structure without Gd: in half-metallic ferrimagnetic Heusler alloys Mn_2Ru_xGa which possesses two inequivalent Mn sublattices¹⁵ and in Co/Tb multilayer^{16,17}. The latter recent work demonstrates that the mechanism is very different to the one observed for Gd based samples.

Experimental results obtained on various magnetic materials demonstrating AO-HIS show the presence of common criterion. First the sample are made of two magnetization sublattice antiferromagnetically coupled resulting either an alloy or a multilayer. In 2017, it has been showed that for the case of alloy samples, the composition showing AO-HIS are close to compensation for which the net magnetization of the sample is close to zero². In addition, the laser fluence needed to obtain AO-HIS is found to be minimum around compensation⁵. Theoretical studies and modeling have demonstrated that the exchange coupling between the two magnetization sublattice play a crucial role in the angular momentum transfer between the sublattices¹⁸. The two main approaches to describe the magnetization dynamic

INTRODUCTION

of the sublattices are the microscopic three-temperature model (M3TM)¹⁹ and the atomistic Landau-Lifshitz-Gilbert equation²⁰⁻²². Those models can predict that the optimal ratio of transition-metal atoms to rare-earth atoms for successful switching is close to the ferrimagnetic alloy compensation³. In 2019, experimental and theoretical studies on Co/Gd bilayers²³ show that contrary to rare-earth transition-metal ferrimagnetic alloys, the bilayers can be switched in the absence of a magnetization compensation temperature. Likewise, it is demonstrated that by changing the intermixing between Co and Gd at the interface the thickness range at which AO-HIS can be observed change drastically as well as the threshold fluence²⁴. However, for future application the presence of rare-earth elements is not recommended because of very low TMR ratio that can be obtained in rare-earth based Magnetic Tunnel Junction^{25,26}.

This thesis manuscript is separated into five chapters. First, a state of the art of all-optical switching will be presented, focusing on the results of the size effect on magnetic materials that exhibited AO-HIS mechanism. In the second chapter, the experimental methods used for the fabrication of the micro- and nano-disks arrays, for the realization of AOS experiments and for the characterization of the studied samples after/before these AOS experiments are detailed. In the third chapter, we investigate the size effect on single pulse AO-HIS in GdFeCo disk array. The behavior of thresholds fluences on disk size highlights the importance of the specific light absorption in nanostructures. In the fourth chapter, we investigate and demonstrate that a [Co/Pt] doped with an infinitesimal amount of Gd at one of the Pt/Co/Pt interfaces show single pulse AO-HIS. This study highlights the dependence of AO-HIS properties with the Gd position and magnitude. Finally, in the fifth chapter, the size effects of AO-HIS in Gd-dusted Pt/Co/Pt disks are studied. The variation of the switching probability with the disks size is precisely measured and explained by a non-uniform switching process.

Chapter 1

State of art

Achieving control of the magnetization at smaller length scale and faster timescale is the horizon of research in magnetism. This interest stems from the ever-increasing need to decrease the reading and writing rate of magnetic memory devices which are made of nanosized magnetic bits. For the manipulation of magnetism in 100 ps range, several efficient techniques (spin-polarized charge currents^{27,28}, electric fields^{29,30}, Terahertz pulses³¹...) have been developed. However, the ultrafast control of the magnetization of a magnetic material by laser pulses with no external magnetic field appears to be another method to manipulate magnetic mediums. Indeed, from the observation in 1996 of the demagnetization of a continuous Ni film by femtosecond laser excitation³² to the reversal of the magnetization of $\text{Gd}_{1-x-y}\text{Tb}_y\text{Co}_x$ alloy using a single laser pulse in 2022⁹, many advances in the understanding of the control of magnetic order in magnetic materials have been made. This increasing research activity around All Optical Switching (AOS) makes sense through its potential for new technologies such as Heat-Assisted Magnetic Recording (HAMR)³³. Although the ferrimagnetic GdFeCo alloy was the first material to have its magnetization manipulated using multiple femtosecond laser pulses in 2007³⁴, El Hadri et al.³⁵ clearly demonstrate ten years later that magnetic material that exhibit AOS should be divided in two categories with different mechanism. However, to go for magnetic recording application, it is the Single Pulse All Optical Switching Helicity Independent Switching (SP-AOHIS) mechanism that turned out to be the best candidate. If ferrimagnetic materials is the most common magnetic material showing SP-AOHIS, Vomir et al. demonstrated surprisingly single-shot AOS in a Pt/Co/Pt film by using focused laser beam spot of 800 nm in size³⁶. Nevertheless, since this switching requires only one laser pulse, its read-write time is very fast (a few picoseconds^{1,37}). It is on magnetic materials that exhibit this type of all-optical switching that we will study the size effect in this thesis. Therefore, in this chapter 1, we aim to give an overview

of recent experimental results and theoretical approaches to all-optical switching with a focus on the size effect in the GdFeCo alloy. In this thesis, we will firstly continue this size study in this ferrimagnetic alloy and then in a new interface-engineered ferromagnet whose full film will also present SP-AOHIS. In section 1.1, we focus on the historical results of laser-induced demagnetization in Ni and the different theoretical approaches to understand ultrafast magnetization dynamics. In section 1.2, we present chronologically different works on light inducing ultrafast magnetization switching in GdFeCo, then to other ferrimagnetic materials. Section 1.3 is devoted to the second category of optical switching observed in ferromagnets, and a discussion of possible mechanisms that may explain this helicity-dependent optical switching is made. Section 1.4 is dedicated to the possibility to observe helicity-independent optical switching in a ferromagnet with the help of a spin current through spin valve. Finally, we review several studies of the size effect on all optical switching performed mainly on ferrimagnetic alloys.

1.1 Laser induced dynamics in metals

1.1.1 Ultrafast demagnetization in Ni film

The study of short timescale magnetization dynamic by instantaneous excitation such as laser pulses presents challenges for fundamental understanding of magnetization processes in the non-equilibrium state and for promising technological applications that need ultrafast control of magnetic materials and devices. In 1991, this investigation field relatively increases with the estimation of the gadolinium demagnetization time, $\tau_M \approx 100 \pm 80$ ps by Vaterlaus et al.³⁸ using time- and spin-resolved photoemission (TSPE) experiments. However, it's in 1996 that the field of light-induced ultrafast magnetization dynamics really started with the discovery by Beaurepaire et al.³², who demonstrated that a Ni thin film can be demagnetized in less than 1 picosecond. Indeed, they performed TR-MOKE pump-probe experiments on a polycrystalline thin Ni films of 22 nm thickness with the help of a femtosecond laser pulse of 60 fs for a laser fluence of 7 mJ/cm². Figure 1.1 displays the variation of the TR-MOKE signal as a function of the delay Δt between the laser pump and the probe. A quick decrease of the magnetization is observed in the first 2 ps, followed by a slower recovery. As this signal was thought to be proportional to the magnetization, this behavior was attributed to a fast increase of the spin temperature T_s during the first picosecond and followed by the partial reconstruction of the magnetization after 15 ps. Moreover, by using a pump-probe transmission experiments, they also measured the electronic temperature T_e as a function of Δt and correlated the increase of

T_s in the first picosecond to the augmentation of T_e up to 550 K in a characteristic time of 1 ps. A phenomenological model that will be presented in the section 1.1.2.1 of this chapter was used by the authors to explain the behavior of these two temperature baths, with the help of the phonon temperature. As lattice showed to be one of the thermalized reservoirs that exchange energy with electron and spin. Several research groups confirmed this result^{39–42} and others ferromagnetic materials like CoPt₃ or Fe showed the same ultrafast demagnetization behavior under the irradiation of a femtosecond laser pulses^{43,44}.

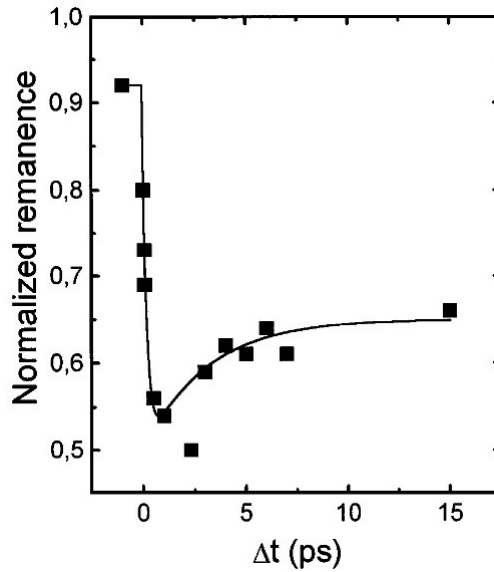


Figure 1.1: Variation of the Normalized transient remanent longitudinal MOKE signal with the delay Δt between the laser pump and the probe of a Ni(20 nm)/MgF₂ (100 nm) film for a laser pump fluence of 7 mJ/cm². Figure taken from³².

1.1.2 Mechanism involved in the ultrafast magnetization dynamics

Many interrogations have been raised to understand the ultrafast spin dynamics of metal compounds. One of these questions was the identification of the microscopic mechanism involved in the ultrafast demagnetization. The more difficult issue was the understanding of the difference in demagnetization time scale between earth-rare ferromagnets ($\tau_M \approx 100 \pm 80$ ps) and transition metal ferromagnets ($\tau_M < 500$ fs). Although these questions are still fully discussed today, in this section we review several models and mechanisms that may be implicated in the dynamics of ultrafast magnetization.

1.1.2.1 Phenomenological three-temperature model (3TM)

This is the first model introduced by Beaurepaire et al.³² to describe the ultrafast demagnetization induced by a femtosecond laser pulse in a magnetic material. As shown in section 1.1.1, Beaurepaire and co-authors demonstrated the ultrafast demagnetization of a Ni thin film due to the excitation by a 60 fs laser pulses. In this phenomenological approach, the material is represented by three baths: electrons, spins and phonons as illustrated in Figure 1.2(a). These three reservoirs interact with each other and are characterized by different thermal behaviors after laser excitation. The total system is defined by three differentials coupled equations:

$$\begin{aligned}
 C_e \frac{dT_e}{dt} &= -G_{el}(T_e - T_l) - G_{es}(T_e - T_s) + P(t) \\
 C_s \frac{dT_s}{dt} &= -G_{es}(T_s - T_e) - G_{sl}(T_s - T_l) \\
 C_l \frac{dT_l}{dt} &= -G_{el}(T_l - T_e) - G_{sl}(T_l - T_s)
 \end{aligned} \tag{1.1}$$

Where (T_e, C_e) , (T_s, C_s) and (T_l, C_l) are the couples (temperature, specific heat) for electrons, spins and lattice, respectively. G_{el} , G_{es} and G_{sl} are the electron-lattice, electron-spin and spin-lattice coupling, respectively. The laser source represented by $P(t)$ is only present in the electronic equation because the electron bath is the first reservoir to be optically heated at these ultrafast frequencies. Thus, the laser first brings the electron bath to high temperature in a few hundred femtoseconds, followed by a redistribution of the stored energy in the rest of the system due to the interactions between reservoirs. Then, a pure energy transfer takes place, resulting in an increase in the spin and lattice bath until all three baths are thermalized as shown in Figure 1.2(b).

This simple model allows us to understand the increase of the spin temperature, which will lead to demagnetization. Moreover, another pure energy transfer theory was introduced by Kazantseva et al⁴⁵ in 2008. This model is an atomistic approach based on the Landau-Lifshitz-Gilbert equation, where the transfer of energy between electrons and spins is realized by a phenomenological coupling constant. However, 3TM and this atomistic approach ignore the conservation of angular momentum, which is the origin of magnetization dynamic.

1.1. LASER INDUCED DYNAMICS IN METALS

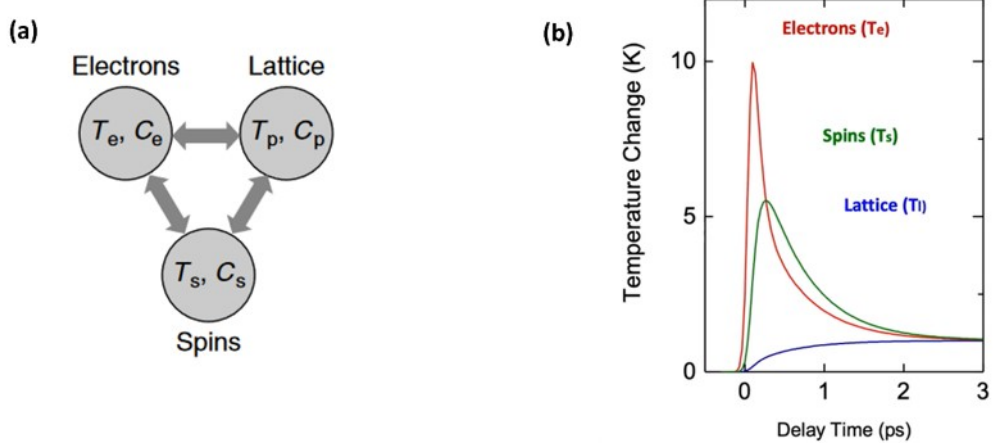


Figure 1.2: (a) Three temperature model represented by 3 baths in interactions. (b) Variation of the three temperatures baths after the excitation by a femtosecond laser pulse (Delay Time above 0 ps). Figure taken from³².

1.1.2.2 Laser-induced demagnetization via spin-orbit coupling

One of the first attempt to explain the ultrafast demagnetization in ferromagnetic metal was carried out by G. P. Zhang and W. Hübner in 2000⁴⁶. In this model, they only consider the external laser excitation and the internal spin-orbit coupling (SOC). Thus, the total Hamiltonian is given by:

$$H = H_{sys} + H_{ex} \quad (1.2)$$

Where

$$H_{sys} = \sum_{i,j,k,l,\sigma,\sigma',\sigma'',\sigma'''} U_{i\sigma,j\sigma',l\sigma'',k\sigma'''} c_{i\sigma}^\dagger c_{j\sigma'}^\dagger c_{k\sigma''} c_{l\sigma'''} + \sum_{\nu,\sigma,K} \mathbb{E}(\mathbf{K}) n_{\nu,\sigma}(\mathbf{K}) + H_{SO} \quad (1.3)$$

And

$$H_{ex} = \tilde{\mathbf{E}}(t) \cdot \mathbf{D} = (\mathbf{E}_1(t) + \mathbf{E}_2(t - \tau)) \cdot \mathbf{D} \quad (1.4)$$

With

$$E_i(t) = A_i e^{-t^2/\Gamma_i^2} \cos(w_i t) \quad (1.5)$$

In the Hamiltonian system H_{sys} , $U_{i\sigma,j\sigma',l\sigma'',k\sigma''}$ is the on-site electron interaction with the orbital indices i, j, k, l and spin indices $\sigma, \sigma', \sigma'', \sigma''$. The last two expressions are the band structure and spin-orbit coupling^{47,48}, respectively. In H_{ex} , $\tilde{\mathbf{E}}(t)$ and \mathbf{D} represents the electric field and the dipolar operator, respectively. Where τ, A_i, Γ_i and w_i is the time delay between

CHAPTER 1. STATE OF ART

two pulses, the amplitude, the temporal width and the incoming laser frequency of the pulse i , respectively. Then, by solving numerically, the Schrodinger equation, they can extracted the transient magnetic moment $M(t)$, given by:

$$M(t) = \langle \Psi(t) | S_z | \Psi(t) \rangle \quad (1.6)$$

Where $|\Psi(t)\rangle$ is the electronic state at the time t , and S_z is the z component of the spin operator. Figure 1.3(a) presents the evolution of $M(t)$ in two different cases:

- For a suppression of the spin-orbit coupling ($\lambda = 0$) and a laser field intensity of $I = 0.3$ u.a , Figure 1.3(a) shows a high constant value of $M(t)$ after the excitation of the system by a laser pulse.
- For zero laser field intensity and maintaining the spin-orbit coupling ($\lambda \neq 0$) the magnetic moment decreases by 2%-5%. This reduction is due to the coupling of triplet and singlet states driven by the SOC.

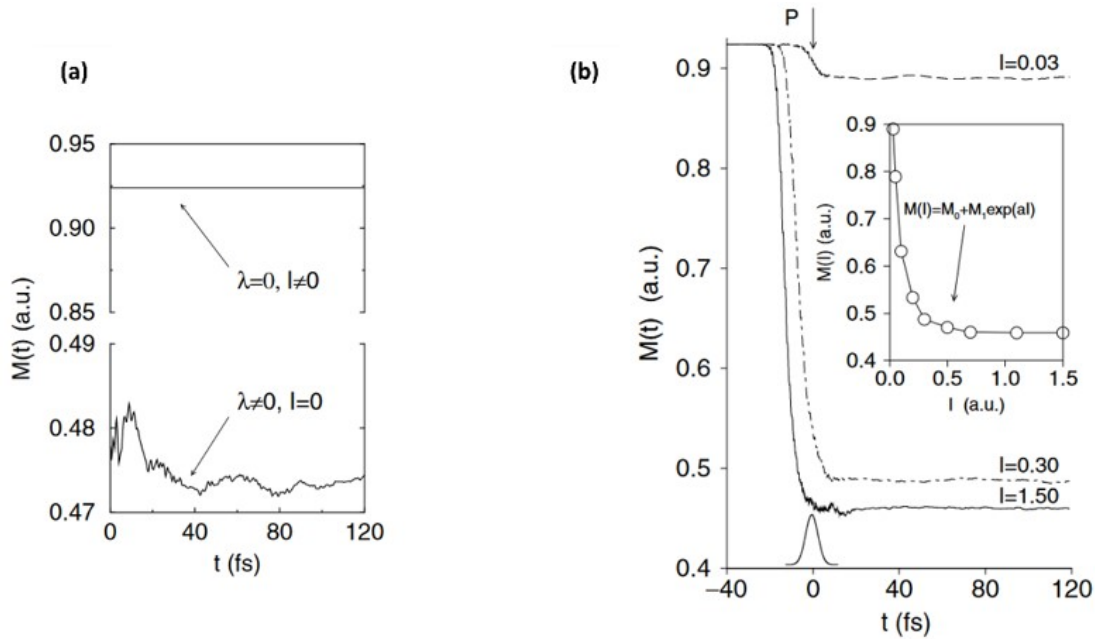


Figure 1.3: Evolution of the magnetic moment $M(t)$ with time after one laser pulse excitation for the case (a) without spin-orbit coupling (upper panel), (a) without laser field (lower panel) and (b) with the presence of both spin-orbit coupling and the laser field for various laser intensity of $I(u.a) = 0.03$ (long-dashed line), 0.3 (dot-dashed line) and 1.5 (solid line). Inset: exponential trends of $M(I)$ with the laser intensity field I . Figure taken from⁴⁶.

1.1. LASER INDUCED DYNAMICS IN METALS

These two scenarios highlighted that no clear spin relaxation for the Hamiltonian H can be obtained by considering the laser field alone and only the SOC is not sufficient to cause a significant decrease of the magnetic moment. However, combining the two cases ($I \neq 0$ and $\lambda \neq 0$), for a given photon energy of $2eV$ and a Gaussian pulse distribution with a temporal width $\Gamma = 10fs$, results in a reduction of more than 40% of the magnetic moment for a laser intensity of $I = 0.3$, in a shorter timescale of $20fs$. In fact, as shows in Figure 1.3(b), ultrafast demagnetization is observed for just one pulse ($A_1 \neq 0$ and $A_2 = 0$), and the reduction ratio of $M(t)$ strongly depends on the laser intensity. Indeed, the reduction ratio goes from 4% for low laser intensity $I = 0.03$ to a maximum of 50% for high laser intensity $I = 1.5$. The authors identified the mechanism involved in the ultrafast demagnetization as a cooperative process between the laser field induced transitions from large-spin ground state to higher energy small-spin states, and the action of spin-orbit coupling enabling the forbidden transition between triplets and singlets on the femtosecond timescale. However, it has been shown that the required conditions are not realized experimentally so far^{49,50}, which does not allow us to fully validate this model.

1.1.2.3 Microscopic three-temperature model (M3TM)

This model was introduced by Koopmans, B. et al.¹⁹ in 2010 and emphasizes that the electron-phonon interaction is the main phenomenon responsible for the rapid laser-induced demagnetization. Indeed, based on the Elliot-Yafet scattering, dissipation of angular momentum was attributed to the probability a_{sf} that an electron flips its spin on emission or absorption of a phonon. This type of electron scattering was also used by Koopmans, B. et al.⁵¹ to explain theoretically the rapid equilibrium of the magnetic order in a ferromagnet at a few hundred femtoseconds after laser pulsed irradiation. Moreover, other experimental results conclude the same necessity of the Elliot-Yafet model to understand the rapid demagnetization of Ni⁵² and Co⁵³ film.

Figure 1.4 represents the microscopic three-temperature model (M3TM). Moreover, the evolution of a_{sf} is function of the temperature of the electron bath, and the decrease of the magnetic moment appears when a_{sf} is high enough. After a characteristic time τ_M , the Elliot-Yafet mechanism leads to an equilibrium, where demagnetization is achieved. In addition, the thermalization mechanism leads to electron-phonon equilibrium after a characteristic time τ_E . Those two effects are encoded in a compact differential equation for the magnetization dynamic determined by using a simple model Hamiltonian H (see all the hypothesis and calculation in^{19,51}):

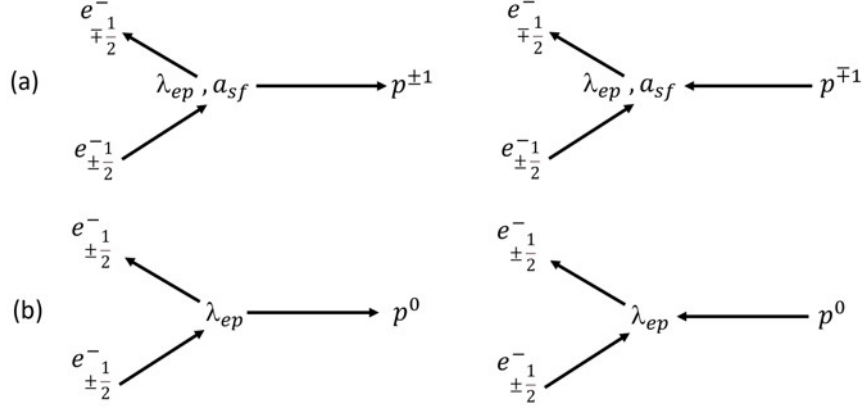


Figure 1.4: Illustration of the M3TM with an Elliot-Yafet mechanism inducing (a) ultrafast demagnetization and (b) thermalization of the electrons bath after emission or absorption of phonons.

$$\frac{dm}{dt} = mR \frac{T_p}{T_C} \left(1 - m \coth \left(\frac{mT_C}{T_e} \right) \right) \quad \text{where} \quad R = \frac{8k_B T_C^2 V_{at}}{(\mu_{at}/\mu_B) E_0^2} a_{sf} \lambda_{ep} \quad (1.7)$$

Coupled at two other differential equations on electrons and phonons in quasi-equilibrium, referred as two temperature model (2TM)⁵⁴

$$\begin{aligned} C_e \frac{dT_e}{dt} &= \nabla_{\perp} (\kappa \nabla_z T_e) + \lambda_{ep} (T_p - T_e) \\ C_p \frac{dT_p}{dt} &= \lambda_{ep} (T_e - T_p) \end{aligned} \quad (1.8)$$

The couples of parameters (T_e, C_e) and (T_p, C_p) are the couples (temperature, heat capacity) for electronics and phonons bath, respectively. T_C and κ represent the Curie temperature and the conductivity of the material. The spin variation is encoded inside two parameters: λ_{ep} the electron-phonon interaction and a_{sf} assimilated to the effective cross-section which drive the demagnetization. μ_{at} is the atomic magnetic moment and $R(s^{-1})$ in the dynamic equation is the term that will characterize the type of demagnetization. In fact, since R is inversely proportional to the characteristic time of demagnetization τ_M , two types of demagnetization occur. To find out which type of demagnetization takes place, a comparison between R and the characteristic time of electron thermalization τ_E was used. Therefore, we have two limiting cases as shows in Figure 1.5:

- $R \gg \tau_E^{-1}$ ($\tau_M \ll \tau_E$): the demagnetization is so rapid that it occurs before the equilibrium between electron and phonon is reached. Around τ_M , we observe a partial recovery of the magnetization (Figure 1.5(a)).

1.1. LASER INDUCED DYNAMICS IN METALS

- $R \ll \tau_E^{-1}$ ($\tau_M \gg \tau_E$): the equilibrium between electrons and phonons is reached before the equilibrium of the spin reservoir. We have a first ultrafast demagnetization step in about hundreds of femtoseconds, followed by a regime change around τ_E (Figure 1.5(b))

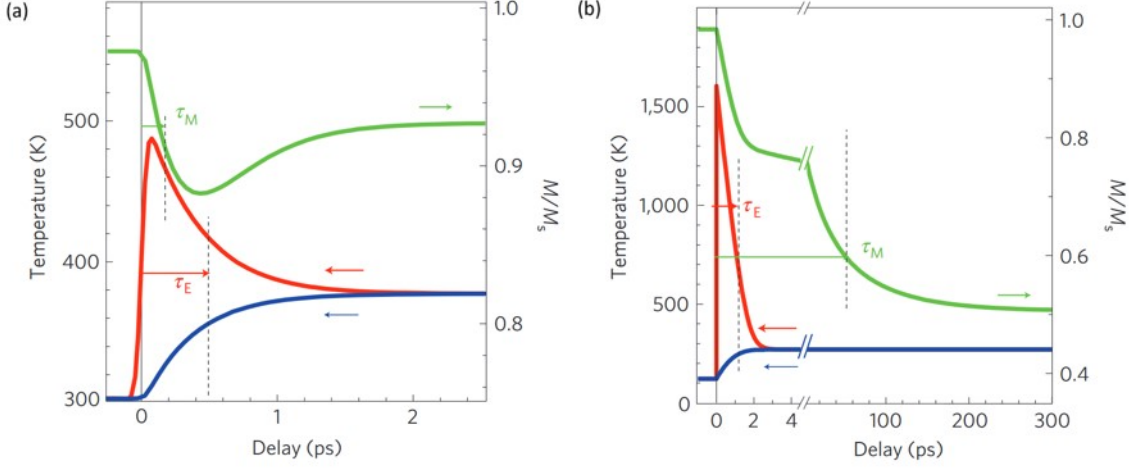


Figure 1.5: Evolution of the electron temperature T_e (red curve), phonon temperature T_p (blue curve) and the magnetization (green curve) as a function of time. These variations are obtained after using the microscopic three-temperature model and showed two different demagnetization behaviors in ferromagnetic materials. Figure taken from¹⁹.

This simulation result fitted well with experimental ultrafast demagnetization observed in ferromagnetic materials. Indeed, the two-step demagnetization observed in the experiment on Gd^{38} is well reproduced with M3TM with a demagnetization time of 100 ps. In addition, the rapid demagnetization in Ni was also reproduced with this theory with demagnetization time in a hundred of femtosecond. However, the microscopic origin of the conservation of angular momentum during the ultrafast demagnetization is still an open question. In fact, by combining TRMOKE and time-resolved reflectivity measurements within an epitaxial Fe thin film, E. Carpene et al.⁵⁵ demonstrated that the laser-induced ultrafast demagnetization can be attributed to the electron-magnon interaction which takes place in a hundred of fs. In this model, the dissipation of angular momentum is correlated to the excitation of hot electron, leading to a rapid reduction of the magnetization, mediated by the spin-orbit coupling. In addition, in this approach, the electron-phonon is only responsible for the partial restoration of spin order due to the Elliott-Yafet spin-flip scattering process on a time scale slightly below the picosecond.

1.2 All Optical switching in ferrimagnet

A ferrimagnetic material is a magnetic material composed of two sublattices of unequal magnetic moment and antiferromagnetically coupled. One of the most interesting ferrimagnets for the study of All Optical Switching (AOS) turned out to be thin film of GdFeCo. Indeed, it is an amorphous alloy with a Rare Earth “RE” (Gd) and transition metal “TM” (FeCo) sublattice, exhibiting perpendicular magnetic anisotropy (PMA)⁵⁶, allowing a possibility of integration in high storage density memories⁵⁷. Moreover, many research groups demonstrated the possibility to manipulate the magnetic characteristics of $\text{Gd}_x(\text{FeCo})_{1-x}$ either with the concentration of both RE and TM or with the sample temperature^{2,34,58}. For $x < x_{com}$ ($x > x_{com}$), the dominant moment contribution comes from the magnetic moment of the TM (RE) sublattice, resulting in the orientation of the total moment \vec{m} ($\vec{m} = \vec{m}_{TM} - \vec{m}_{RE}$) in the direction of FeCo (Gd) sublattice, referred to as “TM-dominant” (“RE-dominant”). For $x = x_{comp}$, the two sublattices have two equal opposite magnetic moments, resulting in a total magnetic moment of zero, referred to as “compensation point”. In this section, we will present in chronological order, the experimental results that demonstrate AOS in ferrimagnetic materials.

1.2.1 AO-HDS in ferrimagnetic materials

With the first discovery of laser-induced ultrafast demagnetization in a metal³², many research groups have attempted to observe the reversal of the magnetization of magnetic materials. It was in 2007 that Stanciu, C. D. et al.³⁴ reported for the first time a deterministic reversal of the magnetization of a 20 nm thin film of $\text{Gd}_{22}\text{Fe}_{76.6}\text{Co}_{3.4}$ by using femtosecond laser pulses. In this discovery, the reversal depended on the helicity of the laser, called All-Optical Helicity Dependent Switching (AO-HDS), and the authors demonstrated the need of several pulses to observe the switching of the magnetization, called Multiple Pulse All-Optical Helicity Dependent Switching (MP-AOHDS). Figure 1.6 shows magneto-optical images that illustrated the effect of the low sweeping (30 m.s^{-1}) by an 800 nm-laser on the sample with a repetition rate of 1 kHz, a fluence of 11.4 mJ/cm^2 and a pulse duration of 40 fs. The magnetic domain pointing “up” (“down”) represented by the light (dark) contrast has its magnetization being reversed by the sweeping of the σ^- (σ^+) polarized laser. For linear polarization L , only demagnetization was obtained, marked by the creation of multi-domains with a random orientation of their magnetization after the passage of the laser, whatever the initial direction of the magnetic domains. In addition, the authors attributed the mechanism of AOS to the combination of a thermal effect with an inverse Faraday effect “IFE” (this effect will be discussed in more detail in section

1.2. ALL OPTICAL SWITCHING IN FERRIMAGNET

1.3.4.2). Indeed, the irradiation of a laser on a material brings both a temperature rise, causing a decrease of the coercive field, and an effective magnetic field, due to circularly polarized light. However, due to the Gaussian distribution of the laser, the power is higher in the center of the laser, which leads to a demagnetization state, due to a loss of magnetic order when the temperature is above the Curie temperature. But, in a narrow fluence range, a thermal effect can decrease the coercive field while maintaining magnetic order and the IFE produces a higher magnetic field than the reduced coercive field, which ultimately leads to the reversal of the magnetization. This theoretical approach also explain the observation of a single pulse causes demagnetization and AO-HDS at the center and ring of the laser spot, respectively (Figure 2 in³⁴). More interesting, by adjusting the power of the laser, they were able to reverse the magnetization of a single magnetic domain with just one femtosecond laser pulse (Figure 4a in³⁴). This Single Pulse All-Optical Helicity Dependent Switching (SP-AOHDS) was clearly confirmed in another GdFeCo alloy by Vahaplar, K. et al.⁵⁹ and another mechanism was reported by Khorsand, A. R. et al.⁶⁰. Indeed, this theoretical approach is based on the fact that a material with a given magnetization absorbs more or less light depending on the polarization of the light, the so-called Magnetic Circular Dichroism “MCD” (this effect will be discussed in more detail in section 1.3.4.1).

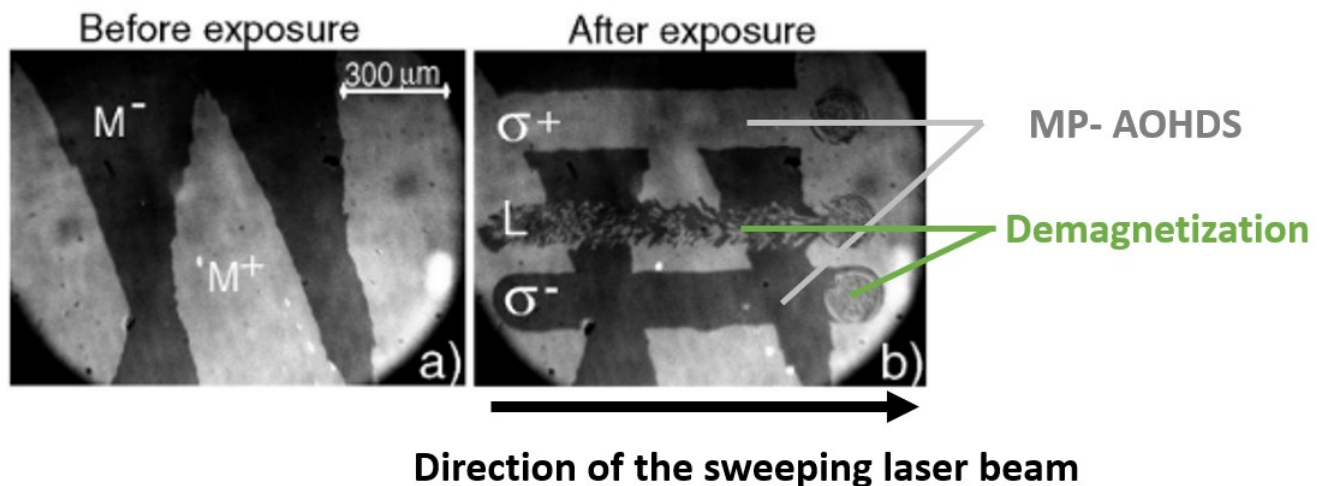


Figure 1.6: Magneto-optical images showing a) initial magnetic state before irradiation of laser on the surface and b) MP-AOHDS in $\text{Gd}_{22}\text{Fe}_{76.6}\text{Co}_{3.4}$ induced by sweeping the laser over the sample with left circular (σ^-), right circular (σ^+) and Linear (L) polarization. The light (dark) contrast represents magnetic domain with the magnetization pointing “up” (“down”). Figure taken from³⁴.

Nevertheless, this AO-HDS was also later observed within various RE-TM materials such as TbCo^{61–63}, DyCo⁶¹, HoFeCo⁶¹, TbFe^{61,64} alloys, Ho/Co and Tb/Co multilayers⁶¹, as well as RE-free Co–Ir-based synthetic ferrimagnetic heterostructures⁶¹. Additionally, several criterions and experimental conditions for the observation AO-HDS in magnetic materials were established: two antiferromagnetically coupled sublattices^{61,65}, a wide range of fluences ranging from the switching threshold to the damage threshold⁶¹, a suitable stoichiometric composition to obtain two sublattices with comparable magnetic moment near or above room temperature, resulting in a low remanence^{58,66}, and the magnetic domain size of the ferrimagnet should be equal or above the size of the laser spot⁶⁷. However, the following sections and paragraphs of this chapter will show that these rules are not general to all magnetic materials.

1.2.2 AO-HIS in ferrimagnetic materials

In 2011, a very surprising result has been demonstrated by Radu, I. et al.¹: a fascinating switching of the magnetization in 12 ps with a single 100-fs linearly polarized laser pulse. In fact, Radu, I. and Co-authors performed ultrafast spin dynamic of the two Gd and FeCo sublattices composing the Gd₂₅Fe_{65.9}Co_{9.4} alloy by using element-specific X-ray Magnetic Circular Dichroism (XMCD). Figures 1.7(a) and 1.7(b) present the temporal evolution of the magnetic moment of Gd and Fe at different time scale. The reversal of the magnetization appears to be the consequence of a rapid demagnetization rate at different time scales of the two sublattices (300 fs for the Fe sublattice and 1.5 ps for the Gd sublattice), followed by a ferromagnetic-like state (where the magnetization of the Fe and Gd sublattices is oriented in the same direction) between 300 fs and 1.5 ps, and ending with the slow recovery of the magnetization of both sublattices in the opposite direction. This type of switching referred as to Single Pulse All-Optical Helicity Independent Switching (SP-AOHIS). One year later, Ostler, T. A. et al.⁶⁸ confirmed these SP-AOHIS mechanism in Gd₂₂Fe_{76.6}Co_{3.4} thin film using a single linearly polarized pulse. Indeed, after suturing the sample, causing the orientation of the magnetization in one of the two OOP directions, the authors showed a toggle switching of the magnetization regardless of the initial direction of the magnetization (Figure 3 in⁶⁸). Since then, many other groups have obtained a similar experimental demonstration of the SP-AOHIS mechanism in GdFeCo amorphous alloy^{2,69–71}.

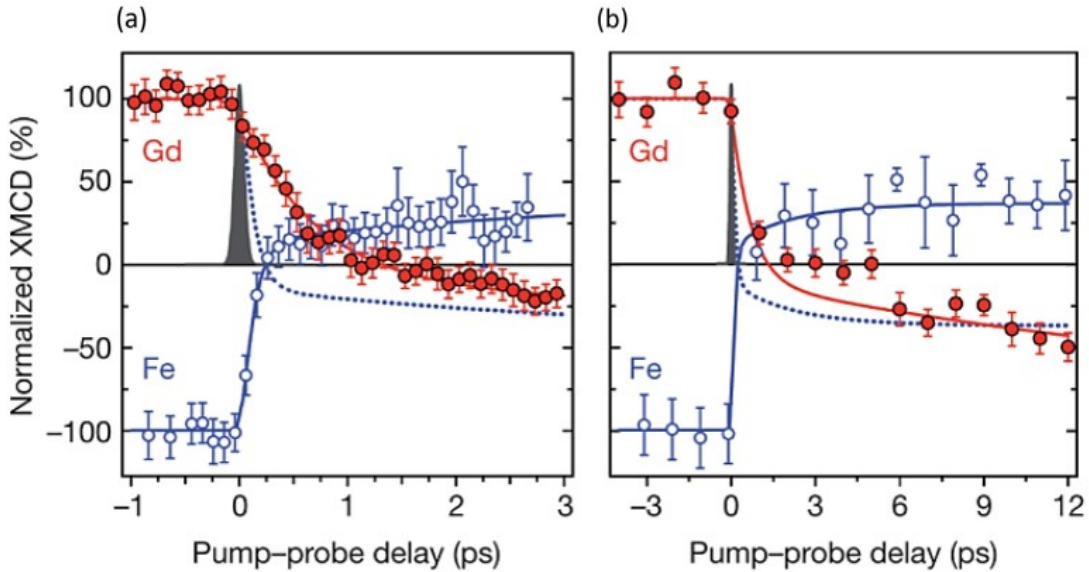


Figure 1.7: XMCD measurement of the magnetization dynamic of the Gd and Fe sublattice obtained after the irradiation of a femtosecond laser pulse for (a) a short-time scale and (b) a long-time scale. Figure taken from¹.

Therefore, the conclusion of a laser-induced AOS by a pure thermal mechanism in GdFeCo ferrimagnetic amorphous alloys was clear. Consequently, GdFeCo alloy both exhibit MP-AOHDS, SP-AOHDS and SP-AOHIS mechanism. These experimental observations raise the question of the microscopic mechanism responsible for the observation of AOS in GdFeCo ferrimagnets. Indeed, the absence of angular momentum in linearly polarized light and the observation of AOS regardless of the direction of a single magnetic domain negate the IFE and MCD mechanisms respectively as the mechanism driving AOS. Moreover, the exhibition of a ferromagnetic-like state is very surprising considering the strong antiferromagnetic coupling between the sublattices in thermal equilibrium. Although we don't yet know the microscopic mechanism behind the experimental demonstration of SP-AOHIS in GdFeCo ferrimagnetic amorphous alloys, the magnetization reversal mechanism in this material can be understood like the excitation of conduction electrons by absorption of photons^{3,70,72} allowing demagnetization under different time scales for the two sublattices (transition metal and earth-rare) thanks to Elliott-Yafet effect and exchange scattering above (conservation of spin angular momentum by exchange between the sublattices). Indeed, the femtosecond laser pulse demagnetizes the TM sublattice four times faster than the Gd sublattice due to the different type of demagnetization they exhibit individually (as discussed in section 1.1.2.3) and a weak inter-sublattice exchange

CHAPTER 1. STATE OF ART

coupling^{73,74}. As the magnetization of the TM sublattice approaches zero, the exchange relaxation^{75,76} primes and angular momentum circulates between Gd and FeCo, maintaining the total angular momentum of the system. This mechanism is maintained for a time scale related to the exchange coupling between the two spin systems, leads to the magnetization of the FeCo sublattice beyond zero, favoring the appearance of a transient ferromagnetic-like state, where FeCo and Gd have a parallel magnetic moment. As the magnetization of TM increases, the magnetization of RE continues to decrease towards zero as total angular momentum is conserved. In the end, the Gd switches, resulting in an antiparallel alignment for the two sublattices, and the lattice and spins equilibrate on different time scales. Further cooling occurs to equilibrium at a switched net magnetization^{1,77,78}. A more detailed review of the literature has recently been carried out by P. Scheid et al.⁷⁹ on the different theoretical approaches to understanding AO-HIS in ferrimagnetic alloys.

So far, most ferrimagnetic materials that exhibit SP-AOHIS are Gd-based RE-TM alloys, spin valves or multilayers, as will be shown in Sections 1.5.3, 1.4 and 1.2.3 for GdCo alloys, Pt/Co/Cu/ $\text{Gd}_x(\text{FeCo})_{1-x}$ heterostructures and synthetic Co/Gd ferrimagnets, respectively. Nevertheless, recent investigations performed by C. Banerjee et al.¹⁵ demonstrated Single shot AO-HIS in a ferrimagnetic Heusler alloys $\text{Mn}_2\text{Ru}_x\text{Ga}$ (MRG) without the presence of Gd. Indeed, this RE-free ferrimagnet has two antiferromagnetically coupled sublattices occupied by the same magnetic Mn atoms in two non-equivalent crystallographic positions (4c and 4a) within its cubic $F\bar{4}3m$ structure, as showed in Figure 1.8(a). While, Figure 1.8(b) shows the toggle switching of the magnetization in $\text{Mn}_2\text{Ru}_{1.0}\text{Ga}$ regardless of the initial direction of the magnetization obtained after the irradiation of 5 consecutive linear laser pulses with a fluence of 11.6 mJ/cm^2 and a pulse duration of 200 fs. Remarkably, static and dynamic MOKE measurements revealed that single AO-HIS was only observed for MRG alloys having a compensation temperature T_{comp} (where the magnetization of the Mn(4c) and Mn(4a) sublattice are equal but in opposite direction) above the room temperature. This remark was confirmed by C. S. Davies et al.⁸⁰ when they investigated the effect of the initial temperature of the sample, the pulse duration and the wavelengths from a free-electron laser on the switching of MRG alloys. This experimental study pushes the authors to suggest that the switching mechanism is like in GdFeCo, but with the exchange scattering favorizing a conservation of angular momentum within the spin systems, to be the driving mechanism for switching in MRG. Moreover, the fact that AOS can not be achieved for sample temperature above compensation temperature (where the magnetic moment of Mn (4a) is larger than the magnetic moment of Mn(4c)) was explained by the fact that the intra-sublattice coupling Mn(4a) is three time larger than Mn (4c). Indeed, for $J_{(4a-4a)} = 3J_{(4c-4c)}$,

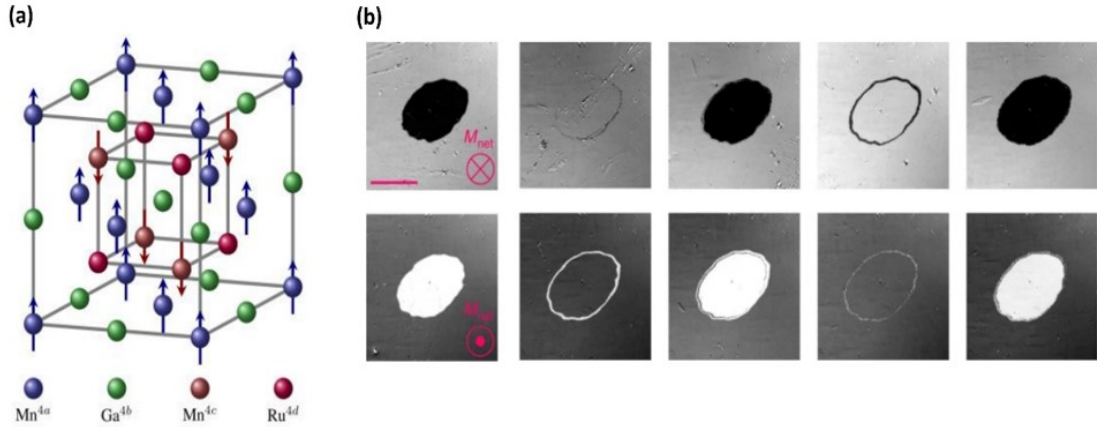


Figure 1.8: (a) Inverted Heusler (XA) crystal unit cell of typical MRG film. (b) Magneto-optical images of $\text{Mn}_2\text{Ru}_{1.0}\text{Ga}$ full film obtained after the action of five consecutive single laser pulse of 200 fs. The dark grey (light grey) area represents the out of plane magnetization of the Mn(4c) sublattice pointing “up” (“down”) as represented by the circled dot (cross). Every single femtosecond pulse with a fluence of 11.6 mJ/cm^2 and a spot diameter of $100 \mu\text{m}$ linearly polarized illuminates the same circular region of the full film and reverses the magnetization within it. The length of the scale bar is $50 \mu\text{m}$. Figure taken from¹⁵.

the sublattice with weaker intra-sublattice coupling Mn(4c) cannot drive the sublattice with a stronger intra-sublattice coupling Mn(4a) across the zero net magnetization state, after the transient ferromagnetic-like state that occurred when Mn(4c) cross zero magnetization first. Consequently, switching is impossible in MRG in this case.

1.2.3 AO-HIS in synthetic ferrimagnetic materials

1.2.3.1 Robust toggle switching

The first experimental demonstration of single-pulse helicity-independent toggle switching in a synthetic ferrimagnetic multilayers was performed by M.L.M. Lalieu et al.⁷ in 2017 on Si: B(substrate)/Ta(4 nm)/Pt(4 nm)/Co(t_{Co})/Gd(3 nm)/Pt(2 nm). They focused their research with $t_{Co} = 0.8, 1, 1.2$ and 1.4 nm . In the case of 1 nm of Co thickness, they performed VSM-SQUID and AOS measurements. Indeed, by using the VSM-SQUID measurement (Figure 1.9(a)), the antiferromagnetic coupling between the Co and Gd layer was demonstrated with the presence of a compensation temperature $T_{com} = 120 \text{ K}$. Below (above) this temperature the magnetic moment of the Gd (Co) layer is larger. Furthermore, they estimated the value of the fully saturated Gd

CHAPTER 1. STATE OF ART

magnetic moment at room temperature to be 0.45 nm and assumed sharp Co/Gd interfaces. This amount of magnetic Gd appears at 300 K due to the exchange interaction with Co near the interface and it is antiparallel to this one. More interestingly, magnetization control in this synthetic ferrimagnet was performed by a linearly polarized laser pulses with a central wavelength of 700 nm and a pulse duration of ≈ 100 fs. Figure 1.9(b) presents the results of the magnetization state after irradiating ten consecutive laser pulses for $t_{Co} = 1.0$ nm. For the two initial magnetization directions, the homogeneous domain is written with the opposite direction of magnetization. This demonstrates that we have SP-AOHIS in the Pt/Co/Gd stack. Furthermore, a strong Co thickness dependence of the threshold fluence was observed. In fact, all Co thickness exhibited AOS and the smallest threshold fluence was obtained with the lowest Co thickness $t_{Co} = 0.8$ nm. They suggested that this threshold fluence behavior is the result of a reduction in the energy required to completely demagnetize the TM layer, which in turn depends on its Curie temperature. For the biggest Co thickness $t_{Co} = 1.4$ nm, speckled domain is written by a single laser pulse (Figure 2d in⁷), they proposed to be the result of a structure close to the spin reorientation limit, observed by the change from a domain wall propagation dominated reversal.

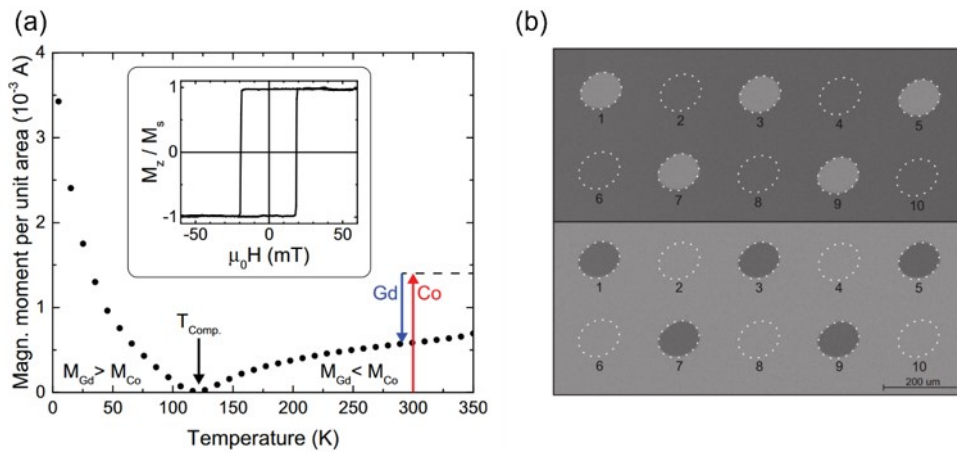


Figure 1.9: (a) VSM-SQUID measurement of the magnetic moment per unit area as a function of the temperature. $T_{comp} = 120$ K represents an AF exchange interaction between the Co and Gd layers. Inset: Polar MOKE measurement performed at RT. The square hysteresis loop with 100% remanence confirms a well-defined PMA. (b) AOS experiments were realized for two opposite initial saturation directions. The numbered areas (dotted circles) correspond to the spots where the structure was irradiated by the laser, where the labels indicate the number of pulses each spot is exposed to. All measurements were performed on Pt(4nm)/Co(1nm)/Gd(3nm) stack. Figure taken from⁷.

1.2.3.2 Comparing AOS in synthetic-ferrimagnetic multilayers and alloys

The demonstration of the SP-AOHIS in both ferrimagnetic alloys and synthetic ferrimagnetic multilayers open new questions on the unicity of the mechanism and conditions for the observation of AOS in ferrimagnetic material. In 2019, M. Beens et al.²³ answered this question by studying the switching mechanism and condition of synthetic ferrimagnets. They identified the switching mechanism as a front of reversed Co magnetization that propagates away from the interface driven by exchange scattering and demonstrated that the magnetization compensation temperature did not play a crucial role.

To achieve this result, they firstly confirmed experimentally a robust single AOS in Pt/FM/Gd(3 nm) stack, FM is a ferromagnetic layer composed of Co(0.2 nm)/[Ni(0.6 nm)/Co(0.2 nm)]_N. Indeed, for N=2,3,4 and 5 they obtained both PMA and SP-AOHIS. Remarkably, for five repetitions, the FM thickness equal to 4.2 nm is much larger than 0.45 nm of fully saturated Gd magnetic moment at room temperature. Indicating that the structure in this case is far from compensated and emphasized that the switching mechanism in the bilayers is independent of a possible compensation temperature. Secondly, they performed simulation in both Gd_{1-x}Co_x alloy and Co/Gd bilayers with an extension of the microscopic three-temperature model (M3TM) (see section 1.1.2.3). Figures 1.10(a) and 1.10(b) shows the phase diagram extracted from the calculation of _{1-x}Co_x alloy and Co/Gd bilayers, respectively. Indeed, figure 1.10(a) and 1.10(b) illustrate the variation of the laser pulse energy P_0 with the Co concentration x of a _{1-x}Co_x alloy, and the number of Co monolayers for a Co/Gd bilayer, respectively. In addition, depending on the state of the Co magnetization after the relaxation (after 100 ps), they authors delimited these diagrams with different colors. The dark-blue areas indicate that the Co magnetization is reversed after the relaxation, illustrating the AOS regime. The vertical dashed line in Figure 1.10(a) represents the compensation point $x_{comp} \sim 0.77$ and is in perfect agreement with the observation of AOS in ferrimagnetic alloys which can only occur for a narrow range of the Co concentration close to the compensation point, as discussed in Section 1.2.1. A net difference is observed when we compare the AOS regime for the bilayers, Figure 1.10(b). For example, bilayers composed of 20 Co monolayers and 3 Gd monolayers can be reverse with high threshold fluence. For this example, the total Co and Gd magnetic moment is $\mu_{Co}/\mu_{Gd} \sim 4$, while AOS in alloys has been demonstrated in a narrow range $\mu_{Co}/\mu_{Gd} \sim 0.9 - 1.3$ ($\mu_{Co}/\mu_{Gd} \sim 1$ at the compensation point). Consequently, this model also demonstrates that the magnetization compensation temperature does not play a crucial role in the switching of the magnetization of synthetic ferrimagnets.

CHAPTER 1. STATE OF ART

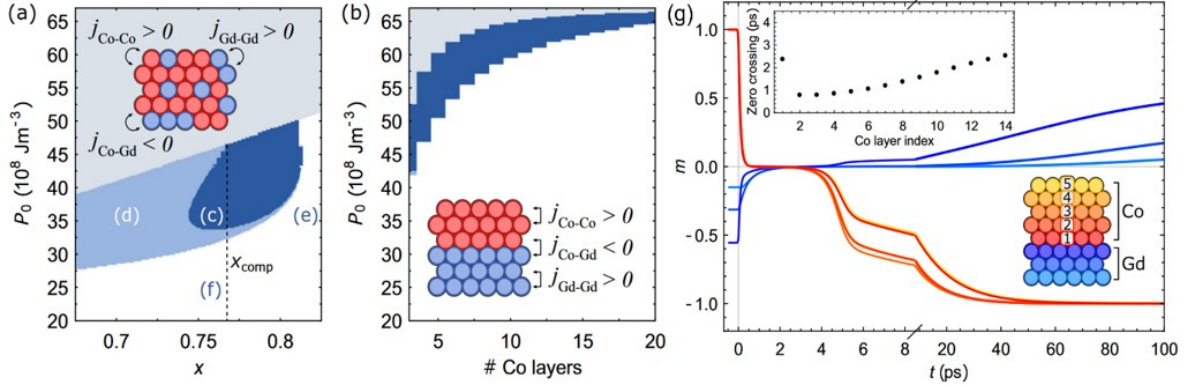


Figure 1.10: Variation of the laser pulse energy P_0 with (a) the Co concentration x for $Gd_{1-x}Co_x$, and (b) the number of Co monolayers in a Co/Gd bilayer. The dark-blue areas indicate that the Co magnetization is reversed after the relaxation (c) and the light-blue areas indicate the exhibition of a transient ferromagnetic state but followed by the relaxation of the magnetization back to its initial direction (d). The white areas indicate the absence of a transient ferromagnetic state, then the magnetization relaxes to its initial direction (e), (f) and the gray areas indicate that the maximum of the phonon temperature is above the Curie temperature. The dashed line in (a) corresponds to the compensation point and the inset in both (a) and (b) present the modeled system with the exchange parameters. (g) Magnetization dynamic in a 5 Co / 3 Gd bilayer for a fixed energy $P_0 = 55 \times 10^8 \text{ J/m}^{-3}$. The inset present the time at which the magnetization of each Co monolayer is reversed for a 14 Co / 3 Gd system for a fixed energy $P_0 = 65 \times 10^8 \text{ J/m}^{-3}$. Figure taken from²³.

Furthermore, to investigate the mechanism behind the observation of AOS in synthetic ferrimagnet, the authors performed a laser dynamic of the normalized magnetization of each Co and Gd monolayer in a 5 Co / 3 Gd synthetic ferrimagnet as represented in figure 1.10((g)). Indeed, by using the same extension of M3TM model, they clearly demonstrate the reverse of the Co magnetization, beginning from the Co layer near the Co/Gd interface in a 14 Co / 3 Gd synthetic ferrimagnet as showed in the inset of figure 1.10(g). The y- and x-axes of the inset in Figure 1.10(g) represent respectively the time at which each Co monolayer switches its magnetization direction and the Co layer position adjacent to the interface. Although the first Co monolayer need more than 2 ps to cross zero because of the change of its dynamics due to the presence of the exchange field coming from slow Gd demagnetization, the second Co monolayer is switched first. Consequently, the reverse of the others Co layer comes from the propagation of the switching driven by exchange scattering between neighboring Co monolayers. Hence, independently of the number of Co monolayer in a synthetic ferrimagnet, AOS can be achieved, explaining why the Co/Gd bilayer can be switched for a relatively large Co thickness.

1.3. ALL OPTICAL SWITCHING IN FERROMAGNET THIN FILMS AND MULTILAYERS

M. Beens et al.²⁴ continued investigation in Co/Gd bilayers with imperfect Co/Gd interface. Indeed, they study the role of interface intermixing in switching Co/Gd bilayers by using M3TM model for layered magnetic systems. The main conclusion of this simulation was the reduction of the threshold fluence and an increase of propagation rate on AOS compared to the ideal Co/Gd interface. Remarkably, the possibility to integrate AOS with spintronics was proven by M. L. M. Laliou et al.⁸¹ by exploiting thermal single pulse demonstrated in Pt/Co/Gd racetrack. In addition, they were able to move these optically written domains by performing transport measurements, using an electric current by exploiting the SHE in the Pt heavy metal seed layer of the Pt/Co/Gd wire.

1.3 All Optical switching in ferromagnet thin films and multilayers

1.3.1 MP-AOHDS in CoPt multilayers

Experimental demonstrations of AOS were initially established on RE (Rare Earth) -TM (Transition Metal) ferrimagnetic materials that exhibited antiferromagnetic coupling on the atomic and nanoscale^{1,34,61,62} like discussed in section 1.2. However, the possibility of changing the magnetic order of ferromagnets possessing perpendicular magnetic anisotropy (PMA) was first observed experimentally by C-H. Lambert et al.⁸² in 2014. The investigation was performed on [Co (0.4 nm)/Pt (0.7 nm)]_N multilayers, where N =3,5,8 represents the number of repeats. For N=3 (Figure 1.11(C)), a complete reversal of the magnetization was observed by scanning the surface of the material with a circularly polarized LASER, as evidence of AO-HDS. However, for N=8 and 5 (Figure 1.11(A) and 1.11(B)), thermal demagnetization was observed, proving by the observation of multi-domains. Moreover, the variation of the size of these multi-domains as a function of N shows the influence of the dipole energy and the magnetic layers thickness in the AO-HDS process. These results were confirmed by El Hadri et al.³⁵ in 2016 thanks to electrical measurements using the anomalous Hall effect⁸³. Indeed, on a Pt/Co/Pt structure a quantitative analysis of the AO-HDS could be done by fabricating this heterostructure on a Hall bar.

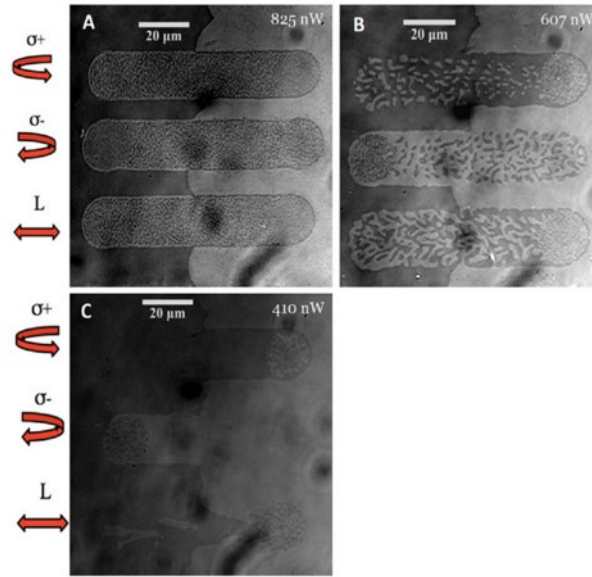


Figure 1.11: Magneto-optical response in a zero applied magnetic field of $[\text{Co} (0.4 \text{ nm})/\text{Pt} (0.7 \text{ nm})]_N$ multilayers at various laser polarization (A) $N = 8$, (B) $N = 5$ and (C) $N = 3$. For each image, the laser is circularly polarized (σ^+ or σ^-) or linearly polarized (L). For (A) - (C), the laser beam was scanned over a region of the sample with two opposite magnetic domains showing a black/white contrast in the images. Figure taken from⁸².

As both ferrimagnetic and ferromagnetic materials exhibit AO-HDS, the question of the microscopic mechanism responsible for AOS was legitimate. In fact, the absence of antiferromagnetic coupling in ferromagnetic layers undermines the requirement for the presence of antiferromagnetic coupling for the observation of AOS. In 2016, El Hadri et al.⁶⁹ distinguished two types of mechanisms taking place during the AOS process for magnetic materials. The first was the $1 \mu\text{s}$ reversal of the magnetization for $\text{Gd}_{28}\text{Fe}_{48}\text{Co}_{24}$ continuous film using a single pulse independently of the polarization of the incident laser (SP-AOHIS). On the other hand, for the ferrimagnetic alloy of $\text{Tb}_{27}\text{Co}_{73}$ and the $\text{Pt} (4.5 \text{ nm})/\text{Co} (0.6 \text{ nm})/\text{Pt} (4.5 \text{ nm})$ heterostructure a different dynamic was observed. Indeed, in the case of Pt/Co/Pt multilayer, the reversal of the magnetization using several femtosecond lasers pulses (about 200) takes place in two steps on different time scales: a demagnetization under 1 ms independent of the nature of the polarization (Figure 1.12(a)), followed by a polarization-dependent reversal (MP-AOHDS) over a duration of 120 ms (Figure 1.12(b)). In sum, a demonstration of AOS as a cumulative and multiple pulse process for ferromagnets. However, for a single incident pulse, we observe only thermal demagnetization marked by the appearance of multi-domains (Figure 1.12(c)). The authors evoked the mechanisms of All Optical Switching Helicity dependent Domain Wall Motion (AOS-HD-

1.3. ALL OPTICAL SWITCHING IN FERROMAGNET THIN FILMS AND MULTILAYERS

DWM) and Magnetic Circular Dichroism (MCD) to explain this MP-AOHDS phenomenon.

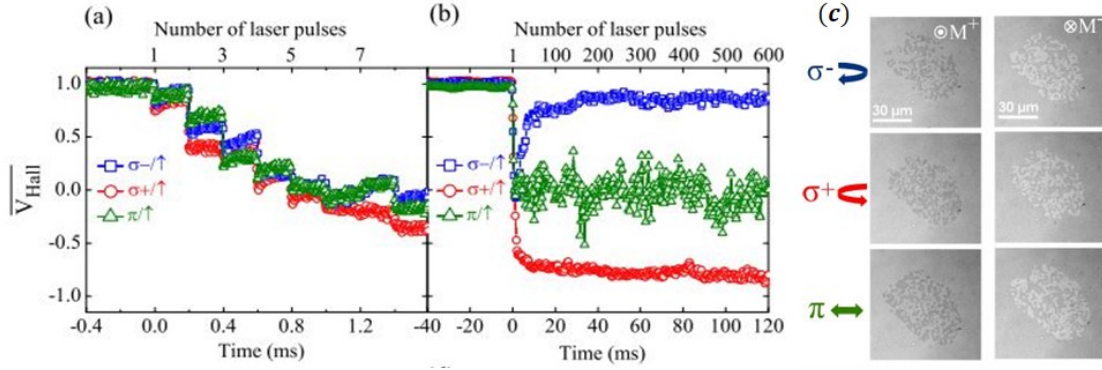


Figure 1.12: (a), (b) Variation of the normalized Hall voltage on the Pt/Co/Pt Hall cross as a function of the number of pulses and the laser polarization: (a) polarization-independent demagnetization over a duration of 1 ms and (b) polarization-dependent magnetization reversal under 120 ms. (c) Magneto-optical image of Pt (4.5 nm)/Co (0.6 nm)/Pt (4.5 nm) after excitation by a single femtosecond laser pulse. For both directions of magnetization saturation (M^+ and M^-), thermal demagnetization is observed with circular (σ^+ and σ^-) and linear (π) polarizations. Figure taken from⁶⁹.

1.3.2 Domain wall helicity dependent switching in CoPt trilayers and multilayers

This hypothesis was investigated in 2017 by Y. Quessab et al.⁸⁴ with the study of the laser-induced domain wall motion on Pt/[Co/Pt]₃/Pt multilayers using multiple picosecond laser pulses. Then, as a function of time and number of laser pulses N, they performed a magneto-optical faraday imaging technique. They realized all these experiments for fluence lower than the switching threshold to avoid AOS and the most important beam position is the location of the hottest region relative to the DW. Figure 1.13(a) presents the trends of the DW in Pt/[Co/Pt]₃/Pt after being irradiated with 2 ps circularly polarized light. The center of the laser beam spot is placed 10 μm from the DW on a domain with either magnetization up (M^+) or magnetization down (M^-). For the four possible combinations of: light polarization and position of laser beam, only two combinations, (σ^+ , M^-) and (σ^- , M^+) presented significant DW displacement. In fact, the Figure 1.13(a) shows the expansion of the M^+ (M^-) domain due to the shift of the DW after the exposure the σ^- (σ^+) laser pulses. Moreover, the same laser induced helicity dependent DW

CHAPTER 1. STATE OF ART

motion in a Pt/Co/Pt layer illuminated with a 40 fs laser pulses when the center of the laser beam was placed in the vicinity of the DW was also established.

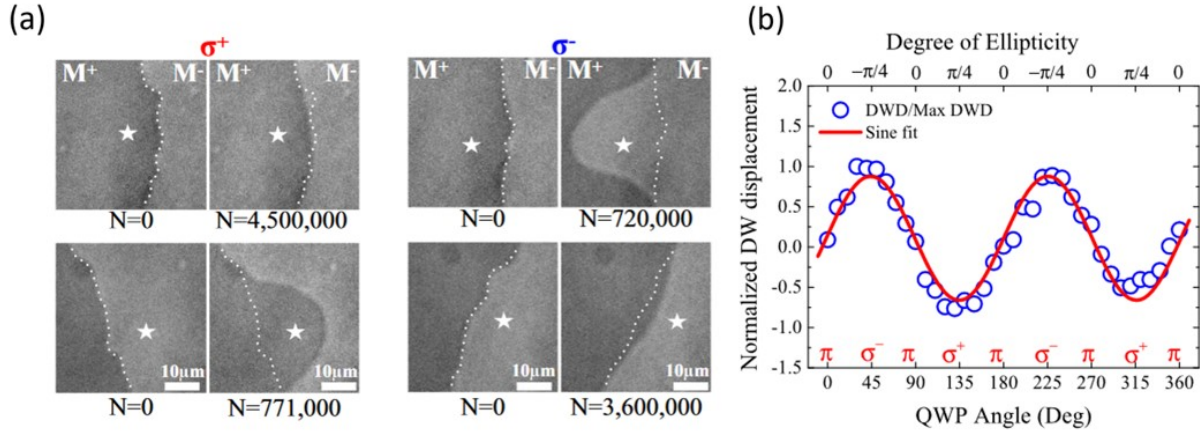


Figure 1.13: (a) Magneto-optical images of domain wall motion in Pt(5 nm)/[Co(0.4 nm)/Pt(0.7 nm)]₃/Pt(2 nm) induced by 2 ps laser pulses with left (σ^-) and right-circular (σ^+) polarization with a fluence per pulse of 0.04 mJ/cm^2 . The white star and N represent the center of the beam spot and the number of laser pulses, respectively. The dotted line shows the initial position of the domain wall before the laser irradiation. (b) Variation of the DWD with degree of ellipticity. The Figure taken from⁸⁴.

More interestingly, Y. Quessab et al investigated the variation of the DWD in the Pt/Co/Pt layer illuminated with a 40 fs laser pulses for different degree of light ellipticity ϵ . Figure 1.13(b) shows the measurement of the farthest stable DW position versus the helicity angle θ of the quarter-wave-plate (QWP). The experiment was realized with the center of the laser beam initially placed on the DW and the angle of the QWP was set to 0° . The DWD behavior has been fitted with a sinusoid and shows two opposite maximum values for the left (σ^+ or $\epsilon = \frac{\pi}{4}$) and the (σ^- or $\epsilon = -\frac{\pi}{4}$) circular polarization. For linearly polarized light (π or $\epsilon=0$), DWD is near to zero, meaning that no motion is observed after the exposure with several laser pulses. The authors attributed the small shift of the curve to the nonuniform distribution of pinning sites on either side of the DW and found that the resulting DW displacement was a balance between the helicity effect and the temperature gradient of the laser. Finally, the perfect agreement between the Fatuzzo-Labrune model^{85,86} with the experiment allowed the authors to suggest that the inverse Faraday effect is a likely explanation for the helicity effect on the DW.

1.3. ALL OPTICAL SWITCHING IN FERROMAGNET THIN FILMS AND MULTILAYERS

1.3.3 State diagram of AOS

More recently, in 2019, G. Kichin et al.⁸⁷ studied the effect of fluence, laser spot size and pulse duration on the AO-HDS of an ultrathin Co (0.6 nm)/Pt (0.7 nm) layer. Indeed, using magneto-optical images obtained on the Kerr effect microscope, giving the magnetic configuration of Co/Pt after laser excitations (600 pulses), a magnetic state diagram could be established (Figure 1.14(a)) for different laser parameters (Fluence, pulse duration and spot diameter). Three regions can be distinguished: for long pulse duration and low fluence, the laser has no influence on the magnetic order. In the case of short pulses and high fluence, multi-domains are observed. Between these two regions, there is a complete reversal of the magnetization of a magnetic domain for specific fluence and pulse duration intervals. Furthermore, in order to achieve SP-AOHDS, for a ferromagnetic layer, the authors performed anomalous Hall voltage measurements with the Co/Pt magnetization OOP and initially patterned on a 5 μm wide Hall cross. The center of the cross is irradiated with a laser beam of 2 ps pulse duration, 11 mJ/cm^2 fluence and with a spot size 14 times larger than the width of the Hall cross. As shown in Figure 1.14(b), V_{AHV} is zero for linearly polarized incident light, characterizing demagnetization. In contrast, with $V_{AHV} = \pm 0.1$ for the two different circular polarizations, denoting a 10% reversal of magnetization. Finally, by combining the previous experimental results with the three-temperature model (3TM), G. Kichin et al. emphasized the need for the spin bath to approach a temperature close to the Curie temperature, followed by angular momentum transfer from light to the magnetic material, to be the mechanism responsible for the AO-HDS observation. Therefore, this criterion rules out the MCD process in understanding AO-HDS.

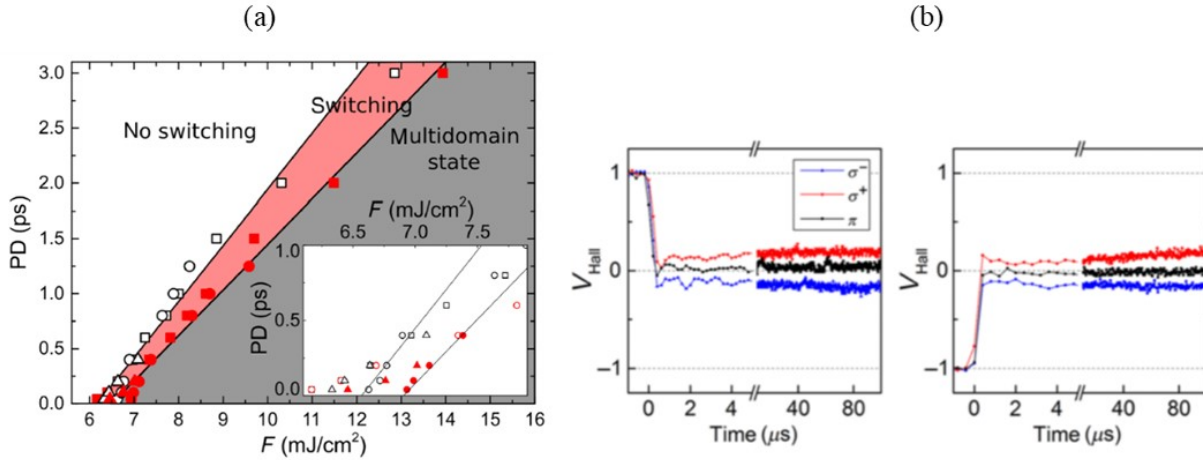


Figure 1.14: (a) Magnetic state diagram of Glass/Ta (3 nm)/Pt(3 nm)/[Co(0.6 nm)/Pt(0.7 nm)]/Pt(3 nm) using circular LASER polarization as a function of fluence, pulse duration and LASER spot diameter (84 μ m for the triangle, 104 μ m for the square, and 168 μ m for the circle). (b) Variation of the normalized Hall voltage as a function of time, giving the dynamics of the Co/Pt magnetization. The sample, initially having a saturated magnetization, is excited by a polarization pulse of σ^+ (red), σ^- (blue) and π (black). Figure taken from⁸⁷.

1.3.4 Mechanism of all-optical switching

In contrast with ferrimagnetic materials where it is established that AOS is driven by a pure thermal effect (see section 1.2.2), the microscopic mechanism involved in the observation of AO-HDS is still on discussion. In fact, initially discover in ferrimagnetic material³⁴, then in ferromagnet, AO-HDS appears to be a mechanism independent of the presence of two sublattices coupled antiferromagnetically in a magnetic material. However, as mentioned in previous section IFE and MCD appears to be most of the 2 best candidates to understand the All-Optical Helicity Dependent Switching mechanism in a ferromagnetic material.

1.3.4.1 Magnetic circular dichroism

As experimentally demonstrated by El Hadri et al.⁶⁹, the effect of the laser heating is to rapidly demagnetize a ferromagnet within 1 ms, followed by a polarization-dependent reversal (MP-AOHDS) over a duration of 120 ms. This implies that within a hundred of ms after the laser pulse, the magnetization can thermally jump the energy barrier of anisotropy. This energy barrier is reduced at high temperatures due to the fluctuations in magnetization that are included in the

1.3. ALL OPTICAL SWITCHING IN FERROMAGNET THIN FILMS AND MULTILAYERS

atomic model⁸⁸. In 2016, Ellis et al.⁸⁹ proposed a multiple pulse stochastic all thermal model of AO-HDS in ferromagnets, taking the example of an ensemble of FePt granular media. This theoretical approach is based on the fact that the absorption in a magnetic material depends on the orientation of its magnetization and the helicity of an incoming laser pulse, due to the MCD. Since this differential absorption will be small (the final magnetization change will be small) with a single pulse, many incident laser pulses will lead to a continuous acquisition of magnetization following each laser pulse. Indeed, considering that each grain is a single domain with a fixed out of plane magnetization (two possible magnetization directions) and by using a two-state Master equation, the time evolution probability of each grain in the ensemble to occupy high (n_+) or low (n_-) absorbing orientation is given by:

$$\frac{\partial n_{\pm}}{\partial t} = -n_{\pm}\tau_{\pm}^{-1} + n_{\mp}\tau_{\mp}^{-1} \quad (1.9)$$

Where τ_{\pm}^{-1} are the transition rates of the grain switching from the high (+) or low (-) absorption states to the other state. These equations describe the behavior of the net magnetization m ($m = n_- - n_+$) as it is subject to a series of pulses. In the case of multiple pulse at a fluence F and a repeat frequency f_l , the transition rates of the grain are described by:

$$\tau_{\pm}^{-1}F = f_l P(F\delta_{\pm}), \quad \text{where} \quad P(F) = \frac{P_{\infty}}{2} \left[1 + \tanh\left(\frac{F - F_0}{\Delta F}\right) \right] \quad (1.10)$$

Where $P(F\delta_{\pm})$ is the probability of the grain switching by a single laser pulse and $\delta_{\pm} = 1 \pm \Delta/2$ is the value representing the difference in the absorbed fluence due to the magnetic circular dichroism (Δ). The Eq 1.10 gives the expression of the switching probability $P(F)$ extracted from the atomistic spin model⁹⁰, with P_{∞} , F_0 and ΔF as fitting parameters. Figure 1.15(a) shows the behavior of the switching probability of a single grain that was used to extract these fitting parameters, for an average of 50 separate pulses in a zero field and with a zero constant external field and ± 1 T. Moreover, in equilibrium the states will satisfy detailed balance and the using the conservation of the total probability ($n_- + n_+ = 1$), allowed to extract the net magnetization reached after a sufficiently long series of laser pulse m^{∞} :

$$m^{\infty} = \frac{\tau_-^{-1} - \tau_+^{-1}}{\tau_-^{-1} + \tau_+^{-1}} = \frac{P(F\delta_-) - P(F\delta_+)}{P(F\delta_-) + P(F\delta_+)} \quad (1.11)$$

Solving 1.9 allows to obtain m^{∞}

$$m(t) = m^{\infty} - (m^{\infty} - m(0)) \exp\left(-\frac{t}{\tau}\right) \quad (1.12)$$

With the time t and switching time τ given by

$$t = Nf_l \quad \text{and} \quad \frac{1}{\tau} = \frac{1}{\tau_+} + \frac{1}{\tau_-} \quad (1.13)$$

Eq 1.12 can be solved numerically for an initial state with equal numbers of grains up and down, $m(t = 0) = 0$ (like the initial state of the experimental performed by Lambert et al.⁸² in granular FePt). Figure 1.15(b) shows the variation of the net magnetization induced by the thermal switching with the laser fluence for MCD value between 1% and 5%. The solid, dashed and dotted lines represent the net magnetization after 100, 1000 and infinite laser pulses, respectively. Since the values of the magnetization are positive, this implies that the system will move towards the low absorption orientation. In particular, around 9.5 mJ/cm², a peak is reached, independently of the MCD value, followed by a reduction of the magnetization due to the increasing thermal instability at high temperatures. For fluences below 9.5 mJ/cm², magnetization is acquired or not, depending mainly on whether the laser heating can induce thermally activated transitions over the energy barriers. More interestingly, a direct comparison with the experimental results where the laser is scanned over the FePtAgC granular film sample for both helicities and different applied field strengths⁸², is shown in figure 1.15(c). As observed by Lambert et al., increasing the field strength improves saturation for σ^+ but for σ^- , it decreases saturation until it completely counters optical switching at 0.1 T.

In the same years, Gorchon et al.⁹¹ arrived at the same conclusion using the same framework. To simulate the probability of switching from one state to the other due to thermal activation and the grain temperature, Gorchon and co-authors used the Néel–Brown formula⁹² and a steplike profile⁹¹, respectively. As Ellis et al.⁸⁹, they showed the reversal of the grain occupying the low absorbing state, while in their case they fully switch the magnetization with just 10 pulses. Several others work reported MP-AOHDS in Co/Pt multilayers and Fe/Pt granular described by a purely thermal effect based on MCD^{93–95}. In addition, in a thin film of Co₇₀Tb₃₀ (20 nm) ferromagnetic alloy, Quessab et al.⁹⁶ gave evidence of the possible role of MCD to the explanation of helicity–dependent domain wall displacement (see section 1.3.2)

1.3. ALL OPTICAL SWITCHING IN FERROMAGNET THIN FILMS AND MULTILAYERS

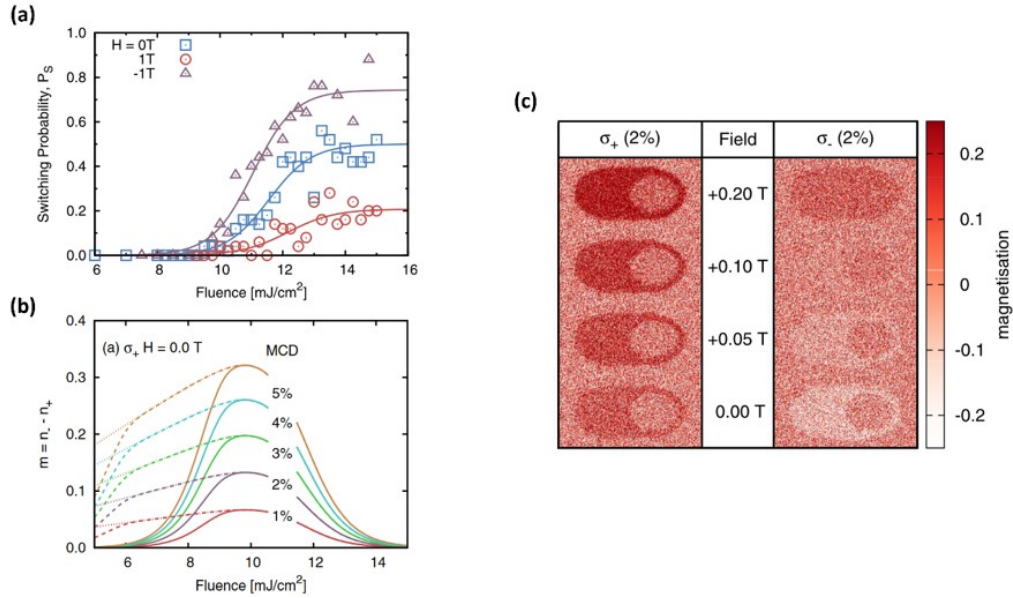


Figure 1.15: (a) Computed probability of a single grain switching over a range of laser fluences in a zero field and with a constant external field $\pm 1\text{ T}$. The lines show a fit to the data. (b) Evolution of the net magnetization after a series of multiple pulses over a range of laser fluences and MCD ratio in a zero field. The solid, dashed and dotted lines represent the net magnetization after 100, 1000 and infinite laser pulses, respectively. (c) Simulations when sweeping the laser with a constant speed and a peak fluence of 20 mJ/cm^2 on a granular structure for different applied fields. A MCD of $\Delta = \pm 2\%$ is used to model the laser polarization and each grain is switched following the probabilities given in Eq 1.10. Figure taken from⁸⁹.

1.3.4.2 Inverse faraday effect

Since magnetic moments have angular momentum, the possibility of controlling the magnetization in a magnetically ordered material by means of circularly polarized light was firstly predicted experimentally by both Beth et al.⁹⁷ and Holbourn et al.⁹⁸ in 1936. Prediction that was established clearly for the first time by Kimel et al.⁹⁹ in 2005 when they demonstrated that spins can indeed be controlled with a circularly polarized fs-laser pulses. These spectacular experiments result were attributed to the creation of a stationary magnetic field due to the excitation with circularly polarized light, referred as Inverse Faraday Effect (as illustrated in Figure 1.16(a)). However, this effect has been predicted firstly by several works^{100–102} in the 1960s. Notably, Van der Ziel et al.¹⁰¹ described the observation of an optically induced magnetization in a non-absorbing material within a zero magnetic field:

$$M_{IFE} = -\frac{\partial F}{\partial H} = -\chi(\epsilon_R \epsilon_R^* - \epsilon_L \epsilon_L^*) \quad (1.14)$$

Where χ , ϵ_R and ϵ_L are the magneto-optical susceptibility, the amplitudes of the right and left circularly polarized light, respectively. From this phenomenological relationship, we can observe that the intensity of M_{IFE} depends strongly on the polarization of the light. In the case of linearly polarized light, marked by the superposition of a circularly left and right polarized light, Eq 1.14 result to $M_{IFE} = 0$. While M_{IFE} is maximized in the case of a purely circularly Left or right polarized light, and its sign is polarization dependent. More interesting, Eq 1.14 can also be described as follows:

$$\vec{M}_{IFE} = \frac{\chi}{16} [\vec{E}(w) \times \vec{E}^*(w)] \quad (1.15)$$

Where is $\vec{E}(w)$ and $\vec{E}^*(w)$ are the electric field of light and its complex conjugate and w the electromagnetic wave frequency. Eq 1.15 shows a proportional relationship between the induced magnetization and the intensity of the light, leading to a zero optically induced magnetization for a vanishing light. Moreover, in recent investigations, quantum theories of IFE supported by an analytical solution of the second order Liouville-von Neumann equation^{103,104} and by ab initio calculations have been developed¹⁰⁵.

However, since Eq 1.14 was initially experimentally verified in non-absorbing materials and in the absence of a magnetic field or a permanent magnetization, the use of the inverse Faraday effect to explain the origin of the AO-HDS in dissipative and magnetized materials is counter-intuitive. Nevertheless, several works have demonstrated that the combination of micromagnetic simulations with an effective "optomagnetic field" can be sufficient to generate AO-HDS in various magnetic materials^{89,103,106}. The table 1.1 below provides an overview of the different micromagnetic approaches, the magnitude and the minimum duration of the inverse Faraday effect allowing to reproduce experimental switching results. The most common model appears to be the coupling of the ultrafast demagnetization induced by laser heating (see Section 1.1.2) with the addition of an effective H_{IFE} magnetic field considering the effect of the polarization of the light. Moreover, the minimum duration of the effective H_{IFE} should be around 0.2 ps and 20 T is needed to generate the switching in a ferri- or ferromagnetic full film. For the case of granular FePt, the field required for AO-HDS is larger than in other materials, but the duration is comparable. This gap in intensity can be attributed to the differences in the uniaxial anisotropy observed within full film and grains.

1.3. ALL OPTICAL SWITCHING IN FERROMAGNET THIN FILMS AND MULTILAYERS

Materials	model	$H_{IFE}(T)$	Minimum $t_{IFE}(ps)$	Ref
Ferrimagnetic GdFeCo alloy	The heating effect of the laser is incorporated using the two-temperature model (2TM) and the spin dynamics was calculated using the Landau-Lifshitz-Bloc (LLB) equation under a macrospin approximation in which a phenomenological expression of the IFE was used.	20	0.25	Vahaplar et al. ¹⁰⁶
Ferromagnetic Co/Pt multilayers	The heating effect of the laser, the ultrafast spin dynamics and the impact of IFE was implemented using the microscopic three-temperature model (M3TM).	20	0.15	Cornelissen et al. ¹⁰³
FePt granular media	The laser heating effect is incorporated using the two-temperature model (2TM) and the spin dynamics has been calculated using a Landau-Lifshitz-Gilbert (LLG) atomic equation in which a flat Gaussian with variable central time has been introduced and representing the IFE.	60	0.2	Ellis et al. ⁸⁹

Table 1.1: Different IFE model to explain all optical switching in magnetic materials.

Although IFE is a good candidate to explain AO-HDS in ferromagnets, many issues are still under discussion. Firstly, it is not clear whether one should consider the IFE as an induced magnetization (case 1) as initially proposed by Van der Ziel et al.¹⁰¹ or as an effective magnetic field (case 2) as suggested in several recent works. Indeed, depending on each case, the induced magnetization dynamics leads to a variation of the longitudinal component of the magnetization for the case 1 or to a purely precessional process for case 2. Secondly, the very high values of the effective field strength are difficult to justify or to explain, unless properties such as the exchange interaction are involved. Furthermore, it is not clear why the duration of the IFE would be longer than the femtosecond laser excitation itself. Finally, although Cornelissen et al.¹⁰³

CHAPTER 1. STATE OF ART

predicted the SP-AOHDS by incorporating the effect of dipole fields in their model (see Figure 1.16(b)), so far, no experience has been reported SP-AOHDS in Co/Pt multilayers or any other ferromagnetic material. However, new theoretical models to explain AO-HDS emerge from the IFE and MCD effect. Indeed, John et al. presented a model including both effects to reproduce the magnetization switching of FePt nanoparticle¹⁰⁷. More recently, P. Schied et al.¹⁰⁸ demonstrated the existence of a dissipative phenomenon, whose contribution grows linearly with both the intensity of the light and with time, when absorbing circularly polarized light. Unlike the IFE, this contribution is due to absorption, so the angular momentum transferred from light to matter is conserved even after the light has disappeared. This makes it one of the most realistic approaches.

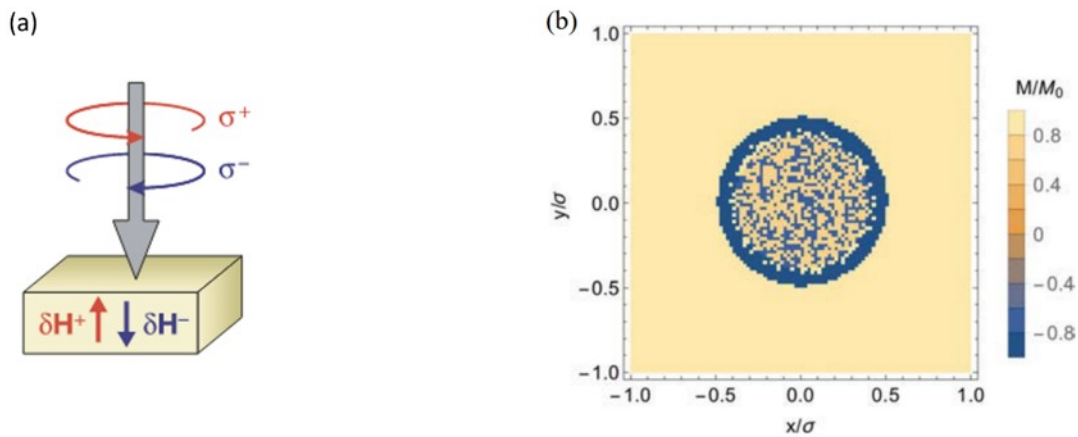


Figure 1.16: (a) Illustration of the IFE for normal incidence light with right (σ^+) and left (σ^-) circular polarization, generating an effective magnetic field δH^+ and δH^- , respectively. (b) Reproduction of the magnetization profile after single-laser pulse irradiation on $[\text{Co} (0.4 \text{ nm})/\text{Pt}(0.7\text{nm})]_3$ and obtained from M3TM simulations. A multi-domain state is observed in the center and a single switched domain is clearly visible in the rim of the laser spot. Figure taken from^{99,103}.

1.4 All-Optical magnetization switching mediated by spin transport: spin valve structure

1.4.1 Spin current induced AOS in ferromagnetic layer

In order to move to ultrafast-spintronic application, we need to understand complex structure like spin valve that will allow magnetic storage and multi-level memories^{109,110}. This objective led Satoshi Iihama et al.¹¹ in 2018 to study the single femtosecond light effect on a $\text{Gd}_{23.3}\text{FeCo}_{76.7}$ (5 nm)/Cu (9.3 nm)/[Co (0.6 nm)/Pt(1 nm)]₄ spin valve structure. Indeed, they demonstrated the accessibility of four possible magnetic configurations in this spin valve with the use of a single laser pulse. These magnetic configurations were firstly obtained by using the variation of MOKE signal (θ_K) with a magnetic field (H) applied out of plane. Figure 1.17(a) allows to distinguish four out of plane magnetic configurations: $P+$ and $P-$ for the magnetization of both GdFeCo and [Co/Pt] parallel and pointing in the positive and negative field direction, respectively. Then, two antiparallel states where the magnetization of GdFeCo and [Co/Pt] are antiparallel, with the magnetization of [Co/Pt] pointing in the positive and negative field direction, named $AP+$ and $AP-$ respectively. Moreover, small loops in blue and red demonstrate that both GdFeCo and [Co/Pt] are magnetically decoupled.

Secondly, four remanent magnetic configurations ($P+$, $AP+$, $AP-$, and $P-$) can be achieved using single 35 fs light pulses without applying a magnetic field. Figure 1.17(b) shows MOKE image with different contrast related to the direction of the magnetization of both GdFeCo and [Co/Pt] layer. In fact, authors reported that 0.5 μJ pulses switch both layers from $P+$ (dark red contrast) to $P-$ (dark blue contrast) and vis versa while 0.2 μJ pulses are sufficient to only switch the GdFeCo layer leaving the [Co/Pt] layer unchanged corresponding to the transition between the $P+$ to $AP+$ (light red contrast) or $P-$ to $AP-$ (light blue contrast) and vis versa. However, the transitions $P+$ to $P-$ and $P-$ to $P+$ clearly demonstrate the single thermal AOS of the [Co/Pt] layer. This manipulation of a ferromagnetic magnetization by a single femtosecond pulse inside a spin valve appeared to be a combination of optical excitation and the transfer of spin-polarized currents generated by the demagnetization of the GdFeCo layers.

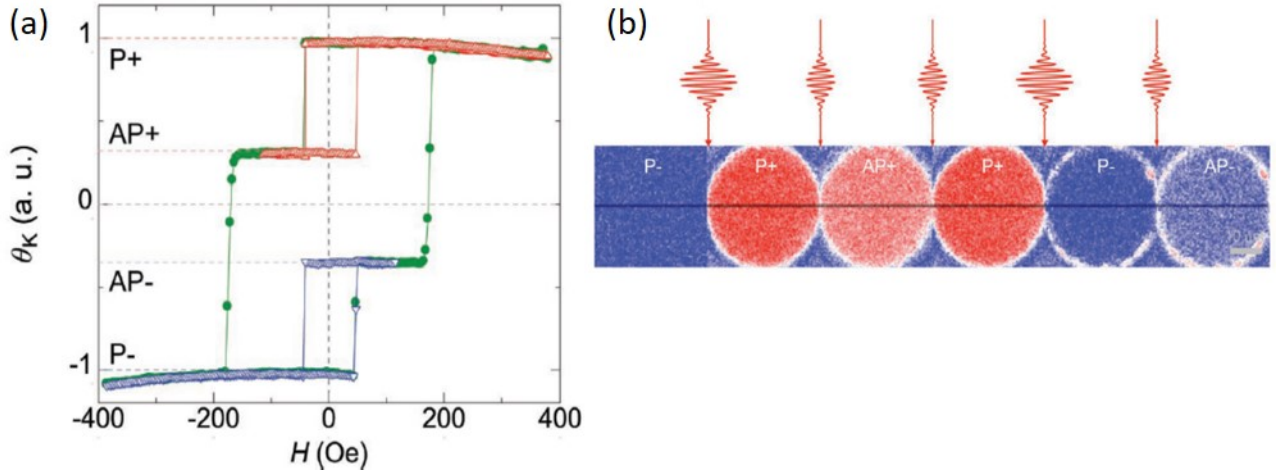


Figure 1.17: (a) Variation of the normalized MOKE (θ_K) with the magnetic field (H) applied out of plane. The reversal which appears at low magnetic field is assigned to the GdFeCo reversal and is represented by the red and blue open symbols. (b) four magnetic configurations obtained consecutively by using high or low pulses energy. Figure taken from¹¹.

1.4.2 Influence of the ferromagnetic Curie temperature

In 2020, Junta Igarashi et al.¹² investigated the effect of the ferromagnet Curie temperature T_C on the single thermal AO-HIS for different ferromagnetic layers (FM) in Gd_{23.3}FeCo_{76.7} (5 nm)/Cu (10 nm)/FM spin valves. In fact, using magneto-optical images obtained on the substrate side, they gave the magnetic state of both Gd_{23.3}FeCo_{76.7} (FeCo rich) and [Co_{*x*}Ni_{1-*x*}/Pt] layers after shooting one, two, three, and four 35 fs single laser pulses beginning from a saturated P+ state for different Co concentration x . This variation of x allows to tune T_C from 400 K to 850 K and all the four possible magnetic configurations have the same definition as mentioned in the previous work of Satoshi Iihama et al.¹¹. Figure 1.18(a) shows MOKE image for a range of fluence between 14 and 21 mJ/cm², where three magnetic configurations can be distinguished: P+ represented by a dark red contrast, P- represented by a dark blue contrast and AP+ state represented by a light red contrast. Although all the samples concentration exhibit AO-HIS for the GdFeCo layer (transition from the P+ to AP+ state and vis versa), only x equal to 0.4, 0.6 and 0.8 can achieved single thermal AO-HIS for both GdFeCo and [Co_{*x*}Ni_{1-*x*}/Pt] layers (transition from the P+ to P- state and vis versa). For $x = 1.0$, the authors reported partial switching of both GdFeCo and TM layer. Particularly, at high fluence, a white contrast was observed prove of the formation of multidomain state due to high energy density in the center of the laser.

1.4. ALL-OPTICAL MAGNETIZATION SWITCHING MEDIATED BY SPIN TRANSPORT: SPIN

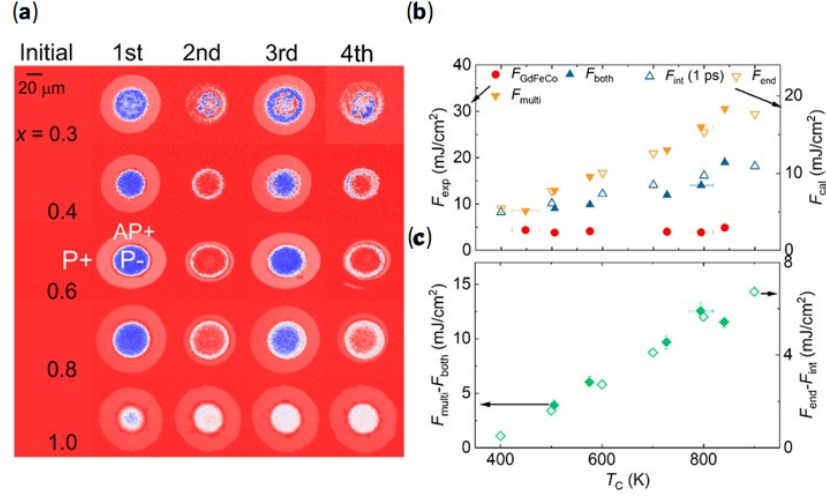


Figure 1.18: (a) MOKE images obtained after exposure of 1 then 2, 3, and 4 fs-laser pulses starting from a $P+$ initial state. (b) Threshold fluences for: the only GdFeCo magnetization switching, AOS of both GdFeCo and the ferromagnetic layers, and multidomain states plotted as a function of the FM layer Curie temperature T_C . (c) Experimental (calculation) variation of $F_{\text{multi}} - F_{\text{both}}$ as a function of T_C represented with closed (opened) symbols. Figure taken from¹².

Moreover, figure 1.18(b) presents the variation of different threshold fluence with the Curie temperature of TM. Although the threshold fluence F_{GdFeCo} to reverse the GdFeCo is constant, the critical fluence for the switching of both layers F_{both} and the observation of multidomain states F_{multi} increases with the augmentation of the TM Curie temperature. Figure 1.18(c), demonstrates a fluence window for the observation of AOS in both layers regarding the increase of the $F_{\text{multi}} - F_{\text{both}}$ difference with increasing T_C up to ~ 800 K. These experimental results can be reproduced with a three-temperature model (3TM) where they calculated the fluence to switch the first CoNi layer at the interface with Cu Fint after 1 ps (time for which FM is sufficiently demagnetized, then the spin current generated and polarized by the Gd reaches the FM layer) and to fully demagnetize at the end of the FM layer F_{end} . In sum, this work illustrated the need of the full demagnetization of the FM to allow its switching when the spin current generated by GdFeCo demagnetization reaches the FM layer. Moreover, F_{both} and F_{multi} behavior can be explained by the fact that demagnetized states of the FM can be obtained with less energy as T_C of the FM layer is lower. Similar argument was used to explain the behavior of F_{both} and F_{multi} in $\text{Gd}_{23.3}\text{FeCo}_{76.7}(5)/\text{Cu}(10)/\text{Co}(t_{\text{Co}})/\text{Pt}(1)/[\text{Co}(0.6)/\text{Pt}(1)]_3/\text{Pt}(3)$ spin valves with the increasing of the thickness of the first Co layer at the interface with the Cu layer.

Other parameters like The Cu thickness¹², the insertion of a layer of Pt within the Cu layer¹¹, the pulse duration of the laser¹² and the chemical composition of the GdFeCo layer¹³ has been demonstrated to play a role on the observation of the single thermal AOS of a ferromagnetic (FM) layer within GdFeCo/Cu/FM spin valve.

1.5 All Optical switching in magnetic micro and nanostructures

Manipulation of the magnetization at smaller length scale and faster timescale is the horizon of research in magnetism. This interest stems from the ever-increasing need to decrease the reading and writing rate of magnetic memory devices which are made of nanosized magnetic bits. Therefore, the study of the size effect on AOS appeared naturally. In this section, we will focus mainly on several studies that reported AOS of GdFeCo in OOP smaller microstructures¹¹¹ or structures at nanoscale size^{12,111,112} by using a single femtosecond laser pulse.

1.5.1 Highly efficient AOS in GdFeCo

Even though L. Le Guyader et al.¹¹² demonstrated the reversal of the magnetization of an OOP domain with sizes down to 200 nm in GdFeCo nanostructures by using a single femtosecond laser pulse, the first investigation of size effect on AOS was realized at microscopic scale. Indeed, in 2012, M. Savoini et al.¹¹¹ reported a strong effect of light within GdFeCo microstructures, resulting in an enhanced energy absorption for smaller regions. To reach this conclusion, they carried out pump-probe measurements in various patterned microstructures realized in a glass/Ti(2 nm)/Pt(8 nm)/SiN(5 nm)/Gd₂₆Fe_{64.5}Co_{9.5}(20 nm)/SiN(20 nm) full film. In fact, they used a 60 fs laser pulses generated by a Ti-sapphire to perform pump-probe magnetization dynamics. Then, they divided this laser in two linearly polarized laser beams with different wavelength (400 and 800 nm of wavelength for the pump and probe beam, respectively) and spot size (5 μm and 800 nm of diameter for the pump and probe beam, respectively). Figure 1.19(a) shows the behavior of the pump-probe dynamics for a fixed $1.9 \pm 0.2 \text{ mJ/cm}^2$ of pump fluence and for various structures size. Although bigger structures of $50 \times 50 \mu\text{m}^2$ and $15 \times 15 \mu\text{m}^2$ (larger than the pump and probe beam sizes) exhibit the same magnetization behavior with the magnetization relaxes back to the initial state, they measured 50% and almost complete demagnetization in the smaller structures of $5 \times 5 \mu\text{m}^2$ and $2 \times 2 \mu\text{m}^2$, respectively. Furthermore, all optical switching is observed in the smallest structure of dimension $1 \times 1 \mu\text{m}^2$.

1.5. ALL OPTICAL SWITCHING IN MAGNETIC MICRO AND NANOSTRUCTURES

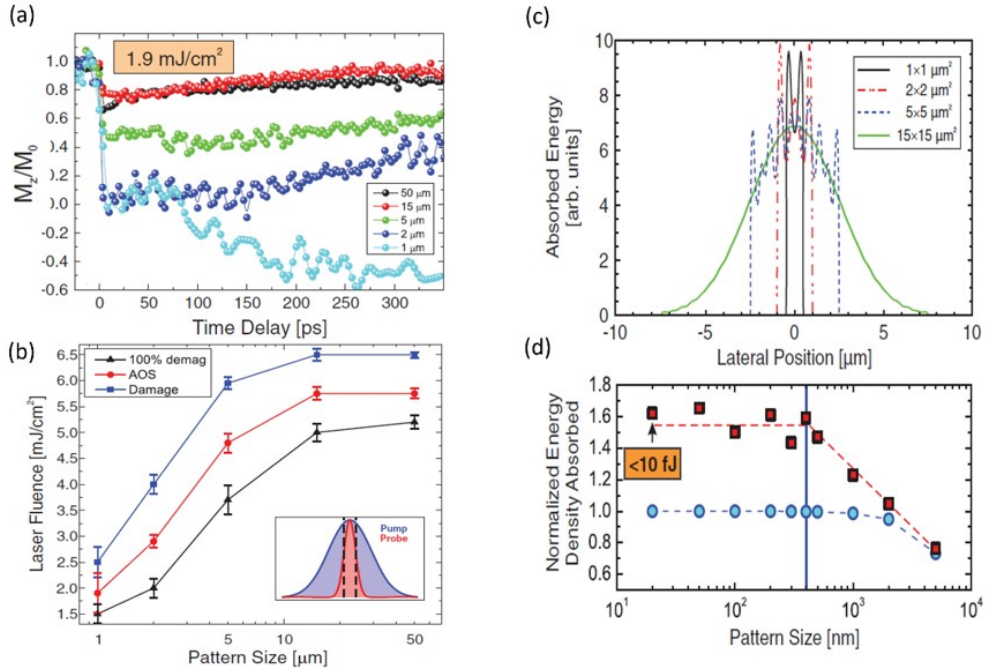


Figure 1.19: (a) pump-probe dynamics for a fixed pump beam fluence of 1.9 ± 0.2 mJ/cm² for various structures size. (b) Variation of the fluence to achieve 100% demagnetization, all optical switching, and the damage with the structure dimension. Inset: Experimental conditions reproducing in scale the dimensions of pump and probe beams. (c) Absorbed energy profiles of the electric field intensity taken at the center of the structures. (d) Normalized simulated energy distribution as a function of the structure size (red squares), compared to the expected behavior in the absence of interference effects (blue circles). Figure taken from¹¹¹.

More interestingly, they plotted the variation of the energy densities needed to induce 100% demagnetization, AOS, and sample damage with the size of the patterned structures. Although Figure 1.19(b) presents an independent trend of the energy requirements as a function of the sample size for bigger structure, a clear reduction of this energy is observed for the smaller ones. To explain this behavior, they performed Finite difference time domain (FDTD) simulations¹¹³ to study the lateral confinement and interference of the optical field distribution in the magnetic stack. Figure 1.19(c) shows the intensity profile across a line through the center for structures ranging in size from $15 \times 15 \mu\text{m}^2$ to $20 \times 20 \text{nm}^2$. It appears that reducing the size of the structure below the pump beam size ($5 \mu\text{m}$) results in the formation of a standing wave pattern due to scattering of the beam by the structure edges. Based on these electric field distributions, they calculated the absorbed energy density in the structure normalized by the area of the absorbed energy distribution within the patterned structure. Figure 1.19(d) shows the trend of this simu-

lated absorbed energy density (red squares), together with the integrated profile of a Gaussian beam normalized by the area of a Gaussian profile matching the absorbed profile of the $15 \times 15 \mu\text{m}^2$ structure (blue circles). While structure sizes above the pump beam wavelength (400 nm) show a decrease of the simulated absorbed energy with increasing structure dimension, structure sizes below 400 nm show a constant absorption. Even though the integrated Gaussian distribution exhibits a similar behavior with the pattern size, the saturation value of the absorption without interference effects appears for more bigger structure size of $5 \times 5 \mu\text{m}^2$ ($400 \times 400 \text{ nm}^2$ for the absorption with interference effects). These trends led to conclude that considering the interference effects, the absorption increases until the size of the structure is equal to the wavelength and remains constant by further reducing the size of the pattern.

1.5.2 Nanoscale sub-100 picosecond AOS in GdFeCo

In 2015, L. Le Guyader et al.¹¹² continued to study the size effect for structures smaller than the free-space diffraction limit at 800 nm of wavelength. Indeed, they showed AOS in a region of 300 nm within $1 \mu\text{m} \times 1 \mu\text{m}$ microstructure and attributed this result to the fact that the wavelength of light propagating inside the GdFeCo layer is about four times smaller than in vacuum due to the GdFeCo refractive index. To achieve this result, they firstly investigated the propagation of an electromagnetic wave for a femtosecond laser pulse within a magnetic GdFeCo layer by using FDTD simulation. Absorption profiles were obtained for a size range from $5 \mu\text{m} \times 5 \mu\text{m}$ to $5 \text{ nm} \times 5 \text{ nm}$ for a small angle of 16° between the structure plane and the laser wave vector \mathbf{k} . Moreover, the direction of the laser entering the plane of the structure were defined by the angle between the planar component of the laser wave vector \mathbf{k} and an edge of the different structures. Figure 1.20(c) and 1.20(f) show the Absorption profile inside the $5 \mu\text{m} \times 5 \mu\text{m}$ structures for the 0° and the 45° incoming laser direction. These figures highlighted two behaviors of the absorption A: the strong dependence of A with the angle of incidence and the inhomogeneous distribution of A within the structure whatever the angle of incidence. Likewise, these two observations were established for all structures size. Remarkably, by evaluating the total energy absorbed by the structure for all sizes, they confirmed M. Savoini et al.¹¹¹ work presented in the previous paragraph, according to which smaller structures are more absorbent and therefore more energy efficient. Moreover, these coupled focusing and energy efficient effects arise from the limitations of the structure and the interference between propagating and absorbing waves in the sample. These effects were also demonstrated for a laser at normal incidence to the plane of the sample.

Secondly, in order to observed AOS in a nanoscale region of GdFeCo structure, they per-

1.5. ALL OPTICAL SWITCHING IN MAGNETIC MICRO AND NANOSTRUCTURES

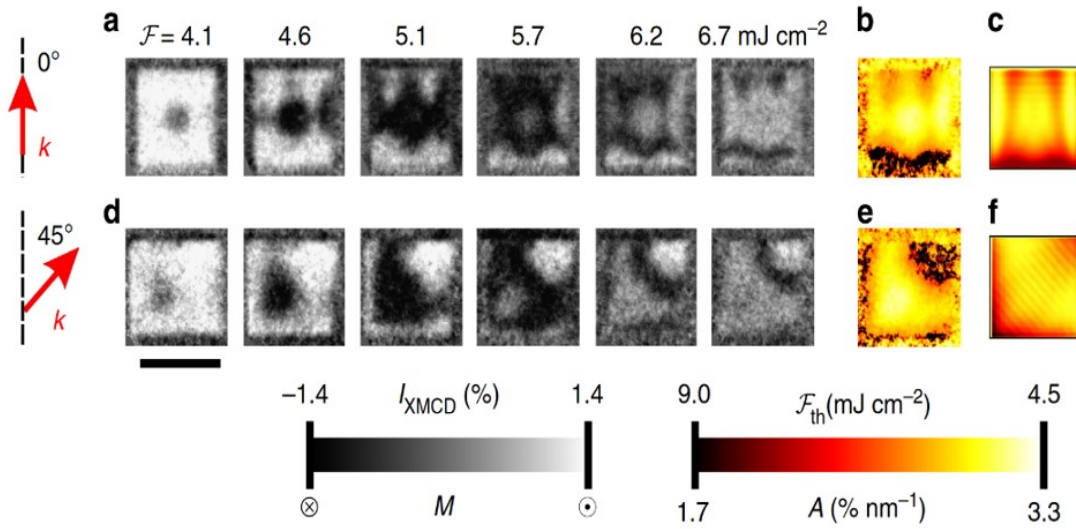


Figure 1.20: Time resolved XMCD PEEM imaging as a function of the incident laser fluence F and for an angle between the planar component of the laser wave vector \mathbf{k} with an edge equal to (a) 0° and (d) 45° . Absorption profile A obtained from the FDTD simulations for the (c) 0° and the (f) 45° incoming laser direction. Threshold Fluence F_{th} patterns obtained from the XMCD time-resolved experiments for the (b) 0° and the (e) 45° incoming laser direction. The experimental observations and simulations were carried out inside $5 \mu\text{m} \times 5 \mu\text{m}$ GdFeCo microstructures. Scale bar 5 nm. Figure taken from¹¹².

formed time-resolved XMCD PEEM. Figure 1.20(a) and 1.20(d) showed XMCD time-resolved images of the $5 \mu\text{m} \times 5 \mu\text{m}$ microstructure with a time delay $t = 400 \text{ ps}$ as a function of the incidence laser direction. Indeed, these Figures give respectively the magnetic configurations of this structure with an incidence angle of 0° and 45° with respect to an edge of the sample. Moreover, at this timescale, the magnetization of the Gd and FeCo sublattices are again in equilibrium with each other¹. This allows the magnetization of the structure to be characterized by measuring the magnetization of a single sublattice. Initially saturated with an applied OOP field, the initial single magnetic domain state is characterized by a white homogeneous XMCD image contrast. Remarkably, Figure 1.20(c), (f) and 1.20(b), (e) shows a direct relationship between the absorption profile A obtained from the FDTD simulations and the threshold Fluence F_{th} patterns obtained from the XMCD time-resolved experiments, respectively. In fact, a good qualitative and quantitative agreement was obtained, as a zone with a low F_{th} corresponds to a zone with high absorption and reciprocally. Consequently, it is not the fluence threshold F_{th} , which changes within the microstructure, but the light absorption A .

Moreover, for a low fluence $F = 4.1 \text{ mJ/cm}^2$, a grey contrast in the center of the structure can be seen in Figure 1.20(a) proving the partial demagnetization. As the fluence increases, the con-

trast between the different areas of the microstructure changes from white to black and then from black to grey. To understand this contrast behavior with the fluence, they performed dynamics measurement of the magnetization by realizing time-resolved XMCD PEEM imaging in time-resolved mode with a fix interval of time t between the laser pump and the X-ray probe. Therefore, the spatial resolution of the intermediate magnetic state in the structure can be recorded during this time interval. They proved that the change in contrast from white to black and from black to grey in Figure 1.20(a) corresponds respectively to the onset of AOS when fluence is increased and the loss of deterministic reversal when you continue to increase the fluence (demagnetization). This well know AOS state diagram with the threshold fluence⁶⁰ was also observed in $2\ \mu\text{m} \times 2\ \mu\text{m}$ and $1\ \mu\text{m} \times 1\ \mu\text{m}$ microstructures with a laser having a planar wave vector making an angle of 45° with an edge of the sample.

1.5.3 AOS in nanostructure of GdCo

More recently, Amal El-Ghazaly et al.⁶ demonstrated SP-AOHIS in amorphous GdCo at nanoscale with OOP magnetization and switched 75% of the magnetization in 2 ps for 200 nm patterned dot. In fact, by using a lift-off technique they patterned Ta(3 nm)/Pt(3 nm)/Gd₃₀Co₇₀(10 nm)/Pt(3 nm) stack. This sample exhibited PMA and AOS at room temperature. Then, they performed single shot experiment of ten consecutive laser as represented in Figure 1.21(a). Indeed, this figure demonstrates a perfect toggle switching on an array of size $25\ \mu\text{m} \times 25\ \mu\text{m}$ filled with equally spaced disks of spacing $2d$, where d equal to 500 nm represent the dot diameter. But clear toggle switching demonstration can't be performed for small 200 nm disks due to the laser detection limit. Moreover, they realized TR-MOKE experiment within micro and nanoscale, where they used a 70 fs laser pulses generated by a Ti-sapphire to perform pump-probe magnetization dynamics. Then, they divided this laser in two laser beams of 95 μm and 15 μm (lower than the magnetic array area) of spot larger for the pump and probe beam, respectively. A fixed pumping fluence of $6.89\ \text{mJ}/\text{cm}^2$ was found to be sufficient to achieve AOS of the smallest disks and Figure 1.21(b) presents the trends of the time to reach 75% of the opposite magnetization as a function of dot size. This time decreases rapidly as the dot size is reduced, from approximately 40 ps for dot of 15 μm to 2 ps for dot of 200 nm diameter. They attributed this faster rate in the smallest structure by the simultaneously increase of the electron-phonon and spin-lattice couplings, allowing faster energy dissipation, thus causing faster spin stabilization and magnetization in the reverse magnetization direction. However, various effects such as the non-uniform absorption profile of the light in the case of oblique incident light on a pattern, the interference patterns generated by the light hitting the nanodot array and the detection limit

1.6. GOALS AND OUTLINE OF THE THESIS

of the laser generate many spurious signals, makes the calculation of the fluence absorbed in the nanostructure difficult.

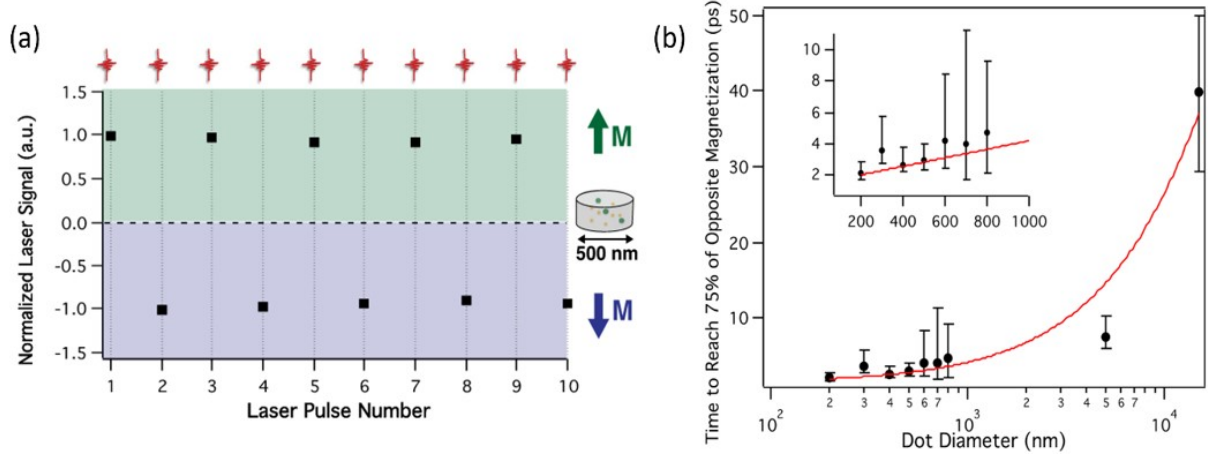


Figure 1.21: (a) Single shot experiment performed with a laser MOKE for dot diameter of 500 nm. Irradiation of 10 consecutive pulses causes the magnetization state to alternate up and down, demonstrating a toggle switching behavior. (b) Variation of the time taken for the magnetization to cross a 75% switching threshold with different dot diameters. The inset shows an extended view of the dot at the nanoscale. Figure taken from⁶.

1.6 Goals and outline of the thesis

The reversal of the magnetization by one ultrashort femtosecond pulse presents a high interest for the scientific community as showed in this first chapter. In particular, the study of the size effect in magnetic materials that exhibit SP-AOHIS appears to be a great fundamental necessity, due to a still insufficient understanding of the microscopic mechanisms involved in optical switching. Therefore, the aim of this thesis is to study the behavior of the optical switching when we are reducing the lateral dimensions from micro- to nanoscale of a magnetic material that exhibit AO-HIS. To build this investigation, we divided our manuscript in 5 chapters, where the first chapter give a state of the art in the field of ultrafast magnetization manipulation by a femto- or picosecond laser pulses.

The second part will present the methods and techniques used to fabricate the full films and nanostructures that have been investigated in this work. Moreover, the MOKE setup that we used to perform AOS will be presented and the detail of the magnetic characterization that we realized

CHAPTER 1. STATE OF ART

using magnetic force microscopy (MFM) will be presented. At the end of this chapter, the reader will find the reasons why we characterize AOS ex-situ with MFM, and we will detail our method to identify the magnetization orientation extracted from the MFM images of our systems.

In the following chapter, we will focus on the size effect of the AO-HIS in GdFeCo periodic structures. Indeed, a systematic study of the magnetization reversal for GdFeCo disks which diameter ranges from 3 μm to 400 nm with 35 fs linear polarization laser pulses will be presented. Toggle switching will be observed for all sizes and a state diagram will be built from fluence variation. The size variation of the threshold and random fluence will reveal a non-monotonic behavior which highlights the importance of the specific light absorption in nanostructures. Finally, the influence of the pulse duration and the period in 400 nm dot will be particularly investigated and will allow us to open outlook.

The next chapter will carry out our investigation of the Gd thickness layer effect on the SP-AOHIS in Pt/Co/Gd(wedge)/Pt, Pt/Gd(wedge)/Co/Pt, Pt/GdCo(wedge)/Pt stack and show that it can be drastically reduced. In fact, in the case of the bottom and top Co/Pt interface, a systematic study of all-optical switching for Gd thickness from 0.06 to 0.77 nm with 35 fs linear polarization laser pulses will be presented. Different regimes will be identified: no switching, multidomain state, switching and perfect toggle switching (PTS). Remarkably, the perfect toggle switching will show to be maintained down to 0.1 nm Gd thickness. Surprisingly the effect of Gadolinium will be very different on top and bottom interfaces.

The last part of this work will concentrate our systematic study of the magnetization reversal for Pt(3.7 nm)/Gd/Co(0.7 nm)/Pt(3 nm) disks which diameter ranges from 3 μm to 400 nm with 35 fs linear polarization laser pulses. In addition, laser parameters like polarization, and the number of pulses will be changed to characterize the reversal in this new interface engineering ferromagnet. Notably, by varying the number of pulses, it will appear that a single toggle switching probability can describe the reversal behavior. The variation of this switching probability will be precisely measured and will degrade as the diameter of the disks is reduced. The "exponential" variation of the switching probability with the disk diameter size will be quite particular and cannot be explained by specific optical effects. On the other hand, a highly non-uniform switching process with a small microscopic switching probability will explain our experimental data. A simple probabilistic model, analog to Condorcet's jury theorem, will be proposed and compared to micromagnetic simulations.

Chapter 2

Experimental methods

The study of the size effect on all-optical switching requires both ultrashort laser excitation, magnetic materials exhibiting full-film all-optical switching, and the ability to reduce the lateral size of these samples to the nanoscale. In this chapter 2, We will first describe the ultrathin film samples that we used to investigate the size effect. Moreover, the nano fabrication process used to fabricate periodic nanostructures that have been investigated in this work will be presented in detail. Secondly, the femtosecond laser setup that we used to perform AOS will be described. In addition, we will present the two static imaging systems (MFM and MOKE imaging) that we used to magnetically characterize full film and patterned system after the AOS experiments. At the end of this chapter, the reader will understand the reasons why we are probing the laser-induced change in magnetization of ferromagnetic nanodisks with the MFM, and we will detail the method used to identify the orientation of the magnetization extracted from the MFM images.

2.1 Full film deposition and nanofabrication

2.1.1 Full film deposition

In this thesis, we used two types of magnetic materials: GdFeCo ferrimagnetic alloy and Pt/Co/Pt ferromagnet doped with Gd. If the SP-AOHIS mechanism of the first material has been studied in several works (see section 1.2), the second magnetic material is a new engineering material. However, for the sake of simplicity, in this chapter, we will focus on the samples that was used in electron beam lithography. Other engineered ferromagnet stacks will be presented in chapter 4. So, Figure 2.1 showss the stack grown by magnetron sputtering on glass substrate (Thanks Pr. Michel Hehn). In fact, Figure 2.1(a) shows the stack of the ferrimagnetic alloy:

CHAPTER 2. EXPERIMENTAL METHODS

glass/ Ta (5 nm)/Cu (5 nm)/Gd₂₄(FeCo)₇₆(20 nm)/Pt (5 nm), where the Pt layer prevents oxidation. While Figure 2.1(b) presents the composition of the ferromagnet: Ta (3 nm)/Pt (3 nm)/Co (0.7 nm)/Pt (3.7 nm) doped with a small amount of Gd at the bottom Co/Pt interface. Where The Ta buffer layer acts as an adhesion and facilitator of the [111] preferred crystallographic orientation of the whole stack.

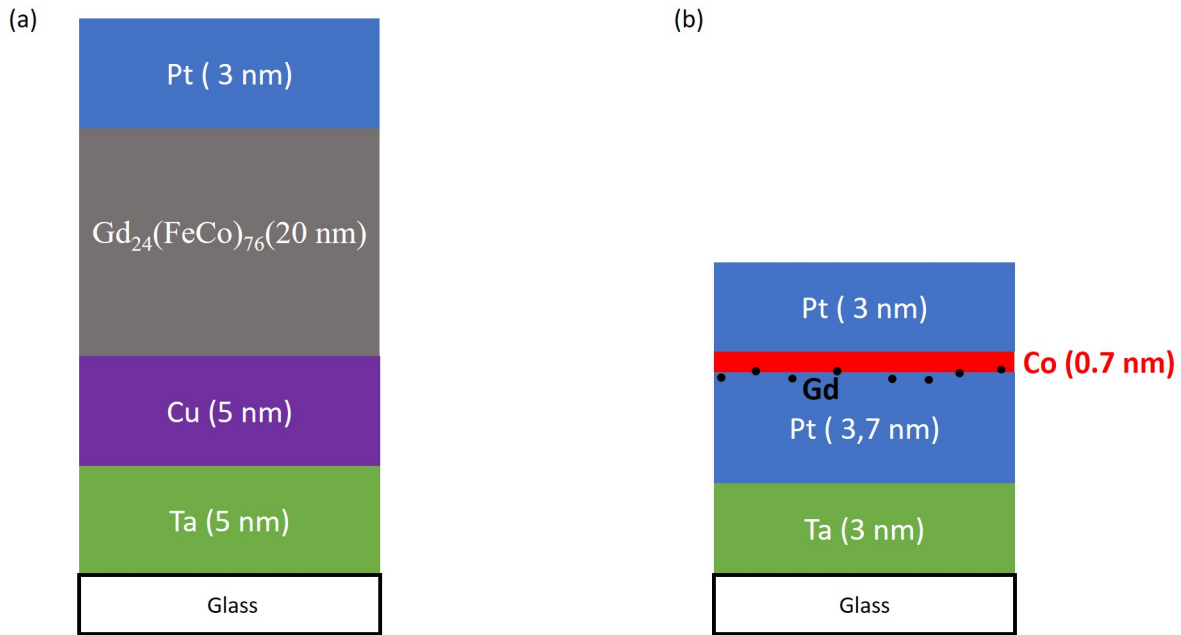


Figure 2.1: (a) Structure of the Gd₂₄(FeCo)₇₆(20 nm) sample and (b) of the tri-layer Pt (3 nm)/Co (0.7 nm)/Pt (3.7 nm) doped with a small amount of Gd at the bottom Co/Pt interface.

2.1.2 Nanofabrication

As all the samples we used in this work were grown by PVD magnetron sputtering, the next step for the elaboration of nanoscale periodic structures requires the use of a high-resolution patterning technique, namely electron beam lithography. Although several other processes can be used to reduce the lateral size of a material, it is this e-beam process that has been used in this thesis. The interest of this technique lies in the use of a short wavelength beam (a few picometers), which makes it possible to avoid the diffraction phenomena observed in photonic optics for the fabrication of sub-micron objects. This microelectronic process consists of the creation of a motif in an electrosensitive material, followed by the transfer of this pattern into the active layer of which we want to make a nanostructure by etching. The specific step of this

2.1. FULL FILM DEPOSITION AND NANOFABRICATION

nanofabrication process is illustrated in Figure 2.2. In the following sections, we will present the different steps that allowed us to realize these small-scale periodic magnetic structures.

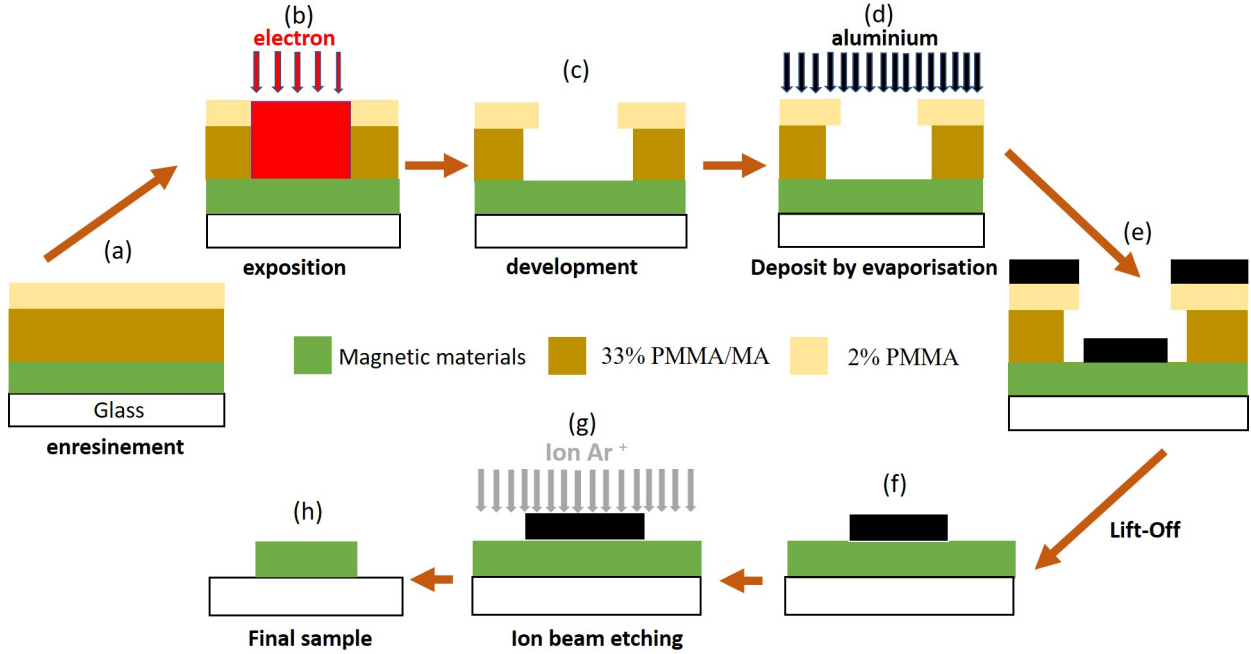


Figure 2.2: electron beam lithography process used in this thesis to realize periodic magnetic structures.

2.1.2.1 Sample preparation and spin coating

Before starting the process, we need to prepare our samples, by cleaning the surface of the stacks with two solvents: acetone (first) and isopropanol. Then, by using nitrogen gas, we can dry the surface of the sample. Then, we can start the first step which consists of depositing a bilayer of PMMA on both Pt/Co/Pt and GdFeCo sample surface with two resist layers exhibiting different molecular weights. Where PMMA (polymethyl methacrylate) is a positive electro-sensitive resist, that has been known for over 50 years¹¹⁴. The use of this resist makes sense since it allows working at high resolution¹¹⁵ (up to 10 nm) with high contrast. However, several other combinations of two resists can be made using a copolymer¹¹⁶ or a LOR/PMGI resist¹¹⁷. During this first step, we used a bilayer of diluted 33% PMMA/MA (bottom resist layer) and 2% PMMA (top resist layer), leading to a good lift-off profile¹¹⁸. Indeed, after e-beam irradiation, the 2% PMMA resist dissolves less quickly than the 33% PMMA/MA resist, which will allow the creation of resist patterns in the form of a cap that will facilitate the lift off (see Figure 2.2(c)).

To achieve this bilayer deposition, we firstly deposited a small quantity of 33% PMMA/MA

CHAPTER 2. EXPERIMENTAL METHODS

on the surface of the sample. Then, by applying a strong rotation of the sample on itself, thanks to the initial deposition of the stack on a spinner, we can spread the resist radially on the surface by centrifugation. This first spin coating step is done at a speed of 5000 rpm, during 90 s and with an acceleration of 7000 rpm/s². This centrifugation operation is followed by an annealing at 180^o C during 5 min to remove the solvent from the resist, which is crucial for the next step. Indeed, the next step is to perform the same deposition process (spin coating followed by annealing) for the second layer of 2% PMMA. At the end, a (PMMA/MA) / PMMA bilayer is therefore made with 200 nm and 100 nm of thickness, respectively (Figure 2.2(a)).

2.1.2.2 Exposition and design of the sample

The second step of the nanofabrication process is to create our periodic micro- and nanostructures. In fact, we drew the pattern on the sample with the help of a mask, thanks to the interaction between the positive electrosensitive resist (described in the previous section) and a focused incident electron beam exposition. This exposure will cause a degradation of the polymer chains under electron irradiation in the exposed areas, leading to their easier dissolution during the development phase than in the unexposed areas. The e-beam lithography equipment used in this thesis is a Raith150-TWO system. Figure 2.3(a) gives an overview of this equipment. It consists of an electron column composed of a cathode that allows work up to an acceleration voltage of 30 kV, a series of magnetic lenses that focus and correct aberrations to obtain the smallest electron beam, a beam deflector and blanker to scan and stop the electron beam over the target, respectively. In addition, an interferometric stage is required to move the substrate from one writing field to another, but also to stop the sample to allow the beam to irradiate the predefined areas on the gdsii file (the e-beam being blocked during the displacement between each field). Figure 2.3(b) shows the schematic diagram of a e-beam lithography (the reader will find more details about the e-beam process in the Roland Salut thesis¹¹⁹ and in various works^{120–122}).

To realize our pattern, key parameters like the number of electrons per unit area (the dose in $\mu\text{C}/\text{cm}^2$) which arrive on the mask, the electron acceleration energy (in kV), the aperture (in μm) and the working distance (in mm) can be adjusted to reach resolutions of the order of ten nanometers. Then, we used in this nanofabrication process a combination of 100 $\mu\text{C}/\text{cm}^2$, 20 kV, 10 μm and 9 mm. Figure 2.4 shows the design we chose to pattern the sample. Indeed Figure 2.4(a) illustrate writing fields with the names A1, A2, A3, A4, A5, A6, A7 and A8 representing areas filled with equidistant disks of diameter 400 nm, 600 nm, 800 nm, 1 μm , 1.2 μm , 1.5 μm , 2 μm and 3 μm , respectively. For the case of 400 nm of dot diameter inside (Figure 2.4(b), we can clearly represents the disk diameter D and the fixed spacing d equal to 300 nm (Figure 2.4(c)).

2.1. FULL FILM DEPOSITION AND NANOFABRICATION

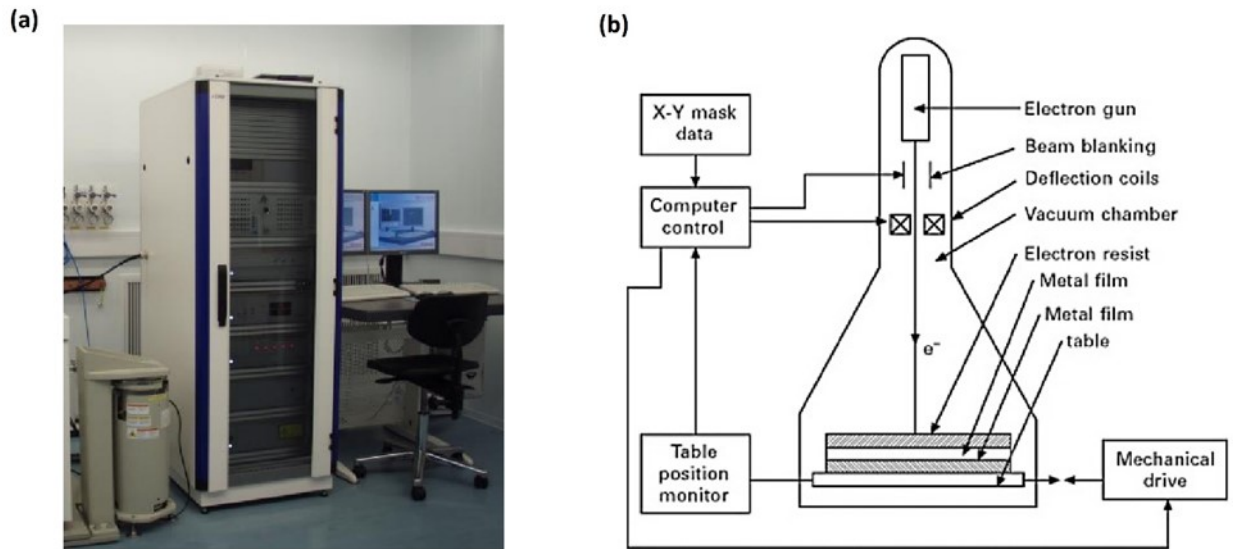


Figure 2.3: (a) Picture of the Raith150-TWO station for the exposure of electro-sensitive resist, installed in the cleanroom of the Jean Lamour Institute. (b) Schematic representation of e-beam lithography. Figure taken from¹²³.

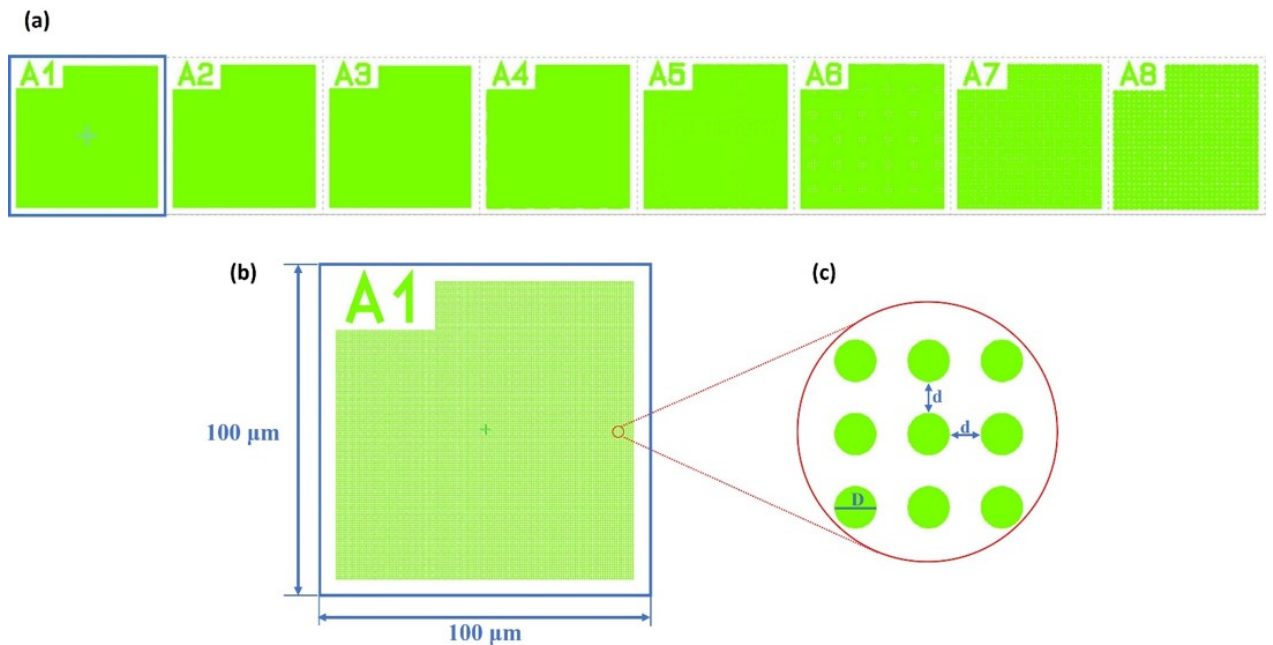


Figure 2.4: Design of the sample. (a) Illustration of the 8 different writing fields and (b) the case of D equal to $400\ \text{nm}$. For each dot diameter D , an area of size $100\ \mu\text{m} \times 100\ \mu\text{m}$ is filled with (c) equally spaced disks with a fixed spacing d equal to $300\ \text{nm}$.

CHAPTER 2. EXPERIMENTAL METHODS

2.1.2.3 Development, Evaporation, Lift-off, and Etching

2.1.2.3.1 Development

After the exposition step, the sample is dipped in a developer. I used a combination of developer (Methyl Isobutyl Ketone (MIBK) and Isopropanol (IPA) with a volume ratio 1:3. Indeed, since the use of MIBK alone is too powerful and can dissolve unexposed areas (although I used positive resist), I mixed with a less powerful developer, IPA. So, the sample remains in the MIBK: IPA (1:3) resist development bath during 1 min, followed by a rinse with IPA for 30 s. After drying with nitrogen, I have the formation of cavities where the magnetic layer is bare and has the shape of the desired patterns, as shows in Figure 2.2(c).

2.1.2.3.2 Evaporation

However, the resist mask over the magnetic layer is limited for the etching process. This is because the PMMA resist will harden during etching, making it difficult to remove after this etching step. For this reason, we evaporated 50 nm (resp. 80 nm) of Aluminum onto the resist mask and the bare ferromagnetic layer (rep. Ferrimagnetic alloy), thus forming a hard metallic mask (Figure 2.2(d) to Figure 2.2(e)). The choice of Al is based on its ease of removal after the lift-off process. Furthermore, the value of the thickness Al was chosen for safety reasons. Indeed, for a thicker Al, the cavity created during development can be blocked, resulting in a partial removal of the Al during the lift-off. On the other hand, for a thinner mask, the Al layer will not be thick enough to protect the magnetic layer from the ion beam during the etching process. This evaporation step has been realized by using an e-beam evaporation from "plassys MEB400S " and the thickness is measured using a quartz crystal microbalance at the IJL's CC Minalor.

2.1. FULL FILM DEPOSITION AND NANOFABRICATION

2.1.2.3.3 Lift-off

The next step is to place the sample in a solvent, which causes the resist and the Al deposited on it to dissolve. Only the Al directly in contact with the ferromagnet remains, forming a mask for the next step, as mentioned in the previous step. In fact, due to the formation of the resist cap (due to the use of the resist bilayer with different dissolution rates), and a directional evaporation of the Al, the deposit will leave a gap between the resist and the Al. As a result, the Al layer will not be continuous, allowing the remover to reach the resist more easily and leaving only the metal deposit on the magnetic material (Figure 2.2(f)). To perform this lift-off step, we first leave the sample in a hot bath of Remover 1165 (at 80° C) for two hours. The sample is then ultrasonicated for 5 minutes to remove the most stubborn resist. This is done twice for better results, before finally rinsing the sample with water.

2.1.2.3.4 Etching

The last step of the Nanofabrication consists of irradiating the sample by an Argon ions (Ar^+) beam (Figure 2.2(g)). At the end of the etching, it remains the magnetic stack protected by the thicker Al mask, a thinner Al hard mask, and collars at the edges of the structures. Figure 2.5 illustrates the evolution of the etching process with time and highlighted the redeposition process during this step.

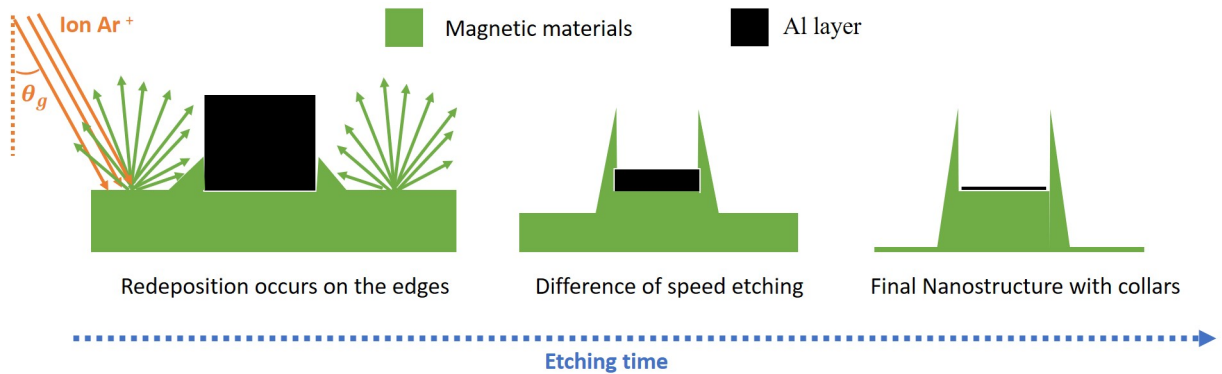


Figure 2.5: Evolution of the etching process with time.

In this step, the most important parameter is the grating angle θ_g . Previous study in our research group reported that the best profile of nanostructures was obtained for a grating at 10^{0124} . Indeed, this angle reduces the redeposition of atoms on the sides of the nanostructure and in particular the formation of collars. However, the creation of these collars is inherent to

CHAPTER 2. EXPERIMENTAL METHODS

the etching process and the use of Al. In fact, because the etching speed of Al is higher than that of the magnetic stack, the collars are observable before the dissolution of the whole Al mask. In addition, during etching step, the etched atoms are analyzed by a mass spectrometer, which allows the progress of the etching process to be monitored in real time. Figure 2.6 shows an example for the ferromagnet Pt/Co/Pt stack doped with Gd. We finish the etching process with a chemical etch to remove the thinner Al hard mask on top of the magnetic stack. We placed the whole stack in a MICROPOSIT MF-319 developer for 120 s at 20⁰ C. Then we rinsed using deionized water.

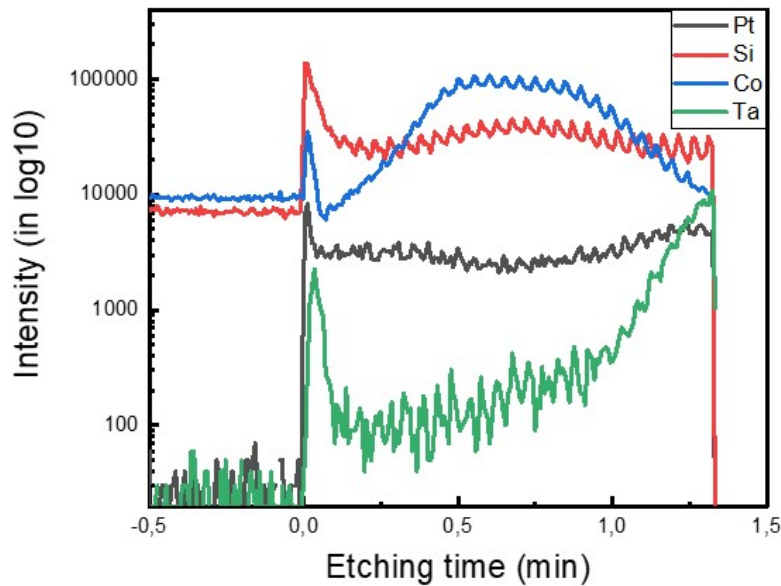


Figure 2.6: Etching of the Gd-doped Pt/Co/Pt trilayer. The increase of the Ta signal marks approximately the end of the operation.

We finally obtained periodic structures, as illustrated by an example of a Scanning Electron Microscopy (SEM) images below. Indeed, Figure 2.7(a) shows an overview of the magnetic GdFeCo dot arrays in a diameter range from 3 μm to 400 nm. In addition, Figure 2.7(b) shows GdFeCo nanostructures in good agreement with the diameter of nanodisks (400 nm) and the pitch of the lattice (300 nm). The white contrast at the edges of each dot is the signature of collars. However, more larger are the structure, smaller are the size of these collars compared to the size of the magnetic disks.

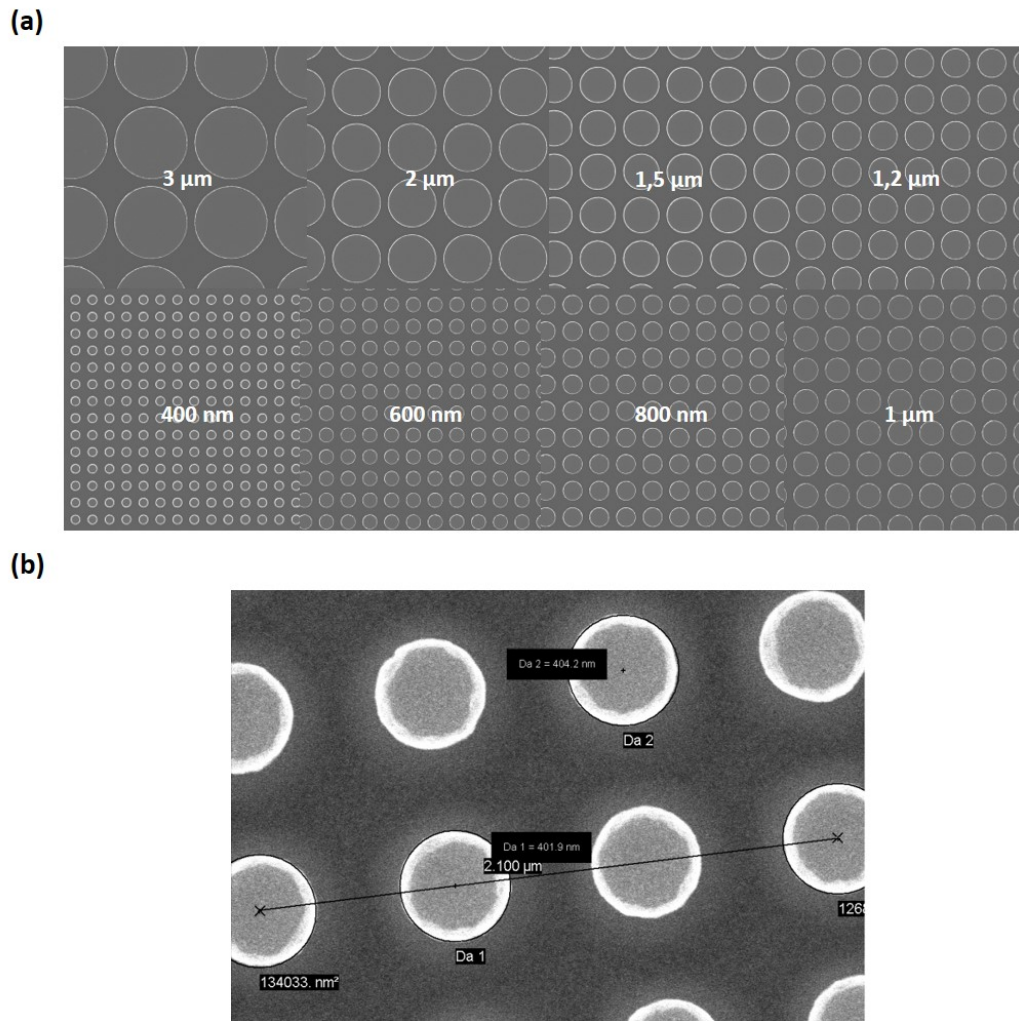


Figure 2.7: SEM image showing (a) an overview of GdFeCo magnetic dot arrays for all dot sizes and (b) the good agreement of the lattice pitch and the dot diameter in the case of 400 nm of dot diameter.

2.2 Magneto-optical and magnetic characterization

The goal of this section is to present the different equipments that I used to characterize our samples. Although I will show structural characterizations of an engineered ferromagnet in chapter 4, I will not present the Transmission Electron Microscope that we used to perform high resolution images. The reason is simple, all these structural measurements like Transmission Electron Microscopy (TEM), High Resolution Transmission Electron Microscopy (HRTEM), Scanning Transmission Electron Microscopy (STEM) or Electron Energy Loss Spectroscopy (EELS) have been performed within the “CC 3M” at the Jean Lamour Institute by Dr Jaafar Ghanbaja. Therefore, in this section, I will focus on techniques that I was the main user.

2.2.1 MOKE magnetometry

The MOKE (Magneto-Optic Kerr Effect) is a phenomenon based on the interaction between a magnetic medium and an electromagnetic field (light). This Kerr effect is the result of the change in polarization of light after reflection from a magnetic material. Depending on the magnetization orientation we have transversal or longitudinal MOKE configuration when the magnetization is in the sample plane, and polar configuration when the magnetization is out of plane. The reflected light has an elliptical polarization, causing an angle θ_K between the polarization and incidence plane. This angle θ_K is called Kerr rotation and is related nontrivially to the magnetization of the transition metal¹²⁵. Indeed, Gd electrons (4f electrons) feel little of the electric field generated by the incident light, due to its shielding by the other electrons of the outermost orbitals. Whereas in the case of transition metals (such as Co and Fe) the 3d electrons are in the front line of the incident electromagnetic wave. Therefore, the response of a Gd-doped Pt/Co/Pt or GdFeCo sample to the exposure of light in a MOKE measurement comes mainly from the Co and Fe atoms. Figure 2.8 depicts a picture of the Kerr measurement setup used in a polar configuration as the Pt/Co/Pt trilayer has a high PMA (Perpendicular Magnetization Anisotropy) and the GdFeCo sample has also exhibited an OOP (Out Of Plane) magnetization after and before the annealing step during the e-beam process (see section 2.1.2.1).

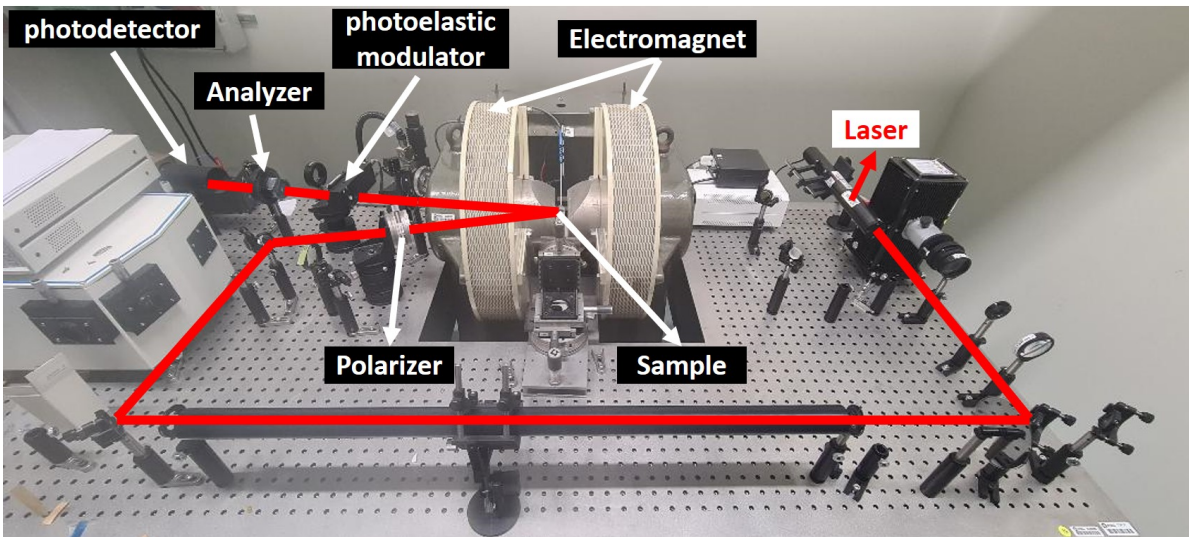


Figure 2.8: In situ picture of the MOKE magnetometry setup used in all this work.

The light source used is a helium neon laser emitting at 650 nm. The beam light coming out of the laser diode then passes through a polarizer which allows the incident beam to be linearly polarized. The beam reflected from the sample is analyzed by crossing successively through a

2.2. MAGNETO-OPTICAL AND MAGNETIC CHARACTERIZATION

photoelastic modulator (PEM) and an analyzer placed at 45° from the polarizer. A photodetector then measures its intensity $I(t)$ which can be written as¹²⁵:

$$I(t) \simeq I_0[1 + 2\theta_K J_0(A_0) - 4\epsilon_K J_1() \sin(wt) + 4\theta_K J_2(A_0) \cos(2wt)] \quad (2.1)$$

Where ϵ_K is the Kerr ellipticity, A_0 is the PEM modulation amplitude introduced at pulsation w and J_n are the Bessel functions. Experimentally, we used the PEM frequency (50 kHz) as a reference frequency for a lock-in amplifier and $A_0 = 3.05 \text{ rad}$ is chosen for the optimization of the second harmonic signal ($4\theta_K J_2(A_0) \cos(2wt)$) to give the Kerr rotation θ_K . The external magnetic field is generated using an electromagnet and controlled by a power supply, which allows us to make hysteresis loop measurements. The output signal of the lock-in amplifier is given up to a certain phase. We choose in this work to calibrate the phase with a GdFeCo alloy below its compensation composition (TM- dominant), such that the output signal be positive at positive external magnetic fields.

2.2.2 MOKE microscopy with femtosecond laser pulse excitation

2.2.2.1 Kerr imaging set-up

To observe the magnetization state of both full films and patterned structures after exposure to laser pulses, we used MOKE microscopy. Indeed, by using a Kerr imaging set-up installed within the Nano-magnetism and Spintronics team at Institut Jean Lamour, we were able to control the magnetization of the micro- and nanostructures by sending laser pulses. Figure 2.9 depicts the static magneto-optical imaging set-up used in this work. The beam source used is a Ti-sapphire laser emitting at 5 kHz repetition rate and a central wavelength of 800 nm. Before reaching to the sample surface, the laser beam crossed several optics namely a Glan-Taylor polarizer, a half-wave plate, and a convex lens (Lens 4). The Glan-Taylor polarizer linearly polarize the laser pulse, while the half-wave plate induces a phase difference of π which allows us to vary the laser power. In addition, the convex lens focuses the laser beam with a Gaussian intensity profile onto the sample surface and its displacement allows the spot size of the beam to be changed. Furthermore, the laser pulse duration can be changed by stretching or compressing the pair of gratings in the pulse picker. Finally, the number of incident laser pulses and the repetition rate can be modified by using a pulse picker.

The magnetic response of thin full films and periodic structures to the femto- or picosecond laser pulses is probed in the other side of the sample (glass side), via a light (the probe) and a pair

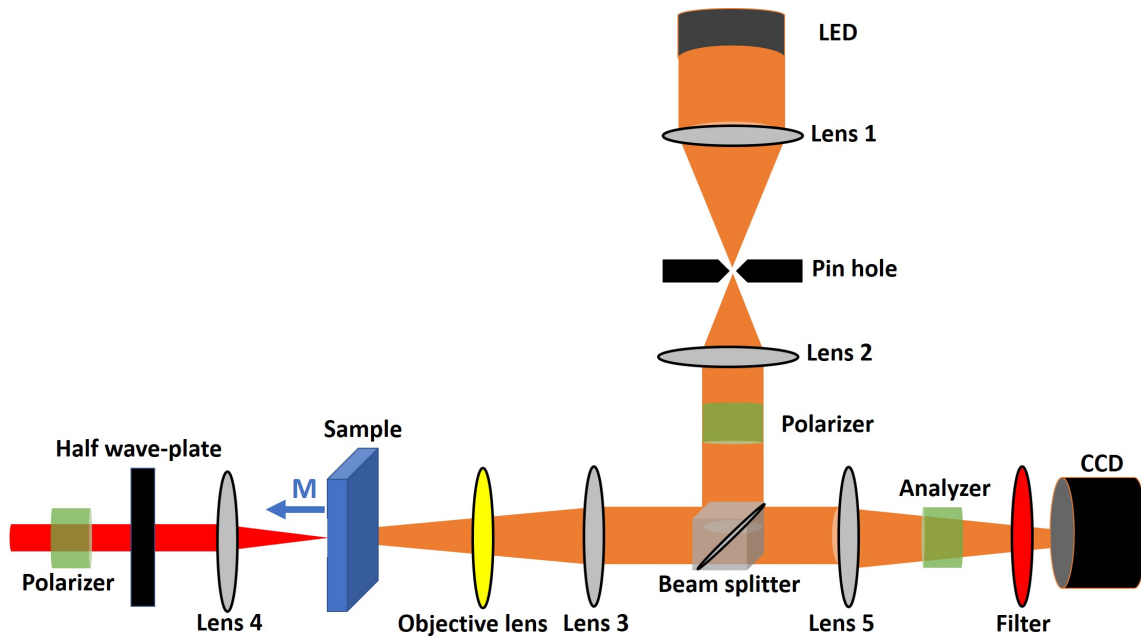


Figure 2.9: Kerr imaging set-up used for magneto-optical characterization of magnetic configuration of patterned or full film samples. The orange color of the LED light has been used for the purpose of representation

of polarizer-analyzer which are placed in Kerr configuration (reflection mode). The probe light used is a diode emitting with a central wavelength around 630 nm and is linearly polarized by the polarizer. This polarizer and analyzer are crossed in a such way that in absence of magnetic sample, a full extinction can be observed (no light is transmitted to the CCD) which allows us to obtain a maximum magneto-optical contrast by even the smallest Kerr rotation (in presence of magnetic sample). Additionally, a filter is insert in front of CCD camera to prevent any laser light and let only the reflected probe light go through. Finally, proper alignment is achieved to overlap the pump (the femtosecond laser pulse) and the probe (the reflected LED) on the sample surface, allowing us to image the magnetic domains directly with the CCD (Charge Coupled Device) camera.

2.2.2.2 MOKE image acquisition

Experimentally, depending on the lateral size and thickness of the magnetic stack, the image acquisition and analysis protocol on the CCD camera after laser pulse irradiation is quite different. However, for all MOKE images (patterned or full film samples), we took a background image with the sample in a magnetic state before sending any laser pulse and we subtract this

2.2. MAGNETO-OPTICAL AND MAGNETIC CHARACTERIZATION

background image from any subsequent image. This imaging process avoids the presence of various non-magnetic contributions like surface morphology in our MOKE images. Moreover, the scale bars are obtained thanks to the calibration that we can realized by using our patterned samples of known dimensions.

For full film case, an example of magneto-optical images is presented in Figure 2.10. Indeed, Figure 2.10 shows the results of the exposure of the femtosecond laser in a single-pulse mode linearly polarized on Pt (3.7 nm)/Gd/Co(0.7 nm)/Pt(3 nm) full film, initially in a single domain state after applying a field of few hundred of mT out of plane (Figure 2.10(a)). The light grey area corresponds to a single domain initially magnetized down. After the excitation of the light grey area with the first pulse with a given fluence, one can see the formation of a dark grey circle region (Figure 2.10(b)). Then, the second pulse with the same fluence reverses the magnetization of the irradiated circle region and we observe a recovering of the initial magnetic state (Figure 2.10(c)). This image acquisition protocol was used in this thesis for the case of ferrimagnet, ferromagnet, and Gd-wedge ferromagnet full film with the help of a magnet to apply the initial magnetic field.

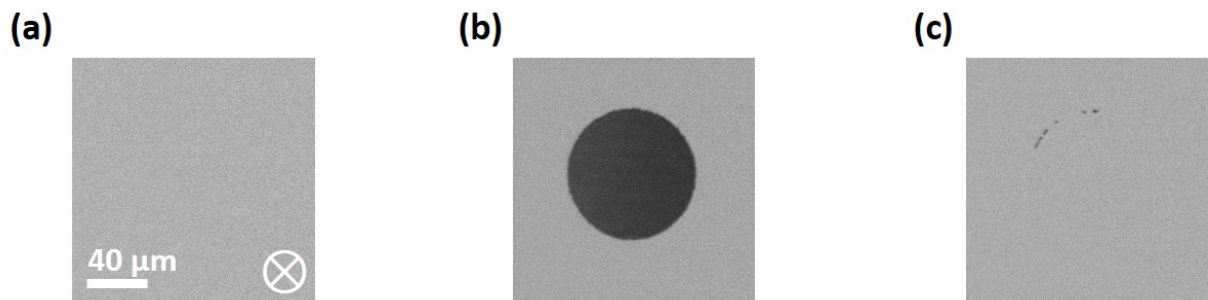


Figure 2.10: Magneto-optical images of Pt(3.7 nm)/Gd/Co(0.7 nm)/Pt(3 nm) full film obtained after the action of (a) zero, (b) one, and (c) two consecutives single laser pulse. The light grey (dark grey) area represents the out of plane magnetization of the film “down” (“up”) as represented by the circled cross. The length of the scale bar is 40 μm .

For periodic magnetic structure case, an example of magneto-optical images is presented in Figure 2.11. In fact, Figures 2.11(a) and (b) shows the results of the exposure of the femtosecond laser in a single-pulse mode on arrays of 400 nm magnetic disks of $\text{Gd}_{24}(\text{FeCo})_{76}$ (20 nm). Initially, each patterned nanostructures are in a single domain after application of an OOP magnetic field of 1 T and a progressive return to zero (in steps of 100 mT). The application of 1 T using an electromagnet is essential to be shore that all structures of all sizes exhibited OOP magnetization in the same orientation and the decrease of the magnetic field to zero is needful

CHAPTER 2. EXPERIMENTAL METHODS

to obtain the direction of the magnetization of each magnetic structures at zero field. After the excitation of the initial state (depicted by a light-grey region) with the first pulse, we see the formation of a dark-grey area (Figure 2.11(a)). The second pulse then reverses the magnetization of the irradiated region forming a light grey area (Figure 2.11(b)). This image acquisition protocol was also used in this thesis for the case of Pt (3.7 nm)/Gd/Co(0.7 nm)/Pt(3 nm) disks, as illustrated in Figures 2.11(c) and 2.11(d) for 400 nm of disk diameter.

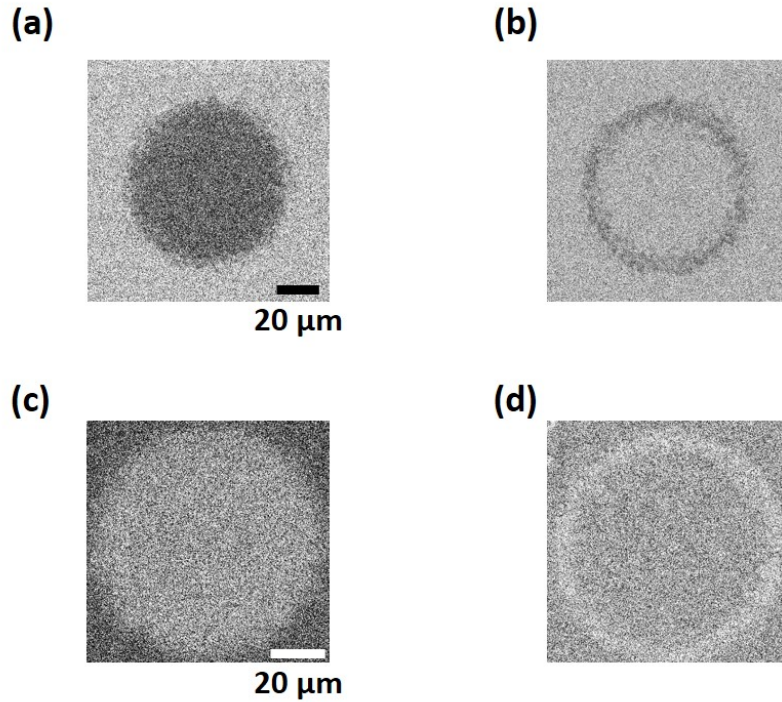


Figure 2.11: Magneto-optical images obtained after the action of (a)((c)) one and (b)((d)) two consecutive single laser pulse for 400 nm periodic magnetic disks of $\text{Gd}_{24}(\text{FeCo})_{76}(20 \text{ nm})$ ($\text{Pt}(3.7 \text{ nm})/\text{Gd}/\text{Co}(0.7 \text{ nm})/\text{Pt}(3 \text{ nm})$).

As we see with Figure 2.11, we can identify the entire array of disks on the CCD camera with this Kerr imaging set-up. But quantitative analyses of the magnetization control of nanostructures proved difficult. Indeed, as the diffraction phenomena start when the size of the object studied is of the order of magnitude of the radiation wavelength (630 nm for the LED), the magneto-optical images do not allow to distinguish the contrasts linked to the orientation of the magnetic domains contained within the micro- and nanodisks. However, for our study of the size effect in GdFeCo the resolution of the CCD camera (images of 2448×2048 pixels), will be enough to qualitatively distinguished the different magnetic state after a femtosecond laser excitation, as was illustrated in Figures 2.11(a) and (b). In the case of Pt/Gd/Co/Pt, magnetic analyses

2.2. MAGNETO-OPTICAL AND MAGNETIC CHARACTERIZATION

will be more complicated. In fact, due to the low magneto-optical contrast compared to GdFeCo, which can be related to the difference of Co thickness in the two samples (20 nm for the GdFeCo ferrimagnet and just 0.7 nm for the Pt/Co/Pt ferromagnet), the MOKE microscopy is limited. Nevertheless, several other characterization techniques can be used to observe the magnetization behavior of magnetic nanostructures after exposure to laser pulses. For example, electrical measurements using the Anomalous Hall Effect (AHE) can give average information about an array of magnetic disks. But if, on the contrary, we want to obtain individual information on the magnetic state of each dot (monodomain or multidomain), Magnetic Force Microscopy (MFM) is one of the best candidates to achieve this high-resolution characterization, since its spatial resolution is 50 nm to 10 nm¹²⁶. In the following section, we will focus on the MFM that we used to obtain a sharper magnetic contrast in order to confirm the switching of the magnetization of each micro- or nanodot in the area exposed to the laser.

2.2.3 Magnetic Force microscopy

To overcome the limitations of small-scale optical microscopy, we used MFM to characterize our Pt (3.7 nm)/Gd/Co (0.7 nm)/Pt (3 nm) periodic structures. All images presented in this manuscript were carry out with Asylum Research microscope of type “ORIGIN+”, and allow the acquisition of high resolution MFM images, with the possibility of making studies in room temperature. Although, we can apply a planar or perpendicular magnetic field with this microscope, all the MFM scan has been realized in a zero apply field. A picture of this equipment is shown in Figure 2.12.

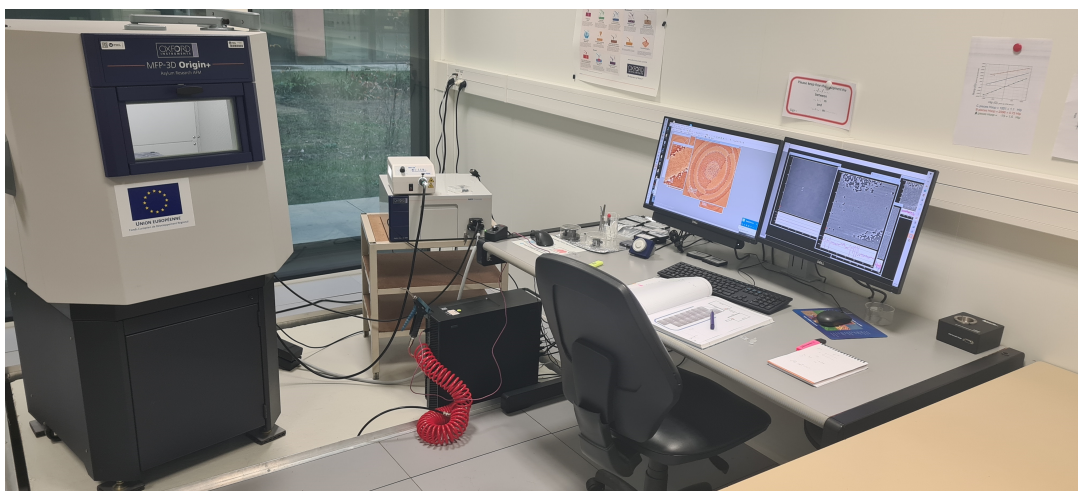


Figure 2.12: MFP3D Asylum Research magnetic force microscope of type “ORIGIN+” used in this work.

CHAPTER 2. EXPERIMENTAL METHODS

The aim of this section is to present the working principle of the MFM used in this work and to give keys to understanding the process that has been used to extract the MFM contrasts for arrays of disks that exhibited out-of-plane magnetization.

2.2.3.1 Working principle

Atomic force microscopy (AFM) is used to study the forces emitted by a sample in interaction with a tip. This tip is placed at the end of a support called cantilever. To obtain MFM images of our patterned sample, the standard AFM tip is covered with a ferromagnetic material (CoCr in our case) which scans the surface of our sample. Indeed, the interaction between a magnetic tip and the magnetic field radiated by a magnetic sample is the base of the magnetic force microscopy. However, several other elements are indispensable for the MFM measurement. In fact, a laser beam is sent to the back of the cantilever, and it is reflected to two photodiodes mounted as a difference signal. In tapping mode (the mode we used), the cantilever oscillates (input signal) at a frequency w_0 close to its resonance. If there is no obstacle, the extremity of the cantilever oscillates (output signal) in phase with the input signal. On the other hand, if the tip approaches a field source, there will be a phase shift between the output signal and the input signal. Figure 2.13 depicts the principle of detection of the vibration of the cantilever.

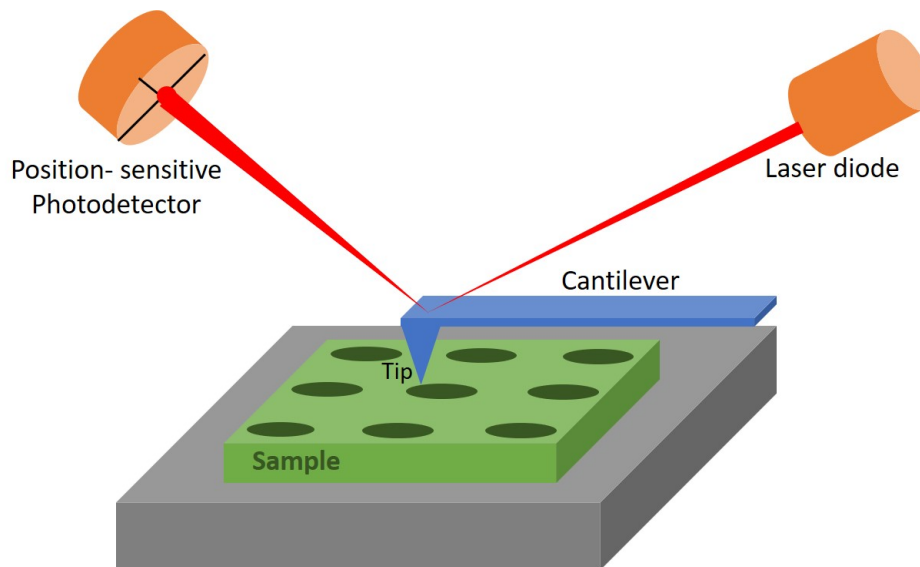


Figure 2.13: Principle of detection of the vibration of the cantilever.

In addition, depending on the type of interaction between the sample surface and the tip, the tapping mode can also give us access to the modification of the amplitude and frequency of the cantilever. The expression of the shift of frequency is given by:

2.2. MAGNETO-OPTICAL AND MAGNETIC CHARACTERIZATION

$$\frac{\Delta w}{w_0} = \frac{w_0 - w_{eff}}{w_0} \simeq \frac{1}{2mw_0^2} \left. \frac{dF(z)}{dz} \right|_{z_0} \quad (2.2)$$

where m is the effective mass of the cantilever and $F(z)$ the forces acting on the cantilever. Furthermore, the amplitude and phase shift also give the gradient of the total forces exerted on the tip by the sample surface. Therefore, the link between the MFM measurement and the magnetic configuration of the sample surface is indirect. Moreover, to consider only magnetic forces (instead of electrostatic forces), we scanned the surface of the sample two times using the lift height technique. This technique is based on the magnitude of the interactions between the tip and the sample surface. A first closed-loop scan is performed closer to the sample surface where the electrostatic forces (Van der Waals forces) are dominant. The purpose of this scan is to measure the topology of the surface (AFM image). Then, a second closed-loop scan is performed with the tip further from the surface, but at a constant height during the scan. This height, called h_{lift} considers the first topological scan and is implemented in order to have constant Van der Waals forces during the second scan. Therefore, magnetic forces related to the magnetic configuration of the surface are dominant. At the end, the change in frequency (Δw), amplitude (ΔA), and phase ($\Delta \phi$) will then only be attributed to the gradient of the magnetic force. Figure 2.14(a) shows magnetic force microscopy mapping of an array of 1 μm diameter disks after exposure to a single laser pulse (Figure 2.14(b) is the corresponding AFM mapping). The light contrast disks located at the edges of the MFM image are those that have not been magnetically altered by the laser pulse. While the dark contrast disks located mainly in the center of the MFM image represent structures with a magnetization totally reversed by the laser pulse excitation. Indeed, when the tip passes over a dot, the measured signal is a light or dark contrast, depending on the orientation of the magnetization and the convention adopted for signal processing. In this work, all microscope images that will be showed in this manuscript were processed with WSxM 5.0 Develop 9.0 software¹²⁷. The reader can find more details about the use of MFM to characterize ultra-thin full film or patterned disks in references^{124, 128–130}. This section was only dedicated to the working principle that we used in this work.

2.2.3.2 Extraction of the contrasts

In this section we will present the process we used to extract the MFM contrast from our Pt/Gd/Co/Pt disk arrays of interest in this work. Briefly, the extraction starts with the determination of the coordinates of the centers of the disks from the AFM image. Then, thanks to this list of coordinates and from the MFM image, the signal (average pixel) associated at each disk is measured. Finally, the corresponding signals are translated into up or down magnetization

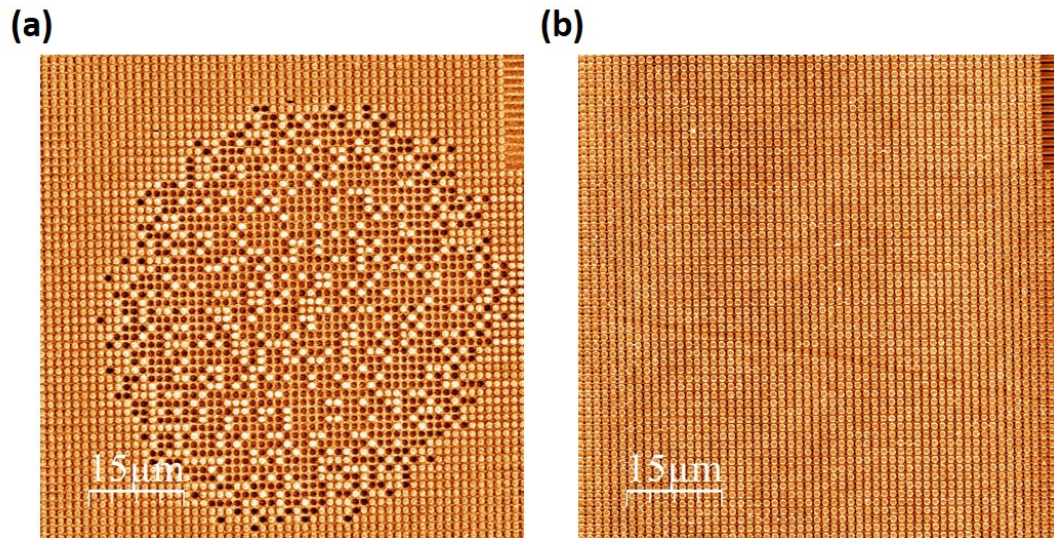


Figure 2.14: (a) MFM mapping and corresponding (b) AFM of a $1 \mu\text{m}$ diameter disks array after exposure to a single laser pulse.

orientation. The purpose of the following paragraphs is to show the reader the different steps to determine the magnetic configurations of disks after exposure to one or more laser pulses. In addition, Wolfram Mathematica 11 (version 11.3.0.0) was the software that we used to perform this extraction process. We focus here on array of $1 \mu\text{m}$ diameter disks depicted in Figure 2.14(a). Moreover, we used the same extraction process for all other arrays with different disk sizes.

2.2.3.2.1 Importation

In this step, it is important that the data is properly processed (e.g. flatten) and properly imported. The images are converted to grayscale for processing, as illustrated in Figure 2.15. The two images must be at the same size and the MFM image is rescaled to have signals (pixel) between 0 and 1.

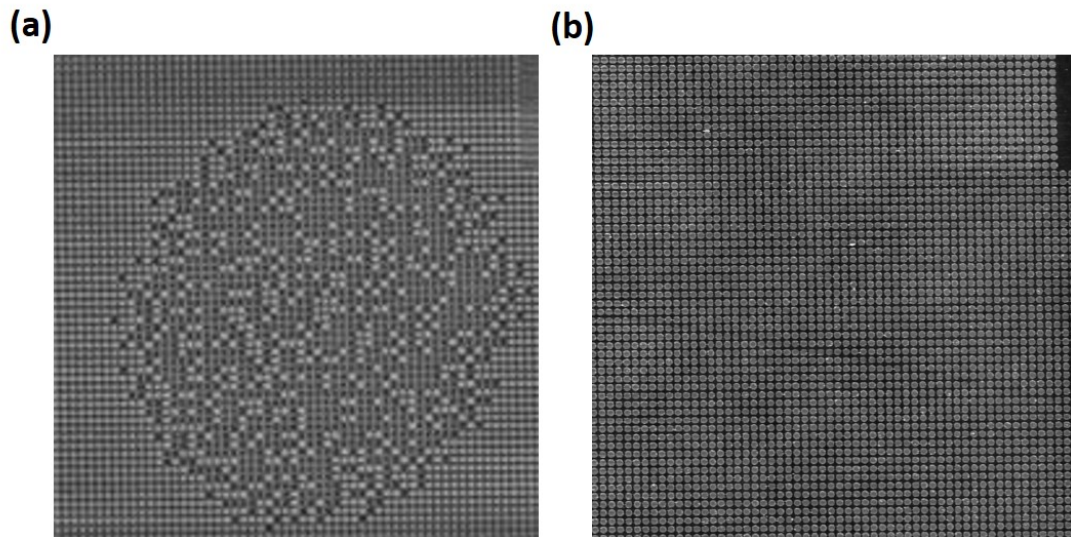


Figure 2.15: (a) MFM mapping and corresponding (b) AFM of a $1 \mu\text{m}$ diameter dot array obtained after grayscale conversion.

2.2.3.2.2 Detection

In the first stage of this step, the grayscale AFM image (Figure 2.15(b)) is binarized (black and white) to be able to detect the structures. Then, a combination of filters, erosion and binarization is used to obtain a suitable image. Figure 2.16(a) presents the result of those two operations. The second stage of this step is to recognize the disks. Three criteria are used to recognize what is a dot and what is not (minimum area, maximum area, aspect ratio). These parameters may need to be adjusted and the images are displayed with the circles for verification, as showed in Figure 2.16(b). Attention, the size of the displayed circles is completely arbitrary for the graphical representation (only the center of the circles is used for the following).

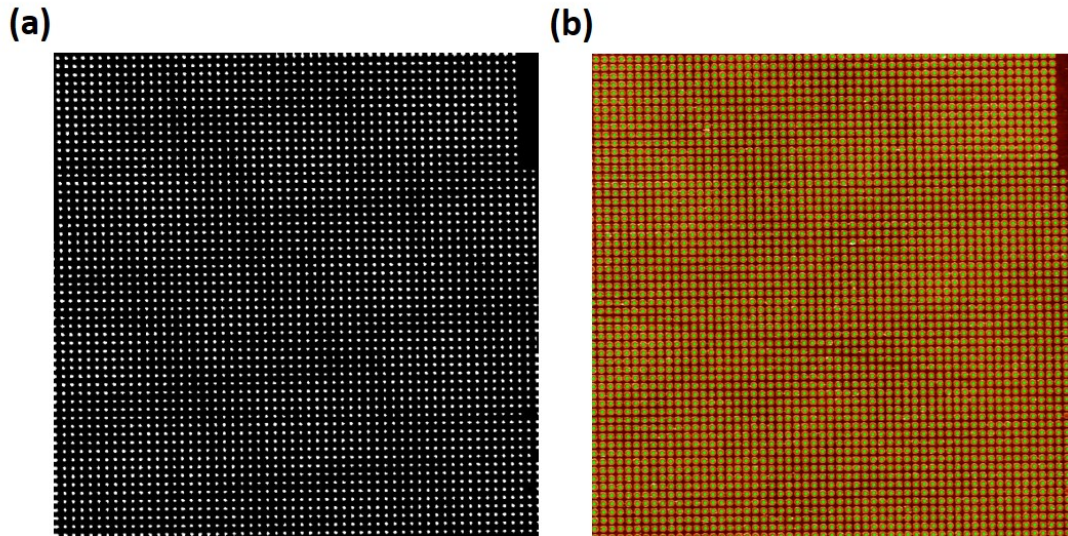


Figure 2.16: (a) AFM binarized images and (b) graphic representation of the position of disks extracted from AFM image. The size of the displayed red and green circles is completely arbitrary.

2.2.3.2.3 Signal measurement

Here, a small part of the grayscale MFM image (Figure 2.15(a)) is cut out around each dot (using the list of disks coordinates obtained in the previous step). The only parameter is the size of the $(2^n + 1)$ square used. This parameter must be adjusted to obtain the best possible separation between the two expected signal levels. The histogram plotted in Figure 2.17 is used to determine the threshold value that will be used to distinguish between up and down magnetizations. Indeed, this histogram give the average pixel P of each identified dot. For values of P between $[0.2-0.34]$ and $[0.38-0.62]$, the disks have upward and downward magnetizations, respectively. Additionally, in this case, the threshold value is slightly less than 0.4.

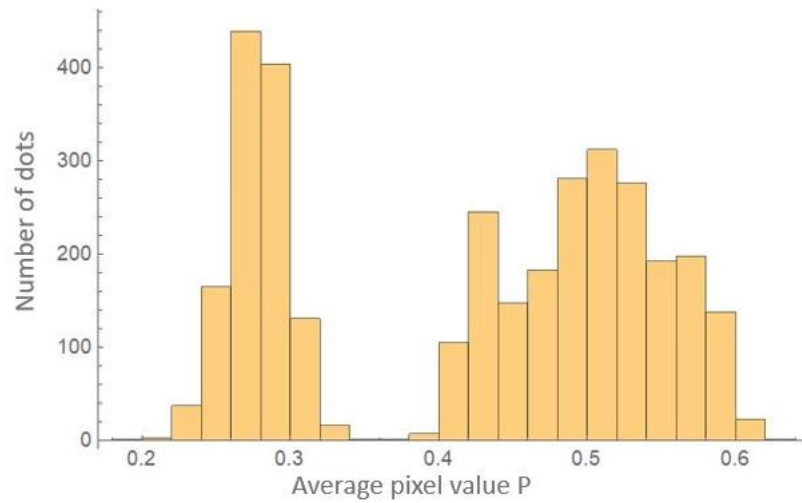


Figure 2.17: Histogram of the average pixel P of each identified dot corresponding to the grayscale MFM image.

2.2.3.2.4 Conversion

In this last step, the preceding histogram makes it possible to determine the threshold to be applied to discriminate the magnetizations orientations. For P_{th} equal to 0.38, Figure 2.18 depicts the results of this conversion process. In fact, the red circles shows the disks whose magnetizations were not changed by the laser pulse (Figure 2.18 (a)). Whereas, the green circles shows the disks whose magnetizations were completely reversed by the excitation of the laser pulse (Figure 2.18 (b)). For the yellow circles presents in Figure 2.18, the value of the pixel (signal) is too close to the threshold pixel P_{th} . In this case, we manually determine the orientation of those disks directly with the MFM images.

At the end, the result is written into a text file and manually checked. Figure 2.19(b) illustrates the resulting numerical image corresponding to the MFM image, where blue circles represent the switched disks. The black circle inside the numerical image represents the limit of the action of the laser on the dot array. The delimitation of this exposed area will be more detail in chapter 5.

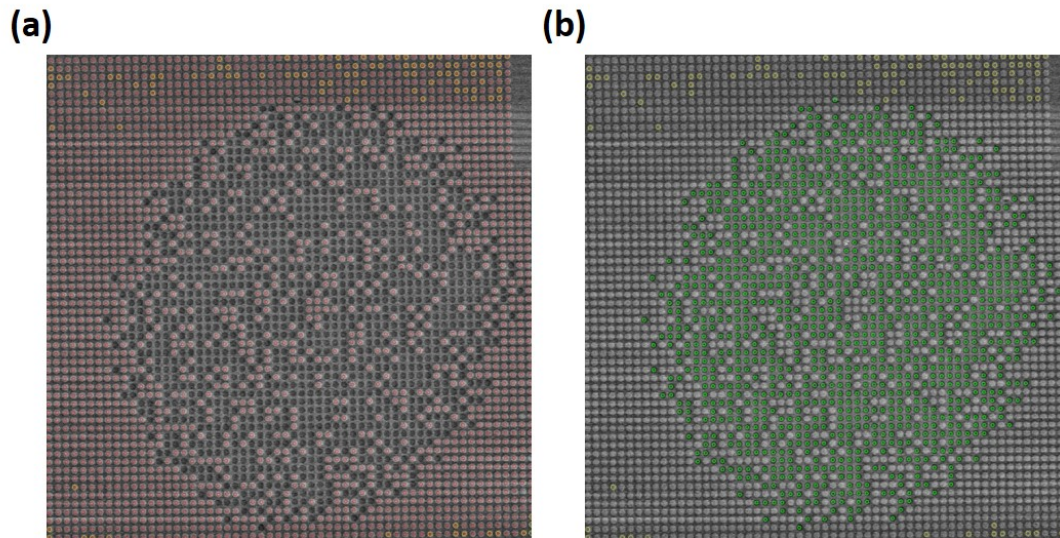


Figure 2.18: MFM images with (a) red circles on unswitched (or unexposed) disks and (b) green circles on switched disks.

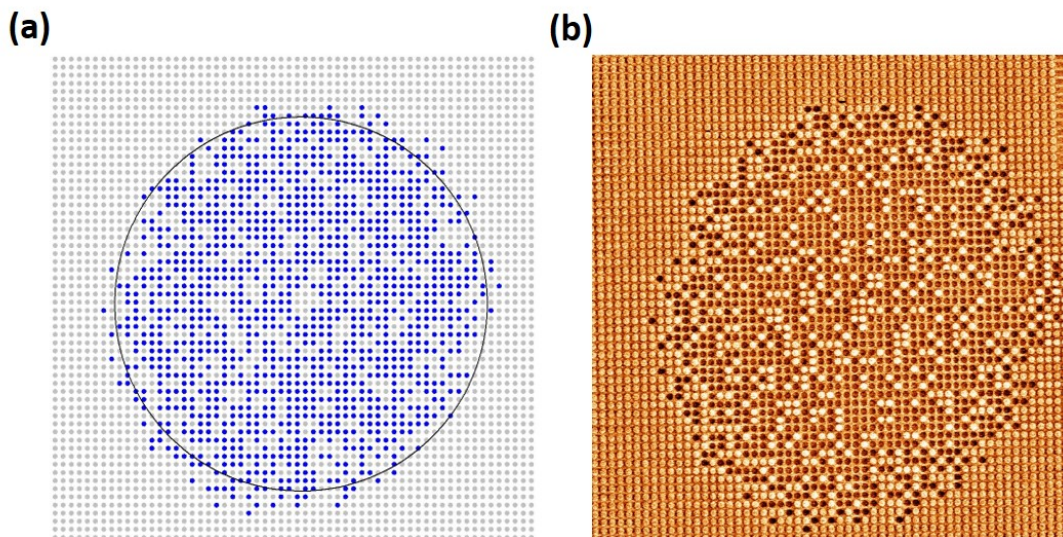


Figure 2.19: (a) Numerical image of the $1\ \mu\text{m}$ Pt/Gd/Co/Pt dot array obtained using the corresponding (b) MFM image. The blue circles represent switched disks.

2.2.3.3 Image acquisition limit

Although the use of MFM imaging in this work was necessary to observe the magnetization behavior of the disks at all size scales studied, this technique has several drawbacks. The first disadvantage of using MFM to characterize our periodic magnetic structures quickly became

2.2. MAGNETO-OPTICAL AND MAGNETIC CHARACTERIZATION

the considerable time required to acquire the magnetic image after the laser pulse excitation. Indeed, in the case of Kerr imaging, the acquisition of images is instantaneous. Whereas to scan an exposed dot area of $80\ \mu\text{m} \times 80\ \mu\text{m}$ with the MFM, we took $1024\ \text{points} \times 1024\ \text{lines}$ and a scan rate of 0.5 Hz, giving a scan time of about 136 minutes for each image. If we decided to reduce the number of points (or lines) for a scan, we immediately reduce the resolution of the image. Therefore, we have always used this number of points (and lines) and adjusted the scanning speed so that the probe does not touch the structures at any time, thus preserving the tip.

The second problem with the MFM imaging technique is the limitation of dot size. Indeed, by using the same scanned dimension ($80\ \mu\text{m} \times 80\ \mu\text{m}$) and points (and lines), we obtain a pixel size around 78.1 nm. This resolution is too close with the structures size if we used 200 or 100 nm of dot diameter. One solution may be to divide a large initial exposed area into smaller scan areas (decreasing the pixel size at the same time) and reconstruct the initial image after. This solution also seems delicate because of the huge stock of data resulting from this image acquisition process. Indeed, for a 400 nm (200 nm) disks array with a period of 300 nm, inside a scanned area of $80\ \mu\text{m} \times 80\ \mu\text{m}$, we should manually verify more than 13 000 (25 000) disks. Therefore, we limited our study to 400 nm dot size, which we believe is a good compromise between the high-resolution technique and the quantitative investigation of the size effect on AOS.

The third issue with the MFM imaging technique is the dependence of the scanned image quality with the roughness of the sample surface. Indeed, if the sample surface is too rough, the tip will hit many dusts and the AFM and MFM images will not be useful for the extraction process described in section 2.2.3.2. Moreover, the presence of collars can be also a problem when characterizing the sample with the MFM, because of the possible interaction between these collars and the MFM tip. Indeed, if the tip is too close to the sample surface, the tip-collars interaction can saturate the signal, causing the tip to be destroyed. While, if the tip is far away from the surface to avoid this saturation effect, a weak magnetic signal will result. To avoid these collars, we can continue to tilt the sample in the etching step (see section 2.1.2.3.4) or use another hard metal mask with a slower etch rate like Titanium¹²⁴ for the evaporation step (see section 2.1.2.3.2). However, we saw in Figure 2.14 that the collars proved to be negligible for Pt/Gd/Co/Pt disks as we were able to achieve excellent MFM images for 1 micron disks (Even for disks ranging from 3 microns to 50 nm of diameter).

Chapter 3

Size effect on GdFeCo ferrimagnetic alloy

3.1 Introduction

To move closer to magnetic recording application, single femtosecond laser pulse turned out to a good candidate due to the demonstration of ultrafast Single Pulse All Optical Switching Helicity Independent Switching (SP-AOHIS) in GdFeCo amorphous ferrimagnetic alloys. The magnetization reversal in this ferrimagnetic materials, made of two antiferromagnetically coupled sub-lattices of rare-earth and transition metal, can be understood as the excitation of electrons by absorption of photons allowing demagnetization at different rates of the two sub-lattices thanks to Elliott-Yafet effect and exchange scattering¹⁹. The difference in demagnetization rates leads to a transient ferromagnetic-like-state that end by a complete ultrafast reversal of the magnetization by conservation of angular momentum^{1,77,78}. Those models based on angular momentum conservation describe the purely heat-driven toggle switching. This phenomenon has been intensively studied in GdFeCo full films with perpendicular anisotropy^{23,34,68,69,131} but studies on the influence of reduced lateral size remains limited^{6,111,112,132}. Particularly, El-Ghazaly et al.⁶ demonstrated AO-HIS in amorphous submicrometric GdCo disks and showed that the reversing time is significantly reduced for disks below 500 nm compared to 15 μm squares. They explained this faster rate by the electron-phonon and spin-lattice interactions. In view of these previous works, question like the behavior of the threshold fluence to observe switching (or multidomain) in GdFeCo magnetic out of plane disks remains open.

We start this chapter by presenting a systematic study of the magnetization reversal for GdFeCo disks which diameter ranges from 10 μm to 3 μm with 35 fs linearly polarized laser pulses. This section will validate the UV lithography and MOKE image acquisition process.

CHAPTER 3. SIZE EFFECT ON GDFECO FERRIMAGNETIC ALLOY

Indeed, for $\text{Gd}_{23}(\text{FeCo})_{77}$ (20 nm) disks size between 10 μm and 3 μm , we will confirm that femtosecond laser pulse can reverse the magnetization of GdFeCo microdisks. Moreover, a slow switching dynamic will be presented and the limitations of studying AOS on larger patterned structures with periods of the same order of magnitude as the laser beam diameter will be clearly highlighted.

The second section of this chapter present a systematic study of the magnetization reversal for GdFeCo disks which diameter ranges from 3 μm to 400 nm with 35 fs linearly polarized laser pulses. This section is nearly identical to the following submitted work: *Size effect on single pulse all-optical helicity-independent switching in GdFeCo disk arrays*¹³³. Where I realized the AOS experiments, I did the data analysis, and I wrote the first draft of the publication. Thus, for $\text{Gd}_{24}(\text{FeCo})_{76}$ (20 nm) disks, switching/random threshold fluence will be precisely determined. The variation of both threshold fluences will reveals a non-monotonic behavior which highlights the importance of the specific light absorption in nanostructures. COMSOL simulations will be performed to reproduce this non-monotonic behavior and the influence of the period in 400 nm dot will be particularly investigated. In addition, the reader will find additional data in this section compared to the corresponding publication. Indeed, all MOKE images will be illustrated and the influence of the laser pulse duration on the AO-HIS in this range of disk size will be discussed.

3.2 From 10 μm to 3 μm disk diameter

The purpose of this section is to introduce the reader to the starting point of our study of the size effect on AO-HIS in periodic GdFeCo structures. Indeed, we began the observation of the control of magnetization within larger and spaced disks. Although the size of these disks is not interesting for a magnetic recording application, it allowed us to confirm AO-HIS and to observe the dynamics of slow domains in this range of disk diameters. We will start this section by presenting the characteristics of the GdFeCo full film used in this section. Then, we will demonstrate the switching of magnetization at these large disk scales with the slow domain dynamics observed at a disk size of 6 μm . We conclude this section by showing the limits observed by using large and widely spaced disks.

3.2.1 Characteristics of the full film

In this part of our work, we used the multilayer presented in Figure 3.1(a). Each layer of the stack is obtained by magnetron sputtering on a glass substrate. The material of interest is the $\text{Gd}_{23}(\text{FeCo})_{77}$ (20 nm) layer sandwiched between two thin layer of Pt(5 nm). Where the top Pt

3.2. FROM 10 μM TO 3 μM DISK DIAMETER

layer prevents oxidation and the Ta buffer layer acts as an adhesion. In addition, with this Gd concentration we are near the compensation^{1,61,68}. Measurement of the hysteresis loop at room temperature of the sample has been performed thanks to MOKE magnetometry setup presented in section 2.2.1. Figure 3.1(b) shows the result of this measure and shows that this ferrimagnetic alloy is FeCo-dominant and exhibited an out of plane magnetization.

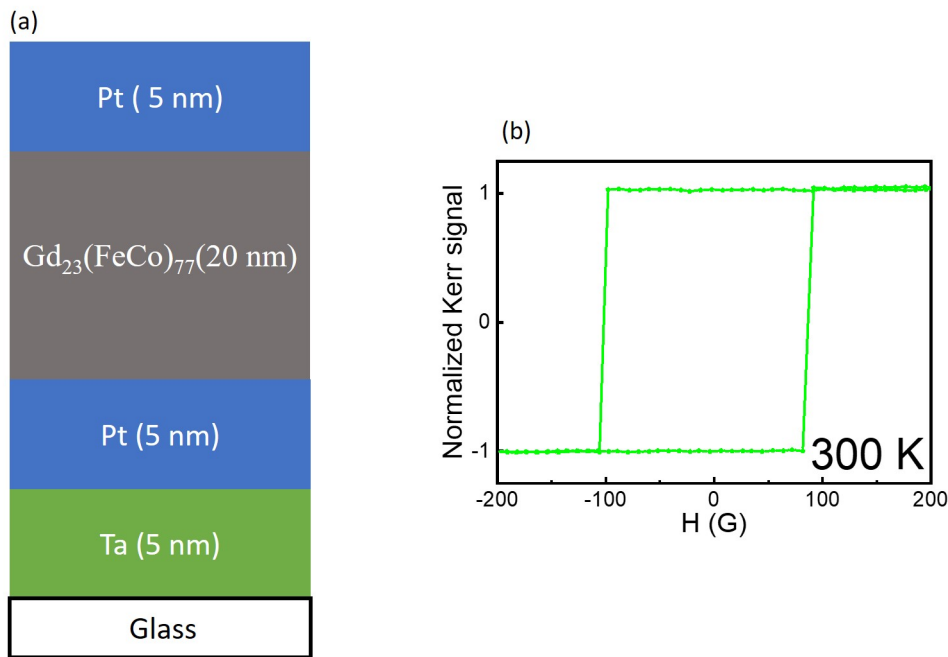


Figure 3.1: (a) Structure of the Gd₂₃(FeCo)₇₇(20 nm) sample and corresponding (b) hysteresis loop measurement with the applied field out of plane.

In addition, to observe the magnetization state of the sample after exposure to laser pulses, we used the Kerr imaging setup presented in section 2.2.2.1 and the MOKE images acquisition process detailed in section 2.2.2.2. Figure 3.2 shows the result of this measure and allows us to conclude that this ferrimagnetic full film exhibited a single shot AO-HIS. Indeed, this AOS measurement is a typical toggle switching experiment realized with a femtosecond laser in a single-pulse mode linearly polarized. The light and dark contrast represent the magnetization of the FeCo-sublattice in opposite directions.

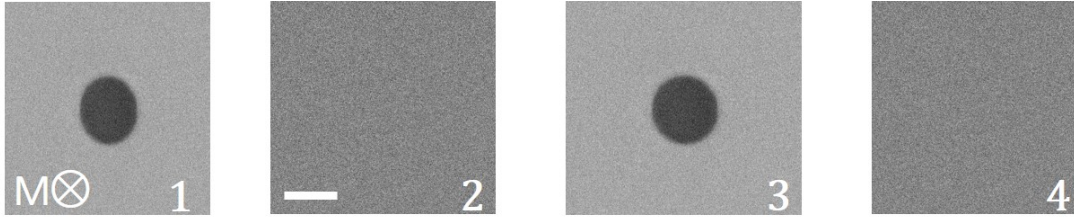


Figure 3.2: Magneto-optical images of Pt(5 nm)/Gd₂₃(FeCo)₇₇(20 nm)/Pt(5 nm) full film obtained after the action of four consecutive single laser pulse. Every single femtosecond pulse with a fluence of 19.1 mJ/cm² and a spot diameter of 50 μm linearly polarized illuminates the same circular region of the full film and reverses the magnetization within it. The length of the scale bar is 20 μm.

3.2.2 AO-HIS in GdFeCo microdisks

3.2.2.1 Design and magnetic characteristic of the patterned sample

The previous section confirms that Gd₂₃(FeCo)₇₇(20 nm) full film exhibited both PMA and single shot AO-HIS at room temperature. To study the size effect, we fabricated arrays of magnetic disks in a diameter range from 10 μm down to 3 μm. The magnetic film has been processed by ion beam etching through an positive resist mask defined by UV lithography and lift-off. This microelectronic process is like the e-beam lithography technique detailed in section 2.1.2. The main difference is the use of photon and photosensitive resist to draw the mask and to realize spin-coating step, respectively. Figure 3.3(a) shows an example of the optical microscope image for 10 μm of disk size obtained after microfabrication. For each disk diameter D, a hexagonal networks of size 7 mm × 5 mm was filled with equidistant disks at a fixed spacing d (d=3D). These patterned areas were sufficiently large compared to the laser diameter of the MOKE magnetometry (810 μm), enabling us to perform hysteresis loop for all disks sizes studied. Figure 3.3(b) shown the result of the measure. Although this Kerr signal is an average of the exposed areas, these hysteresis loop shows that the ferrimagnetic disks remains FeCo-dominant and exhibited an out of plane magnetization, after the microfabrication. Moreover, the coercive fields in this range of microdisks are 10 times higher than that observed in the Gd₂₃(FeCo)₇₇(20 nm) full film (Figure 3.1(b)). This increase of H_c by decreasing the lateral size of the magnetic material is attributed to the reduction of the number of local defects and crystal imperfections, leading to low domain nucleation mechanism. Indeed, the process of magnetization reversal by an applied magnetic field in an OOP magnetic specimen often involves both domain nucleation and domain wall propagation.

3.2. FROM 10 μM TO 3 μM DISK DIAMETER

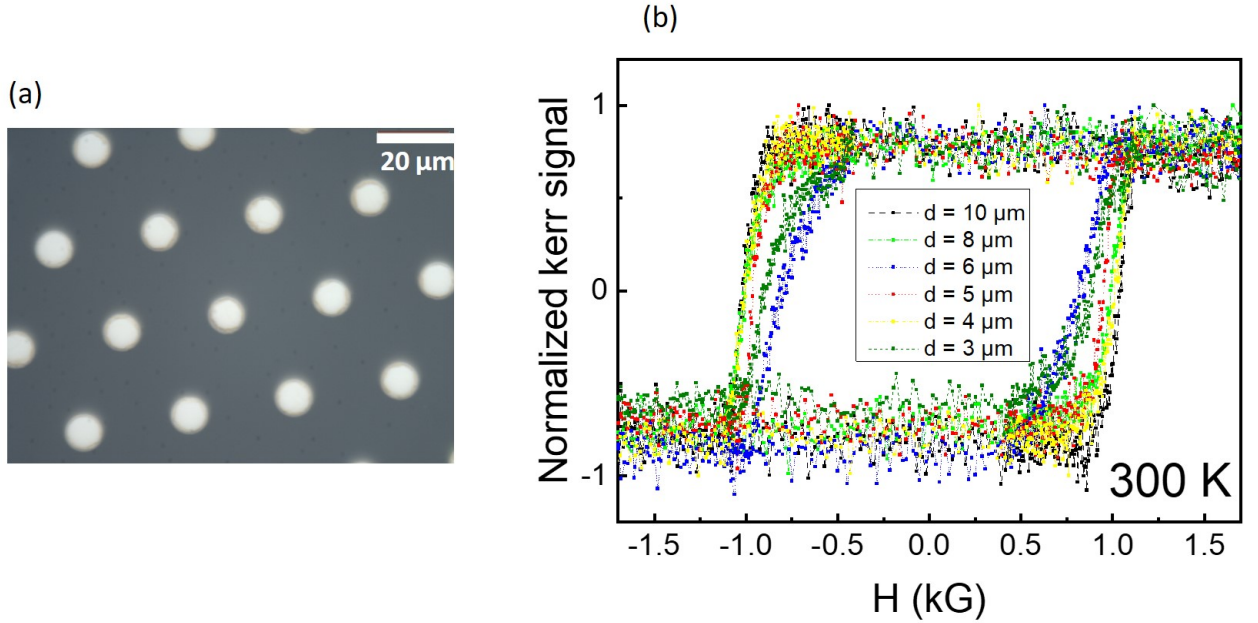


Figure 3.3: (a) Optical images of Pt(5 nm)/Gd₂₃(FeCo)₇₇(20 nm)/Pt(5 nm) disk of size 10 μm and 30 μm of period, obtained after microfabrication. (b) Hysteresis loop of all the studied disk arrays with the applied field out of plane.

3.2.2.2 AOS experiment on patterned sample

3.2.2.2.1 Single shot AO-HIS

The effect of the excitation by 35 fs laser pulses generated by a Ti-sapphire laser was investigated in-situ using the Kerr imaging setup. This laser, operating at 5 kHz, has a central wavelength of 800 nm and is linearly polarized after propagating through a Glan-Taylor polarizer. A convex lens focused the beam with a gaussian intensity profile onto the sample surface down to a full-width half-maximum (FWHM) of 50 μm . By using an electromagnet, we initially applied an out-of-plane magnetic field of 1 T. Then, we irradiated our disks arrays with the femtosecond laser pulses. Figure 3.4 presents the results obtained for 10 μm , 08 μm and 06 μm of disk diameters for linearly polarized laser in single pulse mode. The notation D/P depict the diameter of the disk D and the period of the array P. The dark grey contrast corresponds to disks TM- sublattice magnetized up. After excitation with a first pulse on an array of 10 μm and 06 μm of microstructures sizes, one can see the formation of one and three dark-grey structures, respectively. A second identical pulse subsequently, shined at the same position with a delay of about one second, reverses the magnetization back to the initial state forming a light grey

CHAPTER 3. SIZE EFFECT ON GDFECO FERRIMAGNETIC ALLOY

area. Thus, we were able to achieve toggle switching with four consecutive femtosecond laser pulses for this two disk sizes. In the case of 08 μm , we observe the AO-HIS mechanism for two microstructures, plus a disk split into two magnetic domains after the first, third and fourth pulse irradiation. The orientation of the dark contrast inside the encircle blue disk suggest that this structure is on the edge of the laser spot, where the fluence is closer to the threshold switching fluence. The orientation of the dark contrast within the blue circle suggests that this structure lies approximately at the edge of the laser spot, where the fluence is close to the threshold switching fluence. As we will see in the next paragraph, it is very difficult to follow the evolution of split domains with the number of pulses.

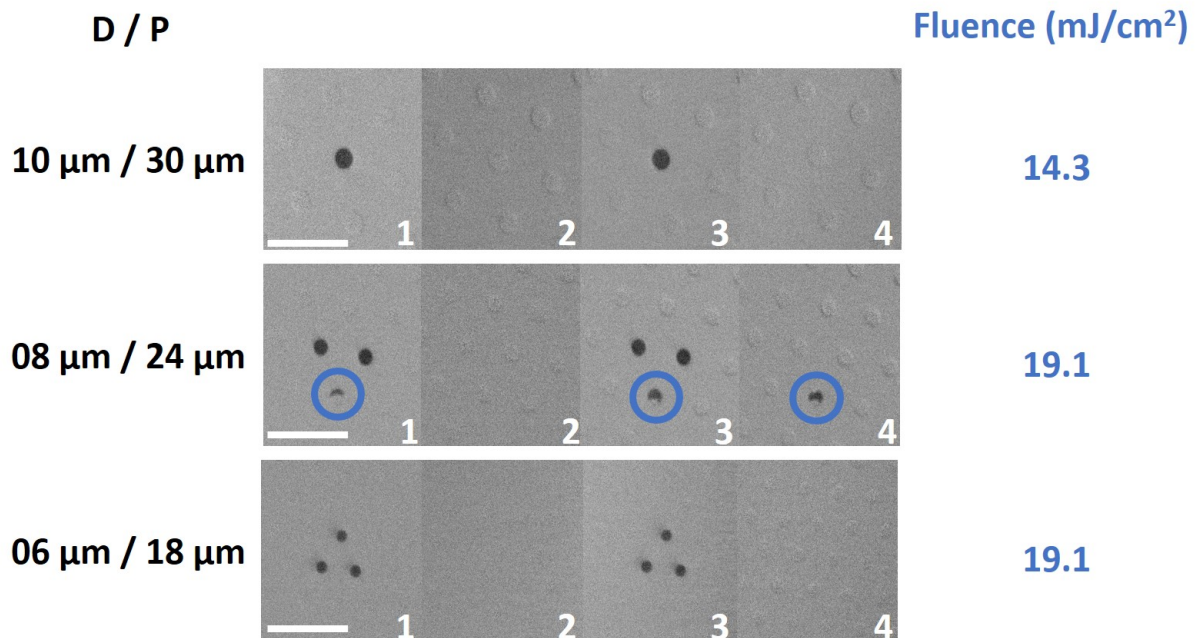


Figure 3.4: Magneto-optical images of magnetic disks made of $\text{Gd}_{23}(\text{FeCo})_{77}$ (20 nm) obtained after the action of consecutive 35 fs linearly polarized laser pulses. Initial single domain of disks with magnetizations “down” (“up”) are represented by the cross (disk). Each laser pulse with a given fluence irradiates the same region of the patterned structure. The scale of the image can be easily related to the diameter of the microstructures and is equal to 40 μm in all the MOKE images.

3.2. FROM 10 μM TO 3 μM DISK DIAMETER

Figure 3.5 shows the results obtained for 05 μm , 04 μm and 03 μm of disks diameters for linearly polarized laser in single pulse mode. The arrays configuration of the disks is the same as for the previous larger structures with P being equal to $3D$. For all these disk sizes, we observed two main behaviors of the magnetization of the structures depending on their position with respect to the laser spot. At the center of the laser spot, the reversal of the magnetization is clear with disks successively showing upward and downward magnetization as a function of the number of pulses. At the edges of the laser spot, it proved difficult to quantify the number of switched disks. The final disks states after excitation reveal the stochastic nature of AOS in this region of the laser beam. Indeed, at the edge of the exposed area, the laser pulse may have no effect on the magnetization of the disks or may cause a multidomain state, and can even reverse the magnetization of the structures. An example of this issue is illustrated in the case of the 05 μm dots where we illustrated the center of the laser spot by an orange circle. Within this circle, seven microdisks switch after each laser pulse. While a split domain is observed outside the orange circle for the first pulse, and two microdisks possess the same dark contrast from the second pulse to the seventh pulse (these two points are even split into domains for the third pulse). Moreover, the enhancement of these edge phenomena and the increase in the number of switched disks are not related to a size effects but are caused by the increase of the statistics when we reduce the diameter of disks D and the period of the patterned array D (increase of the area density). However, Figures 3.4 and 3.5 demonstrate that we can reverse the magnetization of GdFeCo microdots with linearly polarized laser pulses like reported in several works^{111,112,132}

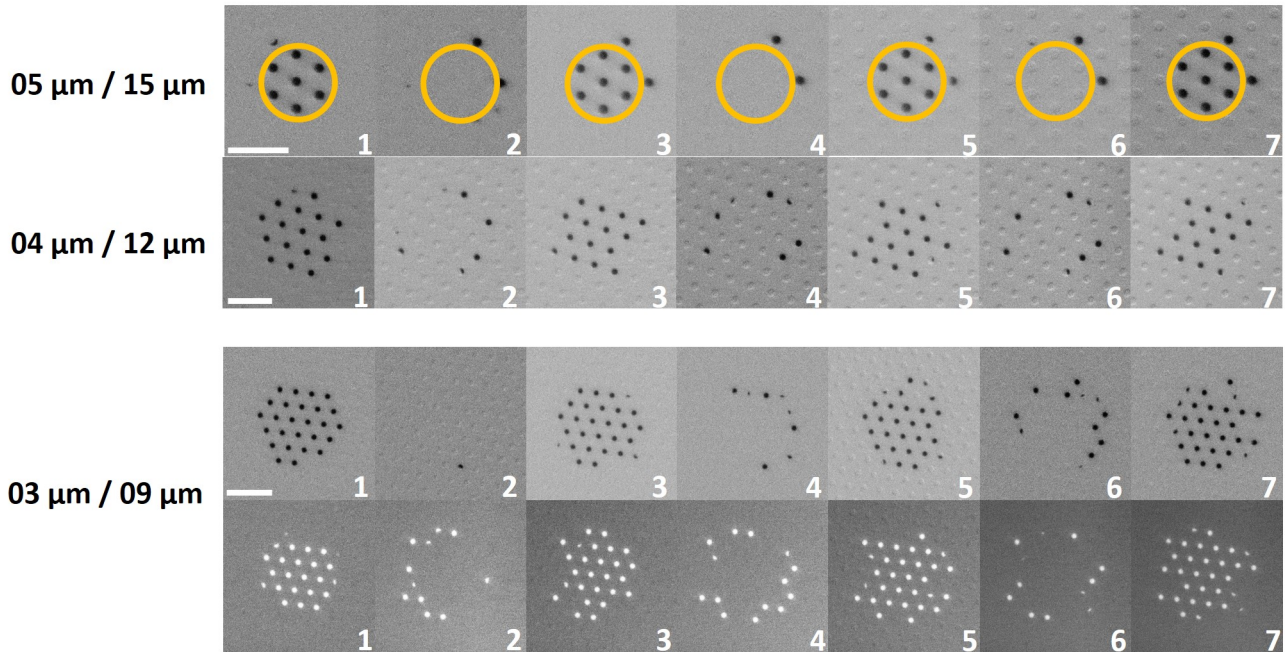


Figure 3.5: Magneto-optical images of magnetic disks made of $Gd_{23}(FeCo)_{77}(20 \text{ nm})$ obtained after the action of consecutive 35 fs linearly polarized laser pulses. Initial single domain of disks with magnetizations “down” (“up”) are represented by the cross (disk). Each laser pulse with a fluence of 24, 25 and 22 mJ/cm^2 irradiates the same region of the patterned 5, 4 and 3 μm structure, respectively. The scale of the image can be easily related to the diameter of the microstructures and is equal to 40 μm in all the MOKE images.

3.2.2.2.2 Slow domain dynamic

Although TR-MOKE (Time-Resolved Magneto-Optical Kerr Effect) experiments were not performed in this work, the Kerr static imaging setup proved sufficient to record a slow (few seconds) dynamic reversal. Figure 3.6 shows the response of the 6 μm disks after the exposure of a femtosecond single pulse linearly polarized, initially oriented in two opposite directions. The first AOS experiment started with Figure 3.6(a) which is the MOKE image directly after the exposure. Five switched disks are observed plus a structure with a dark ring which is highlighted by the red circle. 26 s later, without applying any external magnetic field or laser pulses, this ring slowly expands and approaches the center of the microstructure, as shown in Figure 3.6(b). At the end, 4 s was necessary to see the ring disappears leaving a complete switched disk in place, as illustrated in Figure 3.6(c). This slow switching dynamic was also observed when the magnetization of the microstructure is initially pointing in the other direction, as illustrate

3.2. FROM 10 μM TO 3 μM DISK DIAMETER

in Figure 3.6(d) and 3.6(e). In this second AOS experiment, the switching reversal occurs in only two seconds, but the structures exhibiting this slow dynamic are different in both AOS experiments.

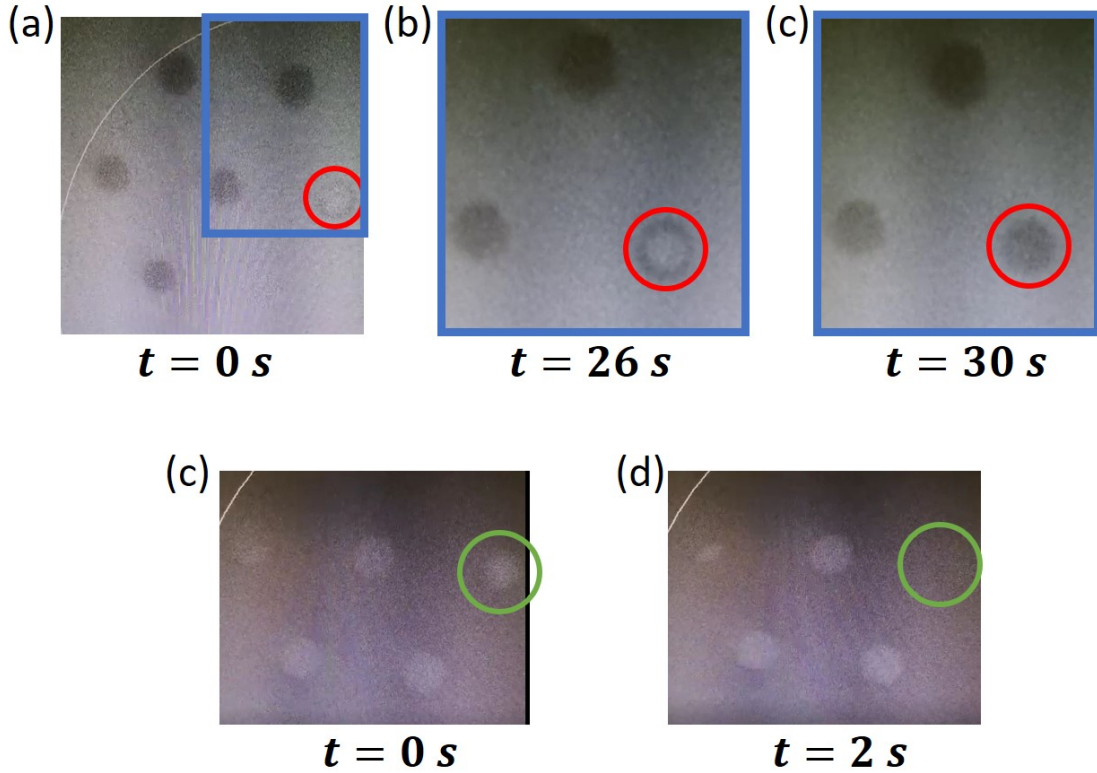


Figure 3.6: Slow domain dynamic observed after the irradiation of 6 μm disks by a single pulse Linearly polarized. The red circle in (a), (b) and (c) represents the structure of interest when we initially applied a magnetic field in the downward direction. The green circle in (d), (e) represents the structure of interest when we initially applied a magnetic field in the upward direction.

It should be noted that this slow dynamic was not observed for the same diameter or even for any disk size when we reversed the magnetization of the disk with a magnetic field using a Kerr microscope. Furthermore, the fact that all the structures that showed this behavior were at the edge of the laser spot, increases the stochastic nature of these dynamics. However, this slow expansion observed in Figure 3.6 can be attributed to the desire of the domain wall to reduce its energy by propagating progressively towards the center of the structure, thereby reducing its size. While the formation of rings can be related to the sample microfabrication process like thinning, oxidation, and modified anisotropy at the edge of the structures¹¹² or/and because of the laser intensity distribution which is not homogeneous inside the structure due to laser

CHAPTER 3. SIZE EFFECT ON GDFECO FERRIMAGNETIC ALLOY

interference within it¹³². Studying this slow domain wall dynamic by varying the disk diameter around 6 μm , by changing the microfabrication process (e-beam lithography), by performing X-ray absorption to investigate the effect of oxidation, and by realizing several microscopies (MFM or SEM) would surely help to understand this dynamic induced by a single femtosecond laser pulse and to compare it with other domain wall driving forces (magnetic field^{134,135}, electric field^{136,137}, current¹³⁸⁻¹⁴¹, thermal gradient^{142,143}). It would be very interesting to conduct these different surveys, but we have not done so for various reasons which I will discuss in the next paragraph.

3.2.3 Limitations

Although the previous paragraphs have allowed us to confirm that we can reverse the magnetization of GdFeCo microdisks, three main limitations arise in the study of the size effect on AO-HIS in GdFeCo for these microstructures. The first issue in this diameter/period range is that the period lengths (distance between structures) are comparable to the diameter of the laser beam. This results in a different number of switched disks, depending on the initial position of the laser beam. Secondly, the diameter of the disks is not much smaller than the diameter of the beam, which leads to the appearance of disks split into domains due to the inhomogeneity of the laser pulse irradiation (with a gaussian distribution) within a microstructure. Finally, the presence of structures divided into domains with stable and/or unstable states did not allow, on the one hand, to carry out MFM measurements after irradiation (due to a possible manipulation of the DW by the ferromagnetic tip of the MFM), on the other hand, to carry out statistics for the stochastic part of the laser beam (located at the edge of the laser spot). The first two limitations are clearly highlighted in Figure 3.7 for 8 μm disks. For the same fluence, we observed in Figure 3.7(a) one disk completely reversed plus one structure split into two domains, while in Figure 3.7(b) it is three disks which are divided into two domains and zero switched disk.

The consequences of the last limitation are on the one hand the observations of the slow dynamics of the domain wall discussed in paragraph 3.2.2.2.2, and on the other hand the difficulty of properly defining parameters such as the switching threshold fluence, the multidomain fluence, the pulse duration limit, and the switching probability involved in the AOS mechanism. To overcome these three limitations, we should reduce the size of the structures and move the disks closer together (increase the areal density by reducing the period) in order to favor the monodomain state after laser pulse irradiation and to increase statistic. This is the aim of the next section.

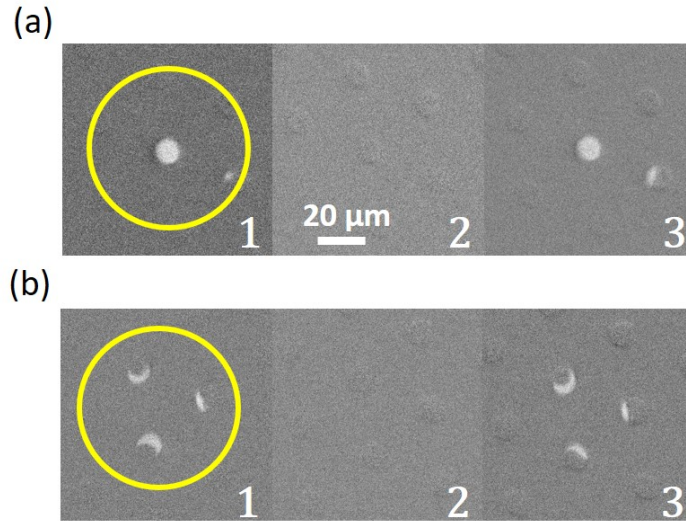


Figure 3.7: Two AOS experiments performed with the yellow circle representing the laser center at (a) the center of a 8 μm disk and (b) approximately the isobarycenter of the three exposed 8 μm disks. Every single femtosecond pulse with a fluence of 17 mJ/cm^2 and a spot diameter of 50 μm linearly polarized illuminates the same circular region of the patterned array.

3.3 From 3 μm to 400 nm disk diameter

The objective of this section is to present our investigation of the size effect on all-optical helicity-independent switching in GdFeCo periodic disks. We will first demonstrate that toggle switching is observed for all sizes and the switching/random threshold fluence will be accurately determined. Then, the evolution of both thresholds fluence with disk size will allow us to plot a state diagram and will reveal a non-monotonic behavior which highlights the importance of the specific light absorption in nanostructures. COMSOL simulation will be used to reproduce this non-monotonic behavior.

3.3.1 Characteristics of the full film

In this section, we used the sample consisted of a thin film of composition Ta(5 nm)/Cu(5 nm)/Gd₂₄(FeCo)₇₆(20 nm)/Pt(5 nm) grown by magnetron sputtering on a glass substrate. The illustration of this stack was made in Figure 2.1(a). Moreover, at this Gd concentration we are near the compensation^{1,61,68}. The measurement of the hysteresis loop at room temperature of the sample was carried out using the MOKE magnetometry device described in detail in section 2.2.1. While the observation of the magnetization state of the sample after exposure to

CHAPTER 3. SIZE EFFECT ON GDFECO FERRIMAGNETIC ALLOY

laser pulses was performed using the Kerr imaging setup presented in section 2.2.2.1. Figure 3.8 shows the results of these two measures. Figure 3.8(a) shows that this ferrimagnetic alloys is Gd-dominant and exhibited perpendicular magnetic anisotropy (PMA). Additionally, Figure 3.8(b) allows us to conclude that this magnetic full film exhibited a single shot AO-HIS with the use of a femtosecond laser in a single-pulse mode linearly polarized.

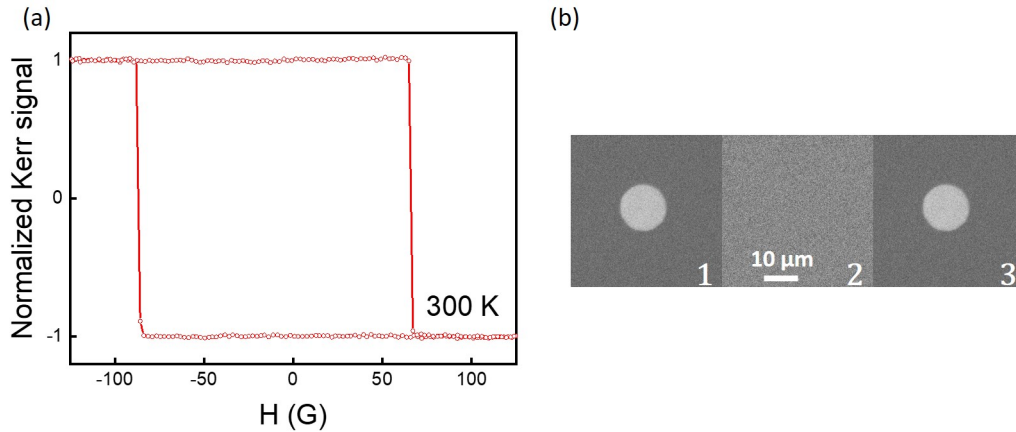


Figure 3.8: (a) Hysteresis loop measurement and (b) AOS experiment performed on the $\text{Gd}_{24}(\text{FeCo})_{76}$ (20 nm) sample. Every single femtosecond pulse linearly polarized with a pulse energy of 15.5 mJ/cm^2 illuminates the same circular region of the full film. The laser beam diameter is around $70 \text{ }\mu\text{m}$.

3.3.2 AO-HIS of GdFeCo disks

3.3.2.1 Design of the patterned sample

To study the size effect, we fabricated arrays of magnetic disks with diameter ranging from $3 \text{ }\mu\text{m}$ down to 400 nm . The magnetic film has been processed by ion beam etching through an aluminum mask defined by electron-beam lithography and lift-off (see section 2.1.2.2). The remaining Al mask is subsequently removed by chemical etching. For each disk diameter D , $90 \text{ }\mu\text{m} \times 90 \text{ }\mu\text{m}$ areas are filled with identical disks on a square lattice. The distance between disks d , is fixed to 300 nm (the lattice period is therefore not constant and equal to $D+d$). The periods of the arrays were chosen to increase the areal density and magneto-optical contrast of the magnetic nanodisks in the MOKE images (to overcome the limitations observed in the large structures). The effect of the excitation by 35 fs laser pulse generated by a Ti-sapphire laser on the magnetic nanostructures is characterized in-situ by MOKE microscopy. This laser

3.3. FROM 3 μM TO 400 NM DISK DIAMETER

delivers 800 nm wavelength laser pulses, linearly polarized after propagating through a Glan-Taylor polarizer. The number of laser pulses and the repetition rate can be modified by using a pulse picker. In this work, we have only use single pulse exposition (two pulses results are obtained manually with more than 1 s between the two pulses). Pulse energy can be changed by rotating a half-wave plate and calibrated by measuring the average beam power. In addition, the laser beam diameter was chosen to ensure a switching region smaller than the 90 μm magnetic area to be able to measure the switching domain of a single array of disks. In paragraph 3.3.2.3.1 we will explain in depth the two methods that we used in this work to evaluate the size of the laser beam. The reader can find more details about the nanofabrication process and the design of patterned sample in section 2.1.2.

3.3.2.2 Single shot AO-HIS

The objective of this section is to show that single shot AO-HIS mechanism can be observed in all the disks sizes studied using a static Kerr imaging setup. Figure 3.9 presents the AO-HIS results for arrays of $\text{Gd}_{24}(\text{FeCo})_{76}$ (20 nm) disks initially saturated. A 1 T out of plane applied field is first applied such that initial magnetization in the disks is pointing down corresponding to the light grey color (Figure 3.9(a)). After excitation with a first pulse, one can see the formation of a dark-grey area (Figure 3.9(b)-(i)) independently of the disk sizes. A second identical pulse subsequently, shined at the same position with a delay of about one second, reverses the magnetization back to the initial state forming a light grey area (Figure. 3.9(j)-(q)). By starting from the opposite magnetic direction (Figure. 3.9(r)), we observed the same behavior. Regardless of the initial disk magnetization direction, after the second femtosecond laser pulse, a ring is formed. These rings are obtained for all disks sizes and appear larger for smaller disks. These ring highlights that in an intermediate range of fluence, the reversing presents a stochastic aspect. This stochastic aspect appears more important for smaller disks. Theses aspects are also reported for larger disks in the previous section of this chapter but are beyond the scope of this work. However, these experimental results demonstrate AO-HIS for all the GdFeCo disk diameters ranging from 3 μm to 400 nm after a single 35 fs linearly polarized laser pulse. Moreover, Figure 3.9 presents a non-monotonic behavior of the switched area size with the disk diameter for a given pulse energy. This trend will be investigated more precisely in the next paragraph.

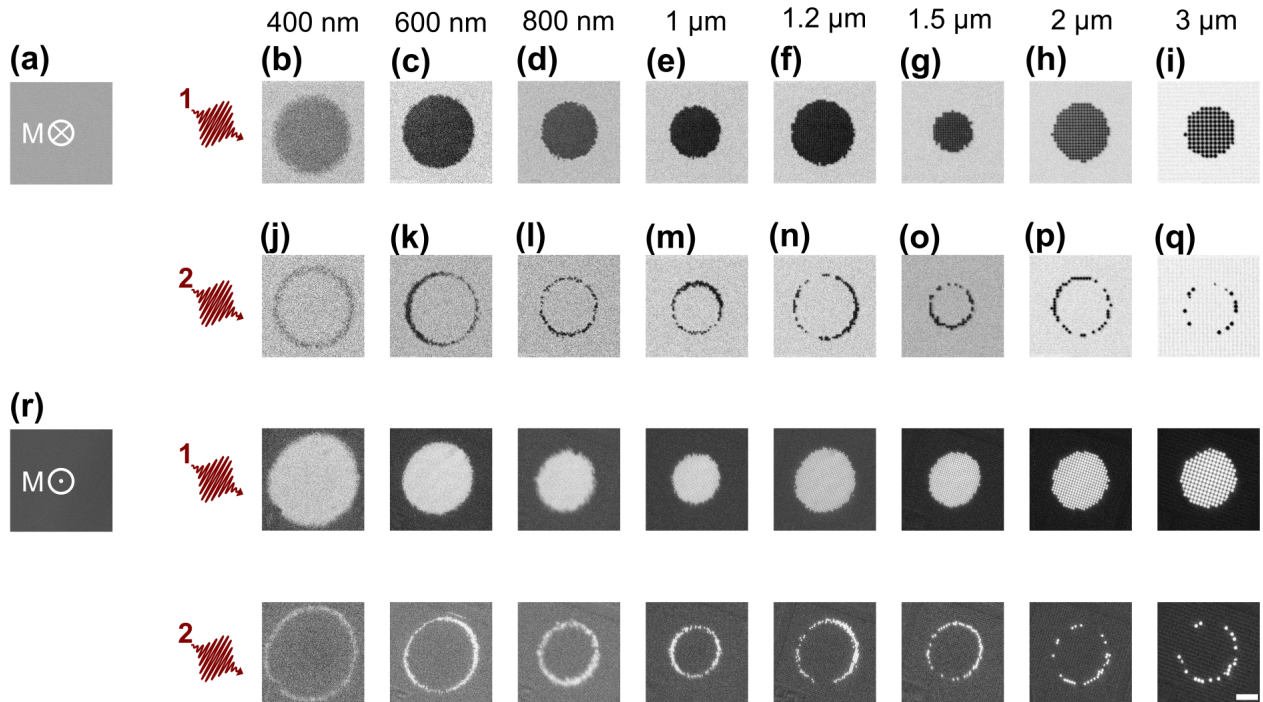


Figure 3.9: Magneto-optical images of magnetic disks made of $\text{Gd}_{24}(\text{FeCo})_{76}$ (20 nm) obtained after the action of one 35 fs linearly polarized pulse and then a second pulse separated by 1 s. Initial single domain of disks with magnetizations “down” (“up”) are represented by the cross (dot). For (b)-(i) ((j)-(q)) the dark grey (light grey) area represents magnetization of disks pointing “up” (“down”). Each laser pulse with an energy of μJ irradiates the same circular region of the patterned structure and reverses the magnetization within it. The length of the scale bar is $20 \mu\text{m}$.

3.3.2.3 AO-HIS of GdFeCo disks as a function of the pulse energy

To investigate the impact of the laser energy on the switched area has been studied as function of disk size, we systematically irradiated each array with 8 different energies and measured the switching/random domain sizes by using a MOKE microscope. Figure 3.10 presents the magnetic state of GdFeCo disks after excitation with a single femtosecond laser pulse. Initially, the arrays were saturated perpendicular with a 1 T field, as previously done in Figure 3.9. On the MOKE images one can observe up to three different magnetic states depending on the pulse energy: no switching, deterministic switching, and randomly oriented disk. For example, in the case of disks with 800 nm diameter, no effect of light on disks is observed for pulse energies below $0.5 \mu\text{J}$ (no switching state) (Figure 3.10(c)), magnetization reversal is achieved for pulses energies between 0.56 and $0.74 \mu\text{J}$ (deterministic switching) (Figure 3.10(i)-(l)) within a circular

3.3. FROM 3 μM TO 400 NM DISK DIAMETER

zone of diameter D_{sw} . For larger energy around 0.8 μJ , at the center, the array of disk is no longer uniformly magnetized (Figure 3.10(m)).

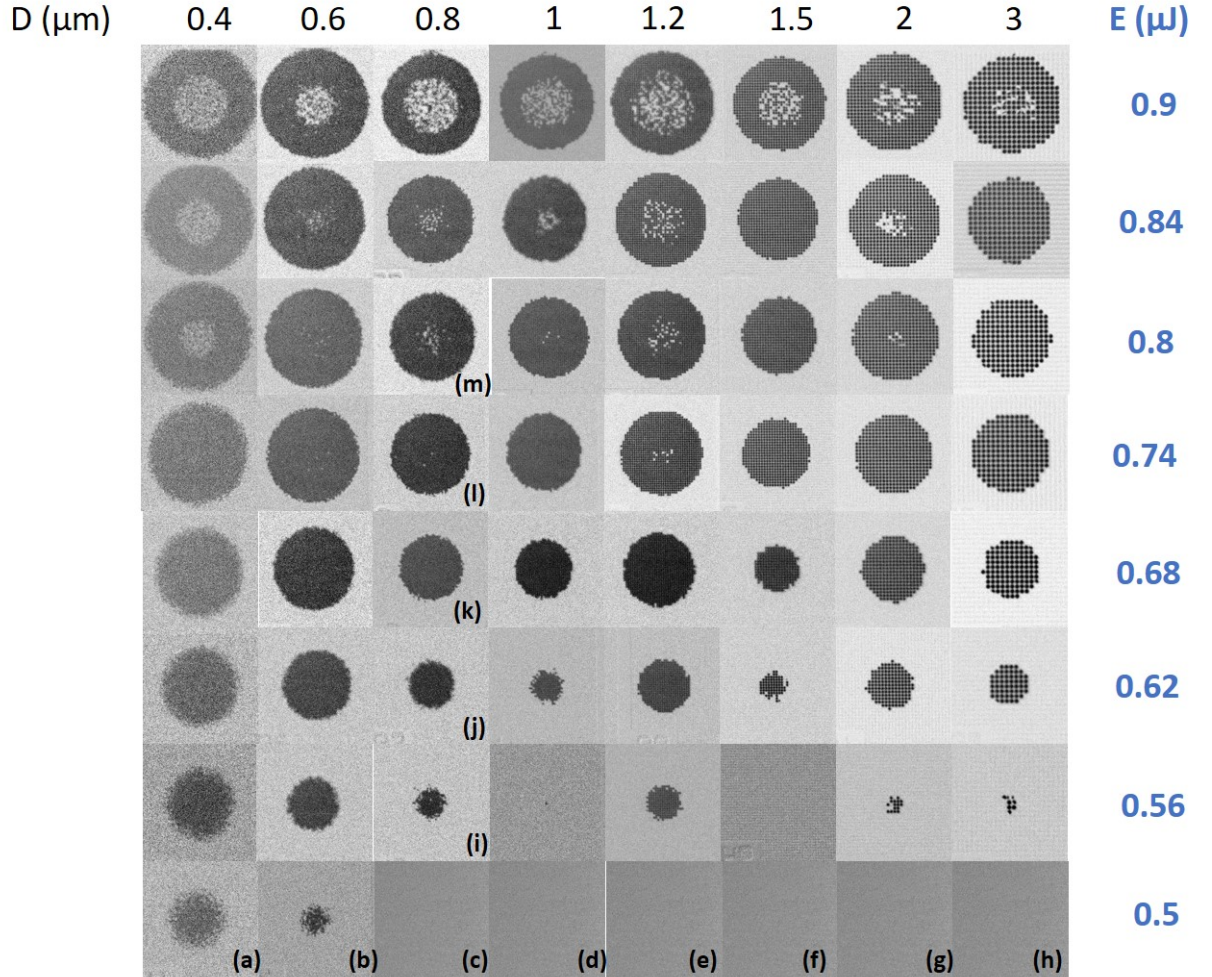


Figure 3.10: Magneto-optical images of $\text{Gd}_{24}(\text{FeCo})_{76}(20 \text{ nm})$ magnetic disks obtained after a single 35 fs laser pulse, linearly polarized. Depending on the pulse energy and the disk diameter, we observe three different magnetic states: (c)-(h) light grey area for no switching at low pulse energy, (a)-(b) homogenous dark grey area for AO-HIS at medium energy and (m) non-homogenous dark grey area for randomly oriented disks at the center of the laser spot for high pulse energy.

This central zone of diameter D_{ra} is marked by two possible magnetic configurations of a disk depending on its size. Indeed, we only observed disks with a single uniform randomly oriented domains for disks up to 1 μm of diameter. While for disks larger than 1 μm single uniform randomly oriented domains and multidomain states are observed. For each disk size, the diameter of the switched / randomized region increases with laser pulse energy but for a

CHAPTER 3. SIZE EFFECT ON GDFECO FERRIMAGNETIC ALLOY

given laser energy, D_{sw} and D_{ra} depend on the dot size. Qualitatively, at the same pulse energy, we observe a non-monotonic behavior of the switching domain surface with the disk size (For instance, although $0.5 \mu\text{J}$ is sufficient to induce AO-HIS in 400 and 600 nm disks, as shown in Figure 3.10(a) and 3.10(b) respectively, this pulse energy is too low to affect the magnetization of larger disks, as shown in Figure 3.10(c)-(h)).

To examine in depth this non-monotonic behavior of the switching domain area with the size of structures, we measured the switching/random diameters and considered a Gaussian distribution of the laser intensity to determine the threshold energies for AO-HIS and randomized state. Figure 3.11 presents in details the analysis. Indeed, we extracted the switching (random) diameter by measuring the circular size of homogenous (non- homogenous) dark-grey area after the first (second) pulse as shows in Figure 3.11(a) (Figure 3.11(b)). Indeed, we manually measured the random diameter with MOKE images of the second pulse because it was much easier to determine the non- homogenous area in those images.

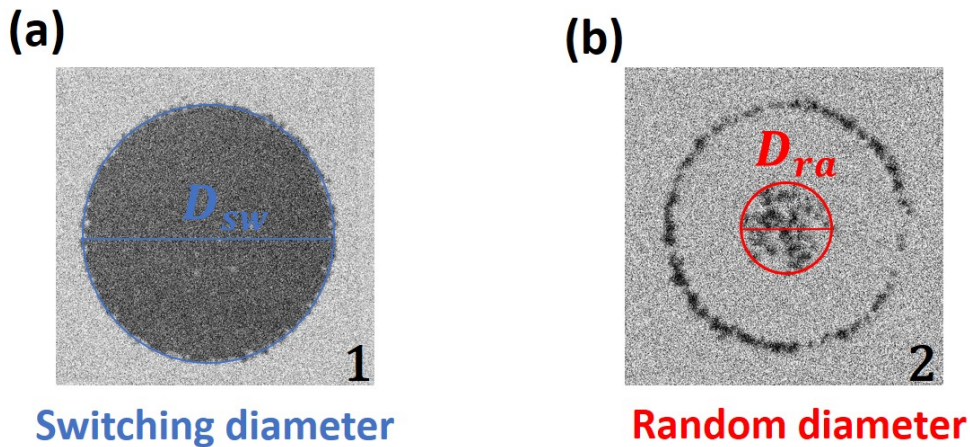


Figure 3.11: Manual determination of the (a) switching and (b) random diameters on MOKE images.

Nevertheless, the reader can see in Figure 3.12 the 128 MOKE images we recorded to show the magnetic states of the $\text{Gd}_{24}(\text{FeCo})_{76}$ (20 nm) disks after the action of two consecutive single 35 fs linearly polarized laser pulses with different energies.

3.3. FROM 3 μM TO 400 NM DISK DIAMETER

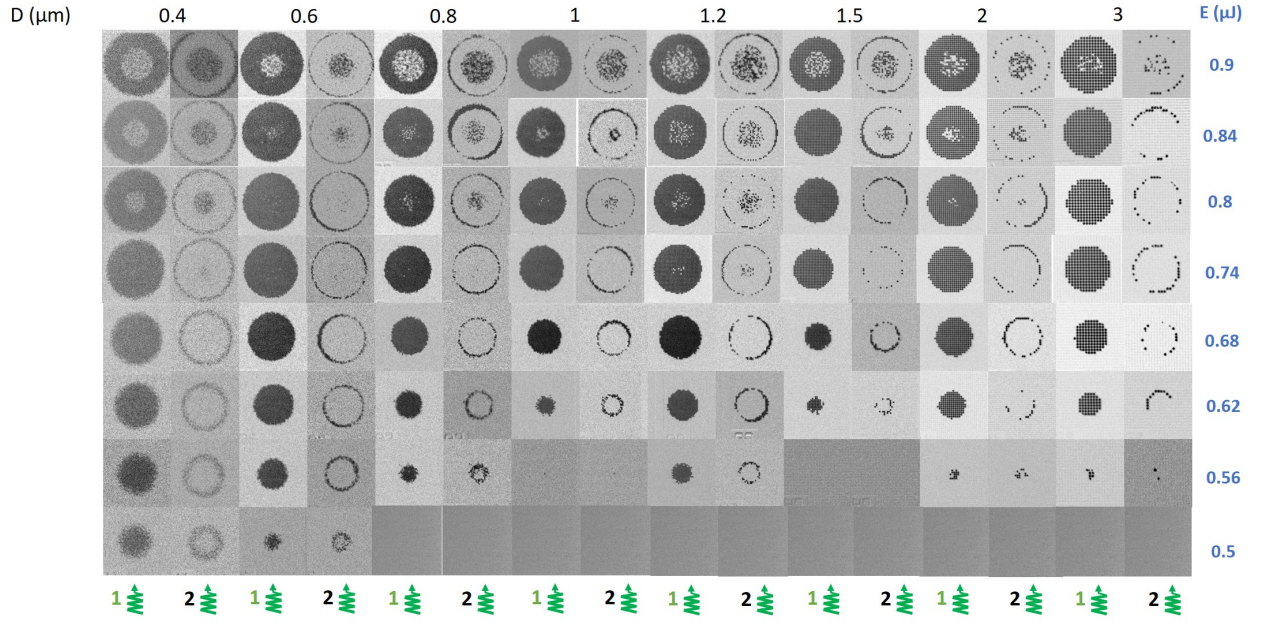


Figure 3.12: Magneto-optical images of magnetic disks of $\text{Gd}_{24}(\text{FeCo})_{76}$ (20 nm) obtained after the action of two consecutive 35 fs laser pulses, linearly polarized. Depending on the pulse energy and the disk size, we observe three different magnetic states: light grey area for no switching at low pulse energy, homogenous dark grey area for switching at medium energy and non-homogenous dark grey area for randomly oriented disks at the center of the laser spot for high pulse energy.

3.3.2.3.1 Extraction of the laser beam diameter

To extract the diameter of the laser beam D_L , the energy needed to observe AOS in each disks array or the threshold energy to observe multidomain state or randomly oriented disks at the center of the laser spot, we used the fluence profile given by (the reader can find more details in the thesis manuscript of Quentin Remy.¹⁴⁴):

$$F(r) = 2\bar{F}e^{-\frac{2r^2}{w^2(z)}} \quad (3.1)$$

Where \bar{F} is the measured laser incident fluence, r is the radius of the domain, and w is the radius of the laser beam where the fluence is divided by e^2 . The switched (random) domain starts to appear when the fluence peak value exceeds a certain threshold value F_{th} . At this time, one would measure a fluence \bar{F} :

$$\bar{F} = \frac{F_{th}}{2} \quad (3.2)$$

Thus, for $F(r) = F_{th}$, and by using equation 3.1 and 3.2, a domain radius r verified the

CHAPTER 3. SIZE EFFECT ON GDFECO FERRIMAGNETIC ALLOY

following equation:

$$r^2 = \frac{w^2}{2} \ln \frac{\bar{F}}{\bar{F}_{th}} \quad (3.3)$$

Moreover, the measured laser incident fluence \bar{F} is calculated by:

$$\bar{F} = \frac{\bar{P}}{f.S} = \frac{\bar{E}}{S} = \frac{4\bar{E}}{\pi D^2} \quad (3.4)$$

Where \bar{P} (respectively \bar{E}) represents the measured pulse power (respectively pulse energy) divided by a factor e^2 , f equal to 5 kHz is the repetition rate of the laser, and S (respectively D) is the beam spot area (respectively the beam spot diameter). However, in this work we used the FWHM to define the laser beam D_L . Where FWHM is the diameter of the laser beam defined here as the full-width half-maximum. By using Equation 3.1 and the definition of FMWH, we can extract the relationship between D_L and w :

$$w^2 = \frac{(FWHM)^2}{2 \ln 2} = \frac{D_L^2}{2 \ln 2} \quad (3.5)$$

Finally, by introducing Equation 3.5 and 3.4 in 3.3, we can extract the relationship between a domain diameter x ($x = 2r$), the measured pulse energy \bar{E} , the measured threshold fluence \bar{F}_{th} and the diameter of the laser beam D_L :

$$x^2 = \frac{D_L^2}{\ln 2} \ln \frac{4}{\pi D_L^2} \frac{\bar{E}}{\bar{F}_{th}} \quad (3.6)$$

In this context, we fit experimental data with Equation 3.6 for all disk sizes. Figure 3.13 present the result of this operation by using the switching diameter data. The slopes of all the fitted lines are equal and we found $D_L = 68.4 \pm 0.6 \mu m$.

3.3. FROM 3 μm TO 400 nm DISK DIAMETER

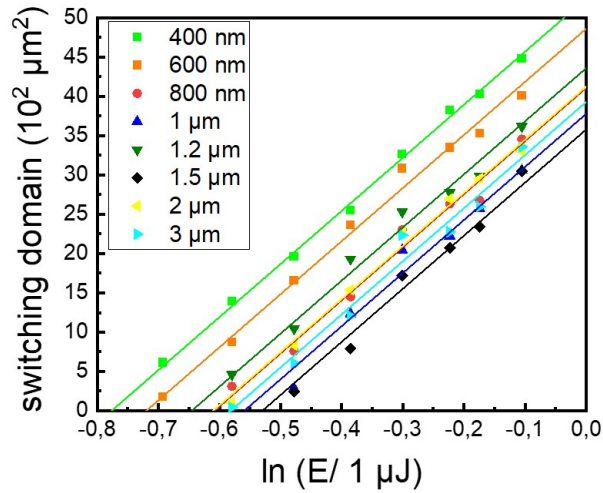


Figure 3.13: Square of the switching diameter as a function of the logarithm of the pulse energy for disk diameter equal to 3 μm , 2 μm , 1.5 μm , 1.2 μm , 1 μm , 800 nm, 600 nm, and 400 nm.

This value of the laser beam diameter is really close to $D_L = 69 \pm 0.5 \mu\text{m}$ obtained after an average of six gaussian fits of the laser spot in six different directions. Figure 3.14 shows an example of direct measurement of the laser beam diameter from an optical image taken with the CCD camera of the Kerr imaging setup.

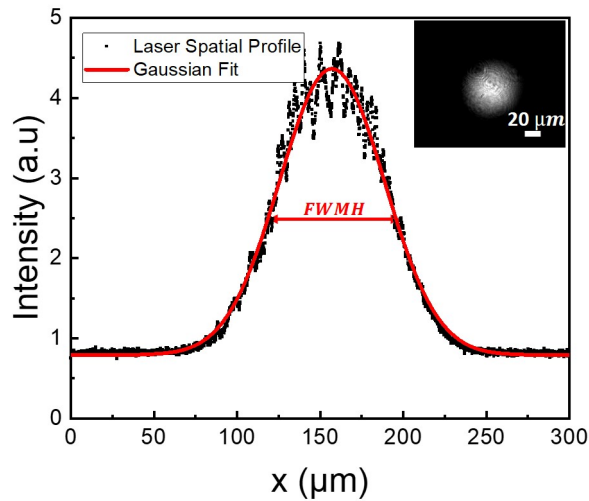


Figure 3.14: Laser beam spatial profile plotted (black curve) and fitted with a gaussian distribution (red curve). The inset shows the optical image taken with a CCD camera.

3.3.2.3.2 Extraction of the threshold fluence

To extract the threshold fluence F_{sw} needed to observe AOS in each disks array or the threshold fluence F_{ra} to observe multidomain state or random oriented disks at the center of the laser spot, we used Equation 3.6. Indeed, we fit experimental data with Equation 3.6 for all disk sizes. Figure 3.15 present the result of this operation for the case of the switching threshold fluence F_{sw} and the random threshold fluence F_{ra} . The blue and red trends stand for switching and random states, respectively. Excellent agreement can be observed between our experimental data and the predictions based on the laser beam profile. The use of fluence rather than energy makes sense since thermally induced magnetizations switching depends only on the energy density given to the magnetic material and not on the total energy of the pulse.

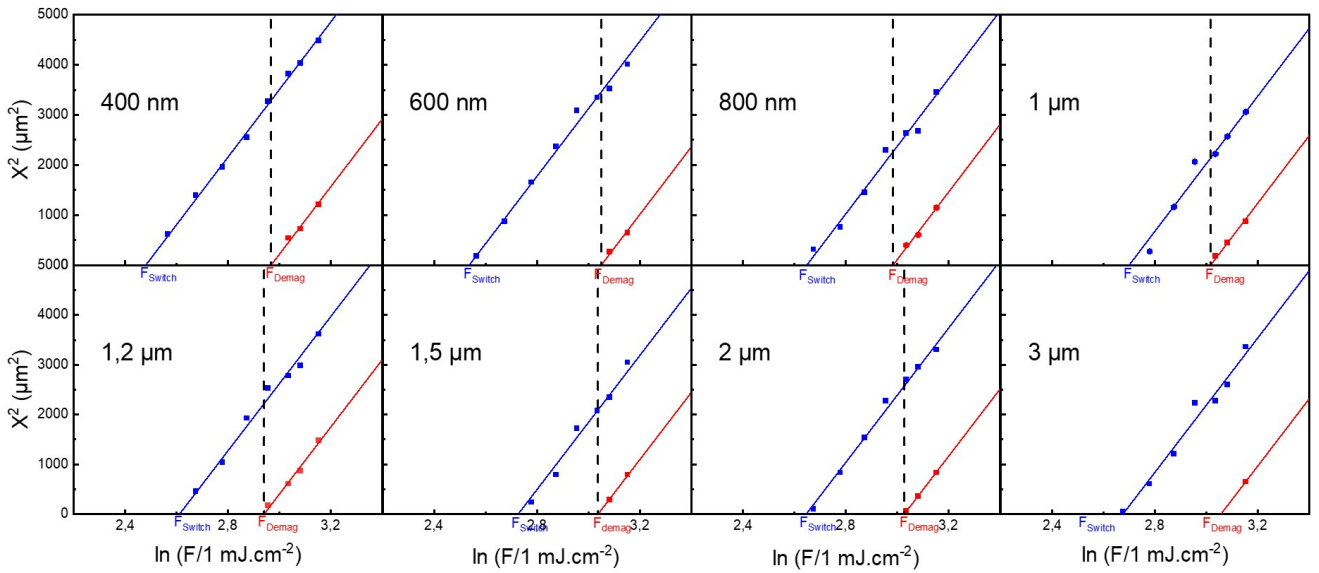


Figure 3.15: Square of the switching (in blue) and random (in red) diameter as a function of the logarithm of the fluence for all the disks size.

3.3.2.3.3 State diagram

The extraction of the different threshold fluences allow us to represent all the MOKE image of Figure 3.10 by a state diagram. Figure 3.16 depicted a state diagram for GdFeCo disk arrays subjected to 35 fs linearly polarized laser pulses where we indicate the dependence of threshold fluencies for switching F_{sw} and random state F_{ra} on disk diameter. Quantitatively, we observe 3 different magnetic states: no switching for low fluence, random oriented disk at high fluence and magnetization reversal between these two. While F_{sw} and F_{ra} have a global tendency to

3.3. FROM 3 μM TO 400 NM DISK DIAMETER

increase with disk diameter, the details of the state diagram indicate a non-monotonic behavior.

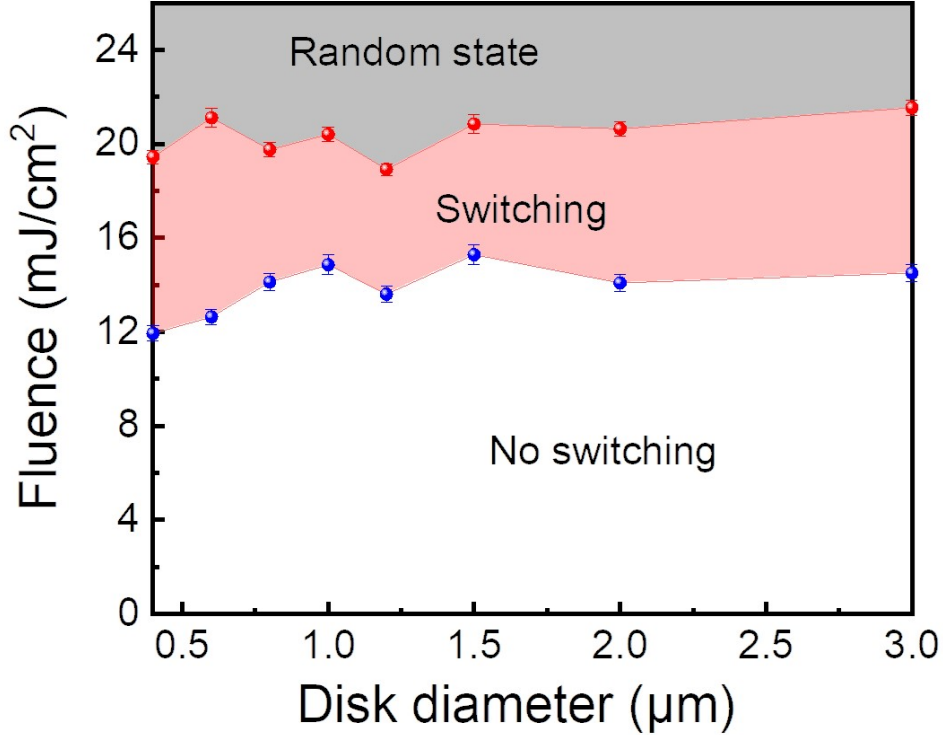


Figure 3.16: AO-HIS state diagram of $\text{Gd}_{24}(\text{FeCo})_{76}$ (20 nm) disks. Threshold fluencies for switching (F_{sw}) and random state (F_{ra}) as function of disk diameter depicted in blue and red disks, respectively. The FWHM of the laser is around $68.4 \mu\text{m}$.

3.3.2.3.4 COMSOL simulations

All the simulations have been realized by Dr Maxime Verges. In this paragraph, we performed simulations with COMSOL Multiphysics with the module Wave Optics to calculate the absorbed energy for different geometries of the periodic arrays of magnetic nanodisks for the same light power fixed to $0.16 \mu\text{W}$. This way we wanted to check out if the non-monotonic evolution of threshold fluence with disk diameter is consistent or not with the evolution of the energy absorption as a function of the disk diameter and the period of the array¹⁴⁵. We considered periodic arrays of magnetic nanodisks with $D = 400, 600, 800, 1000, 1200, 1500, 2000, \text{ and } 3000$ nm with corresponding lattice period $P = 700, 900, 1100, 1300, 1500, 1800, 2300, 3300$ nm for keeping the same edge-to-edge distance between two neighboring disks. The thin film stack

CHAPTER 3. SIZE EFFECT ON GDFECO FERRIMAGNETIC ALLOY

considered is namely glass (substrate) // Ta (5 nm) / Cu (5 nm) / $\text{Gd}_{24}(\text{FeCo})_{76}$ (20 nm) / Pt (5 nm) as for the experimental measurements. We considered a glass substrate and air superstrate with refractive indices of 1.5 and 1, respectively. Concerning the metals, we used the refractive indices from reference¹⁴⁶ for Ta and Pt while we used the data sets from references^{147,148} for Cu and GdFeCo. This specific numerical method considers one unit cell that is why we applied periodic boundary conditions (Floquet periodicity) on its edges to simulate the electromagnetic field distribution in periodic arrangements of GdFeCo nanodisks. The source comes in from the air superstrate at normal incidence and comes out from the glass substrate. To avoid unphysical reflections, perfect matched layer domains on top of air domain and at the bottom of glass substrate was considered. The source is a monochromatic linearly polarized plane wave with p polarization. The wavelength is fixed at 800 nm. The mesh is made of free triangular elements whose maximum size was 2 nm. This method provides the total absorption of the system air+periodic arrays of nanodisks+glass but since air and glass are assumed to absorb no energy, this provides the absorption of the periodic array. To describe the local absorption of light, we scaled any calculated total absorption by the filling factor of the periodic array. We calculated the absorption of the continuous films with the same approach (here the filling factor is 100 %). Figure 3.17(a) shows the calculated inverse of the absorbance which should be proportional to the switching and random threshold fluence. The good qualitative agreement is obtained since the simulations reproduce the decrease of the switching and random fluences for small diameters, showed in Figure 3.16. Furthermore, the non-monotonic variation of the switching fluence is well described while the agreement is not as good for the random threshold fluence. Figure 3.17(b) and 3.17(c) shows the resulting intensity profile along a line through the GdFeCo layer in each structure. In Figure 3.17(b), we show that the decrease in size gives rise to a standing wave in the disk. In fact, the light scatters by the structure edges as observed already¹¹¹. In Figure 3.17(c), we confirm that the absorption peak inside the largest disks appears at the edge of the structures, as we claimed in section 3.2.2.2.2.

3.3. FROM 3 μM TO 400 NM DISK DIAMETER

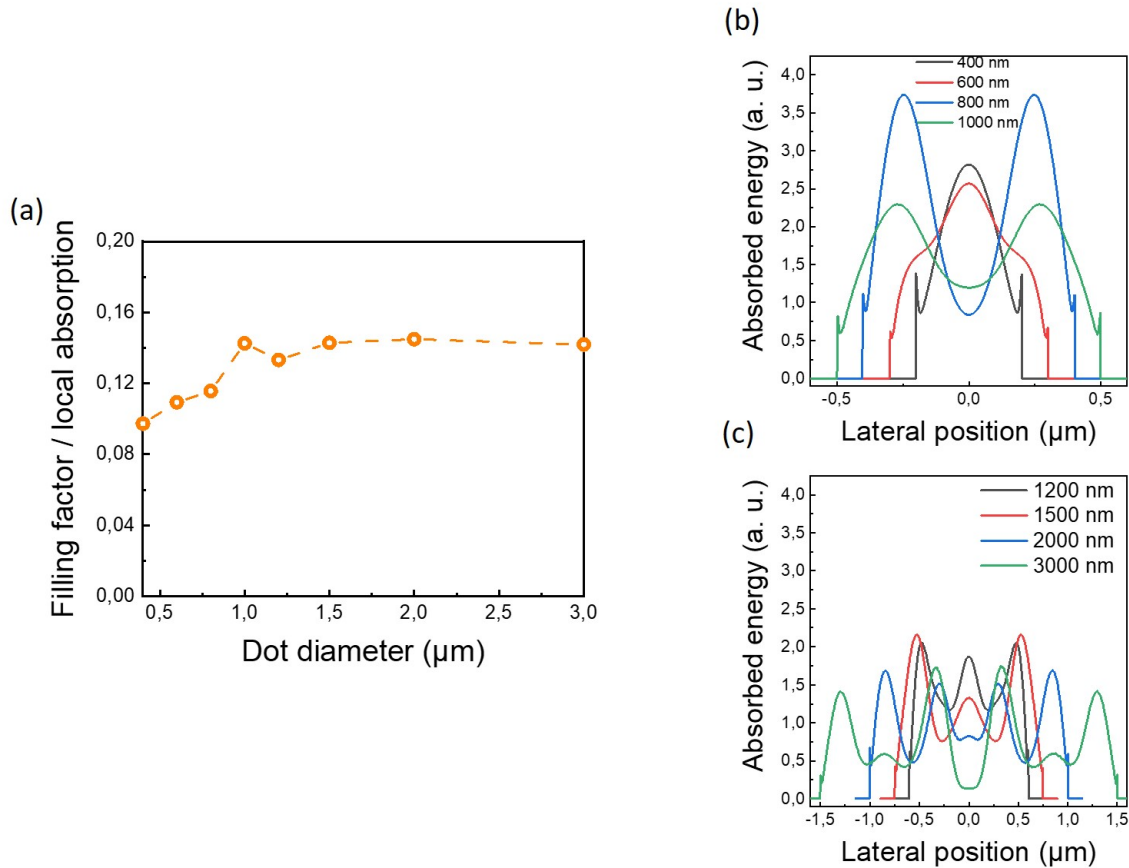


Figure 3.17: (a) Variation of the filling factor divided by the calculated absorbance as a function of the diameter of disk. (b) Absorption profiles in the smaller magnetic disks leading to the formation of standing waves due to light confinement. (c) Absorption profiles in the bigger magnetic disks.

3.3.2.3.5 Discussion

If all-optical switching and random state (multidomain or/and random oriented disk) differ by the physics involved and particularly occurs at different timescales⁷⁰, they are believed to be due to heat assisted effect which are directly related to the absorbed energy. Within this picture, if the disk size only influences only the proportion of incident energy transferred to the nanostructure, the ratio between the random and switching threshold fluences is expected to be constant. This is not experimentally confirmed as shown in Figure 3.17(a). However, the limit of the previous analysis, considering an averaged energy at the scale of the disk, is certainly the non-uniform energy absorption within the magnetic nanostructure. Figure 3.17(b) and 3.17(c) gives the spatial variation of the energy absorption. Variations up to a factor of 3 are predicted. This non uniform energy repartition would lead to non-uniform temperature and

CHAPTER 3. SIZE EFFECT ON GDFECO FERRIMAGNETIC ALLOY

locally different magnetic processes. In that case, it is possible at some fluence that part of the structure experiences a magnetization reversal whereas another part is multidomain. The final configuration would result from a complex process involving micromagnetism and the evolving temperature field. ««

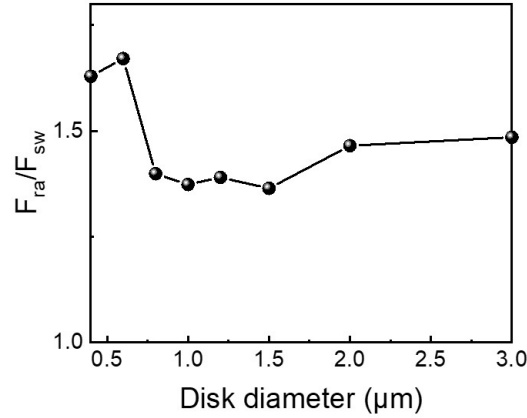


Figure 3.18: Evolution of the fluence ratio F_{ra}/F_{sw} as function of disk diameter.

3.3.2.4 AO-HIS of GdFeCo disks as a function of the period

To observe the variation of one of the key parameters in AO-HIS with the distance between nanodisks, We studied the influence of the period on the threshold fluence for periodic GdFeCo nanostructures made of 400 nm diameter disks. Therefore, we systematically excited with a single 35 fs laser pulse and looked to the reversal in arrays with 500, 550, 600, 700, 800, and 900 nm spacing between the disks. By measuring the switching diameter within an optical microscope for each periodic arrays and using Equation 3.6, we can extract for each patterned areas the switching threshold fluence of nanostructures. Figure 3.19 provides MOKE images of the laser irradiations after a single pulse. While Figure 3.20 shows the variation of the threshold fluence extracted from these images as a function of the period of the 400 nm disk arrays.

Using magneto-optical images, we conclude that toggle switching can be achieved for closer nanodisks, proving that magnetostatic coupling between nanostructures does not play a huge role on ultrafast optical switching in periodic GdFeCo nanodisks. Moreover, Figure 3.20 shown that closer nanodisks need less energy to cause AOS and present a non-monotonic behavior of the threshold switching fluence with the period. In sum, the period of the array is also a parameter to consider when we are decreasing the lateral size of the magnetic material. Therefore, the

3.3. FROM 3 μm TO 400 NM DISK DIAMETER

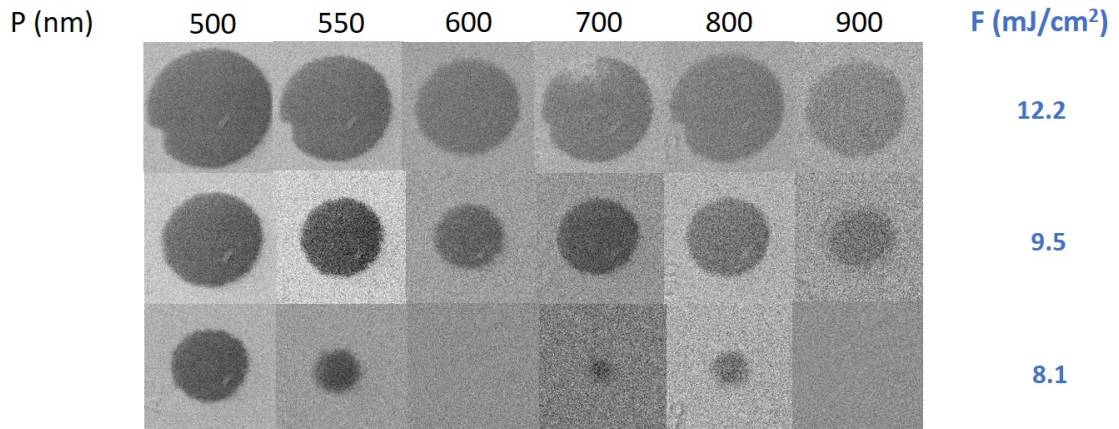


Figure 3.19: Magneto-optical images of 400 nm $\text{Gd}_{24}(\text{FeCo})_{76}(20 \text{ nm})$ disks obtained after the action of a single 35 fs laser pulse, linearly polarized. Depending on the pulse energy and the disk diameter, we observe two different magnetic states: light grey area for no switching and homogenous dark grey area for switching. The diameter of the laser beam is around 75 μm .

influence of period for each disk size needs to be carried out to complete the investigation and understanding of the effect of size on AOS mechanism.

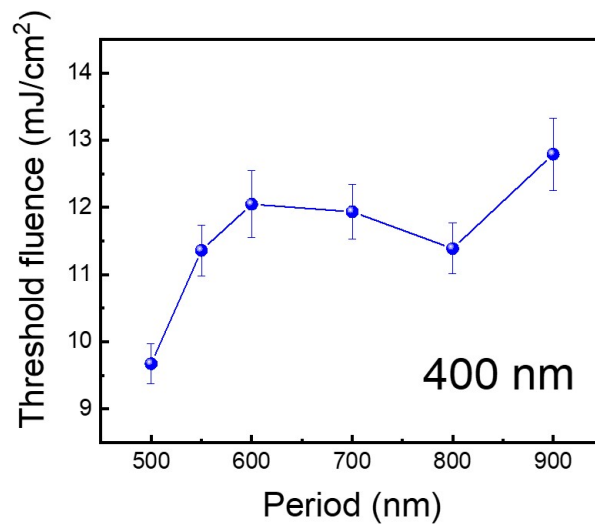


Figure 3.20: Threshold switching fluence on 400 nm $\text{Gd}_{24}(\text{FeCo})_{76}(20 \text{ nm})$ disks as a function of the period. The closer disks need less energy to cause AOS and the non-monotonic behavior of F_{sw} highlights the importance of the specific light absorption in nanostructures.

CHAPTER 3. SIZE EFFECT ON GDFECO FERRIMAGNETIC ALLOY

3.3.2.5 AO-HIS of GdFeCo disks as a function of the pulse duration

As reported in previous works^{5,9,87}, pulse duration is one of the all-optical switching parameters that can influence the magnetization behavior after the irradiation of laser pulses. In the previous section, all AOS experiments were realized with 35 fs laser pulses. This subsection presents the magnetic configuration of the studied GdFeCo disk using the Kerr imaging set-up. Indeed, we systematically irradiated each array with 9 different pulse durations and observed the switching domain by using a MOKE microscope. Figure 3.21 presents the magnetic state of GdFeCo disks after excitation at a given fluence of 16 mJ/cm^2 with a single laser pulse. Initially, the arrays were saturated perpendicular with a 1 T as previously done in Figure 3.10.

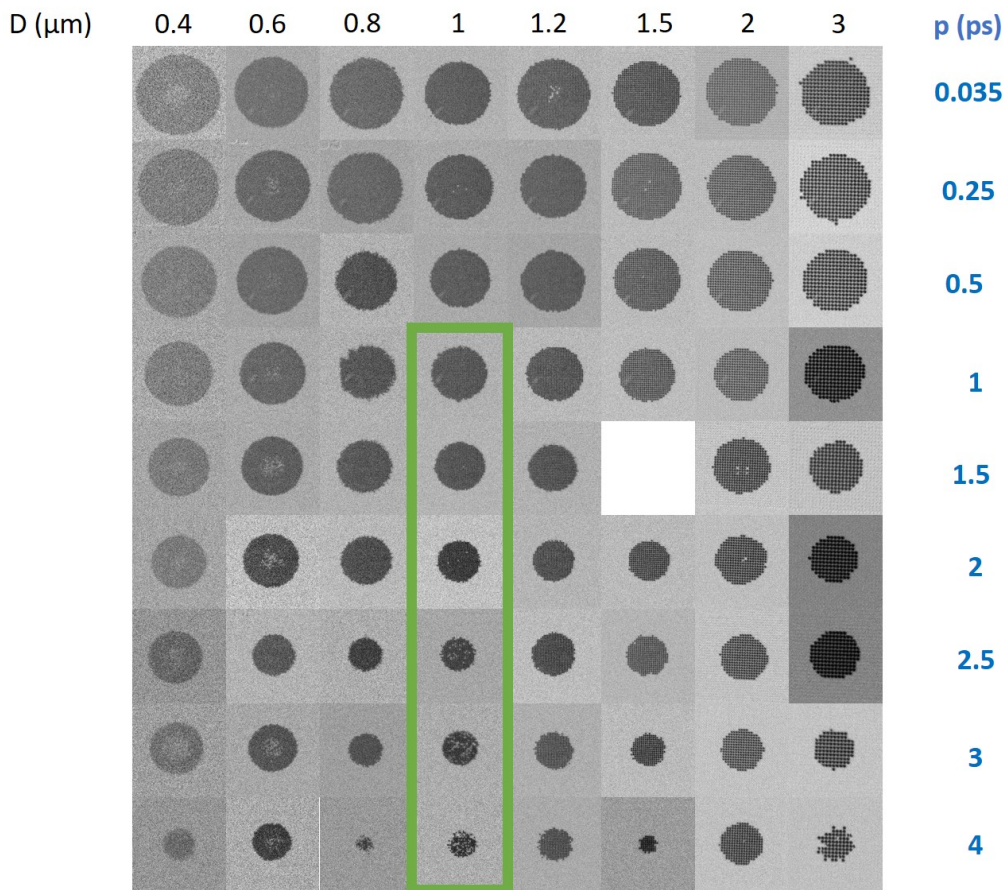


Figure 3.21: Magneto-optical images of $\text{Gd}_{24}(\text{FeCo})_{76}$ (20 nm) magnetic disks obtained after a single laser pulse, linearly polarized at 16 mJ/cm^2 of fluence. Depending on the pulse duration and the disk diameter, we observe two different magnetic states: homogenous dark grey area for AO-HIS and non-homogenous dark grey area for randomly oriented disks. The green rectangle is a particular case at $1 \mu\text{m}$ of disk diameter.

3.3. FROM 3 μM TO 400 NM DISK DIAMETER

We can easily observe that the switching diameter decreases as soon as the pulse broadens. This observation is coherent with the AO-HIS state diagram (fluence vs pulse duration) reported on GdFeCo full film which demonstrated that the threshold switching fluence increases when the temporal distribution of the laser become larger⁵. They attributed this behavior of F_{sw} to the necessity to achieve an overheating of the free electrons which appear to be essential for AO-HIS mechanism (the reader can find more details about the ultrafast dynamic in the first chapter of this work). Moreover, the non-monotonic trends of the switching diameter D_{sw} with the disks size for 35 fs is qualitatively the same as reported in Figure 3.10 and 3.9. This result highlights the reproducibility of the AOS experiments, as these three experiments were performed on three different MOKE measurement days. More Generally, on the MOKE images of Figure 3.21, one can observe up to two different magnetic states depending on the pulse duration and the disk size: deterministic switching, and randomly oriented disk. For 400 and 600 nm disks, regardless of the pulse duration we can easily identify the random state. While for 800 nm and 3 μm disks, all the MOKE images show a uniform switched domain at all the studied pulse duration. Finally, between 1 and 2 μm , the description of the evolution of the magnetic state with the pulse duration is more complicated, since we observed both magnetic configurations at a given size for different pulse duration. Moreover, the variation of the switching diameter with disks size looks proper to each pulse duration. However, to make a more careful analysis, we should perform the same AOS experiments of Figure 3.10 at each pulse duration to extract the variation of both switching and random threshold fluence with disk diameter.

Let us finally zoom inside the green rectangle, where the disk diameter is 1 μm and the pulse duration varies from 1 to 4 ps. Figure 3.22 presents the results of this operation. As the pulse duration increases, it is not only the size of the switched domain that decreases, but also the switching quality that gradually decreases. Indeed, the number of unswitched disks in the exposed area become important as we move from smaller to larger pulse duration magnitudes.

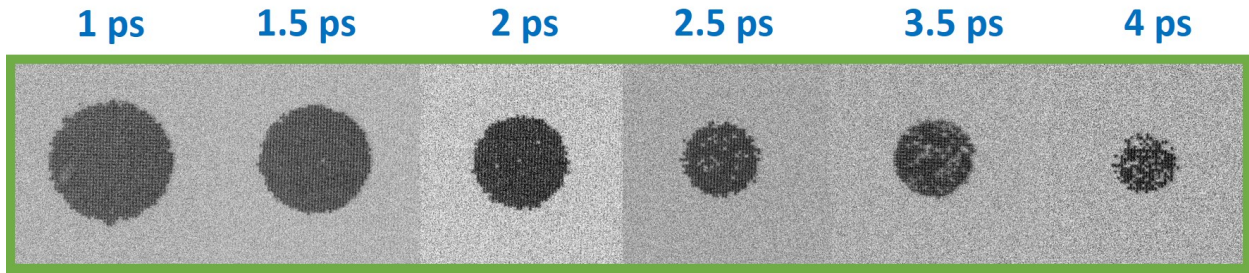


Figure 3.22: Magneto-optical images of $\text{Gd}_{24}(\text{FeCo})_{76}$ (20 nm) magnetic $1 \mu\text{m}$ disks obtained after a single laser pulse, linearly polarized at 16 mJ/cm^2 of fluence. The augmentation of the pulse duration causes the degradation of the switching state indicated by the increase in the unswitched disks within the exposed area.

3.4 Summary

This Chapter was focused on the size effect for AO-HIS in GdFeCo periodic structures. We demonstrate that magnetic micro and nanostructures could be switched deterministically with a single ultrafast laser pulse with a reversal threshold fluence which tends to decrease with disk size. We support this statement with numerical simulations that highlight the creation of standing waves induced by light scattering by structure edges giving a non-uniform distribution of absorption within the disks. However, we point out a non-monotonic behavior of both thresholds for getting switching and random state and we could even reproduce this trend with the simulations. At the end of this chapter, we showed that the period of the arrays and the pulse duration are two parameters which can also influence this study of the size effect on AOS mechanism in GdFeCo disks.

Chapter 4

Gd effect on Pt/Co/Pt ferromagnet

4.1 Introduction

The manipulation of the magnetization by one ultrashort femtosecond pulse under no applied field presents a high interest for the scientific community due to the potential for ultrafast and energy-efficient memory applications. In 2011 Radu et al.¹ and in 2012 T.A. Ostler et al.⁶⁸ published consecutively the first observation of ultra-fast SP-AOHIS in ferrimagnetic GdFeCo alloy. Since then, experimental observations of Single Pulse All Optical Helicity Independent Switching have been reported in various magnetic materials such as rare-earth-free Heusler alloy $\text{Mn}_2\text{Ru}_x\text{Ga}$ ¹⁵, TbCo alloys doped with small amount of Gd⁹, Gd/Co⁷ and Tb/Co synthetic ferrimagnets^{16,17}. Recent experimental and theoretical studies on Co/Gd bilayers^{23,24} show that unlike rare-earth transition-metal ferrimagnetic alloys, the bilayers can be switched in the absence of a magnetization compensation temperature. Moreover, it is demonstrated that by changing the intermixing between Co and Gd at the interface the thickness range at which AO-HIS can be observed change drastically as well as the threshold fluence. By using an extension of the microscopic three-temperature model (M3TM), they also identified the switching mechanism as a front of reversed Co magnetization that propagates away from the interface driven by exchange scattering. Nevertheless, the understanding of the AO-HIS mechanism in Pt/Ferromagnet/Gd synthetic ferrimagnet is remain open. In this chapter, we present a careful analysis of the single pulse all optical switching effect in Pt(3.7 nm)/Co(0.7 nm)/Gd(t_{Gd})Pt (3 nm), Pt(3.7 nm)/Gd(t_{Gd})/Co(0.7 nm)/Pt(3 nm), and Pt(3.7 nm)/Co_xGd_y(t)/Pt(3 nm) wedge samples. Where the thickness of Gd t_{Gd} , the thickness of CoGd alloy t, and the pourcentage x (and y) are varied. This investigation demonstrates that a [Co/Pt] doped with an infinitesimal amount of Gd at one

of the Pt/Co/Pt interfaces show single pulse AO-HIS. In addition, a clear difference between the two interfaces for all optical switching properties is highlighted. Finally, we demonstrate the switching of the magnetization of a ferrimagnetic alloy in the absence of a magnetization compensation.

4.2 Single thermal pulse induced AOS in Pt/Co/Gd(wedge)/Pt full film

The aim of this section is to present our experimental study of the magnetization control of a Pt/Co/Gd(wedge)/Pt full film using linearly polarized femtosecond laser pulses. To achieve this goal, we will first present the stacking we used in our work and show how we converted the Gd-position to Gd-thickness inside the wedge. Next, we will see that all the wedge samples exhibit out of plane magnetization and are Co-dominant. Then, we will clearly define the different regimes present in this chapter. The definition of these regimes will allow us to plot the state diagram describing the magnetic behavior of the Co layer after exposure to a single 35 fs laser pulse linearly polarized as a function of fluence and Gd thickness.

4.2.1 Design of the wedge sample

The samples consisted of thin films of composition glass/Ta(3)/Pt(3.7)/Co(0.7)/Gd(0.14, t_{Gd})/Pt(3) and glass/Ta (3)/Pt(3.7)/Co(0.7)/Gd(0.5, t_{Gd})/Pt(3) (thickness in nm) grown by magnetron sputtering in an AJA machine, without rotation of the Gd target (resulting in a gradient of Gd thickness). Where 0.14 nm and 0.5 nm are the Gd thickness at the middle of each wedge. Figure 4.1 depicted the stacks and the size of the four samples used. In fact, each wedge is composed of two samples of identical dimensions 25 mm × 20 mm. The yellow and the orange mark on the samples allows us to identify the limit of the two wedges. Indeed, the yellow mark was used to indicate the side of the wedge with thinner Gd layer, while the orange mark was used to indicate the side of the wedge with thicker Gd layer. Before presenting the results of the magnetic and AOS measurements on these wedges, it is important to know the Gd thickness at every position of the wedge. That is the goal of the next paragraph.

4.2.2 Conversion of the Gd position to Gd thickness

In order to compare our results with each other or with previous studies and to simplify the reading of this work, it is essential to present our result in term of Gd thickness instead of Gd

4.2. SINGLE THERMAL PULSE INDUCED AOS IN PT/CO/GD(WEDGE)/PT FULL FILM

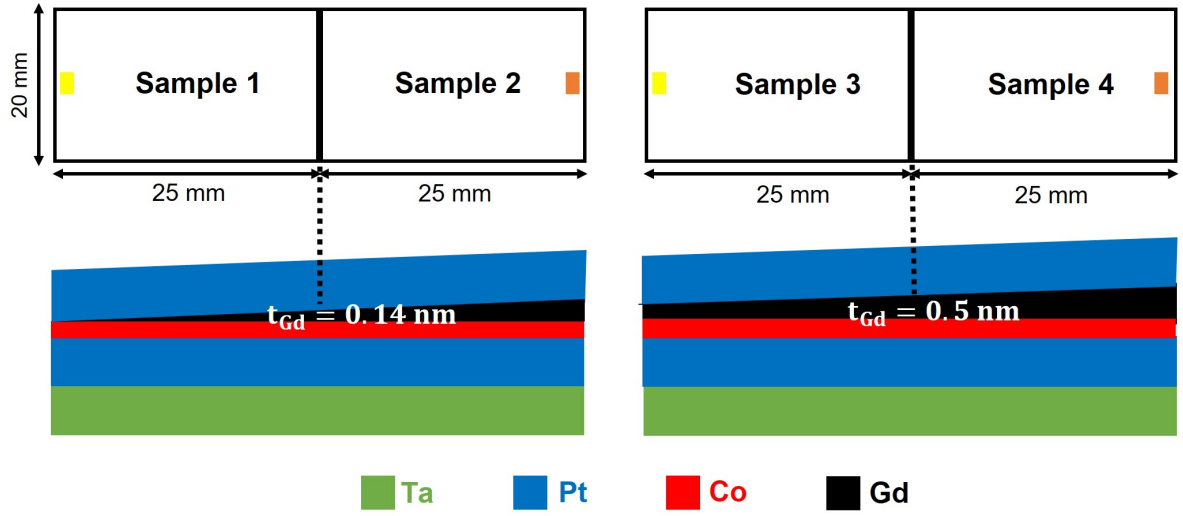


Figure 4.1: Illustration of the four samples needed to form two Gd-wedge. In the middle of the wedge, the thickness of Gd is 0.14 nm and 0.5 nm for the right and left figure, respectively. The yellow and orange mark on the surface of the sample were used to identify the thinner and thicker Gd layer side of each wedge, respectively. The total length of each wedge is 50 mm.

position. To perform this conversion, we have assumed that a A-wedge can be described by a linear variation:

$$t_A(x) = t_0(1 + \alpha.x) \quad (4.1)$$

Where $t_0 = t_A(x = 0)$ is the thickness of the specific element A at the center of the wedge and α is the slope of the line. Physically, the parameter α includes the non-uniformity effect that occurs during the deposition process and is independent of the deposited thickness. Thus, we just need the value of α to perform our conversion. To determine this α value, we grow a thicker Cu-wedge consisting of two identical length samples of 25 mm, as shown in Figure 4.2(a). The exact stack is glass/Ta(3)/Cu(5)/Gd₂₂(FeCo)₇₈(10)/Cu(200, t_{Cu})Pt (5) (thickness in nm) grown by magnetron sputtering. By using a profilometer we extracted the total thickness of the stack in different positions of the wedge. Figure 4.2(b) shows the variation of the Cu thickness across the 50 mm of wedge and where the red line represents the linear fit of the experimental data with equation 4.1. We observe good agreement between our assumption of linear variation and the experimental data, which allows us to obtain 0.022 mm^{-1} as the value of α .

Finally, we can therefore know the thickness of Gd at a given position in each Gd-wedge. Figure 4.3 shows the two Gd-wedges with the Gd thickness at the extremity of each wedge.

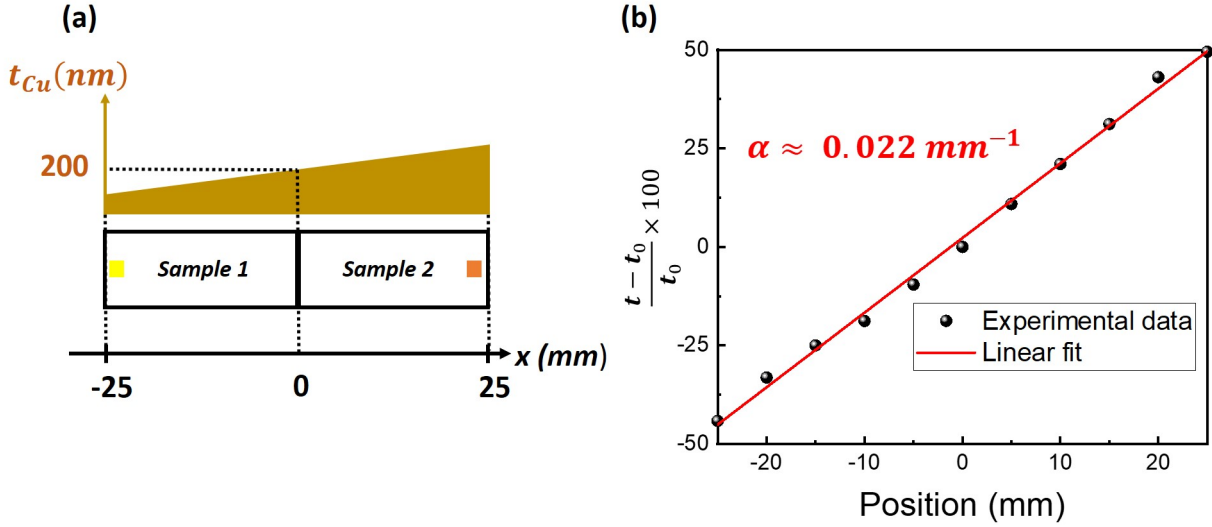


Figure 4.2: (a) Illustration of the two samples needed to form Cu-wedge. At the middle of the wedge, the thickness of Cu is 200 nm. The yellow and orange mark on the surface of the sample were used to identify the thinner and thicker Cu layer side of the wedge, respectively. (b) Evolution of the Cu thickness across the total wedge length. The red line is the linear fit of the experimental data.

For the thinner Gd-wedge (top Figure 4.3), the Gd thickness is between 0.063 and 0.217 nm, while for the thicker one (bottom Figure 4.3), t_{Gd} is between 0.225 and 0.775 nm. Therefore, in the following sections, the results will be presented by combining the two Gd-wedges and the composition of the single wedge sample will be considered as glass/Ta(3)/Pt(3.7)/Co(0.7)/Gd (0.06-0.77)/Pt(3) (thickness in nm).

4.2.3 Magnetic characterization

The material of interest in this section is the Pt/Co/Gd (0.06-0.77 nm) stack deposited on a Ta buffer layer. The magnetic behavior of this tri-layer has been extensively studied in the literature. Indeed, it has been demonstrated that this stack exhibited an antiferromagnetic coupling at the Co/Gd interface^{7,149} (we will come back to this AF coupling in section 4.2.4.4). Moreover, this stack presents a perpendicular magnetic anisotropy (PMA) because when we growth a ferromagnetic metal (Co in our case) on a buffer layer such as Ta, TaOx, and Pt, a preferential [111] crystallographic orientation is achieved¹⁵⁰⁻¹⁵². This [111] direction helps to promote PMA. Remarkably, in 2016, T. H. Pham et al.¹⁴⁹ have been demonstrated a high domain wall velocities in similar Pt/Co/Gd stacks due to the Dzyaloshinskii-Moriya interaction (DMI) present in the Pt/Co interface. Thus, it was not a huge surprise to observe an out of plane magnetization behavior in

4.2. SINGLE THERMAL PULSE INDUCED AOS IN PT/CO/GD(WEDGE)/PT FULL FILM

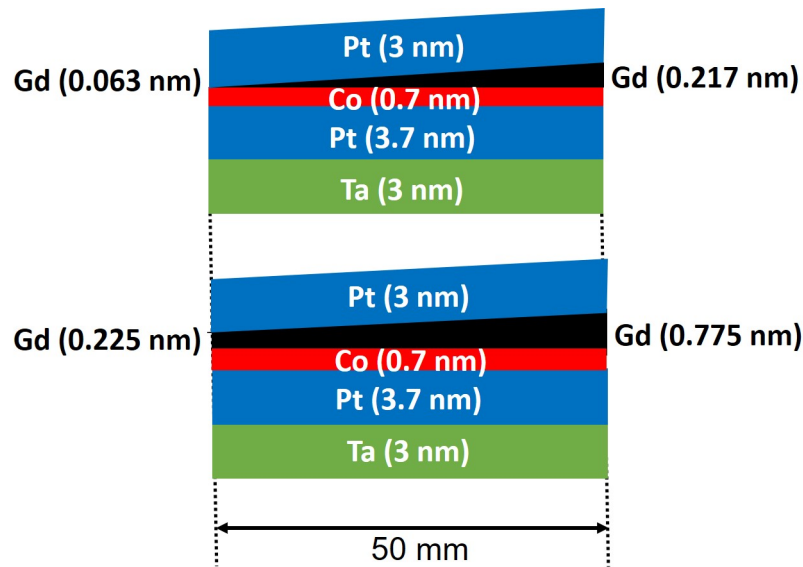


Figure 4.3: Representation of (top) the thinner and (bottom) the thicker Gd-wedge with the thickness value of Gd for the extremity of each wedge.

the Pt/Co/Gd (0.06-0.77 nm) stack, as illustrated in Figure 4.4(a). Indeed, Figure 4.4(a) shows the hysteresis loop at room temperature of the Gd-wedge for t_{Gd} equal to 0.2 nm (black curve) and 0.7 nm (red curve). These measurements allow us to confirm that the Pt/Co/Gd (0.06-0.77 nm) stack is Co-dominant and exhibited an out of plane magnetization. Figure 4.4(b) shows the variation of the coercive field (H_c) with the size of the Gd thickness. A successive increase and decrease of H_c is observed in this Gd thickness range with a maximum value of 232 G at 0.4 nm.

4.2.4 AO-HIS experiments

4.2.4.1 Magnetic behavior (state) definition

To investigate the impact of the Gd thickness deposited into the Co/Pt interface on the SP-AOHIS in Pt/Co/Pt ferromagnet, we systematically irradiated different positions of the Pt(3.7)/Co(0.7)/Gd(0.06-0.77)/Pt(3) (thickness in nm) stack with 35 fs laser pulses at various fluence range. The effect of the excitation was observed in-situ using MOKE microscopy. Figure 4.5 shows the overall magnetization behavior of Co layer that can be observed for the Pt/Co/Gd(0.06-0.77 nm)/Pt wedge sample. We distinguished 5 types of magnetic behavior after the excitation of our wedge sample in single-pulse mode:

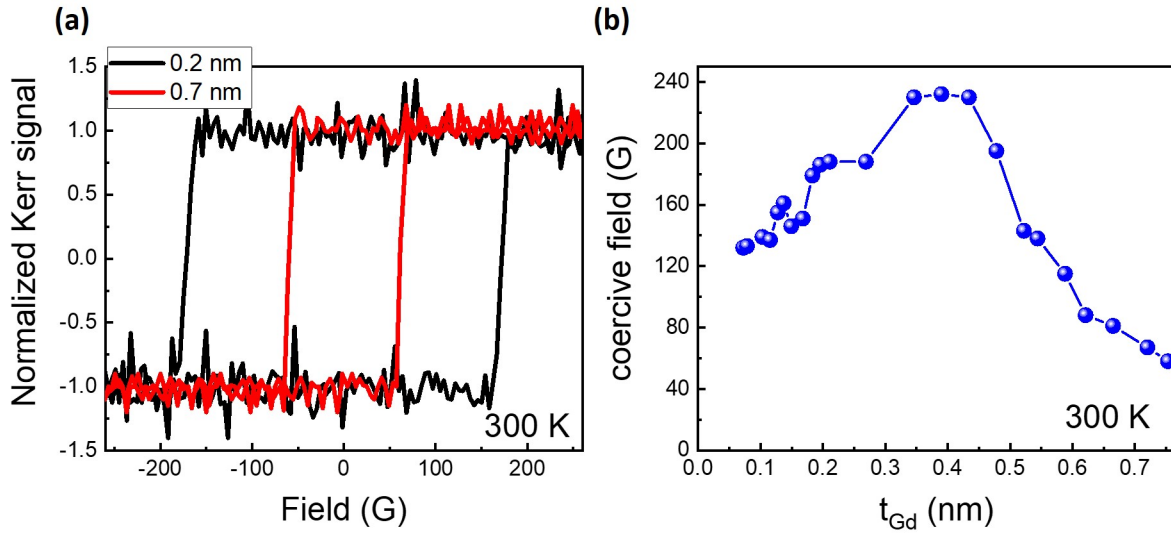


Figure 4.4: (a) Out of plane hysteresis loop for Pt/Co/Gd (0.06-0.77 nm) stack at t_{Gd} equal to 0.2 nm (black curve) and 0.7 nm (red curve). Both curves show a strong PMA and demonstrate that the entire Gd-wedge is Co-dominant. (b) Variation of the coercive field with Gd thickness. A maximum of H_c appears at t_{Gd} equal to 0.4 nm.

- No switching state which is not illustrated in Figure 4.5. Nevertheless, this regime is observed at all Gd thicknesses when the fluence of the laser pulse is not sufficient to cause a magnetic effect on the sample.
- Multidomain state with MOKE images under a light grey rectangle and observed at $t_{Gd} = 0.1$ nm after irradiation with 3 consecutive single laser pulses at the same fluence of 4.7 mJ/cm² for a repetition rate of 1 Hz.
- Demagnetization in the center of the laser spot with MOKE images under a light grey rectangle and observed at $t_{Gd} = 0.6$ nm after irradiation with 3 consecutive single laser pulses at the same fluence of 8.8 mJ/cm² for 1 Hz of rate repetition. At this high fluence regime, demagnetization is illustrated by a multidomain behavior at the center of the laser spot and a uniform reversal ring at the edges due to the laser gaussian spatial profile.
- Switching regime with MOKE images under a light red rectangle and observed at $t_{Gd} = 0.25$ nm after irradiation with 3 and 10001/10002 consecutive laser pulses at the same fluence of 8 mJ/cm² for 1 Hz and 5 kHz of rate repetition, respectively. At the same laser pulse fluence, this regime is marked by a toggle reversal domain for consecutive single laser pulses with 1 Hz of rate repetition, while a multidomain state is observed for

4.2. SINGLE THERMAL PULSE INDUCED AOS IN PT/CO/GD(WEDGE)/PT FULL FILM

10001/10002 consecutive single laser pulses with 5 kHz of rate repetition.

- Perfect toggle switching (PTS) behavior with MOKE images under a dark red rectangle and observed at $t_{Gd} = 0.6$ nm after irradiation with 3 and 10001/10002 consecutive laser pulses at the same fluence of 3.8 mJ/cm^2 for 1 Hz and 5 kHz of rate repetition, respectively. At the same laser pulse fluence, this regime is marked by a toggle reversal domain for consecutive single laser pulses with 1 Hz and for 10001/10002 consecutive single laser pulses with 5 kHz of rate repetition.

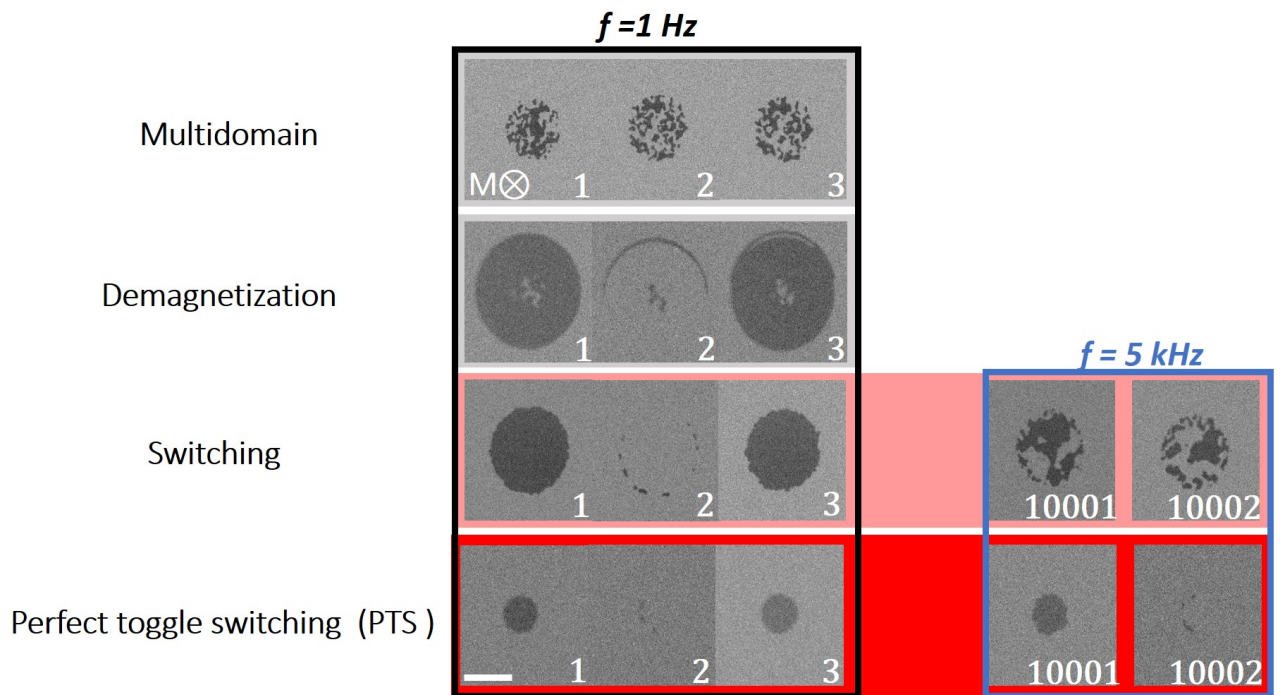


Figure 4.5: Magneto-optical images obtained after exposure of consecutive femtosecond pulses with 1 Hz (inside black rectangle) and 5 kHz (inside blue rectangle) of rate repetition in different regions of Pt/Co/Gd (0.06-0.77 nm) stack. We distinguished 5 types of magnetic behavior after the excitation of our wedge sample in single-pulse mode: No switching (not showed), multidomain state, demagnetization in the center of the laser spot, switching regime, and perfect toggle switching (PTS) behavior. The length of both laser diameter (FWHM) and scale bar is respectively $72 \mu\text{m}$ and $40 \mu\text{m}$ for all the MOKE measurements and images.

4.2.4.2 Transition between the multidomain and the switching regime

In this paragraph, we want to show to the reader the criterion we used to separate the multidomain and the switching state. Indeed, for no or little (0.1 nm) Gd inside the top Co/Pt interface of the Pt/Co/Pt tri-layer, only the multidomain state was reached after exposure of a single femtosecond laser pulse. However, as shown in previous paragraph, 0.25 nm of Gd is sufficient to reach the switching regime. There should therefore be a Gd thickness limit separating the two regimes. To determine this limit, we irradiated the Pt/Co/Gd at low Gd thickness with consecutive single laser pulses at the same fluence of 4.7 mJ/cm^2 for 1 Hz of rate repetition. Figure 4.6 show the result of this operation for t_{Gd} between 0.07 and 0.19 nm.

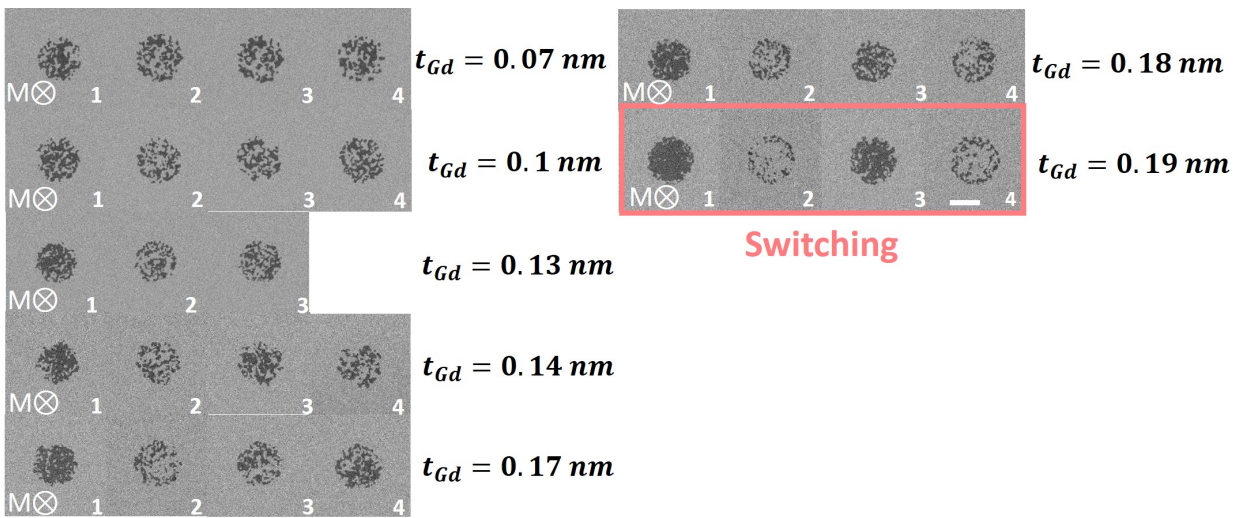


Figure 4.6: Magneto-optical images obtained after exposure of consecutive femtosecond pulses with 1 Hz of rate repetition in different regions of Pt/Co/Gd(0.07-0.19 nm) stack. The transition from the multidomain state to the switching state is achieved at t_{Gd} equal to 0.19 nm (inside light red rectangle). The length of both laser diameter (FWHM) and scale bar is respectively $72 \mu\text{m}$ and $40 \mu\text{m}$ for all the MOKE measurements and images. All incident laser pulses have the same fluence of 4.7 mJ/cm^2 .

4.2. SINGLE THERMAL PULSE INDUCED AOS IN Pt/Co/Gd(WEDGE)/Pt FULL FILM

For a Gd thickness between 0.07 and 0.13 nm, we observed several small domains with randomly oriented magnetizations. Whereas for the thicker Gd (0.14-0.18 nm), the size of the domains increases, and their number is reduced. However, the toggle switching is not achieved in this Gd window. Finally, at a Gd thickness around 0.19 nm, most of the laser spot area is made up of large domains, which show a toggle switching behavior after the exposure of consecutive femtosecond laser pulse. Therefore, we chose this thickness as the threshold Gd thickness to observe the switching regime.

4.2.4.3 Slow domain wall dynamic in the switching regime

Although TR-MOKE experiments were not performed in this work, the Kerr static imaging setup proved to be sufficient to demonstrate a slow dynamic reversal in the switching regime state. Indeed, Figure 4.7(a) and 4.7(b) shows the response of the Pt/Co/Gd(0.21 nm) stack after the exposure of ten femtosecond single pulse at the same fluence of 5 mJ/cm² for 1 Hz and 5 kHz of rate repetition, respectively. In the two AOS experiments, we initially saturated the sample with a magnet. Even if the switched domain is inhomogeneous in Figure 4.7(a) for each laser pulse, toggle switching is maintained after the exposure of 10 laser pulses. However, the presence of this inhomogeneous domain proves that the switching probability is less than 100% in the switching regime. In figure 4.7(b), the laser spot presents a multidomain state after the excitation of 10 laser pulses. The loss of the Co magnetization reversal after few pulses at a frequency of 5 kHz highlights slow domain wall dynamics affecting the definition of the switching regime. We attributed this magnetization trends to a slow domain wall propagation since the time between two pulses (200 ms) in the experiment of Figure 4.7(b) remains 10⁹ less than the time (hundreds of picoseconds) needed to fully reverse the Co magnetization in Co/Gd¹⁵³ or in CoGd alloys⁶.

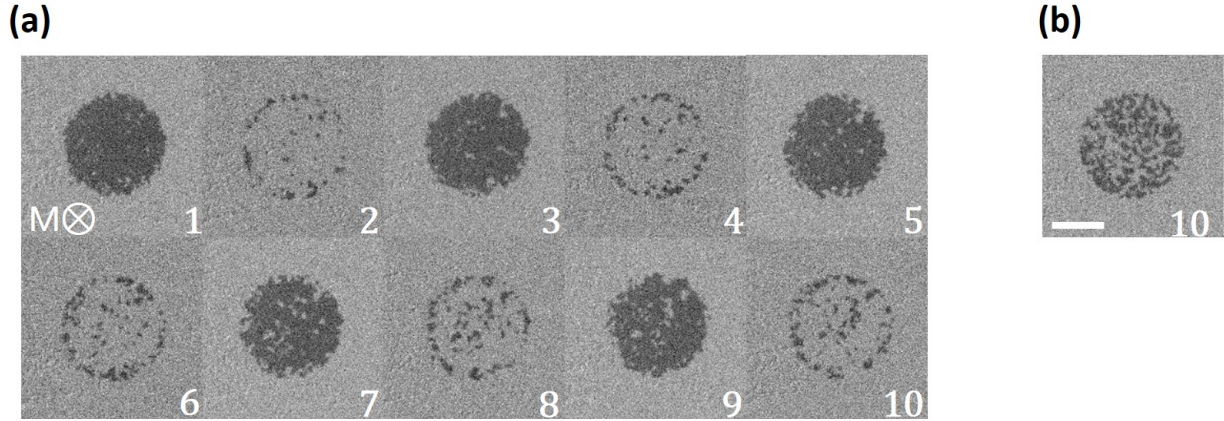


Figure 4.7: Magneto-optical images obtained after exposure of 10 consecutive femtosecond pulses with (a) 1 Hz and (b) 5 kHz of rate repetition in Pt/Co/Gd (0.21 nm) stack. The switching state is maintained for low pulse frequency and disappears at high frequency. These two AOS experiments highlight the slow domain dynamic proper to the switching regime. The length of both laser diameter (FWHM) and scale bar is respectively 72 μm and 40 μm for all the MOKE measurements and images. All incident laser pulses have the same fluence of 5 mJ/cm^2 .

4.2.4.4 State diagram on Pt/Co/Gd/Pt wedge full film

By using the threshold fluence to observe the multidomain state F_{Multi} and the threshold fluence couple (F_{Switch}, F_{Demag}) of both switching and PTS regime, we plotted the AO-HIS state diagram of Pt/Co/Gd (0.06-0.77 nm) stack (Figure 4.8). The dark blue circle (light blue triangle) and the light green square (dark green star) represent respectfully the switching fluence F_{Switch} and the demagnetization fluence F_{Demag} within switching (perfect toggle switching) regime. The black open disk in Figure 4.8 represents the beginning of the multidomain state observed above a threshold fluence. Therefore, we distinguish three behaviors as a function of the Gd thickness: For low Gd thickness (inferior to 0.19 nm), no optical switching is observed. No effect is observed for fluences below 4.4 mJ/cm^2 whereas a multidomain state is directly created for larger fluences after a single pulse. For $0.19\text{nm} \leq t_{Gd} \leq 0.27\text{nm}$, the switching is observed for an intermediate fluence range. However, the single pulse switching cannot be considered as "perfect" since after a large number of pulses (10000) at high rate repetition, the magnetic configuration is a multi-domain state. For a Gadolinium thickness $0.27\text{nm} \leq t_{Gd} \leq 0.76\text{nm}$, perfect toggle switching is achieved.

In addition, the variation of the threshold fluence couple (F_{Switch}, F_{Demag}) in the switching regime can be related to the Gd thickness:

4.2. SINGLE THERMAL PULSE INDUCED AOS IN PT/CO/GD(WEDGE)/PT FULL FILM

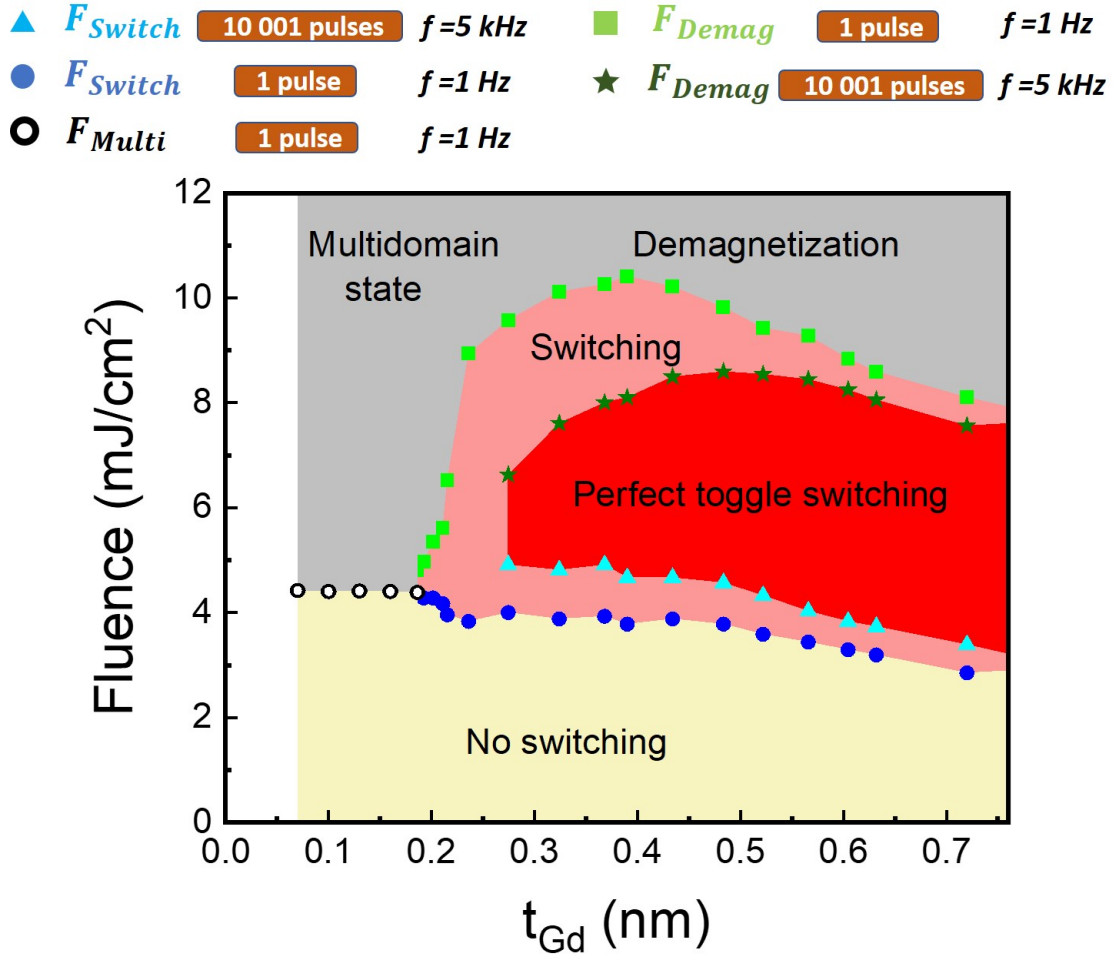


Figure 4.8: AO-HIS state diagram realized on Pt/Co/Gd (0.06-0.77 nm) stack. Magnetization behavior as a function of the Gd thickness t_{Gd} , and the laser fluence F , for Linearly polarized static beam with 70 μm of laser diameter. The dark blue circle (light blue triangle) and the light green square (dark green star) represent respectfully the switching fluence F_{Switch} and the demagnetization fluence F_{Demag} within switching (perfect toggle switching) regime. The black open disk represents the beginning of the multidomain state and the pulse duration is 35 fs for all measurements.

- Above 0.4 nm, the threshold fluence for switching (F_{Switch}) and demagnetization (F_{Demag}) decreases with Gd thickness. Indeed, at this Gd thickness, we should have one full Gd atomic plan⁷, then the growth of the second Gd atomic plan above has a weaker $J_{(Co-Gd)}$ antiferromagnetic exchange because it occurs over a long distance from the Co layer. However, this second Gd atomic layer will interact ferromagnetically with the first one with the help of an internal molecular field and a small induced magnetic moment will appear, as illustrated in Figure 4.9(a). Therefore, above 0.4 nm, increase t_{Gd} lead to a small increase

of M_{Gd} and finally to the reduction of the total magnetization $M_S = M_{Co} - M_{Gd}$ of the stack. Consequently, the Curie temperature of the sample will decrease with t_{Gd} and the energy needed to fully demagnetize the two sublattices (RE and TM) for the achievement of AOS will also decrease, causing a progressive reduction of F_{Switch} . Similar reduction of F_{Switch} was observed by J. Q. Wei et al.⁵ in GdFeCo alloys for Gd concentrations approaching the compensation point. Moreover, the threshold fluence for observing multidomain at the center of a switched region at a higher fluence F_{Demag} occurs when the lattice temperature exceeds the Curie temperature at the laser center⁷⁰. Then, the decrease of T_c leads to the decrease of F_{Demag} . The ratio F_{Demag}/F_{Switch} is nearly constant 2.7 ± 0.1 above 0.4 nm (Figure 4.9(b)) and is similar to the ratio of 2.5 observed for thicker Gd layers (3 nm) by Beens et al.²³.

- Between 0.06 and 0.4 nm it's more complicated to determine the exact composition of the Co/Pt interface. Indeed, several studies highlighted an asymmetric magnetic proximity effect within Pt/Co/Pt tri-layer, with a higher Pt-induced moment at the top Co/Pt interface^{154–156}. In 2022, A. Verna et al.¹⁵⁷ demonstrated in Pt(3 nm)/Co(0.6 nm)/Pt(3 nm) tri-layer a higher interdiffusion of the Co atoms in the top Co/Pt interface (1-2 atomic plan inside the Pt layer), causing a large extension of the Pt-induced magnetic moment parallel to the Co-sublattice. Consequently, for this range of Gd Thickness, we should have Co, Gd and Pt atoms in the interface. Therefore, a structural and magnetic characterization must be performed to clearly understand the trends of both F_{Switch} and F_{Demag} in this Gd thickness range.

4.3. SINGLE THERMAL PULSE INDUCED AOS IN PT/GD(WEDGE)/CO/PT FULL FILM

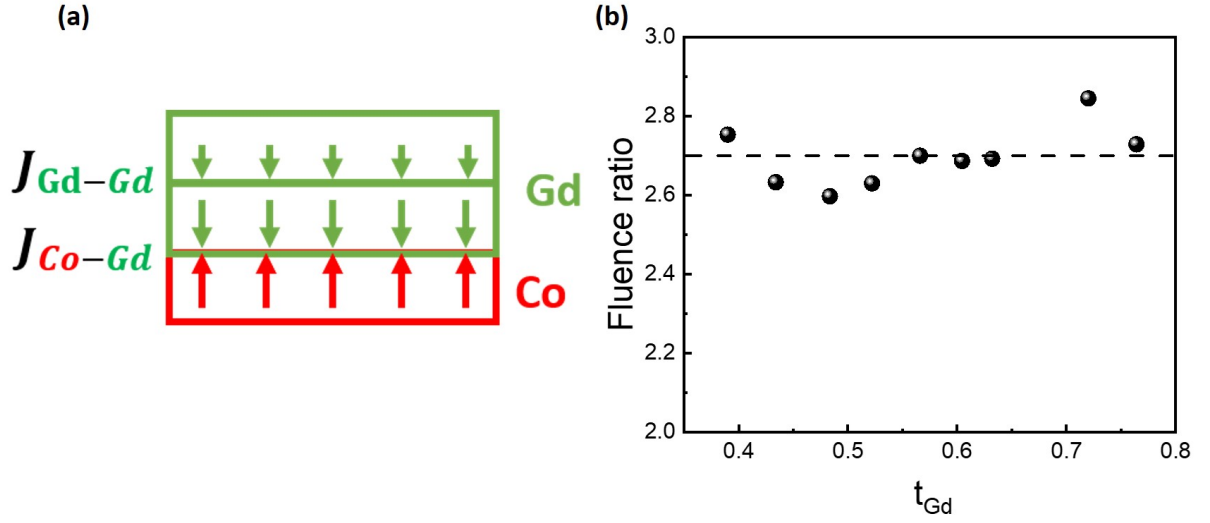


Figure 4.9: (a) Illustration of the local antiferromagnetic coupling between the magnetization of Co and Gd layer near the Co/Gd interface. (b) Evolution of the ratio F_{Demag}/F_{Switch} with the Gd thickness above 0.4 nm. The dashed line represents the average of all the ratio value in this range of thickness.

4.3 Single thermal pulse induced AOS in Pt/Gd(wedge)/Co/Pt full film

In this section, we will first present the stacking we used in our work and show the structural characterization that we performed at a given thickness of the bottom Gd-wedge. Next, we will see that it is not possible to add a "significant" amount of Gd, otherwise the perpendicular magnetization is lost. We will be therefore experimentally limited to a Gd thickness range of range of 0.06 - 0.28 nm. Then, by using the definition of the different regimes illustrated in 4.2.4.1, we will plot a state diagram describing the magnetic behavior of the Co layer after exposure to a single 35 fs laser pulse linearly polarized as a function of fluence and Gd thickness. We ended this section by plotting the magnetic state diagrams (Fluence vs Pulse duration) at two different Gd thickness.

4.3.1 Design of the wedge sample

The samples consisted of thin films of composition glass/Ta(3)/Pt(3.7)/Gd(0.14, t_{Gd})/Co(0.7)/Pt(3) and glass/Ta(3)/Pt(3.7)/Gd(0.5, t_{Gd})/Co (0.7)/Pt(3) (thickness in nm) grown by magnetron sputtering without rotation of the Gd target. Where 0.14 nm and 0.5 nm

CHAPTER 4. GD EFFECT ON PT/CO/PT FERROMAGNET

are the Gd thickness at the middle of each wedge. Figure 4.10 depicted the stacks and the size of the four samples used. In fact, each wedge is composed of two samples of identical dimensions 25 mm × 20 mm. The yellow and the orange mark on the samples allows us to identify the limit of the two wedges. Indeed, the yellow mark was used to indicate the side of the wedge with thinner Gd layer, while the orange mark was used to indicate the side of the wedge with thicker Gd layer. By conversing the Gd position to Gd thickness (see more detailed in section 4.2.2), the composition of the bottom Gd-wedge is considered as glass/Ta(3)/Pt(3.7)/Gd(0.06-0.77)/Co(0.7)/Pt(3) (thickness in nm).

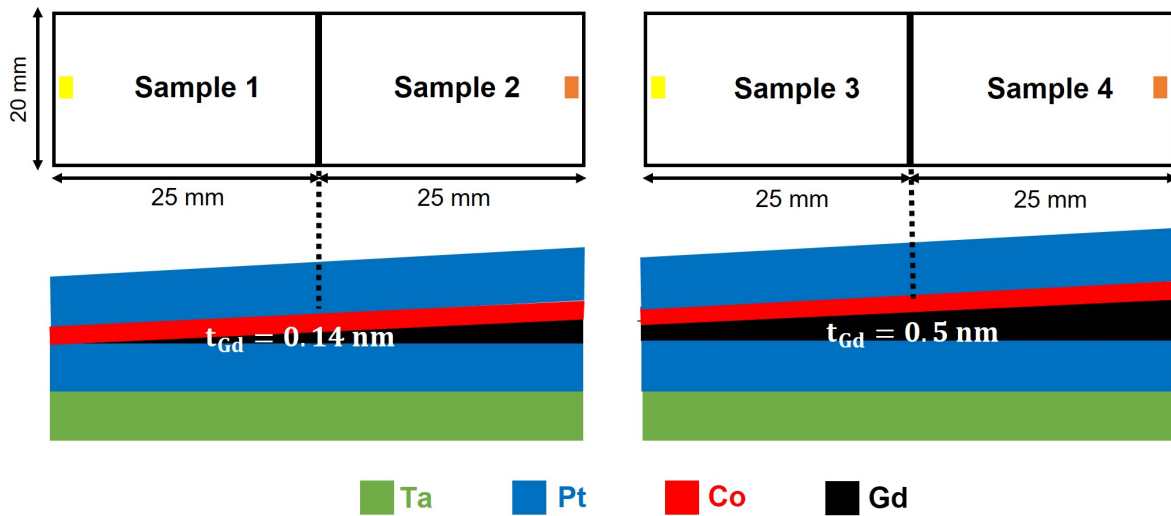


Figure 4.10: Representation of the four samples needed to form two bottom Gd-wedges. In the middle of the wedge, the thickness of Gd is 0.14 nm and 0.5 nm for the right and left figures, respectively. The yellow and orange mark on the surface of the sample were used to identify the thinner and thicker Gd layer side of each wedge, respectively. The total length of each wedge is 50 mm.

4.3.2 Structural and magnetic characterization

All the structural and microstructural analyses in this work were carried out by Dr J. Ghanbaja and performed by using Transmission electron microscopy (TEM) measurements. The TEM used is a JEM - ARM 200F Cold FEG TEM/STEM operating at 200 kV and equipped with a spherical aberration (Cs) probe and image correctors (point resolution 0.12 nm in TEM mode and 0.078 nm in STEM mode). Therefore, the atomic resolution of this microscopy technique is sufficient to clearly dissociate the Ta, Co, and Pt layers within the studied stack. But for a Ta(3)/Pt(3.7)/Gd(0.1)/Co(0.7)/Pt(3) stack (thickness in nm), High-Resolution Transmis-

4.3. SINGLE THERMAL PULSE INDUCED AOS IN PT/GD(WEDGE)/CO/PT FULL FILM

sion Electron Microscopy (HRTEM) will be ineffective in distinguishing Gd atoms, because the thickness of Gd is of the same order of magnitude as the spatial resolution limit of the technique. Thus, Figure 4.11(a) displayed the HRTEM micrograph corresponding to the all stack without Gd layer. The relatively good agreement between the thickness measurements of each layer and the nominal ones, allows us to underline the high precision of the PVD technique.

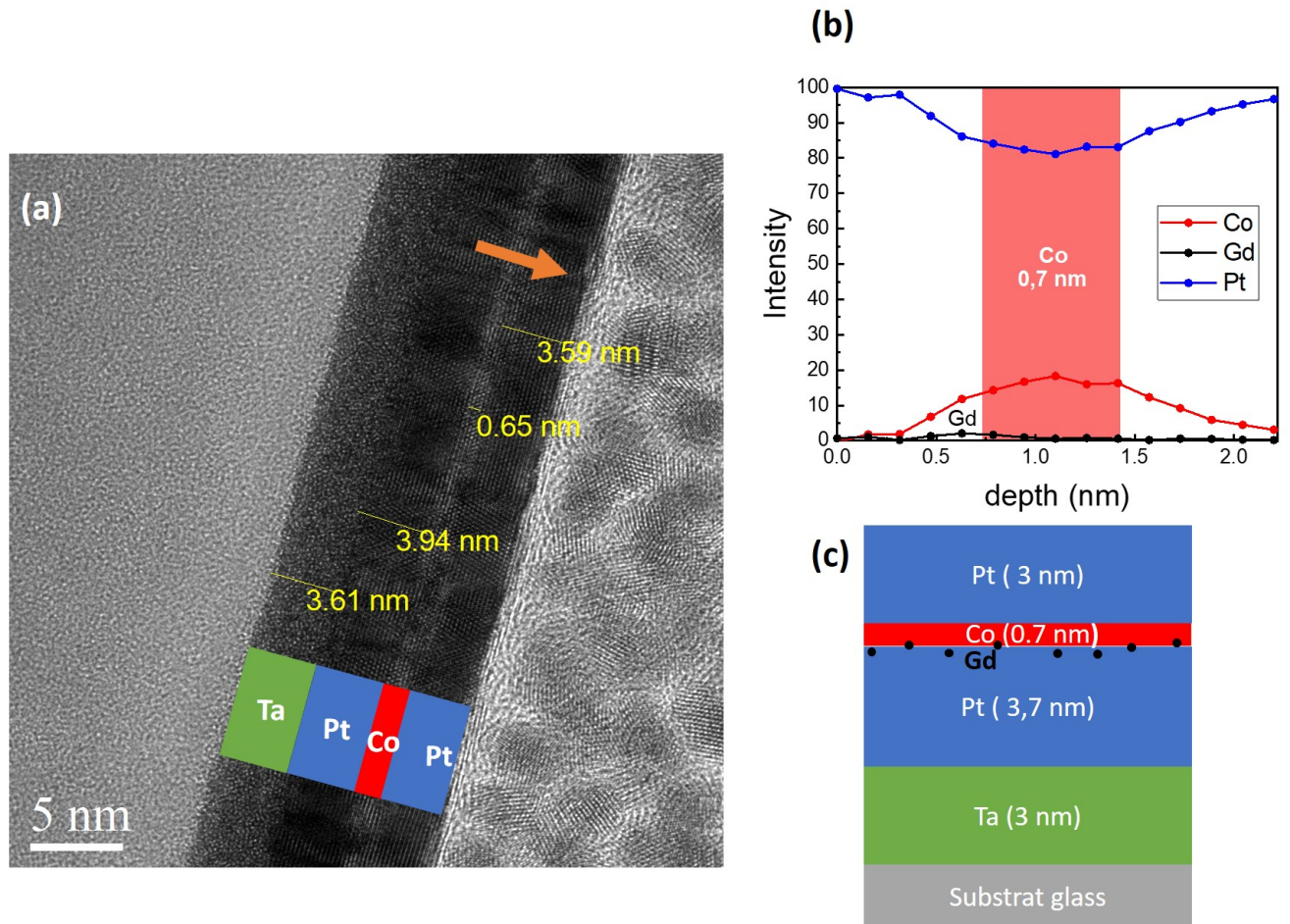


Figure 4.11: Structural characterization of the Glass/ Ta(3 nm)/Pt(3.7 nm)/Gd(0.1 nm)/Co(0.7 nm)/Pt(3 nm) stack.(a) HRTEM micrograph showing the Ta layer (green rectangle), Pt layer (blue rectangle), and Co layer (red rectangle). (b) Intensity depth profile of Pt, Co and Gd using Energy-dispersive X-ray spectroscopy (EDXS) measurement performed along the orange arrow in (a), proving the higher diffusion of Co atoms within the top Pt layer compared to the bottom one and showing the position of the Gd majority atoms after the deposition process. (c) Sketch of the heterostructure.

Figure 4.11(b) shows the result of energy-dispersive X-ray spectroscopy (EDXS) measurement realized along the orange arrow in Figure 4.11(a). In this Figure, the maximum Co

CHAPTER 4. GD EFFECT ON PT/CO/PT FERROMAGNET

intensity (red curve) is observed for the minimum Pt intensity (blue curve) and delimited by a red rectangle at the nominal Co thickness (0.7 nm). Compared to this grey rectangle, the distribution of Co is clearly asymmetric, showing more diffusion through the upper Pt layer. In other words, the bottom Pt/Co interface is more uniform than the top Co/Pt interface. Remarkably, in Figure 4.11(b), the maximum of Gd intensity (black curve) occurs at the bottom Pt/Co interface. It should be emphasized that similar asymmetric interface and Gd position results are found when we realized EDXS measurements in other regions of the Pt(3.7)/Gd(0.1)/Co(0.7)/Pt(3) stack.

To confirm the Gd position into the bottom Pt/Co interface, we carried out the same (TEM) measurements in the Si/Ta(3)/Pt(3.7)/Gd(2)/Co(2)/Pt(3) stack (thickness in nm). The thicker layers of Co and Gd in this sample were chosen to get a better view of the quality of the Gd/Co interface. Figure 4.12(a) and (b) shows High Angle Annular Dark Field (HAADF-STEM) images of the sample. While Figure 4.12(c) presents a Bright Field (BF-STEM) image. As we can see from these STEM pictures, all the namely layer Ta, Pt, Gd and Co are easily identified due to the different atomic numbers Z of each atom. In addition, these STEM images show a sharper and uniform Pt/Gd/Co tri-layers. The latter observation is confirmed by EELS measurements, presented in Figure 4.12(d). This image displayed the elemental maps of Co (red layer) and Gd (green layer) extracted from the yellow rectangle of Figure 4.12(a). Thus, the Gd layer is clearly below the Co layer and shows weak interdiffusion at the Gd/Co interface. Therefore, we concluded that the Gd atoms stay into bottom Pt/Co interface during the deposition process of the Pt/Gd(0.06-0.77 nm)/Co/Pt stack.

4.3. SINGLE THERMAL PULSE INDUCED AOS IN PT/GD(WEDGE)/CO/PT FULL FILM

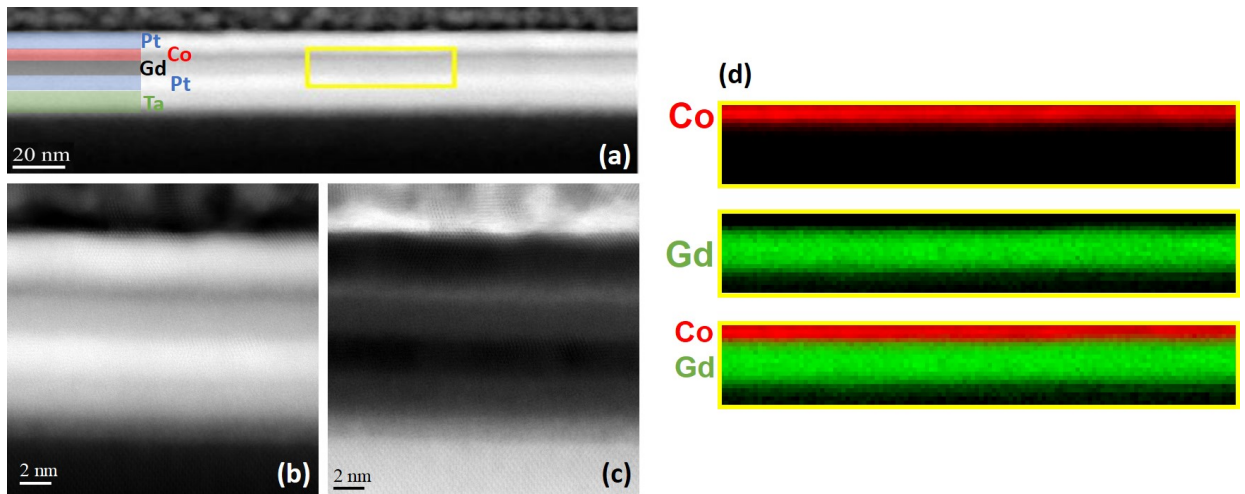


Figure 4.12: Structural characterization of the Ta(3)/Pt(3.7)/Gd(2)/Co(2)/Pt(3) (thickness in nm) stack. (a) and (b) illustrate the HAADF-STEM images of the layered structure. While (c) show the corresponding BF-STEM image of (b). (d) EELS-STEM map depicting the elemental distribution of the Gd (green), and Co (red) layers. These STEM measurements confirm that the Gd is mainly present into bottom Pt/Co interface during the deposition process of the Pt/Gd (0.06-0.77 nm)/Co/Pt stack.

To observe the magnetic behavior of the glass/Ta(3)/Pt(3.7)/Gd(0.06-0.77)/Co(0.7)/Pt(3) (thickness in nm) stack, we performed MOKE magnetometry measurements. The red curve in Figure 4.13(a) shows the hysteresis loop of the Pt(3.7)/Gd(0.3)/Co (0.7)/Pt(3) stack, demonstrating that at a Gd thickness of 0.3 nm, the Co magnetization has shifted in-plane. Nevertheless, for a t_{Gd} equal to 0.07 nm, the black curve in Figure 4.13(b) illustrates the out-of-plane magnetization behavior of the Co layer. This magnetization behavior can be understood by the loose of the [111] crystallographic direction inside the Co layer when we introduce the equivalent of one atomic plane of Gd into the Pt/Co interface. Indeed, by adding one atomic plane of Gd into the bottom Pt/Co interface, we modify the Co layer texture, crystal orientation, stress, roughness, or microstructure (all these effects influence the anisotropy of the sample).

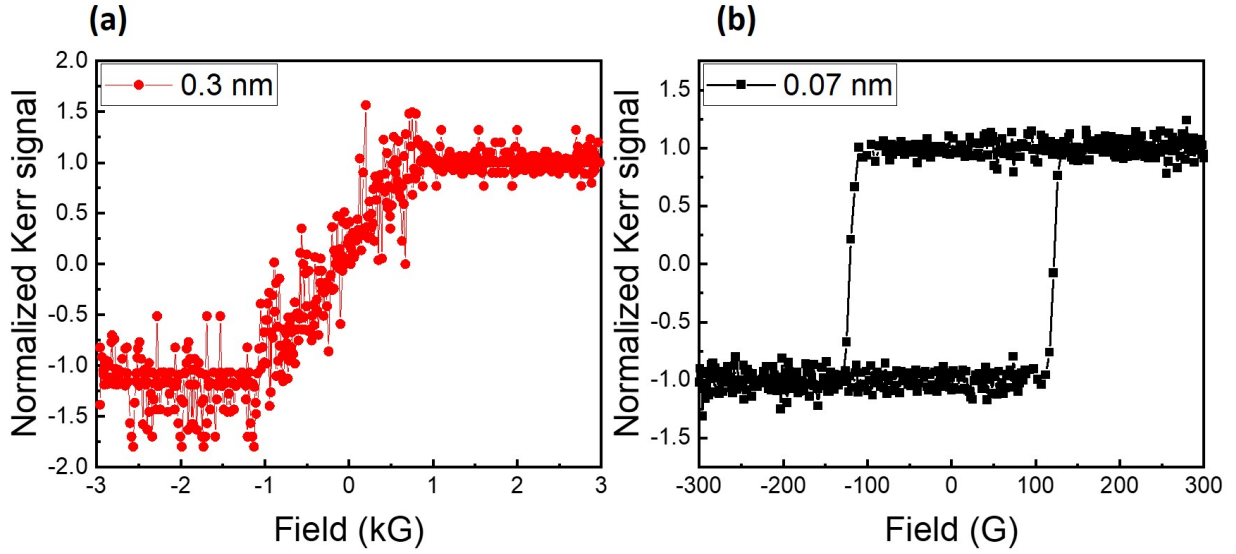


Figure 4.13: Hysteresis loop for Pt/Gd/Co/Pt stack at t_{Gd} equal to 0.07 nm (black curve) and 0.3 nm (red curve). In plane magnetization has been observed within for a Gd thickness of 0.3 nm. While out of plane has been performed for 0.07 nm.

4.3.3 AO-HIS experiments

4.3.3.1 State diagram on Pt/Gd/Co/Pt wedge full film

By using the threshold fluence couple (F_{Switch} , F_{Demag}) of both switching and PTS regime, we plotted the AO-HIS state diagram of Pt/Gd(0.06-0.3 nm)/Co/Pt stack (Figure 4.14). The dark blue circle (light blue triangle) and the light green square (dark green star) represent respectfully the switching fluence F_{Switch} and the demagnetization fluence F_{Demag} within switching (perfect toggle switching) regime. Therefore, we distinguish two magnetic behaviors as a function of the Gd thickness. For low Gd thickness ($0.06 \leq t_{Gd}(nm) \leq 0.26$), the PTS regime is achieved in all this Gd thickness range and the value of the couple (F_{Switch} , F_{Demag}) in the switching and the PTS state is constant. While, for a narrow window of t_{Gd} between 0.26 and 0.28 nm, the switching regime is observed. Finally, for thicker Gd ($t_{Gd} > 0.28nm$), no magnetic contribution in the MOKE images was observed when we applied a magnetic field with a magnet or when we sent femtosecond laser pulses on the sample. This observation originates from the fact that the Co magnetization shifted in plane and our Kerr imaging set-up is not indicated to detect the magnetization for in plane magnetization direction. Furthermore, this understanding agrees with MOKE magnetometry measurements which showed that the magnetization of Pt/Gd(0.3

4.3. SINGLE THERMAL PULSE INDUCED AOS IN Pt/Gd(WEDGE)/Co/Pt FULL FILM

nm)/Co/Pt has shifted in-plane.

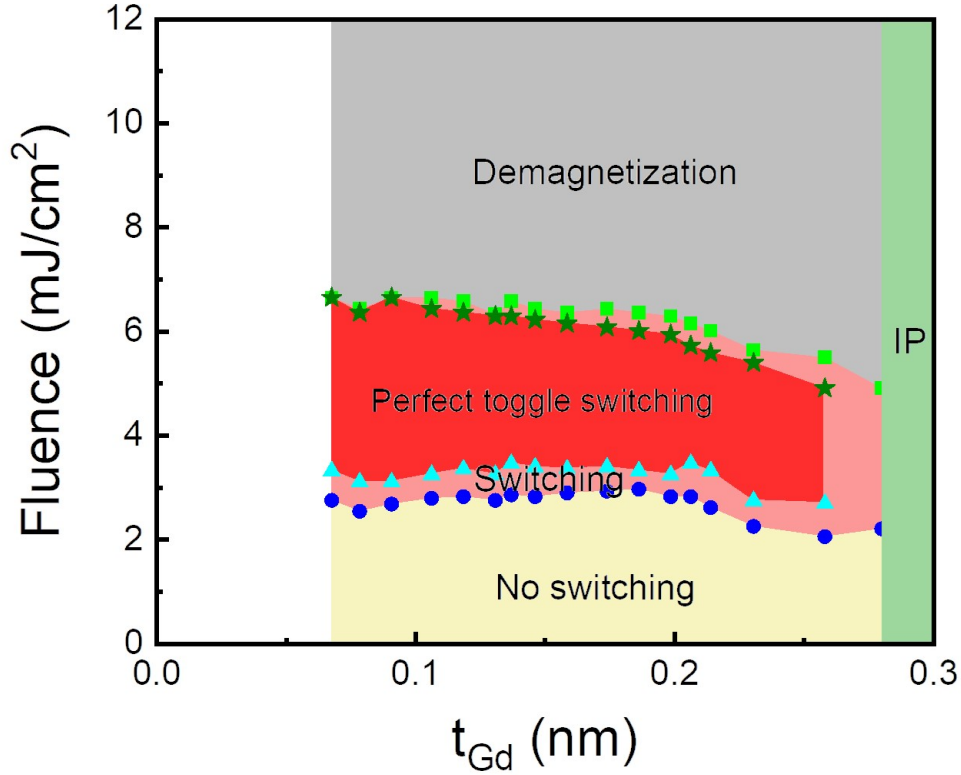


Figure 4.14: AO-HIS state diagram realized on Pt/Gd (0.06-0.3 nm) Co/Pt stack. Magnetization behavior as a function of the Gd thickness t_{Gd} , and the laser fluence F , for Linearly polarized static beam with 60 μm of laser diameter. The dark blue circle (light blue triangle) and the light green square (dark green star) represent respectfully the switching fluence F_{Switch} and the demagnetization fluence F_{Demag} within switching (perfect toggle switching) regime. The pulse duration is 35 fs for all measurements.

This result is amazing due to the achievement of the perfect toggle switching for Gd down to 0.06 nm. At this Gd thickness, it is more logic to take about Gd doping than Gd layer. Thus, we have demonstrated the switching of the magnetization of a Pt/Co/Pt ferromagnet by using a single femtosecond laser pulse linearly polarized with Gd doping at the bottom Pt/Co interface. Moreover, in this doping condition, the effective Gd concentration define as if you would view the Gd/Co bilayer as an alloy is much lower than for an alloy close to compensation concentration. AO-HIS has never been reported for such a big concentration discrepancy between the antiferromagnetically exchange coupled magnetic species. In the following paragraph, we will investigate the laser pulse duration effect on the AO-HIS for this Pt/Gd(wedge)/Co/Pt stack.

4.3.3.2 Influence of the pulse duration

One of the key parameters to characterize all optical switching in various magnetic materials is the laser pulse duration. Indeed, in 2019, G. Kichin et al.⁸⁷ studied the effect of this parameter on the AO-HDS of Pt/Co/Pt ferromagnet and they plotted a state diagram showing the magnetic state of the Co magnetization after the exposure of 600 pulses circularly polarized. Two years later, J. Wei et al.⁵ did the same investigation on the AO-HIS of GdFeCo ferrimagnet and they also plotted a magnetic state diagram which presented a triangular shape. More recently (2022), W. zhang et al.⁹ also reported a magnetic state diagram with a triangular shape in a $Gd_{1-x-y}Tb_yCo_x$ alloys when they highlighted the role of spin-lattice coupling in ultrafast demagnetization and SP-AOHIS. In view of these previous works, we have decided to investigate the impact of the laser pulse duration τ_{pulse} on the switching and PTS regime for the Pt/Gd/Co/Pt stack. In fact, by using magneto-optical images obtained with our Kerr imaging set-up, giving the magnetic configuration of the Co layer after irradiation of laser pulses, magnetic state diagrams could be established.

Thus, we plotted in Figure 4.15 the AO-HIS state diagram realized on Pt/Gd(0.07 nm)/Co/Pt (left Figure) and Pt/Gd(0.21 nm)/Co/Pt (right Figure) with the laser beam diameter around 60 μm . To build these diagrams, we used the threshold fluence couple (F_{Switch} , F_{Demag}) of both switching and PTS regime to delimitate the different magnetic states. Where the dark blue circle (light blue triangle) and the light green square (dark green star) represent respectfully the switching fluence F_{Switch} and the demagnetization fluence F_{Demag} within switching (perfect toggle switching) regime. Moreover, by performing linear fits to separate the switching region with no switching and demagnetization region, the two magnetic state diagrams present a triangular shape for the switching regime, as observed in the GdFeCo and GdTbCo alloys.

At 35 fs, the couple (F_{Switch} , F_{Demag}) exhibit similar value of fluence in the switching regime with a fluence ratio $\Delta_S = F_{Demag}/F_{Switch}$ equal to 2.6 and 2.4 respectively for Pt/Gd(0.07 nm)/Co/Pt and Pt/Gd(0.21 nm)/Co/Pt sample. But, in the PTS regime a higher ratio is observed in the heterostructure with low Gd ($\Delta_{PTS}=2.3$) than the one with high Gd ($\Delta_{PTS}=1.7$).

Moreover, when we increase de pulse duration τ_{pulse} the fluence ration Δ_S (Δ_{PTS}) become smaller and reach closer to 1 (1.1) for long pulse duration. Table 4.1 summarizes Δ_S and Δ_{PTS} limit value in different regimes and the corresponding maximum pulse duration τ_{max} . For a τ_{pulse} above τ_{max} , we observed multidomain state after the exposure of one single laser pulse.

The ratio fluence trends is related to the increase of the threshold switching fluence F_{Switch} and the decrease of the threshold demagnetization fluence F_{Demag} with the augmentation of the pulse duration τ_{pulse} . This behavior of the two fluences results in smaller switching windows

4.3. SINGLE THERMAL PULSE INDUCED AOS IN PT/GD(WEDGE)/CO/PT FULL FILM

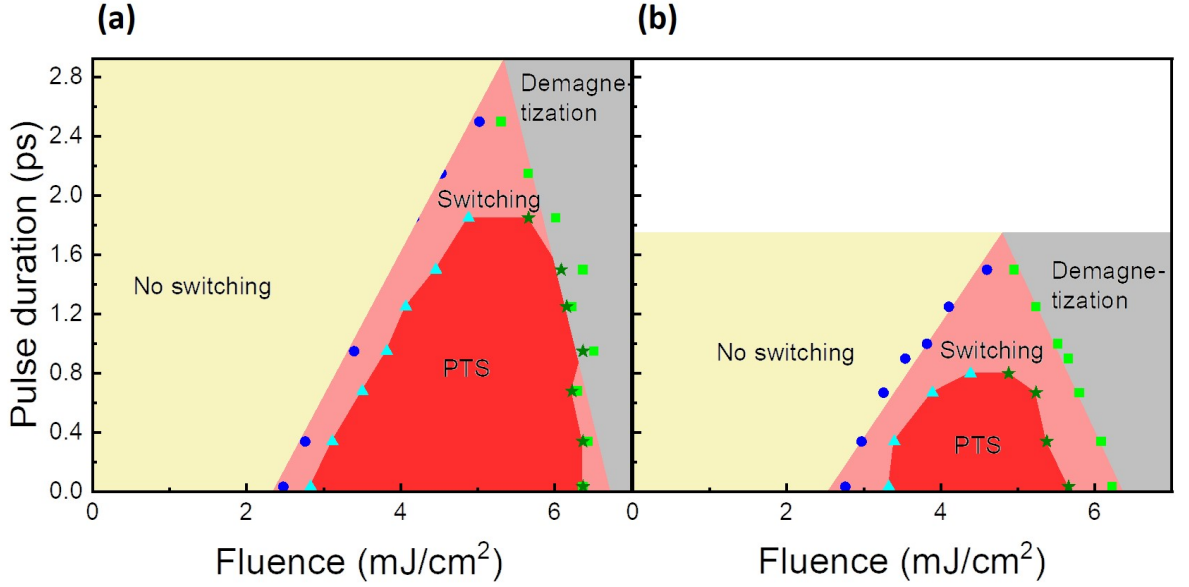


Figure 4.15: AO-HIS state diagram realized on Pt/Gd/Co/Pt. Variation of the fluence and the pulse duration for t_{Gd} equal to 0.07 nm (left) and 0.21 nm (right). The dark blue circle (light blue triangle) and the light green square (dark green star) represent respectively the switching fluence F_{Switch} and the demagnetization fluence F_{Demag} within switching (perfect toggle switching) regime. These magnetic state diagrams were established by performing linear fits to delineate the switching region with no switching and Demagnetization region. The incident laser pulse is linearly polarized and the laser diameter is 60 μm .

Stack	Pt/Gd(0.07 nm)/Co/Pt	Pt/Gd(0.21 nm)/Co/Pt
(Δ_S, τ_{pulse})	(1.06, 2.5 ps)	(1.07, 1.5 ps)
$(\Delta_{PTS}, \tau_{pulse})$	(1.15, 1.85 ps)	(1.11, 0.8 ps)

Table 4.1: Summary of Δ limit values in the switching and PTS regime for thinner and thicker Gd.

in the two states diagram as τ_{pulse} increase. Surprisingly, the area in which perfect single pulse switching is observed is much smaller in the case of larger Gd thickness (0.21 nm). In J. Wei et al.⁵ and W. zhang et al.⁹ the larger switching area and the longer pulse allowing switching τ_{max} are observed close to compensation.

4.4 Single thermal pulse induced AOS in Pt/CoGd(wedge)/Pt full film

The motivation of this work was to investigate the need to reach the compensation point in a CoGd alloy to achieve AO-HIS (at room temperature). To realize this objective, we will first present the sample we used in our work and show how we extracted the (Gd) Co concentration within all the wedge. Next, we will see that all the CoGd-wedge sample exhibit out of plane magnetization and are Co-dominant. Then, by using the definition of the different regimes of section 4.2.4.1, we will build a state diagram describing the magnetic behavior of the Co layer after exposure to a single 35 fs laser pulse linearly polarized as a function of fluence and the concentration of Gd.

4.4.1 Design of the wedge sample

The samples consisted of thin films of composition glass/Ta(3)/Pt(3.7)/Co₉₀Gd₁₀(0.8, t)/Pt(3) (thickness in nm) grown by magnetron sputtering without rotation of the Gd and Co targets (resulting in a gradient of Gd and Co thickness). Where Co₉₀Gd₁₀ and 0.8 nm are respectively the composition and the thickness of the CoGd alloy in the center of the wedge. While t ($t_{Co}+t_{Gd}$) is the alloy thickness at a given position of the full film. Indeed, the CoGd-wedge alloys are made by co-deposition of Co and Gd targets arranged in a geometry shown in Figure 4.16, where the red and black marks on the surface of the sample surface represents the extremity where the alloy is composed of more Co and Gd, respectively. Before presenting the results of the magnetic and AOS measurements on this wedge, it is important to know the Gd (Co) concentration at every position of the wedge. That is the goal of the next paragraph

4.4. SINGLE THERMAL PULSE INDUCED AOS IN PT/COGD(WEDGE)/PT FULL FILM

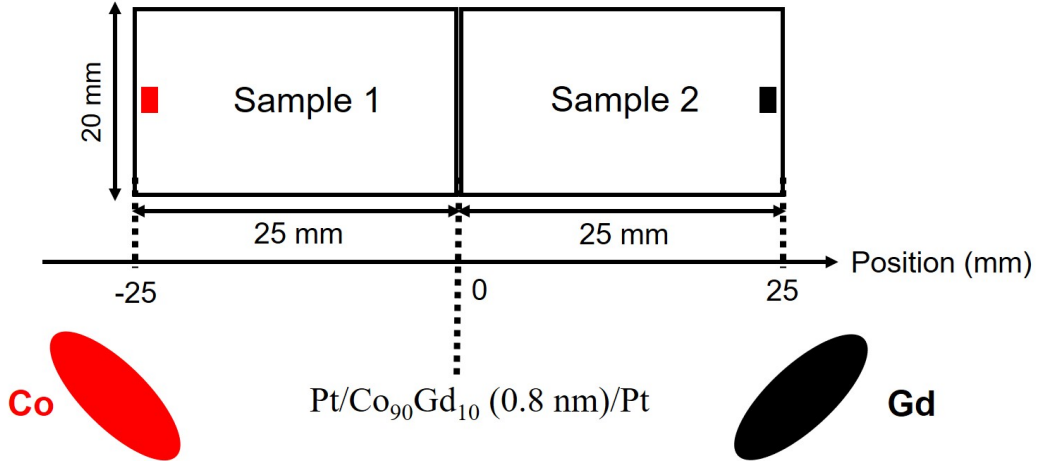


Figure 4.16: Illustration of the two samples needed to form the CoGd-wedge. In the middle of the wedge, the thickness of CoGd alloy is 0.8 nm and the composition is $\text{Co}_{90}\text{Gd}_{10}$. The red and black mark on the surface of the sample were used to identify the region of the wedge where we have more Co and Gd, respectively. The total length of each wedge is 50 mm.

4.4.2 Extraction of the Gd (Co) concentration

To compare our results with previous studies of AOS in ferrimagnetic alloy, it is essential to present our results in term of Gd (Co) ratio instead of CoGd position. To perform this conversion, we have used the same process of section 4.2.2, where we describe the wedge by a linear variation. Nevertheless, in this case, it is a co- deposition of Co and Gd at the same time with the geometry presented in Figure 4.16. In this experimental conditions t_{Co} and t_{Gd} are given by:

$$t_{\text{Co}}(x) = t_{\text{Co}}(0)(1 - \alpha.x) \quad \text{and} \quad t_{\text{Gd}}(x) = t_{\text{Gd}}(0)(1 + \alpha.x) \quad (4.2)$$

Where $t_{\text{Co}}(0)$ (equal to 0.6 nm) and $t_{\text{Gd}}(0)$ (equal to 0.2 nm) are the Co and Gd thickness at the center of the wedge, respectively. α is the same parameter obtained in section 4.2.2. Consequently, we could estimate the alloy thickness t at every position of the wedge. Moreover, by using the following relation:

$$at_{\text{Gd}(\text{Co})}(\%) = \frac{vl_{\text{Gd}(\text{Co})}/\beta_{\text{Gd}(\text{Co})}}{vl_{\text{Co}}/\beta_{\text{Co}} + vl_{\text{Gd}}/\beta_{\text{Gd}}} \times 100 \quad (4.3)$$

We extracted the composition of the CoGd alloy in all the wedge sample. Where $vl_{\text{Gd}(\text{Co})}$ and $\beta_{\text{Gd}(\text{Co})}$ represent the Gd(Co) volume ratio and the flux of Gd(Co) during the deposition, respectively. The values of all the parameters used to perform this conversion are shown in table 4.2. With the rate deposition given at the middle of the wedge.

CHAPTER 4. GD EFFECT ON PT/CO/PT FERROMAGNET

Parameter	value
Co rate deposition ($\text{\AA}/\text{s}$)	0.46267
Gd rate deposition ($\text{\AA}/\text{s}$)	0.15016
Co flux ($10^{-6} \text{ m}^3/\text{mol}$)	6.67
Gd flux ($10^{-6} \text{ m}^3/\text{mol}$)	19.9
$\alpha(\text{mm}^{-1})$	0.022

Table 4.2: Deposit parameters value.

Figure 4.17(a) presents the results of this calculation by showing the evolution of Gd (black curve) and Co (red curve) concentration as a function of the position on the CoGd wedge sample. While Figure 4.17(b) shows the variation of the thickness of the CoGd alloy.

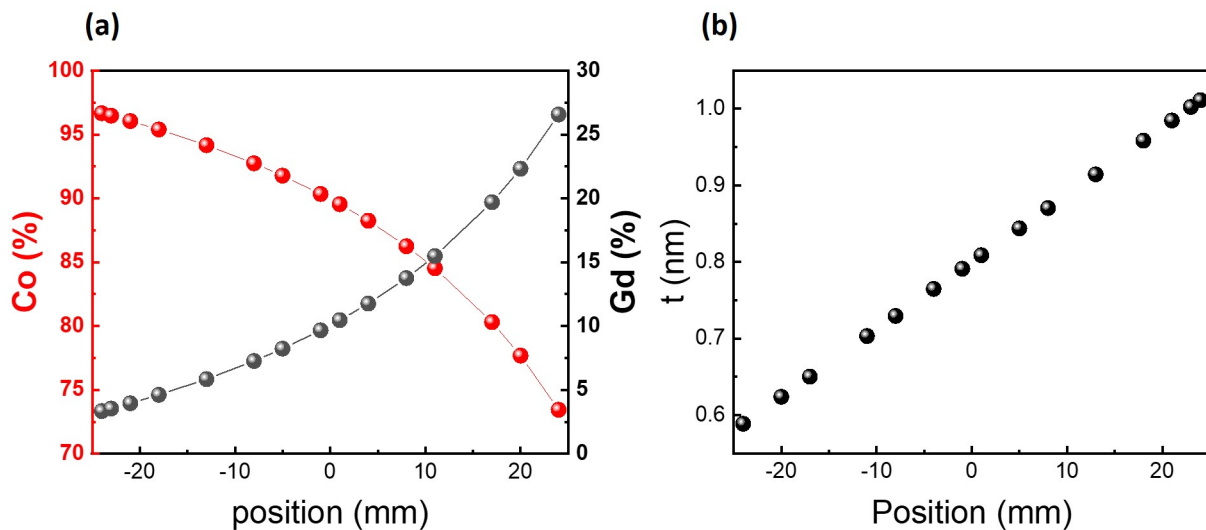


Figure 4.17: Evolution of the (a) Gd(Co) concentration and (b) the thickness of the CoGd alloy as a function of the CoGd-wedge position.

4.4.3 Magnetic characterization

To observe the magnetic behavior of the glass/Ta(3)/Pt 3.7)/CoGd(wedge)/Pt(3) (thickness in nm), we performed MOKE magnetometry measurements. The red and black curves in Figure 4.18(a) shows the hysteresis loop of $\text{Co}_{93}\text{Gd}_7$ and $\text{Co}_{75}\text{Gd}_{25}$, respectively. These measurements allow us to conclude that all the CoGd-wedge is Co-dominant and exhibited an out of plane

4.4. SINGLE THERMAL PULSE INDUCED AOS IN Pt/COGD(WEDGE)/Pt FULL FILM

magnetization. This result agrees with the recent investigation (2021) of J. wang et al.¹⁵⁸ who showed that for t below 2 nm and Gd(%) between 10% and 40%, all the $[\text{Pt}(2.0)/\text{Co}_{100-x}\text{Gd}_x(t)]_{\times 3}/\text{Pt}(2.0)$ samples have a Co-rich composition. Indeed, in the case of thinner CoGd alloy sandwiched by Pt layers, we should consider a proximity-induced magnetic moment in Pt which couple parallel with the Co. Thus, the net magnetization is given by: $M^{net} = M^{Co} - M^{Gd} + M^{Pt}$. In addition, the trend of the H_c in Figure 4.18(b) can be related to the behavior of the net magnetization. At low Gd concentration (below 10%), H_c is constant considering the fact that the Gd antiparallel moments do not affect the net magnetization of the stack much. Above 10%, the augmentation of H_c can be attributed to the decrease of the total magnetization of the stack, since H_c is inversely proportional to M^{net} . However, this hypothesis needs to be verified by performing VSM measurements on our CoGd wedge sample.

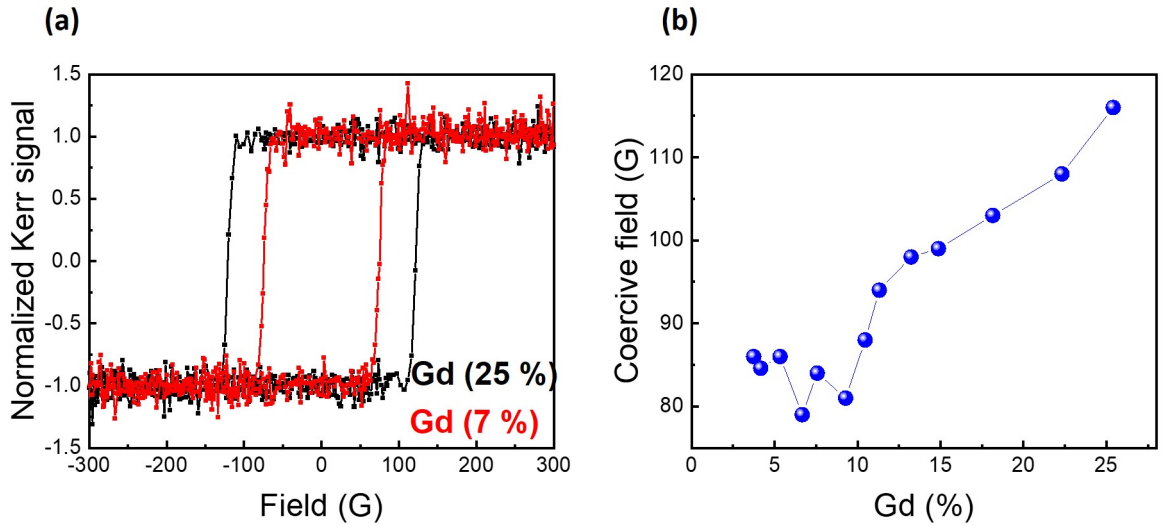


Figure 4.18: (a) Hysteresis loop for Pt/CoGd(wedge)/Pt stack for Co₉₃Gd₇ (red curve) and Co₇₅Gd₂₅ (black curve). Both curves show a Co-dominant stack with an OOP magnetization. (b) Evolution of the coercive field with the Gd concentration.

4.4.4 State diagram of Pt/CoGd (wedge)/Pt full film

In figure 4.19, we plotted the AO-HIS state diagram in a glass/Ta(3)/Pt(3.7)/Co₉₀Gd₁₀(0.8nm-at the center of the wedge)/Pt(3) (thickness in nm) stack, after a single laser pulse (linearly polarized) as a function of the laser pulse fluence and the Gd concentration. The dark blue circle (light blue triangle) and the light green square (dark green star) represent respectfully the switching fluence F_{Switch} and the demagnetization fluence F_{Demag} within switching (perfect

CHAPTER 4. GD EFFECT ON PT/CO/PT FERROMAGNET

toggle switching) regime. The switching regime is achieved for a Gd concentration below 4%. Whereas, for the perfect single pulse switching a threshold Gd concentration is observed at 7.5% to exhibit this state. The decrease of the threshold switching and the demagnetization fluence for Gd (%) above 10% can be attributed to the decrease of the Curie temperature due to the reduction of the net magnetization of the stack. Moreover, at this Gd percentage of 10%, the ratio F_{Demag}/F_{Switch} in the switching regime is equal to 2. This ratio value is in the same order of magnitude of those observed on (1.7) $Gd_{24}(FeCo)_{76}$ ferrimagnetic alloy and (3) $Mn_2Ru_{1.0}Ga$ Heusler ferrimagnetic alloy by J. Wei et al.⁵ and C. Banerjee et al.¹⁵, respectively. In the latter cases, the atomic compositions of the ferrimagnetic alloys are close to the compensation point.

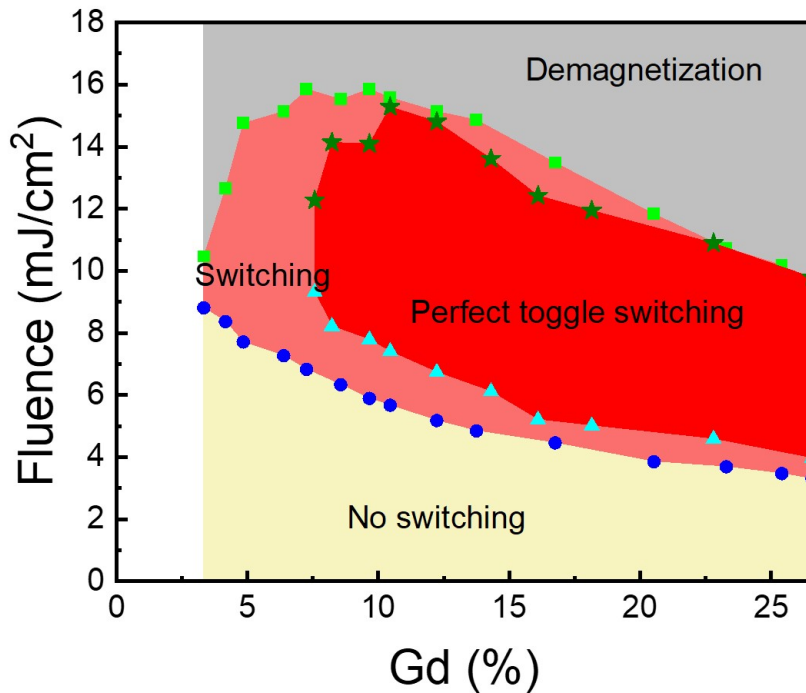


Figure 4.19: AO HIS state diagram realized on Pt/CoGd (wedge)/Pt full film. Magnetization behavior as a function of the Gd concentration, and the laser fluence F , for Linearly polarized static beam with $70 \mu\text{m}$ of laser diameter. The dark blue circle (light blue triangle) and the light green square (dark green star) represent respectively the switching fluence F_{Switch} and the demagnetization fluence F_{Demag} within switching (perfect toggle switching) regime. The pulse duration is 35 fs for all measurements.

4.5 Summary and discussion

In this chapter, we focused on the AOS properties of Co magnetization in Pt/Co/Pt tri-layer when we introduce a small amount of Gd at the two Co/Pt interfaces and in the Co layer itself, after the excitation of linearly polarized laser pulses.

For the Pt/Co/Gd stack, we clearly highlighted the necessity to separate the switching and the perfect toggle switching regime. In the case of the switching regime, a slow domain wall dynamic has been demonstrated by using two AOS experiments at a different rate repetition. Moreover, we demonstrated that we could reduce the Gd thickness from 3 nm (as initially reported in several works^{7,23,81,153} to 0.27 nm (approximately one Gd atomic plan) and still observe the perfect toggle switching mechanism. This experimental result demonstrates that the interfacial effect is the main effect responsible for the achievement of AO-HIS in Pt/Co/Gd stack. Indeed, one can imagine that at $t_{Gd} = 0.27$ nm, the induced magnetization in the Gd near the Co/Gd interface (due to the exchange interaction with the Cobalt) is enough to cause the reversal of Co magnetization near the interface. Then, the reversed Co magnetization propagates away from the interface driven by exchange scattering, as predicted by M. Beens et al²³ in 2019.

For Pt/Gd/Co/Pt stack, we demonstrated that the perfect toggle switching can be achieved down to 0.06 nm Gd thickness. Moreover, by plotting the magnetic state diagram (fluence vs pulse duration) for Gd thickness equal to 0.07 and 0.21 nm, we observed the same triangular switching window demonstrated previously in ferrimagnetic alloys. Remarkably, the less Gd we have inside the bottom Pt/Co interface, the higher the pulse duration maximum τ_{max} will be reached. Finally, for a Gd thickness around 0.3 nm, the Co magnetization goes in plane. For the Pt/CoGd/Pt stack, we have demonstrated that the perfect toggle switching state can be achieved down to 7.5% of Gd and the switching regime down to 4% of Gd.

Nevertheless, the above results raise several important questions: how such a small amount of Gd (0.06 nm) can induce all optical switching? can we reach higher τ_{max} with less Gd? how can the impact of the Gd depend so much on the interface (Pt/Co/Gd/Pt compared to Pt/Gd/Co/Pt)? how can we achieve AOS in GdCo alloy out of the compensation region? The two most surprising results are the demonstration of AO-HIS effect with a Gd thickness around 0.06 nm (If we consider the system as a CoGd alloy, we would have around 3% of Gd Concentration) at one interface and the switching of the CoGd magnetization alloy with less than 3% of Gd. This has never been observed in the case of GdCo or GdFeCo alloys and is in total disagreement with the phenomenological framework reproducing AO-HIS by considering angular momentum flow between the constituent sublattices and from the sublattices to the environment presented

CHAPTER 4. GD EFFECT ON PT/CO/PT FERROMAGNET

in C. S. Davies works^{3,159} and by a model using atomistic spin dynamics methods described in Jakobs article¹⁶⁰. Indeed in C. S. Davies works, the modelling predict AO-HIS for Gd concentration above only 20% and the maximum pulse duration reaching τ_{max} is less 0.5 ps for $x_{Gd} = 22\%$, while τ_{max} increases with x_{Gd} and reach a maximum $\tau_{max}=6$ ps close to compensation for $x_{Gd} = 26\%$. Very similar trend is obtained from the atomistic spin model described in Jakobs article. One could argue that we do not have a GdCo alloy but a Gd/Co bilayer system. Note that the value of the layer's nominal thickness and the cross section obtained by Scanning Transmission Electron Microscopy don't give credit to a sharp Gd/Co interface. However, the composition is certainly non-uniform, and a composition gradient is very likely. Nevertheless, we are not expecting that the GdCo concentration reach $x_{Gd} = 20\%$ anywhere in the sample. Note that Beens et al.²³ theoretically studied AO-HIS in Gd/Co bilayer systems and highlighted the effect of intermixing but in the intermix region the Gd concentration is quite high x_{Gd} equal to 50%.

Chapter 5

Size effect on Gd-dusted Pt/Co/Pt ferromagnet

5.1 Introduction

The objective of this fifth chapter is to investigate the size effect on Pt(3.7 nm)/Gd/Co(0.7 nm)/Pt(3 nm) that exhibited both PMA and single shot AO-HIS at room temperature in continuous full film. Indeed, according to the previous chapter, Gd dusting at the interface is sufficient to induce well define single pulse all optical switching. Thus, the study of the size effect on AOS in these new engineered materials will help us to characterize the magnetization reversal under the excitation of a femtosecond laser pulse. In addition, so far single pulse AOS of micro- and nano-scale patterns was reported only in ferrimagnetic GdFeCo and GdCo alloys (the reader can find all the investigations in section 1.5 and in Chapter 3). Here, we present a systematic study of the magnetization reversal of the studied sample disks whose diameter ranges from 3 μm to 400 nm with laser pulses. The effect of laser excitation was investigated in-situ using a polar MOKE microscope and the quantitative analyze of the switching probability were performed ex-situ by magnetic force microscopy. The variation of this switching probability with the disks size can be precisely measured and explained by a non-uniform switching process. Finally, the influence of the laser pulse duration and the laser helicity on the AOS in this range of disk size will be reported.

5.2 Structural, magnetic and all optical switching

5.2.1 Structural properties

The sample consisted of thin film of composition glass/Ta (3nm)/Pt(3.7 nm)/Gd(t_{Gd} nm)/Co(3 nm)/Pt(3 nm) presented in figure 5.1. The sample has been grown by magnetron sputtering on a glass substrate, the nominal thickness of the Ta, Pt, Co layer could be accurately controlled, but the amount of Gd dust could not be controlled. The Ta, Pt and Co layers can clearly be identified in the High-Resolution Transmission Electron Microscopy (HRTEM) image cross section shown in Figure ??(a). The Green, dark blue, light blue, and red rectangle in this HRTEM micrograph correspond to the region where we realized FFT pattern within Ta layer, lower Pt layer, upper Pt layer and all Pt/Gd/Co/Pt layers, respectively. The Ta buffer is amorphous and is illustrated by a diffusion picture with diffuse bands. The paired bright spot inside the dark blue rectangle is due to the crystal structure of the lower Pt layer in contact with Ta. This Pt crystallized gives the crystallographic direction [111] of the whole deposit. Showing that we did not lose the preferential [111] crystallographic orientation for weaker Gd thickness at the bottom Pt/Co interface. In addition, Energy-dispersive X-ray spectroscopy (EDXS) measurement (Figure ??(b)) was necessary to confirm the presence of Gd, to observe its position at the bottom Pt/Co interface and estimate a Gd net concentration of less than 2 or 3 % considering a GdCo alloy. This Gd estimation is based on the similarity between the AO-HIS and EDXS measurements of this sample with the Pt/Gd(0.07 nm)/Co/Pt stack reported in the previous chapter, but also to similar magnetic properties of the studied sample with a normal Pt/Co/Pt tri-layer, as we will see in the following paragraph.

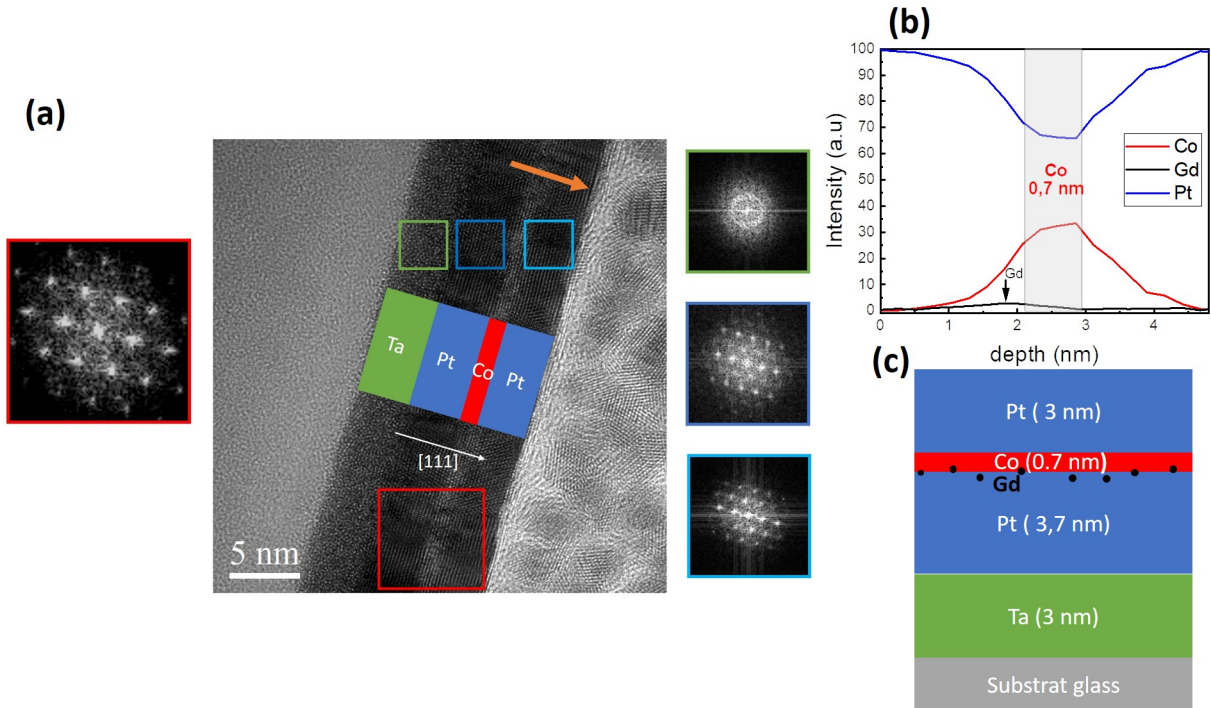


Figure 5.1: Characterization of the Glass/Ta(3nm)/Pt(3.7 nm)/Gd/Co(0.7nm)/Pt(3nm) stack. (a) HRTEM micrograph with the FFT electron diffraction pattern of the Ta layer (green rectangle), lower Pt layer (dark blue rectangle), upper Pt layer (light blue rectangle) and all Pt/Gd/Co/Pt layers (red rectangle). The crystallographic [111] direction remains unchanged despite the presence of a small amount of Gd in the bottom Pt/Co interface. (b) Intensity depth profile of Pt, Co and Gd using Energy-dispersive X-ray spectroscopy (EDXS) measurement performed along the orange arrow in (a). (c) Sketch of the heterostructure.

More structural characterizations have been performed on this sample. Indeed, Figure 5.2(a) and (b) illustrated two High Angle Annular Dark Field (HAADF)-STEM images of the stack, whereas the bright field (BF)-STEM image is displayed in Figure 5.2(c). All the namely layer Ta, Pt and Co are easily identified due to the different atomic numbers Z of each atom, resulting in different contrast in the images. Moreover, Figure 5.2(b) and (c) allows us to compare the HAADF and BF-STEM images of the same area of the stack. In fact, the four consecutive atomic planes are continuous from the buffer Ta (3 nm) layer to the capping Pt (3 nm) of the sample without deformations inside the Co (0.7 nm) layer in both STEM images. However, with a Gd thickness below the spatial resolution of the STEM mode (0.078 nm) it is not possible to observe the Gd dusting. This latter issue is confirmed by electron energy loss spectroscopy (EELS) measurements, displayed in Figure 5.2(d).

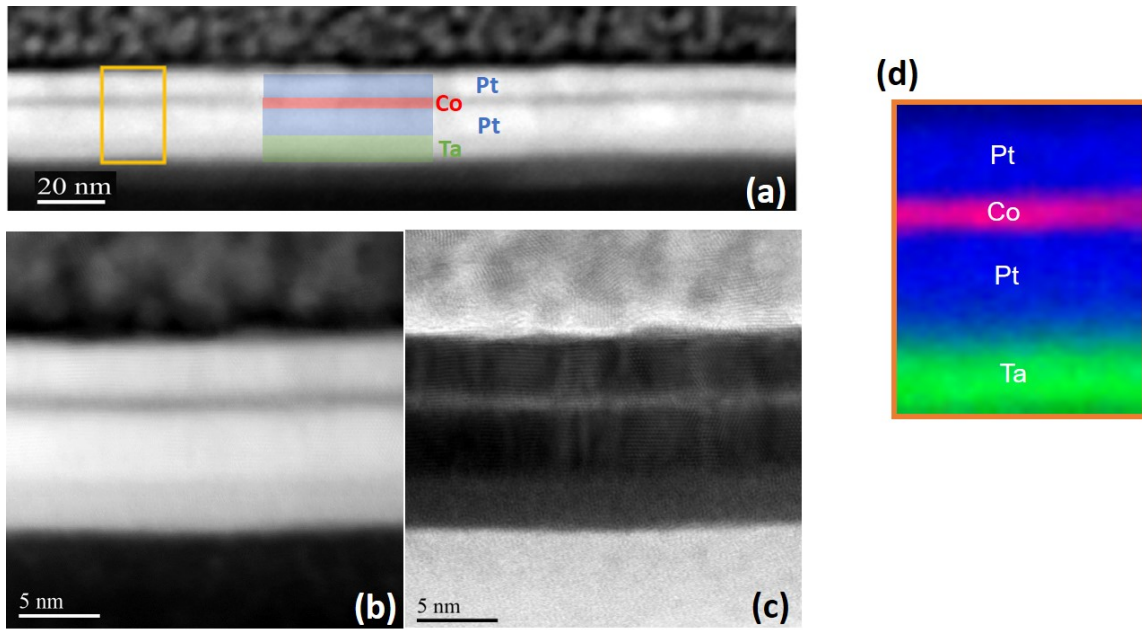


Figure 5.2: Characterization of the Glass/Ta (3 nm)/Pt (3.7 nm)/Gd/Co (0.7 nm)/Pt (3 nm) stack. (a) and (b) illustrate the HAADF-STEM images of the layered structure. While (c) show the corresponding BF-STEM image of (b). (d) EELS-STEM map depicting the elemental distribution of the stack: Ta (green), Pt (blue), and Co (red). The absence of Gd in (a), (b), (c), and (d) is due to the Gd thickness below the spatial resolution limit of the STEM.

5.2.2 Magnetic characterizations

To observe the magnetic response of the studied sample, we realized MOKE and vibrating sample magnetometry measurements. Figure 5.3(a) and (b) shows the evolution of the Normalized Kerr signal and magnetization with the applied magnetic field, respectively. Figure 5.3(a) illustrate a typical squared hysteresis loop for the magnetic field applied perpendicular to the sample's plane. The perpendicular magnetization anisotropy (PMA) present in this stack is due to the crystallographic preferential [111] direction¹⁶¹. Interfacial hybridization between the Co-3d and Pt-5d bands for Pt/Co/Pt tri-layer was also found to play an important role in the establishment of the PMA^{162–164} and in the induce of magnetic moment in Pt heavy metal¹⁶¹. In Figure 5.3(b), the response of the magnetization M under magnetic field IP (red curve) and OOP (black curve), allowed us to determine the effective saturation magnetization M_s . The latter value is obtained by performing the ratio between the measured saturation moment by the nominal Co volume in the film. Thus, a M_s equal to 1650 ± 50 kA/m is obtained for our studied sample. As this value is much higher than the magnetization of bulk Co (1420 kA/m), this measurement

5.2. STRUCTURAL, MAGNETIC AND ALL OPTICAL SWITCHING

highlights the contribution of Pt-induced magnetic moment parallel to the Co-sublattice. Moreover, a value very close to our M_s has been reported recently (2022) by Adriano Verna et al.¹⁵⁷ in Pt (3 nm)/Co (0.6 nm)/Pt (3 nm) tri-layer deposited on Ta (3 nm) buffer (1700 ± 50 kA/m). This similarity between these two M_s demonstrates the extreme low concentration of Gd within the sample, since the Gd-induced magnetic moment is antiparallel to the Co sublattice¹⁶⁵. Therefore, although the Gd thickness in this studied sample is not precisely determined, the results presented in the structural and magnetic characterization section, clearly justified the use of the term "Gd dusting" to describe the proportion of Gd at the bottom Pt/Co interface.

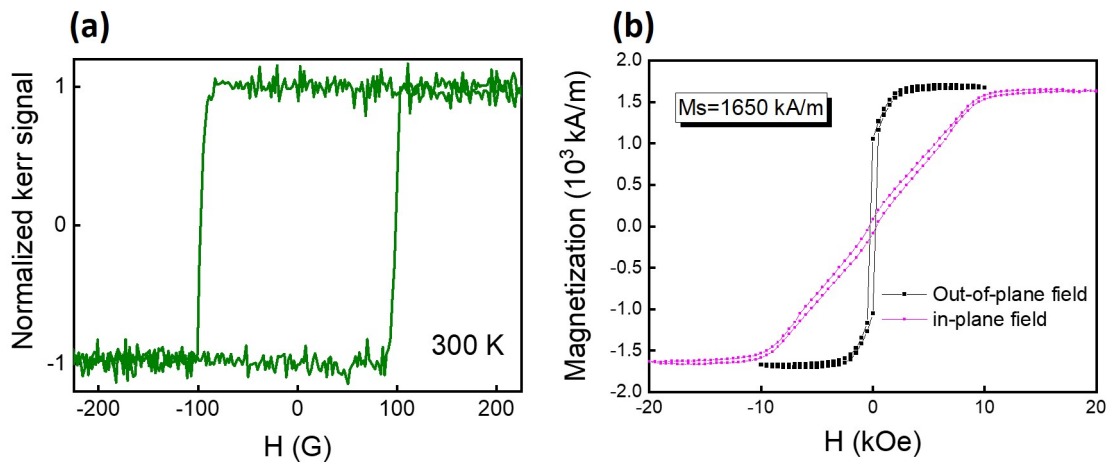


Figure 5.3: Out of plane hysteresis loop for Glass/Ta (3 nm)/Pt (3.7 nm)/Gd/Co (0.7 nm)/Pt (3 nm) stack performed through (a) MOKE magnetometry and (b) Vibrating Sample Magnetometer. All the measurements have been realized at room temperature.

5.2.3 AOS properties

The sample described above shows a strong Perpendicular Magnetic Anisotropy and magnetic properties very similar to the [Co/Pt] sample showing all optical switching properties. However contrary to the [Co/Pt] samples showing a multiple pulse, Helicity dependent magnetization^{35,69,166} (AO-HDS) with a very characteristic state diagram⁸⁷, the sample with a Gd dusting at the interface shows a clear single pulse AO-HIS switching as shown in figure 5.4(a). Indeed Figure 5.4(a) show the toggle switching of the magnetization in the studied sample regardless of the initial direction of the magnetization obtained after the irradiation of 5 consecutive linear laser pulses with a fluence of 11.9 mJ/cm^2 , a pulse duration of 35 fs and a laser beam diameter of $80 \mu\text{m}$. While the evolution of the magnetic state after the exposure of a single linear laser pulse

CHAPTER 5. SIZE EFFECT ON GD-DUSTED PT/CO/PT FERROMAGNET

is displayed in Figure 5.4(b). The AO-HIS magnetic state shows the variation of the threshold switching fluence F_{Switch} (blue disk) and the demagnetization fluence F_{Demag} (green square) as a function of the pulse duration. An example of variation of the switching domain size at a fixed fluence of 11.9 mJ/cm^2 is shown in Figure 5.4(c) as soon as we increased the pulse duration from 35 fs to 2.6 ps. These images show that we need more pulse energy for larger pulse duration. However, for a pulse duration value above the maximum τ_{max} (3.5 ps in this case) where we cannot achieve single thermal AOS, only multidomain state is observed, as depicted in Figure 5.4(d) for single shot at 4 ps of pulse duration.

These results confirm the observations from the AOS measurements in the previous chapter for the case of the Pt/Gd(wedge)/Co/Pt full film in which Gd is deposited at the bottom interface, showing that a tiny amount at the interface can induce single pulse AO-HIS. It has been shown that a thickness as small as 0.06 nm is sufficient to induce AO-HIS. In addition, two main reasons based on the magnetic state diagrams plotted in the previous chapter (section 4.3) suggest that in the studied sample of this chapter, the Gd thickness is lower than 0.06 nm. Firstly, the state diagram (Fluence vs Gd thickness) of the Gd bottom wedge indicate that even a thickness below 0.06 nm should also demonstrate AO-HIS with a constant switching window from 0.26 nm to 0.06 nm. Secondly, the increase of the maximum pulse duration from 1.6 ps at 0.21 nm of Gd thickness to 2.8 ps at 0.07 nm of Gd thickness suggest that less we have Gd at the bottom interface, higher would be τ_{max} . Thus, with a τ_{max} equal to 3.5 ps in the studied sample, the trends of τ_{max} with the Gd thickness also indicate that we should have a Gd thickness below 0.06 nm. In those structural, magnetic and AOS conditions the effective Gd concentration define as if you would view the Gd/Co bilayer as an alloy is much lower than for an alloy close to compensation concentration. Therefore, the sample studied in this chapter is the one showing an AO-HIS mechanism with an unprecedented concentration gap between the magnetic sublattices coupled by antiferromagnetic exchange.

5.3. AO-HIS IN NANOSTRUCTURES AT FEMTOSECOND PULSE DURATION

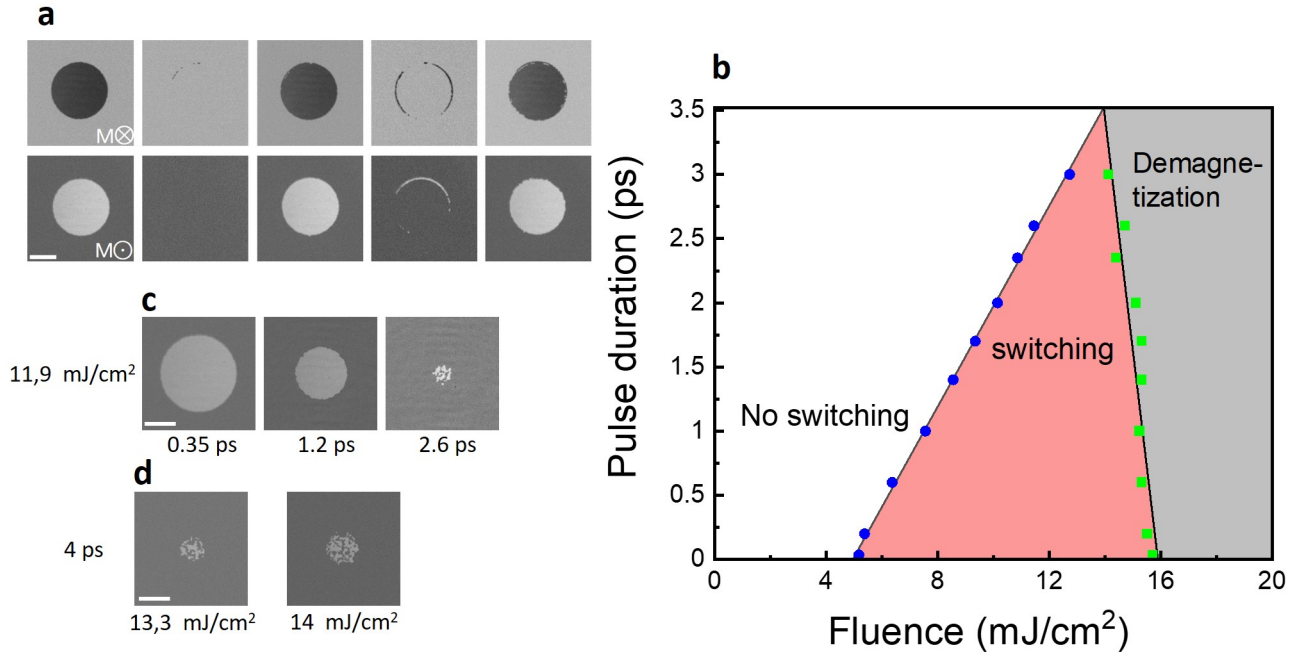


Figure 5.4: Magneto-optical images of Pt(3.7 nm)/Gd/Co(0.7 nm)/Pt(3 nm) full film obtained after the action of five consecutive single laser pulse of 35 fs. The dark grey (light grey) area represents the out of plane magnetization of the film pointing “up” (“down”) as represented by the circled disk (cross). Every single femtosecond pulse with a fluence of 11.9 mJ/cm² illuminates the same circular region of the full film and reverses the magnetization within it. b) AO-HIS state diagram realized by Varying the fluence and the pulse duration. The dark blue circle and light green square represent respectively the threshold switching fluence F_{Switch} and the demagnetization fluence F_{Demag} within switching state. These magnetic state diagrams were established by performing linear fits to delineate the switching region with no switching and multidomain state region. c) Size evolution of the switched domain with the pulse duration at a fixed fluence of 11.9 mJ/cm². d) Multidomain state obtained after the action of a single pulse at 4 ps of pulse duration with two different laser pulse fluence. In all the AOS experiments, the incident laser pulse is linearly polarized, and the laser diameter is 80 μ m. The length of the scale bar is 40 μ m.

5.3 AO-HIS in nanostructures at femtosecond pulse duration

5.3.1 Design of the patterned sample

To study the size effect, we fabricated arrays of magnetic disks with diameter ranging from 3 μ m down to 400 nm. The magnetic film has been processed by ion beam etching through an aluminum mask defined by electron-beam lithography and lift-off (see more details in section

CHAPTER 5. SIZE EFFECT ON GD-DUSTED PT/CO/PT FERROMAGNET

2.1.2). The remaining mask is subsequently removed by chemical etching. Several investigations in the literature reported that [Co/Pt]_N multilayers disks exhibit an out-of-plane magnetic anisotropy in the studied range diameter^{167–169}. Moreover, for each disk diameter D , areas of size $90\ \mu\text{m} \times 90\ \mu\text{m}$ were filled with identical disks on a square lattice. The gap between disks d , is fixed to $300\ \text{nm}$ (the lattice period is therefore not constant and equal to $D+d$). The effect of the excitation by $35\ \text{fs}$ laser pulses generated by a Ti-sapphire laser on the magnetic nanostructures was observed in-situ by MOKE microscopy and the quantitative analysis was carried ex-situ by scanning the exposed regions with a magnetic force microscope (The reader can find more details on image acquisition with these two microscopy techniques in the section 2.2.2.2). In addition, the laser beam diameter (FWHM) of $60\ \mu\text{m}$ was chosen to ensure a switching region smaller than the $90\ \mu\text{m}$ magnetic array area to be able to measure the switching domain of a single array of disks.

5.3.2 Single shot AO-HIS

Figure 5.5 shows the results of AO-HIS on arrays of Pt(3.7 nm)/Gd/Co(0.7 nm)/Pt(3 nm) disks initially saturated by a 1 T out of plane applied field. In this MOKE figure, dark and light grey areas correspond to disks magnetized up and down, respectively. After the excitation of the dark grey region with one pulse, one can see for all the disk sizes the formation of a light grey area (Figure 5.5(a-h)). While, after the exposure of two consecutive femtosecond laser pulses at a rate repetition of 5 kHz in an unexposed array of disks, all the disk size presents a dark grey area (Figure 5.5(i-p)). This latter MOKE contrast clearly demonstrate that the disks magnetization switched two time after the excitation with two consecutive pulses. These experimental results demonstrate the reversal of the magnetization for Pt(3.7 nm)/Gd/Co(0.7 nm)/Pt(3 nm) disks whose diameter ranges from $3\ \mu\text{m}$ to $400\ \text{nm}$ with $35\ \text{fs}$ linearly polarized laser pulses.

In addition, Figure 5.5 presents a constant trend of the switched domain size with the disk diameter for a given fluence. This behavior allowed us to conclude that optical or plasmonic effects are not dominant in this disk size range, contrary to the GdFeCo alloy case¹⁷⁰. On the other hand, after the irradiation of two pulses, a ring is formed. These rings are obtained for all sizes of disks and the thickness also varies very little with the size of the structures. These ring highlights that in an intermediate range of fluence between no effect and deterministic switching, the reversing presents a stochastic aspect. Theses aspects are beyond the scope of this work and in the following sections, we will focus our investigation on what happen in the center of the laser spot.

5.3. AO-HIS IN NANOSTRUCTURES AT FEMTOSECOND PULSE DURATION

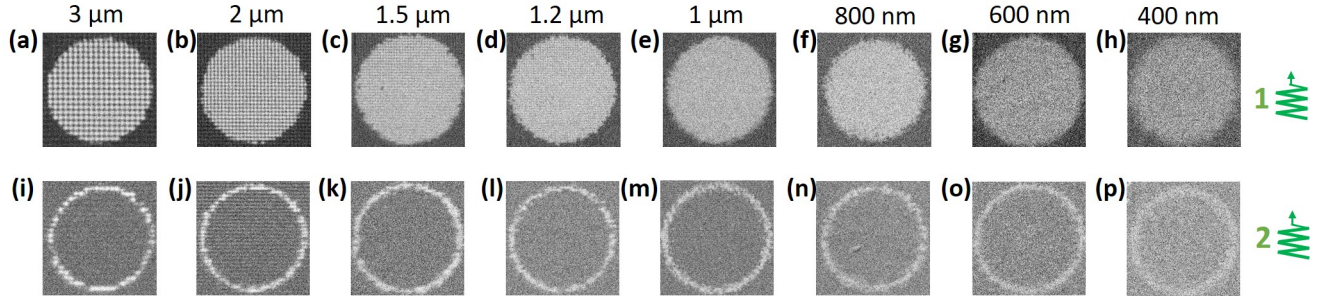


Figure 5.5: Magneto-optical images of magnetic disks made of Pt(3.7 nm)/Gd/Co(0.7 nm)/Pt(3 nm) obtained after the action of (a-h) a single and (i-p) two consecutive 35 fs linearly polarized laser pulses. For (a)-(h) ((i)-(p)) the light grey (dark grey) area represents magnetization of disks pointing “down” (“up”). Each laser pulse with a fluence of 9.2 mJ/cm^2 irradiates different array of the patterned structure.

5.3.3 AO-HIS as a function of the number of pulses

5.3.3.1 Kerr imaging

As demonstrated in the previous chapter, the number of pulses can be used to qualify the quality of the switching in a magnetic material. Indeed, we clearly demonstrate that the studied family sample present the perfect toggle switching mechanism, since after the exposure of 10 000 femtosecond pulses at a rate repetition of 5 kHz on the surface of the sample, the toggle switching is maintained. We therefore decided to carry out the same type of experiment at different disk sizes by changing the number of pulses at a rate repetition of 5 kHz using a MOKE microscope. Figure 5.6 presents the magnetic state of the Gd dusting sample disks after excitation with 1, 2, 3, 599 and 600 femtosecond laser pulse at a fixed fluence of 9.2 mJ/cm^2 . Initially, all the patterned areas were saturated with a 1 Tesla magnetic field, situation analog to Figure 5.5. Consequently, the light and dark grey area observed at the center of each MOKE image shows the reversal of the magnetization in one of the possible magnetization orientations (up and down).

Qualitatively, we distinguish two magnetic behaviors as a function of the disk size and the number of pulses. For bigger disks (above $1.5 \mu\text{m}$) the switching of the magnetization is maintained for all the number of pulses used. Whereas, for smaller disks (less than $1.5 \mu\text{m}$), the switching slowly degrades as we decrease the size of the disks and increase the number of pulses. Moreover, as mentioned in the previous paragraph, the switched domain size is constant and the formation of rings is visible for 2, 3, 599 and 600 pulses. But the main difficulty in further analyzing this AOS experiment with our Kerr imaging setup is due to the onset of the diffraction

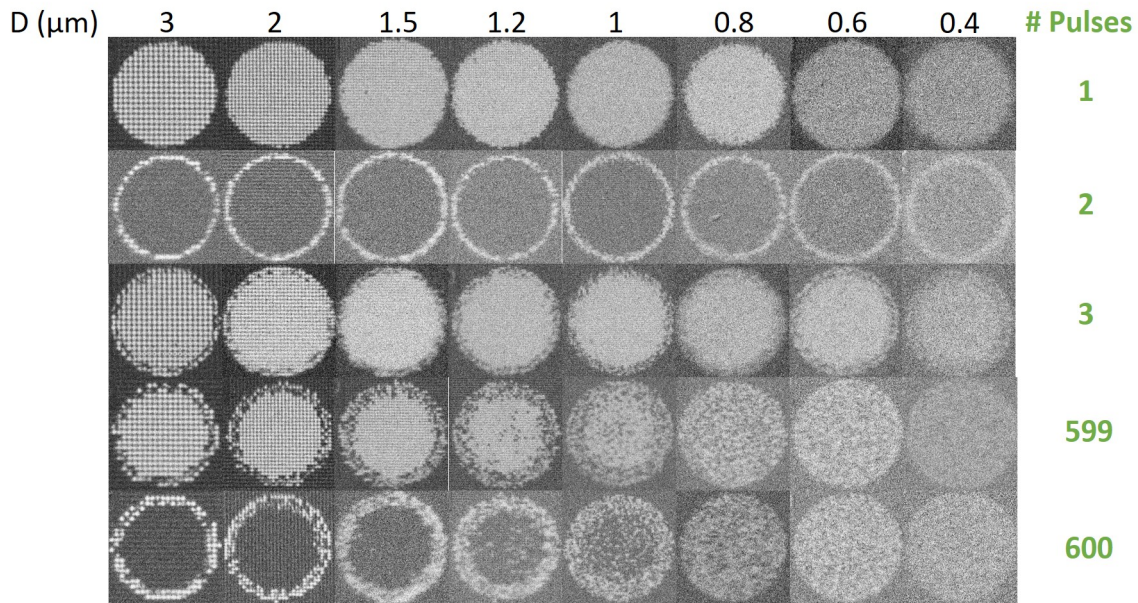


Figure 5.6: Magneto-optical images of magnetic disks made of Pt (3.7 nm)/Gd/Co (0.7 nm)/Pt (3 nm) obtained after the action of 1, 2, 3, 599 and 600 consecutive 35 fs linearly polarized laser pulses. The light grey (dark grey) area represents magnetization of disks pointing “down” (“up”). Each laser pulse with a fluence of 9.2 mJ/cm^2 irradiates different array of the patterned structure.

phenomenon, which occurs when the size of the object being studied is of the order of magnitude of the wavelength of the probe radiation (the reader can find a brief discussion about this MOKE imaging limit in paragraph 2.2.2.2). Nevertheless, these MOKE images help us to limit the study of the size effect on this engineered material to disk diameters smaller than 1.5 microns, because beyond this size the behavior of the disk magnetization is quite similar to the full film.

5.3.3.2 MFM imaging

To perform more qualitative and quantitative analysis, we need to see the magnetic state of individual nanostructure in each array. Therefore, we scanned all the exposed region with MFM after the AOS experiment initially realized in the laser room. Figure 5.7 shows the corresponding magnetic force microscopy mapping for an array of 1 μm , 800 nm, 600 nm, and 400 nm disks diameter after exposure to a single laser pulse. The light contrast of disks located mainly at the edges of the MFM images are those that have not been magnetically altered by the laser pulse. While the dark contrast disks located principally in the center of the MFM image represent structures with a magnetization totally reversed by the laser pulse excitation (More details on the interpretation of the MFM contrast have been provided in section 2.2.3).

5.3. AO-HIS IN NANOSTRUCTURES AT FEMTOSECOND PULSE DURATION

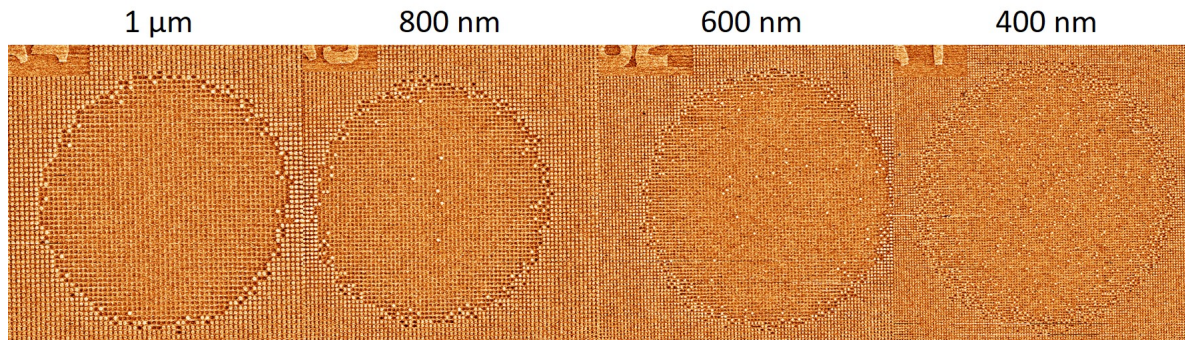


Figure 5.7: MFM mapping of 1 μm , 800 nm, 600 nm, and 400 nm diameter disks array after exposure to a single laser pulse. The dark contrast corresponds to the reversed disks. The field of view is 80 μm for all MFM images.

Those MFM images shows that all the exposed nanostructures are monodomains and as the size of the disks decreases, the proportion of unswitched increases. Consequently, the loose of the switching state for smaller disks for a higher number of pulses at 5 kHz of rate repetition observed in MOKE images is strongly related to the disk dimension. Thus, as 100% switching is not achieved with a single pulse for nanostructures, the proportion of unswitched disks will increase with the number of pulses, as confirmed in Figure 5.8. This Figure shows the corresponding magnetic force microscopy mapping for an array of 800 nm disks after exposure to 1, 2, 3, 599 and 600 consecutive laser pulses.

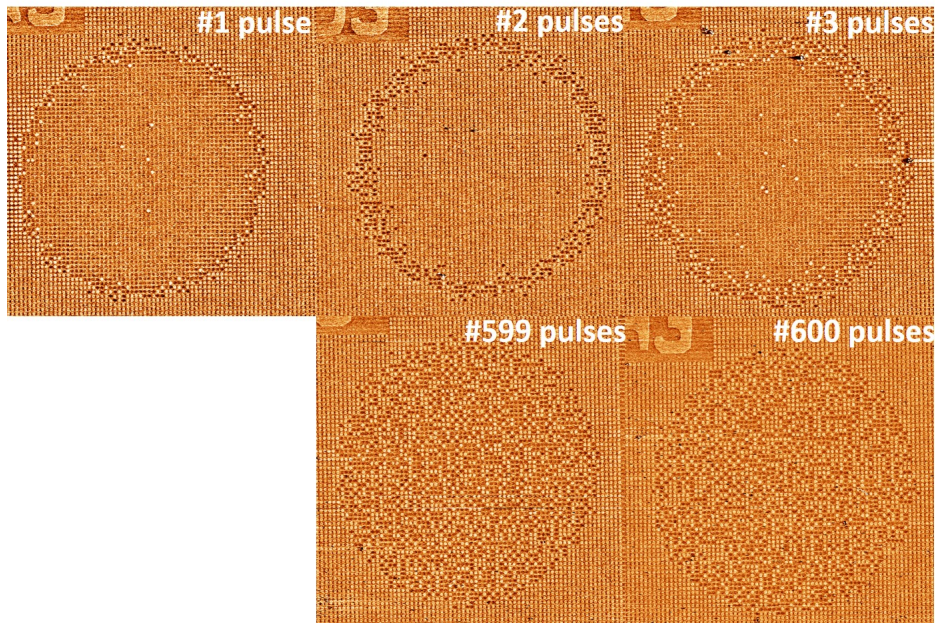


Figure 5.8: MFM mapping of 800 nm diameter disks array after exposure to 1, 2, 3, 599 and 600 consecutive laser pulses. The dark contrast corresponds to the reversed disks. The field of view is 80 μm for all MFM images.

5.3.3.3 Quantitative analysis

After extracting the contrasts from the MFM maps of disk arrays (all the different steps of contrast extraction using the Wolfram Mathematica 11 software are presented in paragraph 2.2.3.2), we proceeded to the quantitative analysis of the proportion of switched structures, or in fact here the resulting magnetization (between -1 and +1). Moreover, this analysis requires considering the intrinsically inhomogeneous profile of the beam. The first step is to locate a posteriori the center of the beam in the corresponding numerical image of the MFM maps. In the case of single domain configurations, the center of the beam can be simply considered as the barycenter of the switched disks. As for the determination of the switching ratio as a function of the distance to the center, it is hampered by the finite number of elements considered and therefore by an intrinsic statistical dispersion. Figure 5.9(a) represents an example of the normalized magnetization profile as a function of the distance to the center by "integrating" on circular rings of several thicknesses for a switching radius around 30 μm . Obviously, a compromise must be found between the amplitude of the statistical fluctuations and the spread of the spatial variations, particularly visible in the 20-30 μm zone. Another solution is to work with a constant number of disks (or constant crown area). As shown in the Figure 5.9(b), this approach allows a better

5.3. AO-HIS IN NANOSTRUCTURES AT FEMTOSECOND PULSE DURATION

description of the 20-30 μm zone but does not allow the description of the zone closest to the center. Thereafter, we will favor a "mixed" approach by integrating both a maximum thickness criterion for the crown (10 μm) and a maximum number of disks (400). Figure 5.9(c) allowed us to compare this approach with previous ones.

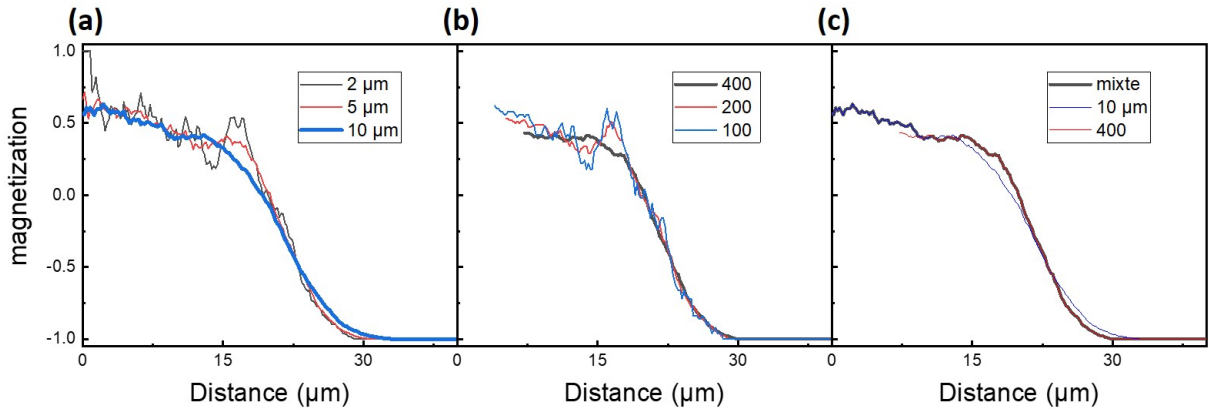


Figure 5.9: Radial profile of a AOS experiment realized by integrating on (a) different circular rings thickness, and on (b) constant number of disks. (c) mixed approach of (a) and (b).

By performing the previous data processing on the MFM maps corresponding to the MOKE images in Figure 5.6, we obtained the radial switching profiles for this AOS experiment. Figure 5.10 represents the radial switching profiles of a set of disks whose diameter is between 1.5 μm and 400 nm for several laser pulses equal to 1, 2, 3, 599 and 600. This figure confirms the behavior of the switched domain size with a diameter average of $40 \pm 1 \mu\text{m}$ for the single pulse excitation. Moreover, Figure 5.10 show the presence of a constant switching area of $36 \pm 1 \mu\text{m}$ around the exposed region center. The difference of the magnetization behavior between the latter area is due to the reduction of the fluence as soon as we move away from the laser beam center (due to the gaussian spatial distribution of the laser). In the following, we will focus only on the constant switching area.

5.3.3.4 Toggle switching probability

Let us first introduce the notations and the two assumptions that we done in this section. Indeed, we considered two equivalent directions of disks magnetization (no external magnetic field, or effect of light polarization), and no interaction between disks. Then, we note m_i the average magnetization of an assembly of disks after i pulses. In the case of a perfect toggle switching

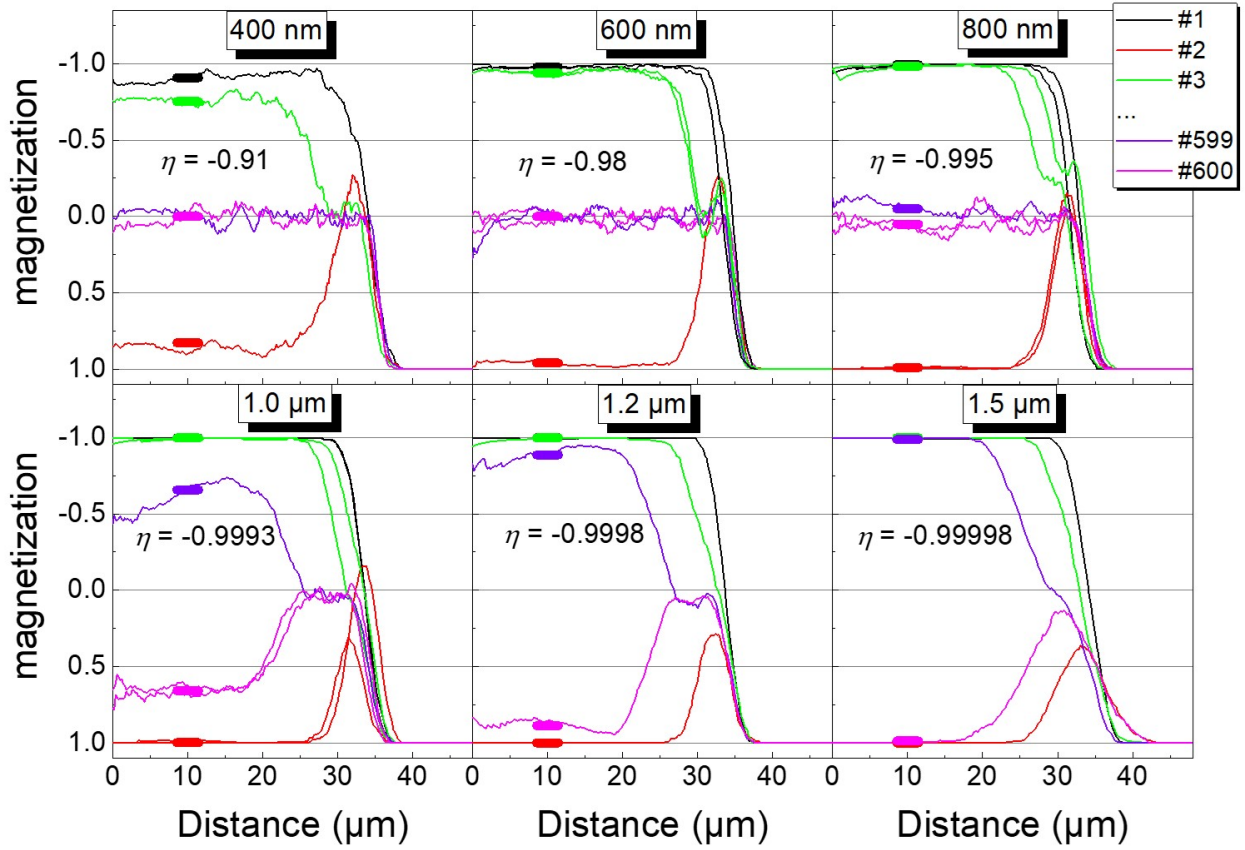


Figure 5.10: Radial switching profiles of magnetic disks made of Pt (3.7 nm)/Gd/Co (0.7 nm)/Pt (3 nm) obtained after the action of 1 (black curves), 2 (red curves), 3 (green curves), 599 (blue curves) and 600 (magenta curves) consecutive 35 fs linearly polarized laser pulses.

(starting from a configuration $m_0 = +1$), we have:

$$m_1 = -1, m_2 = 1, m_3 = -1, \dots, m_i = (-1)^i \quad (5.1)$$

Nevertheless, in the general toggle switching case, the probability of reversal after a pulse is independent of the magnetic state and can be written as $\frac{1}{2}(1 - \eta)$:

- $\eta = -1$ corresponds to perfect toggle switching,
- $\eta = 0$ corresponds to a completely random demagnetization process and
- $\eta = +1$ corresponds to no toggle switching.

η is directly the correlation coefficient between the magnetic states of a nanostructure between two pulses. Then, the average magnetization after the first pulse (starting from a configuration

5.3. AO-HIS IN NANOSTRUCTURES AT FEMTOSECOND PULSE DURATION

$m_0 = +1$) is $m_1 = \eta$. After the second pulse, $m_2 = \eta^2$ and in general $m_i = \eta^i$ (it must be stressed that these relationships are only true within the constant switching area and more details of the calculation are contained in ANNEX A). Therefore, by using several numbers of laser pulses, it is possible to determine η for the different disks size, as can be seen in Figure 5.10. It is remarkable that this rate varies over almost four orders of magnitude. Finally, Figure 5.11 shows the exponential evolution of the toggle switching (it's more like the non-switching rate $-\eta$) with the magnetic disk diameter. This exponential size dependence is remarkable because it is unusual in magnetism. Indeed, this has nothing to do with the size dependencies observed in disk systems of perpendicular anisotropy^{167,171}. Several phenomena could be involved in the observation of this remarkable behavior. The aims of the next section will be to discuss the different possible switching models.

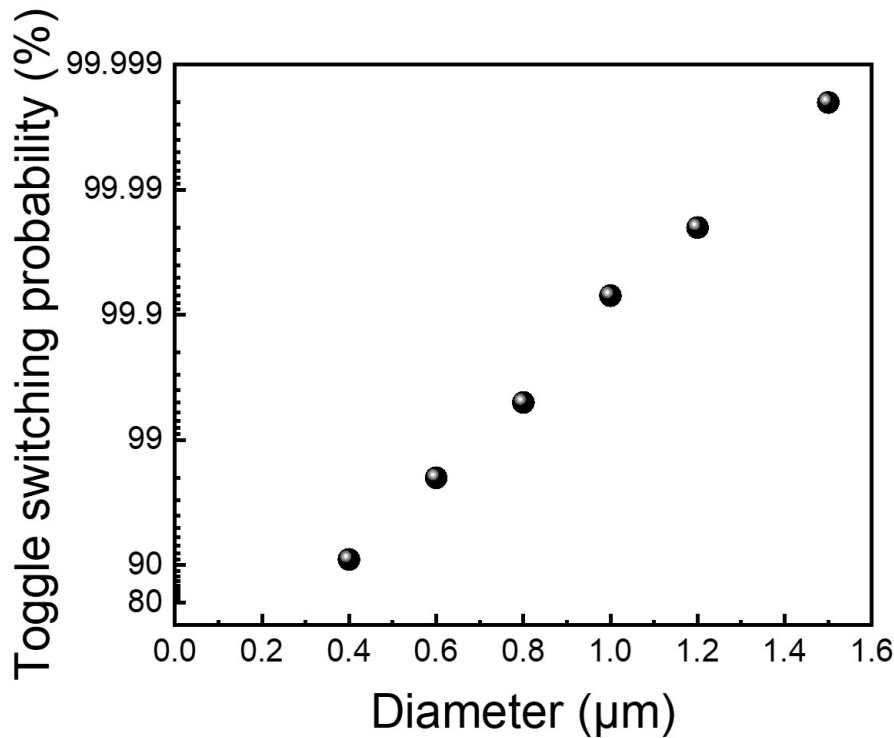


Figure 5.11: Variation of the toggle switching probability with the disk diameter in Pt (3.7 nm)/Gd/Co (0.7 nm)/Pt (3 nm) heterostructure.

5.4 Modeling of all-optical switching in nanostructures

The demonstration of the magnetization reversal of full film, micro and nanostructures for the studied engineered ferromagnet by laser pulses linearly polarized, allows us to conclude that the switching mechanism is due to purely thermal effects. In this section, two possible models to understand the behavior of the toggle switching probability with structures size will be presented: (i) a thermal activation process, (ii) inhomogeneous reversal.

5.4.1 Thermal activation

Generally observed on elements as large as ours^{171,172}, thermal activation process is possible after switching. Consider the very simplistic assumption that the thermal activation phenomenon with a characteristic time τ takes place after inversion, at a constant temperature T for a time t . The effective switching rate after perfect reversal would then be of the form (more details of the calculation are contained in ANNEX A):

$$\eta = -e^{-\frac{2t}{\tau}} \quad (5.2)$$

(τ converges to 0 when thermal activation is predominant). Given the high reversal rates observed experimentally, this would correspond to small process times in front of the characteristic time ($\frac{t}{\tau} = 5.10^{-3}$ for the highest value). Moreover, If the characteristic time is related to the thermal activation above a single potential barrier, it can be written as an Arrhenius law¹⁷³:

$$\tau = \tau_0 e^{\frac{\Delta E}{K_B \cdot T}} \quad (5.3)$$

By using equation 5.2 and 5.3, it is possible to relate the barrier height directly to the experimental fall rate:

$$\frac{\Delta E}{K_B \cdot T} - \ln \frac{2t}{\tau_0} = -\ln(-\ln(-\eta)) \quad (5.4)$$

This quantity is shown in Figure 5.12. The remarkable linear evolution of the energy barrier with the diameter observed in Figure 5.12, indicate that in our studied structures, the reversal occurs by nucleation followed by domain wall propagation. This type of switching is coherent with the size range of the studied structures. Indeed, in ultra-thin film structures with perpendicular magnetization, two types of thermally activated magnetization reversal can be achieved, depending on the size¹⁷²:

- A coherent magnetization rotation for which the barrier height is proportional to the square of the diameter (for structures size below the critical diameter d_c^*).

* d_c (about ten nanometers) is the diameter where the domain wall energy becomes less than the energy barrier

5.4. MODELING OF ALL-OPTICAL SWITCHING IN NANOSTRUCTURES

- A nucleation and domain wall propagation reversal process of the magnetization for which the barrier height depends linearly on the diameter (for structures size above d_c).

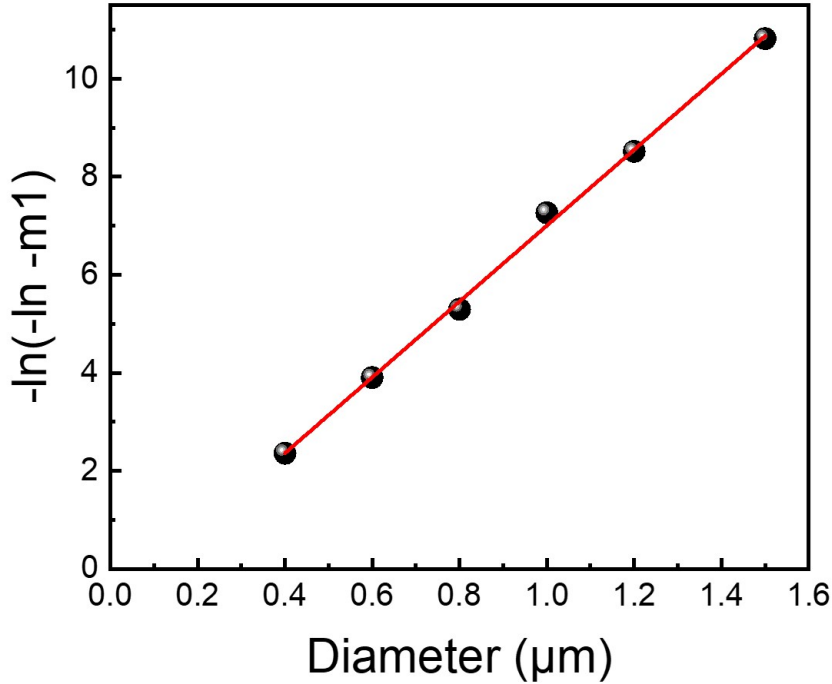


Figure 5.12: Variation of the energy barrier ΔE with the disk diameter in Pt (3.7 nm)/Gd/Co (0.7 nm)/Pt (3 nm) heterostructure.

Then, if we consider that $\frac{t}{\tau_0}$ is independent of size, we determined the coefficient of the barrier height $\Delta E/K_B.T$ equal to $7.7 \mu\text{m}^{-1}$. According to micromagnetic simulations (Performed by Francois Montaigne), the linear wall energy ΔE is of the order of $10^{-17} \text{ J}.\mu\text{m}^{-1}$. Therefore, $K_B.T=1.32 \cdot 10^{-18} \text{ J}$ and we deduce an estimated temperature of 10^5 K invalidating the thermal activation hypothesis.

5.4.2 Analytical and micromagnetic simulations approach

We will show that this size dependence can in fact be explained by an inhomogeneous optical reversal. Let us assume that the reversal is intrinsically an inhomogeneous process with the possibility of switching, or not, locally, at the scale of an elementary volume (typically of the order of the coherent reversal). This diameter depends on the square root of the ratio of the exchange constant and the effective anisotropy.

CHAPTER 5. SIZE EFFECT ON GD-DUSTED PT/CO/PT FERROMAGNET

of d_c). It can then be envisaged that after an initial demagnetization-switching phase, the largely inhomogeneous magnetic structure evolves towards a monodomain magnetic configuration, the direction of which depends on the proportion of elementary volumes that have been switched or not. The greater the number of elementary volumes, the greater the probability of reversal, like the Condorcet jury theorem. In this case, there would be a microscopic probability of reversal η' , independent of the size of the plot, which would translate into a macroscopic probability η depending on the number of consequent elementary volumes and thus on the size of the plot. If we consider that the symmetry breaking induced by the initial imbalance fixes the final configuration, we have a "majority judgment" type of evolution and the macroscopic probability for N elementary domains (N odd) is given by:

$$\sum_{i=0}^{\frac{N-1}{2}} \binom{N}{i} ((1 + \eta')^{N-i}(1 - \eta')^i - (1 + \eta')^i(1 - \eta')^{N-i}) \quad (5.5)$$

Figure 5.13(a) shows the variation of this law for elementary domains of size equal to 16 nm^2 for η' values of -0.013 and -0.02. If the increase of the switching rate with size is well reproduced by this hypothesis, the variation obtained is much "faster" than the experimental variation observed.

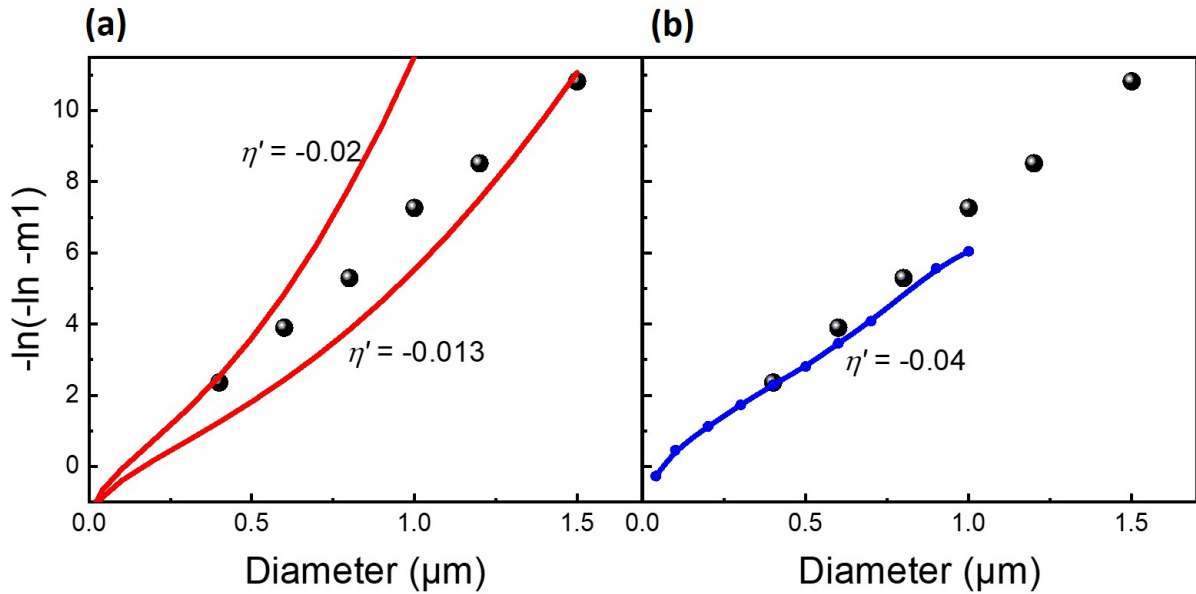


Figure 5.13: Evolution of the toggle switching (black disks) compared with (a) a simple probabilistic model analog to Condorcet's jury theorem represented by the red curves for η' equal to -0.013 and -0.02, and (b) micromagnetic simulations represented by the blue curve for η' equal to -0.04.

However, the process of "re-magnetization" is much more complex than a simple "majority

5.5. AO-HIS IN NANOSTRUCTURES AT PICOSECOND PULSE DURATION

judgment". Indeed, a magnetic disk that presents a multidomain configuration with a non-zero magnetization in one direction may very well relax to a monodomain configuration of opposite magnetization. It is then essential to consider the micromagnetic aspects and more particularly the topology of the walls. Thus, we have performed micromagnetic finite difference simulations. The effect of the laser pulse is simulated by a random initial configuration where the magnetization of each cell is fixed at ± 1 . Assuming a homogeneous configuration before the pulse at $+1$, the probability for a given cell to be at -1 is given by $\frac{1}{2}(1 - \eta)'$. This initial configuration is then relaxed until the single-domain state is obtained and the calculation is repeated many times to derive the macroscopic value η . Figure 5.13(b) shows the expected evolution for a cell size of $4 \times 4 \text{ nm}^2$ and a value $\eta)'$ equal to -0.04 . This figure shows that a highly non uniform switching process with a microscopic switching probability explains our experimental data.

5.5 AO-HIS in nanostructures at picosecond pulse duration

As already highlighted in section 4.3.3.2 and 5.2.3, the pulse duration is one of the degrees of freedom to characterize all optical switching in magnetic materials. In the previous section, all AOS experiments were performed with 35 fs laser pulses. Although the magnetic state of the studied sample has already been presented in Figure 5.4 with few MOKE images at high pulse duration, the aim of this section is to investigate further the magnetization behavior of the full film and of the nanostructures after the excitation of picosecond laser pulses. We will show that the single shot AO-HIS is no longer perfect at this pulse duration scale and the reduction of the disks size will induce a decrease of the switching rate, as also observed at 35 fs.

5.5.1 Single shot AO-HIS

Figure 10 shows the results of AO-HIS on Pt (3.7 nm)/Gd/Co (0.7 nm)/Pt (3 nm) full film, initially saturated out of plane with a magnet. In this MOKE images, dark and light grey areas correspond to the magnetization pointing up and down, respectively. In the case of linearly polarized pulses with 2 ps of pulse duration, Figure 5.14(a) presents a toggle switching of the magnetization obtained after the irradiation of two consecutive linear laser pulses with 1 s between pulses and a fluence range from 10.7 to 16 mJ/cm². Due to the gaussian laser distribution of the laser, the size of the switched domain increase with the augmentation of the fluence. The observation of the switching state in this fluence range and at 2 ps agrees well with the state diagram in Figure 5.4. However, regardless of the fluence magnitude, the switched domain is inhomogeneous with the presence of small unswitched domains inside the exposed area. The

CHAPTER 5. SIZE EFFECT ON GD-DUSTED PT/CO/PT FERROMAGNET

latter inhomogeneity is reinforced as soon as we continue to extend the pulse duration to 2.5 ps, as can be seen in Figure 5.14(b) when we exposure two consecutive laser pulses with a fluence of 12.8 mJ/cm^2 onto the initially saturated study sample in the same direction as the AOS 2 ps experiment. The consequence of this high inhomogeneity at long pulse duration within switching domain will be the loss of the switching state after several pulses, as demonstrated in paragraph 4.2.4.1 when we defined the different AO-HIS regime. Finally, this result is in good agreement with the magnetic state diagram realized on Pt (3.7 nm)/Gd (0.07 nm)/Co (0.7 nm)/Pt (3 nm) full film and displayed in section 4.3.3.2. Indeed, the latter diagram showed that the maximum pulse duration τ_{max} value where we can still achieve perfect toggle switching is equal to 1.8 ps.

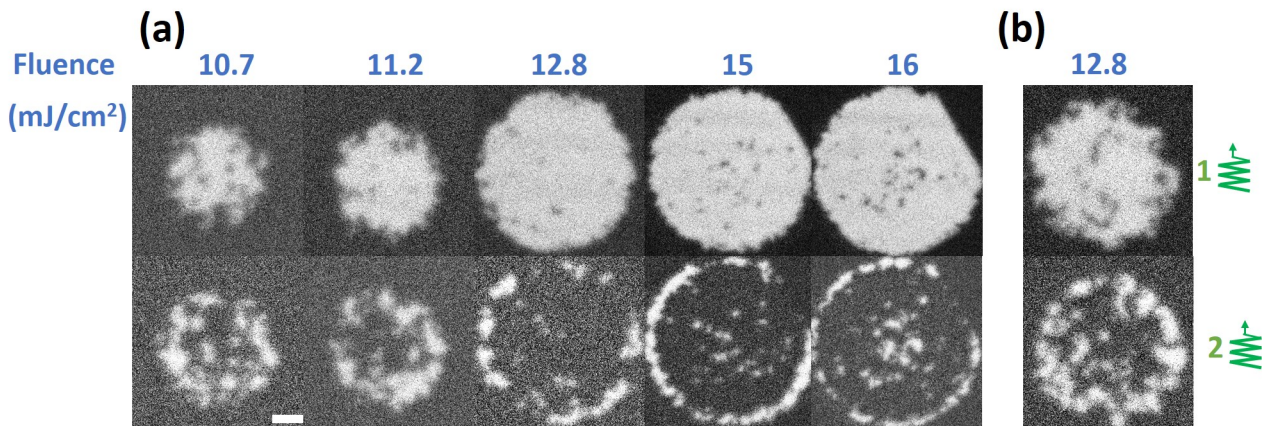


Figure 5.14: Magneto-optical images of Pt (3.7 nm)/Gd/Co (0.7 nm)/Pt (3 nm) full film obtained after the action of two consecutive single laser pulse of (a) 2 ps and (b) 2.5 ps. The dark grey (light grey) area represents the out of plane magnetization of the film pointing “up” (“down”) as represented by the circled disk (cross). The AOS experiments were performed for a fluence range from 10.7 to 16 mJ/cm^2 and an inhomogeneous switching domains are observed. The length of the scale bar is $40 \mu\text{m}$ and the laser beam diameter is $70 \mu\text{m}$.

5.5.2 AO-HIS as a function of the number of pulses and light polarization

The study of the AO-HIS by varying the number of pulses allowed us to characterize the quality of the switching in Chapter 4. But it was also instrumental in demonstrating the non-uniform switching process exhibited by the studied sample in the case of 35 fs incident laser pulses (section 5.3.3). Consequently, we performed the same type of measurement at $1 \mu\text{m}$, 800 nm , 600 nm , and 400 nm disks and by shifting the number of pulses at a rate repetition of 5 kHz. The reduction in the range of the disk diameter compared to the previous section fine is justification

5.5. AO-HIS IN NANOSTRUCTURES AT PICOSECOND PULSE DURATION

to the introduction of another parameter of AOS: the laser polarization. Indeed, Figure 5.15 presents the magnetic state of the 1 μm disks after excitation with 1, 2 and 600 picosecond laser pulse at a fixed fluence of 11 mJ/cm^2 for left, right circular and linear polarization. Initially, all the patterned areas were saturated with a 1 Tesla magnetic field in the opposite direction of the situation of Figure 5.14 and 5.6. Therefore, the dark contrast of disks located mainly at the edges of the MFM images are those that have not been magnetically altered by the laser pulse. While the light contrast disks located principally in the center of the MFM image represent structures with a magnetization reversed by the laser pulse excitation.

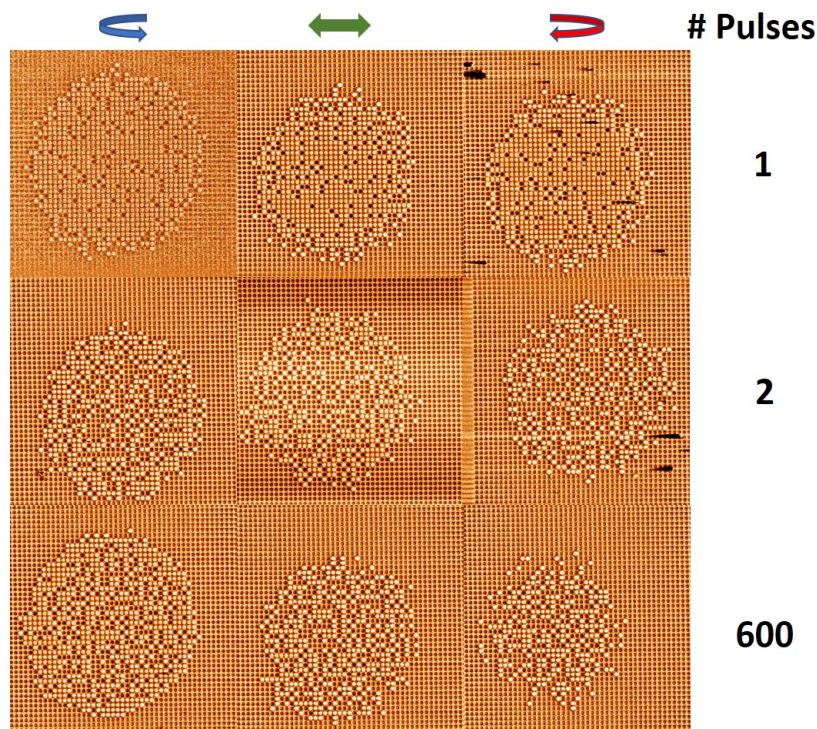


Figure 5.15: MFM mapping of 1 μm diameter disks array after exposure to 1, 2 and 600 consecutive laser picosecond pulses with the circularly left (blue circle), right (red circle) and linearly (green arrow) polarized light. The light contrast corresponds to the reversed disks. The field of view is 80 μm for all MFM images.

These MFM scans show that the exposed structures are monodomains and the number of switched disks after the irradiation of a pulse is similar regardless of the polarization of the laser pulses. For 2 and 600 picosecond incident laser pulses, it is more complicated to analysis the switching or even to conclude whether we have a helicity effect on the reversal. A careful quantitative approach is necessary to continue the description. However, the higher number of unswitched disks in this case of long pulse duration is not related to the size of the disk, or to the

helicity of the light but is coherent with the inhomogeneous switched domains observed on full film (see Figure 5.14). Therefore, the loose of the switching state for a higher number of pulses (600) at 5 kHz of rate repetition observed in MFM images is strongly related to the degradation of the AO-HIS at 2 ps. It should be emphasized that this behavior has been observed for other nanostructure sizes, as will be shown in the next paragraph using radial profiles.

5.5.3 Preliminary quantitative analysis

By realizing the data processing explained in paragraph 5.3.3.3, we obtained the radial switching profiles of the MFM images of Figure 5.15. Figure 5.16 shows the result of this operation with the behavior of m (average magnetization) as a function of the structures position. Indeed, for a radius below $15 \pm 1 \mu\text{m}$, indicated by the yellow rectangle, the reversal of the magnetization with a picosecond pulse is independent of the laser polarization. Moreover, in this region near the center of the laser spot, whatever the helicity of the light, m is negative for two incident pulses, indicating that most of the structures switched back. For 600 circularly right and linearly polarized pulses, m reaches a permanent state where there is an equal probability of switching in both directions (up and down). While for 600 circularly left polarized pulses, m is close to zero, but it remains positive. For a radius between $15 \mu\text{m}$ and $30 \mu\text{m}$, indicated by the light blue rectangle, we clearly see a dependence on the trends of m with the light helicity. This helicity-dependence is enhanced for 600 laser pulses, as illustrated at $r = 20 \mu\text{m}$, where m equal to 0.5, -0.85, -0.3 for the circularly left, right, and linearly polarized light, respectively. In sum, qualitatively, we find in this region the multiple pulses helicity-dependent AOS characteristic of a Pt/Co/Pt ferromagnet^{35,69,82,87,174}.

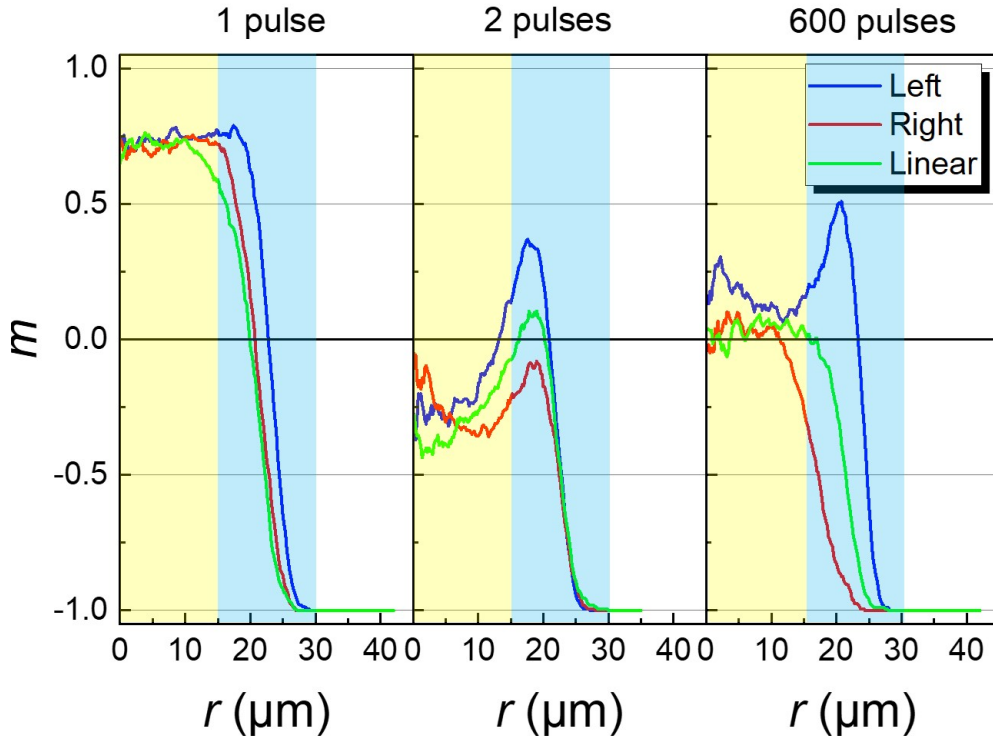


Figure 5.16: Radial switching profiles of magnetic 1 μm disks made of Pt (3.7 nm)/Gd/Co (0.7 nm)/Pt (3 nm) obtained after the action of 1, 2 and 600 consecutive picoseconds pulses with the circularly left (blue curves), right (red curves) and linearly (green curves) polarized light.

All the radial profiles for disk diameter from 1 μm to 400 nm with 3 light polarizations at a given laser fluence was performed and displayed in Figure 5.17. Here again, two regions with two different magnetization behavior are observed. Indeed, for a radius of $15 \pm 1 \mu\text{m}$ and in the case of one pulse, the average magnetization is reduced when the disk diameter decreases. This latter observation is true for the three laser helicities. While, in the case of 600 pulses, although m equal to zero for the right circular and linear polarization, m remains positive for the left circular polarization. For a radius between 15 μm and 30 μm , we observed the same dependence on the trends of the magnetization with the light helicity. Even for 400 nm disks, we still observe the multiple pulse effect at the edge of the laser spot.

To clearly illustrate the latter observations, we extracted in all the radial profiles of Figure 5.17, the value of m at 10 μm from the laser spot center. We choose this radius because at this distance, we are still in the constant region of m . Figure 5.18 depicted this extraction for the three light polarizations used. However, we did not continue the quantitative analysis. Indeed, the extraction of the switching probability has become complicated due to the poor statistics

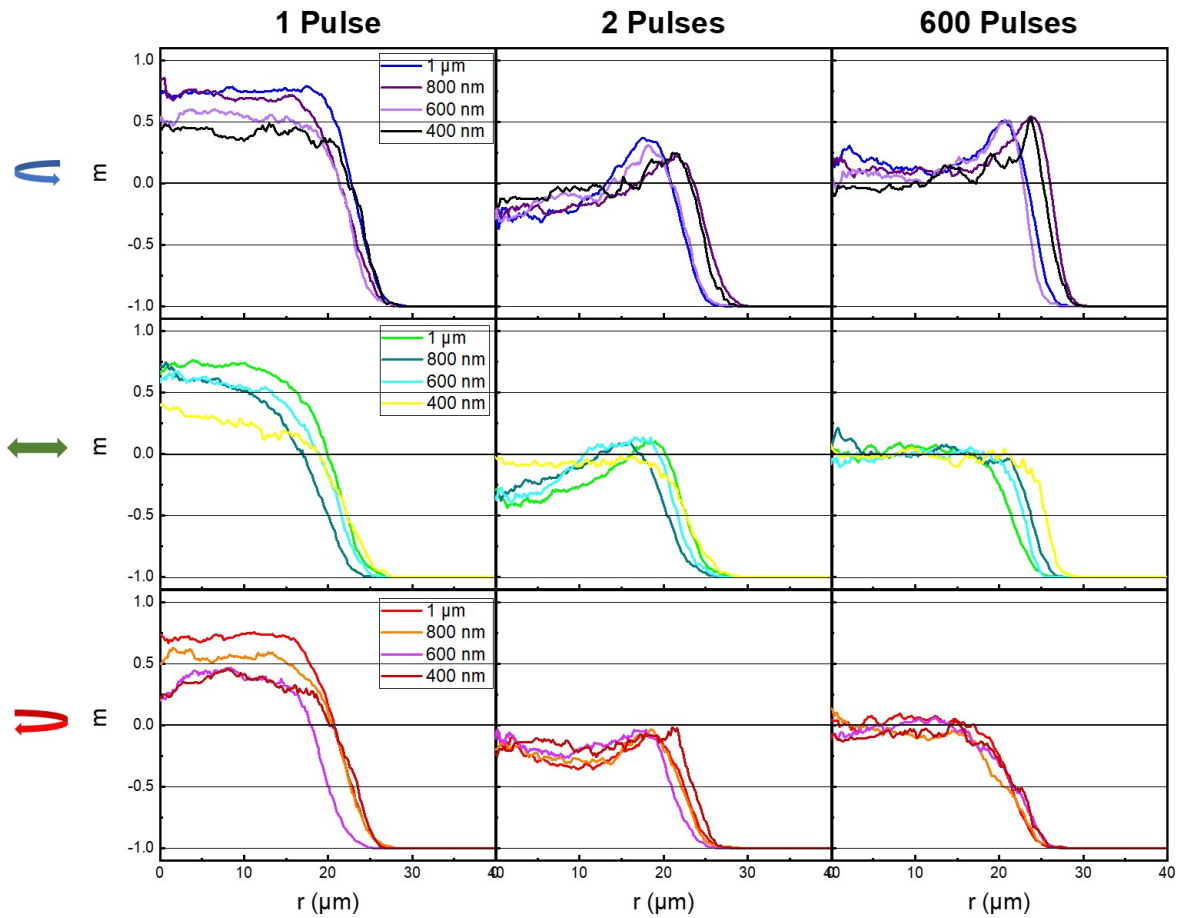


Figure 5.17: Radial switching profiles of magnetic disks from $1\ \mu\text{m}$ to $400\ \text{nm}$ made of Pt ($3.7\ \text{nm}$)/Gd/Co ($0.7\ \text{nm}$)/Pt ($3\ \text{nm}$) obtained after the action of 1, 2 and 600 consecutive picoseconds pulses with the circularly left, right and linearly polarized light.

(just three number of laser pulses with one radial profile for each number) and to the integration of the helicity in the analytical calculation.

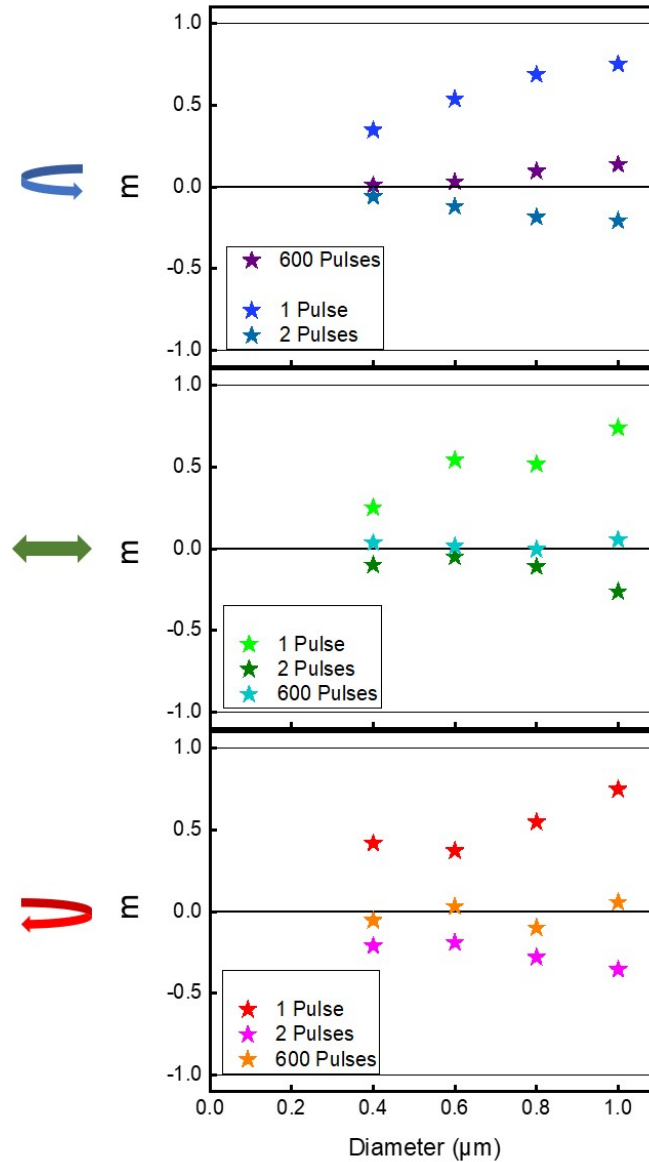


Figure 5.18: Evolution of the average magnetization m of 1 μm to 400 nm disks made of Pt (3.7 nm)/Gd/Co (0.7 nm)/Pt (3 nm) obtained after the action of 1, 2 and 600 consecutive picoseconds pulses with the circularly left, right and linearly polarized light.

5.6 Summary

In this last chapter, we studied the size effect on the single-shot AO-HIS for the Pt/Co/Pt tri-layer when we introduced a Gd dusting at the bottom Pt/Co interface after the excitation of femtosecond and picosecond laser pulses. Firstly, we showed that the structural and magnetic proper-

CHAPTER 5. SIZE EFFECT ON GD-DUSTED Pt/Co/Pt FERROMAGNET

ties of the studied sample are like those of the ferromagnetic Pt/Co/Pt. Unexpectedly, we have demonstrated the switching of the magnetization of the continuous film using a single linearly polarized femtosecond laser pulse. Indeed, this finding contrasts with previous works which indicated that we needed multiple circularly polarized laser pulses to switch the magnetization of a ferromagnetic material. Moreover, a magnetic state diagram has been built and presented the same triangular switching shape as the GdFeCo ferrimagnetic alloy with a stoichiometric composition near the compensation point.

Then, the third section of this chapter presents our study of the AO-HIS mechanism on disk arrays ranging from 3 μm to 400 nm in diameter with 35 fs linearly polarized laser pulses. By varying the number of laser pulses, it appears that a single toggle switching probability can describe the reversal behavior. The variation of this switching probability can be accurately measured in the range of 99.99% to 90% for disk arrays ranging from 1.5 μm to 400 nm. Thus, the switching probability degrades as the diameter of the structure is reduced. Moreover, the "exponential" variation of the switching probability with the disk diameter size is quite particular and cannot be explained by specific optical effects. On the other hand, a highly non uniform switching process with a low microscopic switching probability explains our experimental data. A simple probabilistic model, analog to Condorcet's jury theorem has been proposed and compared to micromagnetic simulations.

Finally, the impact of the pulse duration on the AOS mechanism has been accurately investigated on the full film and on disk arrays ranging from 1 μm to 400 nm at 2 ps. At this "long" pulse duration, we demonstrated that the switching is no longer perfect, and we lose the switching regime regardless of the light helicity after several (600) pulses. Nevertheless, the reduction of the lateral size continues to cause a qualitative decrease of the switching probability, thus following the same behavior demonstrated in the case of a femtosecond laser pulse.

Conclusion and perspectives

The aims of this thesis were to investigate the size effect on all-optical helicity-independent switching (AO-HIS) in systems showing this reversal mechanism at the full film scale. Although the approaches to describe the magnetization dynamic remains highly debated, our work in this field of research was to study the impact of reducing the lateral dimension of magnetic materials with "quasi-static" AOS experiments. Indeed, we have fabricated arrays of disks which diameter ranges from 3 μm to 400 nm for two types of magnetic thin film (GdFeCo alloy and Gd-dusted Pt/Co/Pt tri-layer) and systematically irradiated laser pulses on the patterned regions. If the importance of specific light absorption in nanostructures is revealed by the dependence of the threshold switching fluence with disk size for the GdFeCo alloy, thermal effects do not explain the behavior of the switching probability as a function of disk size for the Gd-dusted Pt/Co/Pt tri-layer.

The first part of this work reviews the main results published in the field of ultrafast manipulation of magnetization by ultrashort laser pulses. We started this chapter by presenting the first experimental demonstration of laser-induced dynamics in a ferromagnetic material. In this section, the different possible mechanisms involved in the ultrafast magnetization dynamics are presented. Then, the second section focuses on the static and dynamic observation of all-optical switching in ferrimagnetic materials. The starting point for the reversal of magnetization by light is the discovery in 2007 of deterministic switching of GdFeCo magnetic domains using several pulses for a given helicity and then a single linearly polarized pulse. In this section, we therefore present other ferrimagnetic materials that exhibit AO-HIS, with a focus on synthetic ferrimagnetic materials. Furthermore, the absence of angular momentum in linearly polarized light and the observation of AOS independent of the direction of a single magnetic domain demonstrate that the pure thermal effect is the mechanism driving AOS in this type of material. The dynamics of the magnetization has also been reported and approaches to describe the observed ultrafast dynamics are still very much debated. However, another class of magnetic materials exhibiting AOS is ferromagnet. Indeed, from full film to granular media, it is now well known that a complete reversal of magnetization in one direction for one helicity and in the opposite di-

CONCLUSION AND PERSPECTIVES

rection for the opposite helicity can be obtained, called all-optical helicity-dependent switching (AO-HDS). It has been shown that nucleation and domain wall propagation are the switching process for this type of reversal. In addition, the inverse Faraday effect (IFE) and magnetic circular dichroism (MCD) appear to be the two best candidates for understanding the AO-HDS mechanism in this magnetic material. In the next section, the use of ultrafast spin currents to drive the magnetization switching of a ferromagnet inside a spin valve by using femtosecond laser pulses is presented. At the end of this chapter, the various studies of the size effect on AO-HIS performed mainly in the GdFeCo alloy are reviewed.

In chapter 3, we present a systematic study of the magnetization reversal for GdFeCo disks which diameter ranges from 10 μm to 400 nm with 35 fs linearly polarized laser pulses. For bigger micro-disks (between 10 and 3 μm), we confirm that larger patterned GdFeCo structures exhibit all-optical switching. Remarkably, the formation of a ring, followed by its expansion towards the center of the structure is observed and illustrates a slow switching dynamic of about 30 s for 6 μm disks. However, since the distance between structures and the disks diameter are comparable to the diameter of the laser beam, difficulties soon arose in studying the size effect at this lateral dimensional scale. One of them is the proper definition of parameters such as the switching threshold fluence, the demagnetization fluence, the pulse duration limit, and the switching probability involved in the AOS mechanism. To overcome this limitation, we continued to reduce the size of the disks from 3 μm to 400 nm in diameter while moving them closer together. We experimentally demonstrate single pulse toggle switching of the magnetization of GdFeCo disks in this size range by using 35 fs linearly polarized laser pulses. Two different magnetic states can be observed depending on the laser fluence: either a deterministic switching of the disks magnetization or a randomly oriented disk. We show that the fluence required to observe both magnetic states show a non-monotonic behavior with disk diameter, and that the smallest disks require the lowest minimum fluence for achieving single pulse all-optical helicity-independent switching. Different evolution of the fluence thresholds for both phenomenon as a function of the disk size is observed and discussed. We end this chapter by showing that an augmentation of the pulse duration magnitude induces a progressively decrease of the quality of the AO-HIS.

In chapter 4, we present a careful analysis of the Gd magnitude and position effects on single pulse all-optical switching mechanism in Pt/Co/Pt ferromagnet. Three types of Gd wedge samples are realized: Pt/Gd/Co/Pt, Pt/GdCo/Pt and Pt/Co/Gd/Pt. Indeed, we used a wedge deposition process to vary progressively the Gd thickness in all the full film. For the Pt/Co/Gd stack, we demonstrate the necessity to separate the switching and the perfect toggle switching

regime. Indeed, the clear difference in magnetization behavior appears in these two regimes when a multidomain state is observed for the switching regime while a toggle reversal domain is achieved for PTS, in the case of 10000 consecutive single laser pulses with 5 kHz of rate repetition. Moreover, we demonstrate that we could reduce the Gd thickness from 3 nm to 0.27 nm and still observe the perfect toggle switching mechanism. This experimental result demonstrates that the interfacial effect is the main effect responsible for the observation of AO-HIS in Pt/Co/Gd stack. For Pt/Gd/Co/Pt, we demonstrate the perfect toggle switching down to 0.06 nm Gd thickness. Moreover, by plotting the magnetic state diagram (fluence vs pulse duration) for Gd thickness equal to 0.07 and 0.21 nm, we observe the same triangular switching window demonstrated previously in ferrimagnetic alloys. Remarkably, the less Gd in the lower Pt/Co interface, the higher the maximum pulse duration. However, for a Gd thickness around 0.3 nm, the Co magnetization goes in plane. Finally, in the case of GdCo alloy sandwiched by two Pt layers, we demonstrate that the PTS state can be achieved down to 7.5% of Gd and the switching regime down to 4% of Gd.

In chapter 5, we present a systematic study of the size effect on AO-HIS in Gd-dusted Pt/Co/Pt disks which diameter ranges from 3 μm to 400 nm with 35 fs linear polarization laser pulses. The effect of laser excitation is investigated in-situ using a polar MOKE microscope and the quantitative analyze of the switching probability were performed ex-situ by magnetic force microscopy. The variation of this switching probability with the disks size is precisely measured and explained by a non-uniform switching process. Finally, the influence of the laser pulse duration and the laser helicity on the AOS in this range of disk size is discussed.

In the light of all this work, many questions will need to be addressed in the future. The following paragraph give some perspectives on this work.

In chapter 3, for GdFeCo disks arrays between 3 micron and 400 nm of diameter, if the study of the size effect on AOS can be continued by decreasing the disk size, it is crucial to study the influence of the period on AO-HIS at a given size for this range disk diameter. This would allow to know if the non-monotonic behavior of threshold fluence are both observed in the disk size and in the period of the disk array. In addition, more complex optical simulations need to be performed if we want to understand in detail the behavior of the random threshold switching or the ratio fluence in this diameter range. In chapter 4, theoretical approaches must be realized to understand why we have such a dependence of the AO-HIS mechanism with the Gd position. The clear evidence of this remarkable difference is the observation of perfect toggle switching and multidomain state when we introduce 0.06 nm of Gd at the bottom and top Co/Pt interface,

CONCLUSION AND PERSPECTIVES

respectively. In addition, theoretical, analytical or simulations should also be performed to investigate our experimental achievement of AO-HIS for a GdCo alloy and Pt/Gd/Co stack with just 3% of Gd. Indeed, at this proportion of Gd we are far away from the compensation point, and since the discovery of single thermal AOS in ferrimagnetic alloy presented the compensation point to be indispensable for ultrafast reversal, our results raise questions about the mechanisms involved on AO-HIS. We also believe that TR-MOKE experiment must be realized in all the studied sample: did the reversal process and timescale are like GdFeCo alloy or to Pt/Co/Gd stack? In chapter 5, if the question of how we can achieve single thermal all-optical switching in Pt/Co/Pt with a Gd dusting remains open, It will be interesting here to continue to decrease the size of the disk and to highlight the behavior of the switching probability as a function of the disk size. In addition, by combining MFM scanning with electrical measurements, it may be possible to study the size effect more efficiently, since MFM characterizations alone have proved to be time consuming at thesis timescale.

However, we believe that this work will surely change the understanding of the all-optical switching mechanism of the last 15 years. Indeed, the demonstration that a very small amount of Gd is needed not only opens new application possibilities, but also challenges the theoretical description of the all-optical switching mechanism. Finally, the study of the size effect is necessary to get closer to the application level and to highlight new phenomena hidden in this magnetization reversal process.

Appendix A

Details of the quantitative analysis

The purpose of this annex is to give some lines of calculation that allowed us to perform our quantitative analysis of the switching probability behavior with the disk diameter. Indeed, in Chapter 5, we performed an MFM scans on Gd-dusted Pt/Co/Pt disk arrays after the AOS experiments and we were able to convert the MFM maps into digital images. Therefore, the problem of determining the switching probability emerges quickly since the switching state degrades when we have reduced the disk size. To achieve this goal, this appendix is divided into two parts. First, we present the parameter, notation and reasoning we used to establish the relationship between the average magnetization of the experiment and the switching (or non-switching) probability. Then we show the different equations used to relate the switching probability to the thermal activation process.

A.1 Magnetization and switching probability

Let us first introduce the notations and the two assumptions that we done. Indeed, we considered two equivalent directions of disks magnetization (no external magnetic field, or effect of light polarization), and no interaction between disks. Only one parameter is necessary to understand the probability to switch the disk magnetization from up to down and down to up. Indeed, in the general toggle switching case, the probability of reversal after a pulse is independent of the magnetic state and can be written as $\frac{1}{2}(1 - \eta)$:

- $\eta = -1$ corresponds to perfect toggle switching,
- $\eta = 0$ corresponds to a completely random demagnetization process and
- $\eta = +1$ corresponds to no toggle switching.

APPENDIX A. DETAILS OF THE QUANTITATIVE ANALYSIS

η is directly the correlation coefficient between the magnetic states of a nanostructure between two pulses. Figure A.1 give a view of this switching probability between two consecutive pulses.

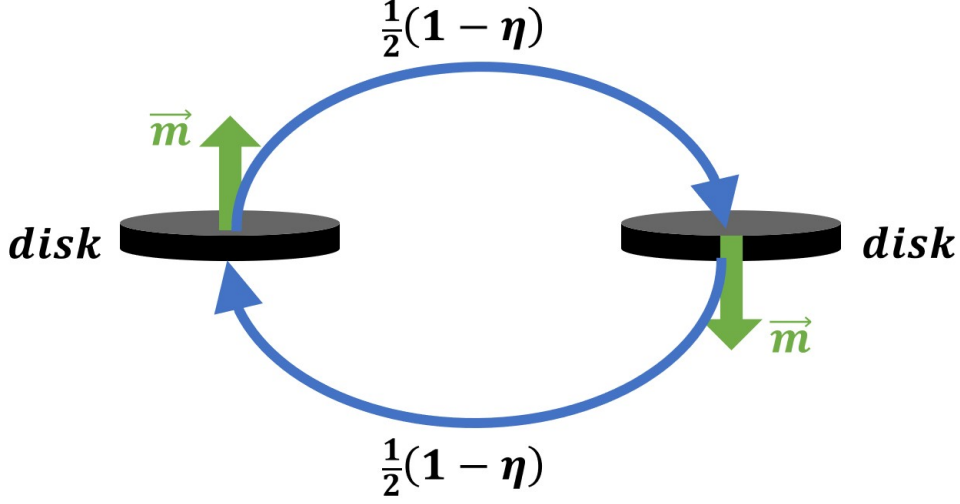


Figure A.1: View of the switching probability

Let's note P_i^\uparrow the probability of being in a given state after the i^{th} pulse

$$P_{i+1}^\uparrow = P_i^\uparrow - \alpha.P_i^\uparrow + \beta.P_i^\downarrow \quad (\text{A.1})$$

$$P_{i+1}^\downarrow = P_i^\downarrow - \beta.P_i^\downarrow + \alpha.P_i^\uparrow$$

Where α (respectively β) is the probability of reversal from up \uparrow to down \downarrow (respectively down \downarrow to up \uparrow) and is equal to $\frac{1}{2}(1 - \eta)$. Then, by replacing α and β in Equation A.1, we have:

$$P_{i+1}^\uparrow = \eta.P_i^\uparrow + \frac{1}{2}(1 - \eta) \quad (\text{A.2})$$

$$P_{i+1}^\downarrow = \eta.P_i^\downarrow + \frac{1}{2}(1 - \eta)$$

Let us now consider that the starting configuration is $P_0^\uparrow = 1$ and $P_0^\downarrow = 0$ (all the disks are pointing in the upward \uparrow direction). The probabilities for the first and second pulses is given by:

$$P_1^\uparrow = \frac{1}{2}(1 + \eta) \quad , \quad P_1^\downarrow = \frac{1}{2}(1 - \eta) \quad (\text{A.3})$$

$$P_2^\uparrow = \frac{1}{2}(1 + \eta^2) \quad , \quad P_2^\downarrow = \frac{1}{2}(1 - \eta^2)$$

Experimentally, after the first pulse we measure m^{sw} the magnetization after a pulse in the switching direction, and m^{non-sw} the magnetization after a pulse in the non-switching direction, so with $P_0^\uparrow = 1$:

A.2. SWITCHING PROBABILITY AND THERMAL ACTIVATION

$$m^{sw} = 2.P^\downarrow - 1 \tag{A.4}$$

$$m^{non-sw} = 2.P^\uparrow - 1$$

By introducing A.3 in A.4 we obtain the relation between the magnetization and η for the first and second pulse:

$$\neq 1pulse : m^{sw} = -\eta \quad \neq 2pulse : m^{sw} = -\eta^2 \tag{A.5}$$

$$\neq 1pulse : m^{non-sw} = \eta \quad \neq 2pulse : m^{non-sw} = \eta^2$$

The same reasoning can be realized for the third, fourth and i^{th} pulse:

$$m^{sw} = -\eta^i \tag{A.6}$$

$$m^{non-sw} = \eta^i$$

A.2 switching probability and thermal activation

We consider a system with two states (up \uparrow and down \downarrow). We define a characteristic (thermally activated) transition time τ between the two states. If we denote by P^\uparrow and P^\downarrow the probabilities of being in each state, we have:

$$\frac{dP^\uparrow}{dt} = -\frac{1}{\tau}P^\uparrow + \frac{1}{\tau}P^\downarrow = \frac{1}{\tau} - \frac{2}{\tau}P^\uparrow \tag{A.7}$$

$$\frac{dP^\downarrow}{dt} = -\frac{1}{\tau}P^\downarrow + \frac{1}{\tau}P^\uparrow = \frac{1}{\tau} - \frac{2}{\tau}P^\downarrow$$

And so the temporal solutions:

$$P^\downarrow(t) = \frac{1}{2} + \left(P^\downarrow(0) - \frac{1}{2} \right) e^{-\frac{2t}{\tau}} \tag{A.8}$$

The system converges well to $P^\uparrow = P^\downarrow = \frac{1}{2}$ If we think in terms of magnetization, we have :

$$m(t) = P^\uparrow(t) - P^\downarrow(t) = (P^\uparrow(0) - P^\downarrow(0))e^{-\frac{2t}{\tau}} \tag{A.9}$$

Let us consider that just after the first pulse, the switching is perfect: $m_1(0) = -1$ and after a certain time t ,

$$m_1(t) = \eta = -e^{-\frac{2t}{\tau}} \tag{A.10}$$

Bibliography

- [1] Radu, I. *et al.* Transient ferromagnetic-like state mediating ultrafast reversal of antiferromagnetically coupled spins. *Nature* **472**, 205–208 (2011).
- [2] Xu, Y. *et al.* Ultrafast magnetization manipulation using single femtosecond light and hot-electron pulses. *Advanced Materials* **29**, 1703474 (2017).
- [3] Davies, C. *et al.* Pathways for single-shot all-optical switching of magnetization in ferrimagnets. *Physical Review Applied* **13**, 024064 (2020).
- [4] Xu, Y. *et al.* From single to multiple pulse all-optical switching in GdFeCo thin films. *Physical Review B* **100**, 064424 (2019).
- [5] Wei, J. *et al.* All-optical Helicity-Independent Switching State Diagram in Gd-Fe-Co Alloys. *Physical Review Applied* **15**, 054065 (2021).
- [6] El-Ghazaly, A. *et al.* Ultrafast magnetization switching in nanoscale magnetic dots. *Applied Physics Letters* **114**, 232407 (2019).
- [7] Lalieu, M., Peeters, M., Haenen, S., Lavrijsen, R. & Koopmans, B. Deterministic all-optical switching of synthetic ferrimagnets using single femtosecond laser pulses. *Physical review B* **96**, 220411 (2017).
- [8] Ceballos, A. *et al.* Role of element-specific damping in ultrafast, helicity-independent, all-optical switching dynamics in amorphous (Gd,Tb)Co thin films. *Physical Review B* **103**, 024438 (2021).
- [9] Zhang, W. *et al.* Role of spin-lattice coupling in ultrafast demagnetization and all optical helicity-independent single-shot switching in $\text{Gd}_{1-x-y}\text{Tb}_y\text{Co}_x$ alloys. *Physical Review B* **105**, 054410 (2022).

BIBLIOGRAPHY

- [10] Gorchon, J. *et al.* Single shot ultrafast all optical magnetization switching of ferromagnetic Co/Pt multilayers. *Applied physics letters* **111**, 042401 (2017).
- [11] Iihama, S. *et al.* Single-shot multi-level all-optical magnetization switching mediated by spin transport. *Advanced Materials* **30**, 1804004 (2018).
- [12] Igarashi, J. *et al.* Engineering single-shot all-optical switching of ferromagnetic materials. *Nano Letters* **20**, 8654–8660 (2020).
- [13] Remy, Q. *et al.* Energy efficient control of ultrafast spin current to induce single femtosecond pulse switching of a ferromagnet. *Advanced Science* **7**, 2001996 (2020).
- [14] Remy, Q. *et al.* Accelerating ultrafast magnetization reversal by non-local spin transfer. *Nature Communications* **14**, 445 (2023).
- [15] Banerjee, C. *et al.* Single pulse all-optical toggle switching of magnetization without gadolinium in the ferrimagnet $\text{Mn}_2\text{Ru}_x\text{Ga}$. *Nature communications* **11**, 1–6 (2020).
- [16] Avilés-Félix, L. *et al.* Integration of Tb/Co multilayers within optically switchable perpendicular magnetic tunnel junctions. *Aip Advances* **9**, 125328 (2019).
- [17] Avilés-Félix, L. *et al.* Single-shot all-optical switching of magnetization in Tb/Co multilayer-based electrodes. *Scientific reports* **10**, 1–8 (2020).
- [18] Mentink, J. H. *et al.* Ultrafast spin dynamics in multisublattice magnets. *Physical review letters* **108**, 057202 (2012).
- [19] Koopmans, B. *et al.* Explaining the paradoxical diversity of ultrafast laser-induced demagnetization. *Nature materials* **9**, 259–265 (2010).
- [20] Ostler, T. A. *et al.* Crystallographically amorphous ferrimagnetic alloys: Comparing a localized atomistic spin model with experiments. *Physical Review B* **84**, 024407 (2011).
- [21] Atxitia, U., Nieves, P. & Chubykalo-Fesenko, O. Landau-lifshitz-bloch equation for ferrimagnetic materials. *Physical Review B* **86**, 104414 (2012).
- [22] Atxitia, U. & Ostler, T. Ultrafast double magnetization switching in GdFeCo with two picosecond-delayed femtosecond pump pulses. *Applied Physics Letters* **113**, 062402 (2018).

-
- [23] Beens, M., Laliou, M. L., Deenen, A. J., Duine, R. A. & Koopmans, B. Comparing all-optical switching in synthetic-ferrimagnetic multilayers and alloys. *Physical Review B* **100**, 220409 (2019).
- [24] Beens, M., Laliou, M. L., Duine, R. A. & Koopmans, B. The role of intermixing in all-optical switching of synthetic-ferrimagnetic multilayers. *AIP Advances* **9**, 125133 (2019).
- [25] Min, B., Lodder, J. & Jansen, R. Sign of tunnel spin polarization of low-work-function Gd/Co nanolayers in a magnetic tunnel junction. *Physical Review B* **78**, 212403 (2008).
- [26] Meservey, R. & Tedrow, P. Spin-polarized electron tunneling. *Physics reports* **238**, 173–243 (1994).
- [27] Krause, S., Berbil-Bautista, L., Herzog, G., Bode, M. & Wiesendanger, R. Current-induced magnetization switching with a spin-polarized scanning tunneling microscope. *Science* **317**, 1537–1540 (2007).
- [28] Liu, L. *et al.* Current-induced magnetization switching in all-oxide heterostructures. *Nature nanotechnology* **14**, 939–944 (2019).
- [29] Lottermoser, T. *et al.* Magnetic phase control by an electric field. *Nature* **430**, 541–544 (2004).
- [30] Ohno, H. *et al.* Electric-field control of ferromagnetism. *Nature* **408**, 944–946 (2000).
- [31] Kubacka, T. *et al.* Large-amplitude spin dynamics driven by a THz pulse in resonance with an electromagnon. *Science* **343**, 1333–1336 (2014).
- [32] Beaurepaire, E., Merle, J.-C., Daunois, A. & Bigot, J.-Y. Ultrafast spin dynamics in ferromagnetic nickel. *Physical review letters* **76**, 4250 (1996).
- [33] Kryder, M. H. *et al.* Heat assisted magnetic recording. *Proceedings of the IEEE* **96**, 1810–1835 (2008).
- [34] Stanciu, C. D. *et al.* All-optical magnetic recording with circularly polarized light. *Physical review letters* **99**, 047601 (2007).
- [35] El Hadri, M. S. *et al.* Electrical characterization of all-optical helicity-dependent switching in ferromagnetic hall crosses. *Applied Physics Letters* **108**, 092405 (2016).

BIBLIOGRAPHY

- [36] Vomir, M., Albrecht, M. & Bigot, J.-Y. Single shot all optical switching of intrinsic micron size magnetic domains of a Pt/Co/Pt ferromagnetic stack. *Applied Physics Letters* **111**, 242404 (2017).
- [37] Graves, C. *et al.* Nanoscale spin reversal by non-local angular momentum transfer following ultrafast laser excitation in ferrimagnetic GdFeCo. *Nature materials* **12**, 293–298 (2013).
- [38] Vaterlaus, A., Beutler, T. & Meier, F. Spin-lattice relaxation time of ferromagnetic gadolinium determined with time-resolved spin-polarized photoemission. *Physical review letters* **67**, 3314 (1991).
- [39] Hohlfeld, J., Matthias, E., Knorren, R. & Bennemann, K. Nonequilibrium magnetization dynamics of nickel. *Physical review letters* **78**, 4861 (1997).
- [40] Hohlfeld, J. *et al.* Ultrafast magnetization dynamics of nickel. *Applied Physics B: Lasers & Optics* **68** (1999).
- [41] Güdde, J., Conrad, U., Jähnke, V., Hohlfeld, J. & Matthias, E. Magnetization dynamics of Ni and Co films on Cu (001) and of bulk nickel surfaces. *Physical Review B* **59**, R6608 (1999).
- [42] Scholl, A., Baumgarten, L., Jacquemin, R. & Eberhardt, W. Ultrafast spin dynamics of ferromagnetic thin films observed by fs spin-resolved two-photon photoemission. *Physical review letters* **79**, 5146 (1997).
- [43] Beaurepaire, E. *et al.* Spin dynamics in CoPt₃ alloy films: A magnetic phase transition in the femtosecond time scale. *Physical Review B* **58**, 12134 (1998).
- [44] Kampfrath, T. *et al.* Ultrafast magneto-optical response of iron thin films. *Physical Review B* **65**, 104429 (2002).
- [45] Kazantseva, N. *et al.* Towards multiscale modeling of magnetic materials: Simulations of FePt. *Physical Review B* **77**, 184428 (2008).
- [46] Zhang, G. & Hübner, W. Laser-induced ultrafast demagnetization in ferromagnetic metals. *Physical review letters* **85**, 3025 (2000).
- [47] Hübner, W. & Zhang, G. Ultrafast spin dynamics in nickel. *Physical Review B* **58**, R5920 (1998).

-
- [48] Hübner, W. & Zhang, G. Femtosecond spin dynamics probed by linear and nonlinear magneto-optics. *Journal of magnetism and magnetic materials* **189**, 101–105 (1998).
- [49] Guidoni, L., Beaurepaire, E. & Bigot, J.-Y. Magneto-optics in the ultrafast regime: Thermalization of spin populations in ferromagnetic films. *Physical review letters* **89**, 017401 (2002).
- [50] Chan, L.-O. *et al.* Ultrafast demagnetization measurements using extreme ultraviolet light: Comparison of electronic and magnetic contributions. *Physical Review X* **2**, 011005 (2012).
- [51] Koopmans, B., Ruigrok, J., Dalla Longa, F. & De Jonge, W. Unifying ultrafast magnetization dynamics. *Physical review letters* **95**, 267207 (2005).
- [52] Stamm, C. *et al.* Femtosecond modification of electron localization and transfer of angular momentum in nickel. *Nature materials* **6**, 740–743 (2007).
- [53] Cinchetti, M. *et al.* Spin-flip processes and ultrafast magnetization dynamics in Co: Unifying the microscopic and macroscopic view of femtosecond magnetism. *Physical review letters* **97**, 177201 (2006).
- [54] Anisimov, S., Kapeliovich, B., Perelman, T. *et al.* Electron emission from metal surfaces exposed to ultrashort laser pulses. *Zh. Eksp. Teor. Fiz* **66**, 375–377 (1974).
- [55] Carpene, E. *et al.* Dynamics of electron-magnon interaction and ultrafast demagnetization in thin iron films. *Physical Review B* **78**, 174422 (2008).
- [56] Hansen, P., Clausen, C., Much, G., Rosenkranz, M. & Witter, K. Magnetic and magneto-optical properties of rare-earth transition-metal alloys containing Gd, Tb, Fe, Co. *Journal of applied physics* **66**, 756–767 (1989).
- [57] Awano, H. *et al.* Magnetic domain expansion readout for amplification of an ultra high density magneto-optical recording signal. *Applied physics letters* **69**, 4257–4259 (1996).
- [58] Medapalli, R. *et al.* Efficiency of ultrafast laser-induced demagnetization in $\text{Gd}_x\text{Fe}_{100-x-y}\text{Co}_y$ alloys. *Physical Review B* **86**, 054442 (2012).
- [59] Vahaplar, K. *et al.* All-optical magnetization reversal by circularly polarized laser pulses: Experiment and multiscale modeling. *Physical review B* **85**, 104402 (2012).

BIBLIOGRAPHY

- [60] Khorsand, A. *et al.* Role of magnetic circular dichroism in all-optical magnetic recording. *Physical review letters* **108**, 127205 (2012).
- [61] Mangin, S. *et al.* Engineered materials for all-optical helicity-dependent magnetic switching. *Nature materials* **13**, 286–292 (2014).
- [62] Alebrand, S. *et al.* Light-induced magnetization reversal of high-anisotropy TbCo alloy films. *Applied Physics Letters* **101**, 162408 (2012).
- [63] Alebrand, S. *et al.* Subpicosecond magnetization dynamics in TbCo alloys. *Physical Review B* **89**, 144404 (2014).
- [64] Hassdenteufel, A. *et al.* Thermally assisted all-optical helicity dependent magnetic switching in amorphous $\text{Fe}_{100-x}\text{Tb}_x$ alloy films. *Advanced Materials* **25**, 3122–3128 (2013).
- [65] Kimel, A. V. Three rules of design. *Nature materials* **13**, 225–226 (2014).
- [66] Hassdenteufel, A. *et al.* Low-remanence criterion for helicity-dependent all-optical magnetic switching in ferrimagnets. *Physical Review B* **91**, 104431 (2015).
- [67] El Hadri, M. S. *et al.* Domain size criterion for the observation of all-optical helicity-dependent switching in magnetic thin films. *Physical review B* **94**, 064419 (2016).
- [68] Ostler, T. *et al.* Ultrafast heating as a sufficient stimulus for magnetization reversal in a ferrimagnet. *Nature communications* **3**, 1–6 (2012).
- [69] El Hadri, M. S. *et al.* Two types of all-optical magnetization switching mechanisms using femtosecond laser pulses. *Physical review B* **94**, 064412 (2016).
- [70] Gorchon, J. *et al.* Role of electron and phonon temperatures in the helicity-independent all-optical switching of GdFeCo. *Physical Review B* **94**, 184406 (2016).
- [71] Wang, S. *et al.* Dual-shot dynamics and ultimate frequency of all-optical magnetic recording on GdFeCo. *Light: Science & Applications* **10**, 1–8 (2021).
- [72] Yang, Y. *et al.* Ultrafast magnetization reversal by picosecond electrical pulses. *Science advances* **3**, e1603117 (2017).
- [73] Kazantseva, N., Nowak, U., Chantrell, R. W., Hohlfeld, J. & Rebei, A. Slow recovery of the magnetisation after a sub-picosecond heat pulse. *EPL (Europhysics Letters)* **81**, 27004 (2007).

-
- [74] Atxitia, U. & Chubykalo-Fesenko, O. Ultrafast magnetization dynamics rates within the Landau-Lifshitz-Bloch model. *Physical Review B* **84**, 144414 (2011).
- [75] Bergard, N. *et al.* Ultrafast angular momentum transfer in multisublattice ferrimagnets. *Nature communications* **5**, 1–7 (2014).
- [76] Gridnev, V. Ferromagneticlike states and all-optical magnetization switching in ferrimagnets. *Physical Review B* **98**, 014427 (2018).
- [77] Wienholdt, S., Hinzke, D., Carva, K., Oppeneer, P. M. & Nowak, U. Orbital-resolved spin model for thermal magnetization switching in rare-earth-based ferrimagnets. *Physical Review B* **88**, 020406 (2013).
- [78] Kalashnikova, A. & Kozub, V. Exchange scattering as the driving force for ultrafast all-optical and bias-controlled reversal in ferrimagnetic metallic structures. *Physical Review B* **93**, 054424 (2016).
- [79] Scheid, P., Remy, Q., Lebègue, S., Malinowski, G. & Mangin, S. Light induced ultrafast magnetization dynamics in metallic compounds. *Journal of Magnetism and Magnetic Materials* **560**, 169596 (2022).
- [80] Davies, C. *et al.* Exchange-driven all-optical magnetic switching in compensated 3d ferrimagnets. *Physical Review Research* **2**, 032044 (2020).
- [81] Laliou, M. L., Lavrijsen, R. & Koopmans, B. Integrating all-optical switching with spintronics. *Nature communications* **10**, 1–6 (2019).
- [82] Lambert, C.-H. *et al.* All-optical control of ferromagnetic thin films and nanostructures. *Science* **345**, 1337–1340 (2014).
- [83] Luttinger, J. Theory of the Hall effect in ferromagnetic substances. *Physical Review* **112**, 739 (1958).
- [84] Quessab, Y. *et al.* Helicity-dependent all-optical domain wall motion in ferromagnetic thin films. *Physical Review B* **97**, 054419 (2018).
- [85] Fatuzzo, E. Theoretical considerations on the switching transient in ferroelectrics. *Physical review* **127**, 1999 (1962).

BIBLIOGRAPHY

- [86] Labrune, M., Andrieu, S., Rio, F. & Bernstein, P. Time dependence of the magnetization process of RE-TM alloys. *Journal of magnetism and magnetic materials* **80**, 211–218 (1989).
- [87] Kichin, G. *et al.* From multiple-to single-pulse all-optical helicity-dependent switching in ferromagnetic Co/Pt multilayers. *Physical Review Applied* **12**, 024019 (2019).
- [88] Asselin, P. *et al.* Constrained Monte Carlo method and calculation of the temperature dependence of magnetic anisotropy. *Physical Review B* **82**, 054415 (2010).
- [89] Ellis, M. O., Fullerton, E. E. & Chantrell, R. W. All-optical switching in granular ferromagnets caused by magnetic circular dichroism. *Scientific reports* **6**, 1–9 (2016).
- [90] Ellis, M. O. *et al.* The Landau–Lifshitz equation in atomistic models. *Low Temperature Physics* **41**, 705–712 (2015).
- [91] Gorchon, J., Yang, Y. & Bokor, J. Model for multishot all-thermal all-optical switching in ferromagnets. *Physical review B* **94**, 020409 (2016).
- [92] Brown Jr, W. F. Thermal fluctuations of a single-domain particle. *Physical review* **130**, 1677 (1963).
- [93] Takahashi, Y. *et al.* Accumulative magnetic switching of ultrahigh-density recording media by circularly polarized light. *Physical Review Applied* **6**, 054004 (2016).
- [94] Medapalli, R. *et al.* Multiscale dynamics of helicity-dependent all-optical magnetization reversal in ferromagnetic Co/Pt multilayers. *Physical review B* **96**, 224421 (2017).
- [95] Tsema, Y. *et al.* Helicity and field dependent magnetization dynamics of ferromagnetic Co/Pt multilayers. *Applied Physics Letters* **109**, 072405 (2016).
- [96] Quessab, Y. *et al.* Resolving the role of magnetic circular dichroism in multishot helicity-dependent all-optical switching. *Physical Review B* **100**, 024425 (2019).
- [97] Beth, R. A. Mechanical detection and measurement of the angular momentum of light. *Physical Review* **50**, 115 (1936).
- [98] Holbourn, A. Angular momentum of circularly polarised light. *Nature* **137**, 31–31 (1936).
- [99] Kimel, A. *et al.* Ultrafast non-thermal control of magnetization by instantaneous photomagnetic pulses. *Nature* **435**, 655–657 (2005).

-
- [100] Pitaevskii, L. Electric forces in a transparent dispersive medium. *Sov. Phys. JETP* **12**, 1008–1013 (1961).
- [101] Van der Ziel, J., Pershan, P. S. & Malmstrom, L. Optically-induced magnetization resulting from the inverse faraday effect. *Physical review letters* **15**, 190 (1965).
- [102] Pershan, P., Van der Ziel, J. & Malmstrom, L. Theoretical discussion of the inverse faraday effect, raman scattering, and related phenomena. *Physical review* **143**, 574 (1966).
- [103] Cornelissen, T., Córdoba, R. & Koopmans, B. Microscopic model for all optical switching in ferromagnets. *Applied Physics Letters* **108**, 142405 (2016).
- [104] Battiato, M., Barbalinardo, G., Carva, K. & Oppeneer, P. M. Beyond linear response theory for intensive light-matter interactions: Order formalism and ultrafast transient dynamics. *Physical Review B* **85**, 045117 (2012).
- [105] Battiato, M., Barbalinardo, G. & Oppeneer, P. M. Quantum theory of the inverse faraday effect. *Physical review B* **89**, 014413 (2014).
- [106] Vahaplar, K. *et al.* Ultrafast path for optical magnetization reversal via a strongly nonequilibrium state. *Physical review letters* **103**, 117201 (2009).
- [107] John, R. *et al.* Magnetisation switching of FePt nanoparticle recording medium by femtosecond laser pulses. *Scientific reports* **7**, 1–8 (2017).
- [108] Scheid, P., Malinowski, G., Mangin, S. & Lebègue, S. Ab initio theory of magnetization induced by light absorption in ferromagnets. *Physical Review B* **100**, 214402 (2019).
- [109] Lavrijsen, R. *et al.* Magnetic ratchet for three-dimensional spintronic memory and logic. *Nature* **493**, 647–650 (2013).
- [110] Suto, H. *et al.* Three-dimensional magnetic recording using ferromagnetic resonance. *Japanese Journal of Applied Physics* **55**, 07MA01 (2016).
- [111] Savoini, M. *et al.* Highly efficient all-optical switching of magnetization in GdFeCo microstructures by interference-enhanced absorption of light. *Physical Review B* **86**, 140404 (2012).
- [112] Le Guyader, L. *et al.* Demonstration of laser induced magnetization reversal in GdFeCo nanostructures. *Applied Physics Letters* **101**, 022410 (2012).

BIBLIOGRAPHY

- [113] Koene, B., Savoini, M., Kimel, A. V., Kirilyuk, A. & Rasing, T. Optical energy optimization at the nanoscale by near-field interference. *Applied Physics Letters* **101**, 013115 (2012).
- [114] Hatzakis, M. Electron resists for microcircuit and mask production. *Journal of the electrochemical society* **116**, 1033 (1969).
- [115] Van der Gaag, B. & Scherer, A. Microfabrication below 10 nm. *Applied physics letters* **56**, 481–483 (1990).
- [116] Howard, R. E., Hu, E. L. & Jackel, L. D. Multilevel resist for lithography below 100 nm. *IEEE Transactions on Electron Devices* **28**, 1378–1381 (1981).
- [117] Chen, Y., Peng, K. & Cui, Z. A lift-off process for high resolution patterns using PMMA/LOR resist stack. *Microelectronic engineering* **73**, 278–281 (2004).
- [118] Loschonsky, M. *et al.* Electron-beam processed SAW devices for sensor applications. In *2009 6th International Multi-Conference on Systems, Signals and Devices*, 1–4 (IEEE, 2009).
- [119] Salut, R. *Etude des moyens de lithographie haute résolution pour la fabrication de résonateurs à ondes élastiques de surface: application aux sources embarquées*. Ph.D. thesis, Université de Franche-Comté (2011).
- [120] Li, P. A review of proximity effect correction in electron-beam lithography. *arXiv preprint arXiv:1509.05169* (2015).
- [121] Murai, F., Yoda, H., Okazaki, S., Saitou, N. & Sakitani, Y. Fast proximity effect correction method using a pattern area density map. *Journal of Vacuum Science & Technology B: Microelectronics and Nanometer Structures Processing, Measurement, and Phenomena* **10**, 3072–3076 (1992).
- [122] McCord, M. A. & Rooks, M. J. Electron beam lithography. *Handbook of microlithography, micromachining, and microfabrication* **1**, 139–249 (1997).
- [123] Wei, J. Manipulation de l'aimantation par un courant de spin et par pulse laser ultra-rapide (2021).
- [124] Oukaci, K. A. *Domaines magnétiques périodiques pour la propagation guidée d'ondes de spin*. Ph.D. thesis, Université de Lorraine (2021).

-
- [125] Lounis, L. *Propriétés magnétiques et structurales de fe/mnas/gaas (001) et dynamique photo-induite des transitions de phases dans mnas/gaas (001)*. Ph.D. thesis, Université Paris sciences et lettres (2017).
- [126] Schwarz, A. & Wiesendanger, R. Magnetic sensitive force microscopy. *Nano Today* **3**, 28–39 (2008).
- [127] Horcas, I. *et al.* WSXM: A software for scanning probe microscopy and a tool for nanotechnology. *Review of scientific instruments* **78**, 013705 (2007).
- [128] Zhu, X., Grütter, P., Metlushko, V. & Ilic, B. Magnetic force microscopy study of electron-beam-patterned soft permalloy particles: Technique and magnetization behavior. *Physical Review B* **66**, 024423 (2002).
- [129] Hartmann, U. Magnetic force microscopy. *Annual review of materials science* **29**, 53–87 (1999).
- [130] Hehn, M. *Elaboration, étude des propriétés structurales et magnétiques de couches et réseaux de plots submicroniques a base de cobalt*. Ph.D. thesis, Université Louis Pasteur-Strasbourg I (1997).
- [131] Xu, Y. & Mangin, S. Magnetization manipulation using ultra-short light pulses. *Journal of Magnetism and Magnetic Materials* 170169 (2022).
- [132] Le Guyader, L. *et al.* Nanoscale sub-100 picosecond all-optical magnetization switching in GdFeCo microstructures. *Nature communications* **6**, 1–6 (2015).
- [133] Nyoma, D. P. G. Size effect on single pulse all-optical helicity-independent switching in GdFeCo disk arrays. *submitted* **0**, 0 (2023).
- [134] Gorchon, J. *et al.* Pinning-dependent field-driven domain wall dynamics and thermal scaling in an ultrathin Pt/Co/Pt magnetic film. *Physical Review Letters* **113**, 027205 (2014).
- [135] Atkinson, D. *et al.* Magnetic domain-wall dynamics in a submicrometre ferromagnetic structure. *Nature materials* **2**, 85–87 (2003).
- [136] Van de Wiele, B., Laurson, L., Franke, K. J. & Van Dijken, S. Electric field driven magnetic domain wall motion in ferromagnetic-ferroelectric heterostructures. *Applied Physics Letters* **104**, 012401 (2014).

BIBLIOGRAPHY

- [137] Franke, K. J. *et al.* Reversible electric-field-driven magnetic domain-wall motion. *Physical Review X* **5**, 011010 (2015).
- [138] Meier, G. *et al.* Direct imaging of stochastic domain-wall motion driven by nanosecond current pulses. *Physical review letters* **98**, 187202 (2007).
- [139] Heyne, L. *et al.* Direct observation of high velocity current induced domain wall motion. *Applied Physics Letters* **96**, 032504 (2010).
- [140] Kläui, M. *et al.* Controlled and reproducible domain wall displacement by current pulses injected into ferromagnetic ring structures. *Physical review letters* **94**, 106601 (2005).
- [141] Miron, I. M. *et al.* Fast current-induced domain-wall motion controlled by the rashba effect. *Nature materials* **10**, 419–423 (2011).
- [142] Torrejon, J. *et al.* Unidirectional thermal effects in current-induced domain wall motion. *Physical review letters* **109**, 106601 (2012).
- [143] Tetienne, J.-P. *et al.* Nanoscale imaging and control of domain-wall hopping with a nitrogen-vacancy center microscope. *Science* **344**, 1366–1369 (2014).
- [144] Remy, Q. *Ultrafast spin dynamics and transport in magnetic metallic heterostructures*. Ph.D. thesis, Université de Lorraine (2021).
- [145] Vergès, M. *et al.* Energy efficient single pulse switching of [Co/Gd/Pt]_N nanodisks using surface lattice resonances. *Advanced Science* **10**, 2204683 (2023).
- [146] Werner, W. S., Glantschnig, K. & Ambrosch-Draxl, C. Optical constants and inelastic electron-scattering data for 17 elemental metals. *Journal of Physical and Chemical Reference Data* **38**, 1013–1092 (2009).
- [147] Johnson, P. B. & Christy, R.-W. Optical constants of the noble metals. *Physical review B* **6**, 4370 (1972).
- [148] Hendren, W. *et al.* Optical and magneto-optical characterization of TbFeCo and GdFeCo thin films for high-density recording. *Journal of Physics: Condensed Matter* **15**, 1461 (2003).
- [149] Pham, T. H. *et al.* Very large domain wall velocities in Pt/Co/GdOx and Pt/Co/Gd trilayers with dzyaloshinskii-moriya interaction. *EPL (Europhysics Letters)* **113**, 67001 (2016).

-
- [150] Kanak, J. *et al.* Influence of buffer layers on the texture and magnetic properties of Co/Pt multilayers with perpendicular anisotropy. *physica status solidi (a)* **204**, 3950–3953 (2007).
- [151] Emori, S. & Beach, G. S. Optimization of out-of-plane magnetized Co/Pt multilayers with resistive buffer layers. *Journal of applied physics* **110**, 033919 (2011).
- [152] Parakkat, V. M., Ganesh, K. & Anil Kumar, P. Tailoring curie temperature and magnetic anisotropy in ultrathin Pt/Co/Pt films. *AIP Advances* **6**, 056118 (2016).
- [153] Peeters, M., Van Ballegooie, Y. & Koopmans, B. Influence of magnetic fields on ultrafast laser-induced switching dynamics in Co/Gd bilayers. *Physical Review B* **105**, 014429 (2022).
- [154] Rowan-Robinson, R. M. *et al.* The interfacial nature of proximity-induced magnetism and the dzyaloshinskii-moriya interaction at the Pt/Co interface. *Scientific reports* **7**, 1–11 (2017).
- [155] Lau, Y.-C. *et al.* Giant perpendicular magnetic anisotropy in Ir/Co/Pt multilayers. *Physical Review Materials* **3**, 104419 (2019).
- [156] Mukhopadhyay, A. *et al.* Asymmetric modification of the magnetic proximity effect in Pt/Co/Pt trilayers by the insertion of a Ta buffer layer. *Physical Review B* **102**, 144435 (2020).
- [157] Verna, A. *et al.* Disclosing the nature of asymmetric interface magnetism in Co/Pt multilayers. *ACS applied materials & interfaces* **14**, 12766–12776 (2022).
- [158] Wang, J., Seki, T., Lau, Y.-C., Takahashi, Y. & Takanashi, K. Origin of magnetic anisotropy, role of induced magnetic moment, and all-optical magnetization switching for $\text{Co}_{100-x}\text{Gd}_x/\text{Pt}$ multilayers. *APL Materials* **9**, 061110 (2021).
- [159] Davies, C., Mentink, J., Kimel, A., Rasing, T. & Kirilyuk, A. Helicity-independent all-optical switching of magnetization in ferrimagnetic alloys. *Journal of Magnetism and Magnetic Materials* **563**, 169851 (2022).
- [160] Jakobs, F. & Atxitia, U. Bridging atomistic spin dynamics methods and phenomenological models of single-pulse ultrafast switching in ferrimagnets. *Physical Review B* **106**, 134414 (2022).

BIBLIOGRAPHY

- [161] Cheng, L. *et al.* Pd polarization and interfacial moments in Pd-Fe multilayers. *Physical Review B* **69**, 144403 (2004).
- [162] Engel, B. N., Wiedmann, M. H., Van Leeuwen, R. A. & Falco, C. M. Anomalous magnetic anisotropy in ultrathin transition metals. *Physical Review B* **48**, 9894 (1993).
- [163] Bruno, P. *et al.* Hysteresis properties of ultrathin ferromagnetic films. *Journal of applied physics* **68**, 5759–5766 (1990).
- [164] Nakajima, N. *et al.* Perpendicular magnetic anisotropy caused by interfacial hybridization via enhanced orbital moment in Co/Pt multilayers: Magnetic circular x-ray dichroism study. *Physical Review Letters* **81**, 5229 (1998).
- [165] Coey, J. M. D., Chappert, J., Rebouillat, J. & Wang, T. Magnetic structure of an amorphous rare-earth transition-metal alloy. *Physical Review Letters* **36**, 1061 (1976).
- [166] El Hadri, M. S., Hehn, M., Malinowski, G. & Mangin, S. Materials and devices for all-optical helicity-dependent switching. *Journal of Physics D: Applied Physics* **50**, 133002 (2017).
- [167] Thielen, M., Kirsch, S., Weinforth, H., Carl, A. & Wassermann, E. Magnetization reversal in nanostructured Co/Pt multilayer dots and films. *IEEE transactions on magnetics* **34**, 1009–1011 (1998).
- [168] Carl, A., Kirsch, S., Lohau, J., Weinforth, H. & Wassermann, E. Magnetization reversal of nanostructured Co/Pt multilayer dots and films studied with magnetic force microscopy and MOKE. *IEEE transactions on magnetics* **35**, 3106–3111 (1999).
- [169] Krone, P. *et al.* Investigation of the magnetization reversal of a magnetic dot array of Co/Pt multilayers. *Journal of Nanoparticle Research* **13**, 5587–5593 (2011).
- [170] Vergès, M. *et al.* Energy efficient single pulse switching of [Co/Gd/Pt]_N nanodisks using surface lattice resonances. *Advanced Science* 2204683 (2022).
- [171] Suess, D. *et al.* Calculation of coercivity of magnetic nanostructures at finite temperatures. *Physical Review B* **84**, 224421 (2011).
- [172] Chaves-O’Flynn, G. D., Wolf, G., Sun, J. Z. & Kent, A. D. Thermal stability of magnetic states in circular thin-film nanomagnets with large perpendicular magnetic anisotropy. *Physical Review Applied* **4**, 024010 (2015).

-
- [173] Arrhenius, S. On the reaction velocity of the inversion of cane sugar by acids. In *Selected readings in chemical kinetics*, 31–35 (Elsevier, 1967).
- [174] Battiato, M., Barbalinardo, G., Carva, K. & Oppeneer, P. M. Beyond linear response theory for intensive light-matter interactions: Order formalism and ultrafast transient dynamics. *Physical Review B* **85**, 045117 (2012).

Résumé de la thèse

La possibilité de manipuler l'aimantation de manière déterministe avec une seule impulsion laser femtoseconde a attiré l'attention sur les applications de stockage de données magnétiques, de mémoires et de logique à grande vitesse et à faible consommation d'énergie. En 2011, la première observation un renversement indépendante de l'aimantation par une seule impulsion optique ultra-rapide (*all-optical helicity-independent switching "AO-HIS"*) a été rapportée¹. Depuis, l'AO-HIS a été réalisée dans divers échantillons ferrimagnétiques à base de Gd, tels que les films amorphes minces de $Gd_x(FeCo)_{1-x}$ ¹⁻⁵, les films amorphes minces de Gd_xCo_{1-x} ⁶, les multicouches de Gd/Co⁷ et les alliages de $Gd_{1-x-y}Tb_yCo_x$ ^{8,9}. De plus, en 2016, en profitant du couplage d'échange entre une multicouche Co/Pt et GdFeCo, il a été démontré la retournement de l'aimantation du Co/Pt induite par une seule impulsion laser femtoseconde¹⁰. Deux ans plus tard (2018), l'AO-HIS a également été rapporté dans des hétérostructures plus complexes telles que les valves de spin à base de $Gd_x(FeCo)_{1-x}$ ¹¹. L'étude de ce retournement à origine purement thermique dans les valves de spin pour différents matériaux magnétiques reste un domaine d'intérêt majeur pour la communauté scientifique, car la physique est riche dans ces structures complexes^{?,?,?}. En 2020, la première observation du mécanisme AO-HIS sans Gd a été rapportée pour deux types de structure sans Gd: dans les alliages Heusler ferrimagnétiques semi-métalliques Mn_2Ru_xGa qui possèdent deux sous-réseaux Mn non équivalents¹⁵ et dans la multicouche Co/Tb^{16,17}. Ce dernier travail récent démontre que le mécanisme est très différent de celui observé pour les échantillons à base de Gd.

Les résultats expérimentaux obtenus sur divers matériaux magnétiques présentant un renversement indépendante de l'aimantation par une seule impulsion optique ultra-rapide montrent la présence des critères communs. Tout d'abord les échantillons sont constitués de deux sous-réseaux d'aimantation antiferromagnétiquement couplés, résultant soit à un alliage soit à une multicouche. En 2017, il a été montré que dans le cas d'échantillons en alliage, la composition montrant AO-HIS est proche de la compensation pour laquelle l'aimantation nette de l'échantillon est proche de zéro². De plus, la fluence laser nécessaire pour obtenir AO-HIS est minimale autour de la compensation⁵. Les études théoriques et la modélisation ont démontré

RÉSUMÉ DE LA THÈSE

que le couplage d'échange entre les deux sous-réseaux d'aimantation joue un rôle crucial dans le transfert de moment angulaire entre les sous-réseaux¹⁸. De plus, les deux principales approches pour décrire la dynamique de l'aimantation des sous-réseaux sont le modèle microscopique à trois températures¹⁹ et l'équation atomistique de Landau-Lifshitz-Gilbert²⁰⁻²². Ces modélisations permettent de prédire que le rapport optimal entre les atomes de métaux de transition et les atomes de terres rares pour une commutation réussie est proche de la compensation de l'alliage ferrimagnétique³. En 2019, des études expérimentales et théoriques sur les bicouches Co/Gd²³ montrent que, contrairement aux alliages ferrimagnétiques de métaux de transition à base de terres rares, les bicouches peuvent être commutées en l'absence d'une température de compensation de l'aimantation. De même, il est démontré qu'en changeant le mélange entre Co et Gd à l'interface, la gamme d'épaisseur à laquelle AO-HIS peut être observée change drastiquement ainsi que la fluence seuil²⁴. Cependant, pour les applications futures, la présence d'éléments de terres rares n'est pas recommandée en raison du très faible rapport de magnétorésistance à effet tunnel qui peut être obtenu dans les jonctions magnétiques à effet tunnel à base de terres rares^{25,26}.

Les objectifs de cette thèse étaient d'étudier l'effet de la taille sur le retournement tout optique indépendant de l'hélicité (AO-HIS) dans des systèmes présentant ce mécanisme de renversement à l'échelle du film continu. Bien que les approches pour décrire la dynamique de l'aimantation restent très débattues, notre travail dans ce domaine de recherche a consisté à étudier l'impact de la réduction de la dimension latérale des matériaux magnétiques avec des expériences magnéto-optiques "quasi-statique". En effet, nous avons fabriqué des réseaux de disques avec des diamètres allant de 3 μm à 400 nm pour deux types de films minces magnétiques (alliage GdFeCo et tri-couche Pt/Co/Pt saupoudré de Gd) et avons systématiquement irradié des impulsions laser sur les régions modelées. Alors que l'importance de l'absorption spécifique de la lumière dans les nanostructures est révélée par la dépendance de la fluence seuil de renversement par rapport à la taille du disque pour l'alliage GdFeCo, les effets thermiques n'expliquent pas le comportement de la probabilité de retournement en fonction de la taille du disque pour la tri-couche Pt/Co/Pt saupoudré de Gd.

La première partie de ce travail passe en revue les principaux résultats publiés dans le domaine de la manipulation ultra-rapide de l'aimantation par des impulsions laser ultra-courtes. Nous avons commencé ce chapitre en présentant la première démonstration expérimentale de dynamique induite par laser dans un matériau ferromagnétique. Dans cette section, les différents mécanismes possibles impliqués dans la dynamique de l'aimantation ultrarapide sont présentés. Ensuite, la deuxième section se concentre sur l'observation statique et dynamique de la commu-

tation tout-optique dans les matériaux ferrimagnétiques. Le point de départ du renversement de l'aimantation par la lumière est la découverte en 2007 de la commutation déterministe de domaines magnétiques de GdFeCo à l'aide de plusieurs impulsions pour une polarisation circulaire donnée puis d'une seule impulsion polarisée linéairement. Dans cette section, nous présentons donc d'autres matériaux ferrimagnétiques qui présentent un AO-HIS, en mettant l'accent sur les matériaux ferrimagnétiques synthétiques. En outre, l'absence de moment angulaire dans la lumière polarisée linéairement et l'observation de l'AOS indépendamment de la direction d'un seul domaine magnétique démontrent que l'effet thermique est le mécanisme qui conduit l'AOS dans ce type de matériau. La dynamique de l'aimantation a également été rapportée et les approches pour décrire la dynamique ultrarapide observée sont encore très débattues. Cependant, les ferromagnétiques constituent une autre classe de matériaux magnétiques présentant ce retournement tout optique. En effet, du film continu au milieu granulaire, il est maintenant bien connu que l'on peut obtenir un renversement complet de l'aimantation dans une direction pour une polarisation circulaire et dans la direction opposée pour la polarisation circulaire opposée, appelé retournement tout-optique dépendant de la polarisation circulaire de la lumière (*all-optical helicity-dependent switching "AO-HDS"*). Il a été démontré que la nucléation et la propagation des parois de domaine constituent le processus de renversement pour ce type de retournement. De plus, l'effet Faraday inverse (IFE) et le dichroïsme circulaire magnétique (MCD) semblent être les deux meilleurs candidats pour comprendre/expliciter le mécanisme AO-HDS dans ce matériau magnétique. Dans la section suivante, l'utilisation de courants de spin ultrarapides pour piloter la commutation de l'aimantation d'une couche ferromagnétique à l'intérieur d'une valve de spin en utilisant des impulsions laser femtosecondes est présentée. À la fin de ce chapitre, les différentes études de l'effet de taille sur le mécanisme AO-HIS réalisées principalement dans l'alliage GdFeCo sont passées en revue.

Dans le chapitre 3, nous présentons une étude systématique du retournement de l'aimantation pour des disques de GdFeCo de diamètre compris entre 10 μm et 400 nm avec des impulsions laser de 35 fs polarisées linéairement. Pour les micro-disques plus grands (entre 10 et 3 μm), nous confirmons que les structures GdFeCo à motifs plus larges présentent un renversement tout optique. De façon remarquable, la formation d'un anneau, suivie de son expansion vers le centre de la structure est observée et illustre une dynamique de renversement lente d'environ 30 s pour les disques de 6 μm . Cependant, comme la distance entre les structures et le diamètre des disques sont comparables au diamètre du faisceau laser, des difficultés sont rapidement apparues pour étudier l'effet de taille à cette échelle dimensionnelle latérale. L'une d'entre elles est la définition correcte des paramètres tels que la fluence seuil de renversement, la fluence de

RÉSUMÉ DE LA THÈSE

désaimantation, la durée limite d'impulsion et la probabilité de commutation impliquée dans le mécanisme de l'AO-HIS. Pour surmonter cette limitation, nous avons encore réduit la taille des disques de 3 μm à 400 nm de diamètre tout en les rapprochant les uns des autres. Nous démontrons expérimentalement le renversement grâce à une seule impulsion de l'aimantation des disques de GdFeCo dans cette gamme de taille en utilisant des impulsions laser polarisées linéairement de 35 fs. Deux états magnétiques différents peuvent être observés en fonction de la fluence laser : soit un retournement déterministe de l'aimantation du disque, soit un disque orienté de façon aléatoire (multidomain pour des disques micrométriques et domaine unique pour des disques nanométriques). Nous montrons que la fluence requise pour observer les deux états magnétiques présente un comportement non monotone avec le diamètre du disque, et que les plus petits disques nécessitent la fluence minimale la plus faible pour obtenir une commutation tout-optique indépendante de l'hélicité en une seule impulsion. L'évolution différente des seuils de fluence pour les deux phénomènes en fonction de la taille du disque est observée et discutée. Nous concluons ce chapitre en montrant qu'une augmentation de la durée d'impulsion induit une diminution progressive de la qualité AO-HIS.

Dans le chapitre 4, nous présentons une analyse minutieuse des effets de l'amplitude et de la position de Gd sur le mécanisme de renversement tout optique à impulsion unique dans le ferromagnétique Pt/Co/Pt. Trois types d'échantillons de *wedge* de Gd sont réalisés : Pt/Gd/Co/Pt, Pt/GdCo/Pt et Pt/Co/Gd/Pt. En effet, nous avons utilisé un procédé de dépôt en *wedge* pour varier progressivement l'épaisseur de Gd dans tout le film continu. Pour l'empilement Pt/Co/Gd, nous démontrons la nécessité de séparer le régime de retournement et le régime de retournement parfait. En effet, une nette différence dans le comportement de l'aimantation apparaît dans ces deux régimes lorsqu'un état multidomaine est observé pour le régime de retournement alors qu'un domaine parfaitement renversé est atteint pour le régime de retournement parfait, dans le cas de 10000 impulsions laser consécutives avec une fréquence de répétition de 5 kHz. De plus, nous démontrons que nous avons pu réduire l'épaisseur de Gd de 3 nm à 0.27 nm tout en observant le mécanisme parfait de retournement. Ce résultat expérimental démontre que l'effet interfacial est le principal effet responsable de l'observation de AO-HIS dans l'empilement Pt/Co/Gd. Pour le cas de Pt/Gd/Co/Pt, nous démontrons le parfait retournement de l'aimantation de la couche de Co jusqu'à 0.06 nm d'épaisseur de Gd. De plus, en traçant le diagramme d'état magnétique (fluence en fonction de la durée d'impulsion) pour des épaisseurs de Gd égales à 0.07 et 0.21 nm, nous observons la même fenêtre de renversement triangulaire démontrée précédemment dans les alliages ferrimagnétiques de GdFeCo. Remarquablement, moins il y a de Gd dans l'interface inférieure Pt/Co, plus la durée d'impulsion maximale est élevée. Cependant, pour une épaisseur

de Gd de l'ordre de 0.3 nm, l'aimantation du Co passe dans le plan. Enfin, dans le cas d'un alliage GdCo pris en sandwich par deux couches de Pt, nous démontrons que l'état PTS (*Perfect toggle switching*) peut être atteint jusqu'à 7.5% de Gd et le régime de retournement jusqu'à 4% de Gd.

Dans le chapitre 5, nous présentons une étude systématique de l'effet de taille sur AO-HIS dans des disques de Pt/Co/Pt saupoudré de Gd dont le diamètre varie de 3 μm à 400 nm avec des impulsions laser à polarisation linéaire de 35 fs. L'effet de l'excitation laser est étudié in-situ à l'aide d'un microscope polaire MOKE et l'analyse quantitative de la probabilité de commutation a été réalisée ex-situ par microscopie à force magnétique. La variation de cette probabilité de retournement avec la taille des disques est précisément mesurée et expliquée par un processus de renversement non uniforme. Enfin, l'influence de la durée de l'impulsion laser et de l'hélicité du laser sur le retournement tout optique dans cette gamme de taille de structures est discutée.

Nous pensons que ce travail va certainement changer la compréhension du mécanisme de retournement tout optique de ces 15 dernières années. En effet, la démonstration qu'une très petite quantité de Gd est nécessaire ouvre non seulement de nouvelles possibilités d'application, mais remet également en question la description théorique du mécanisme dudit retournement. Enfin, l'étude de l'effet de taille est nécessaire pour se rapprocher des potentielles applications du retournement ultra-rapide et enfin de mettre en évidence de nouveaux phénomènes cachés dans ce processus de renversement de l'aimantation induit par impulsion laser femtosecond de polarisation linéaire.

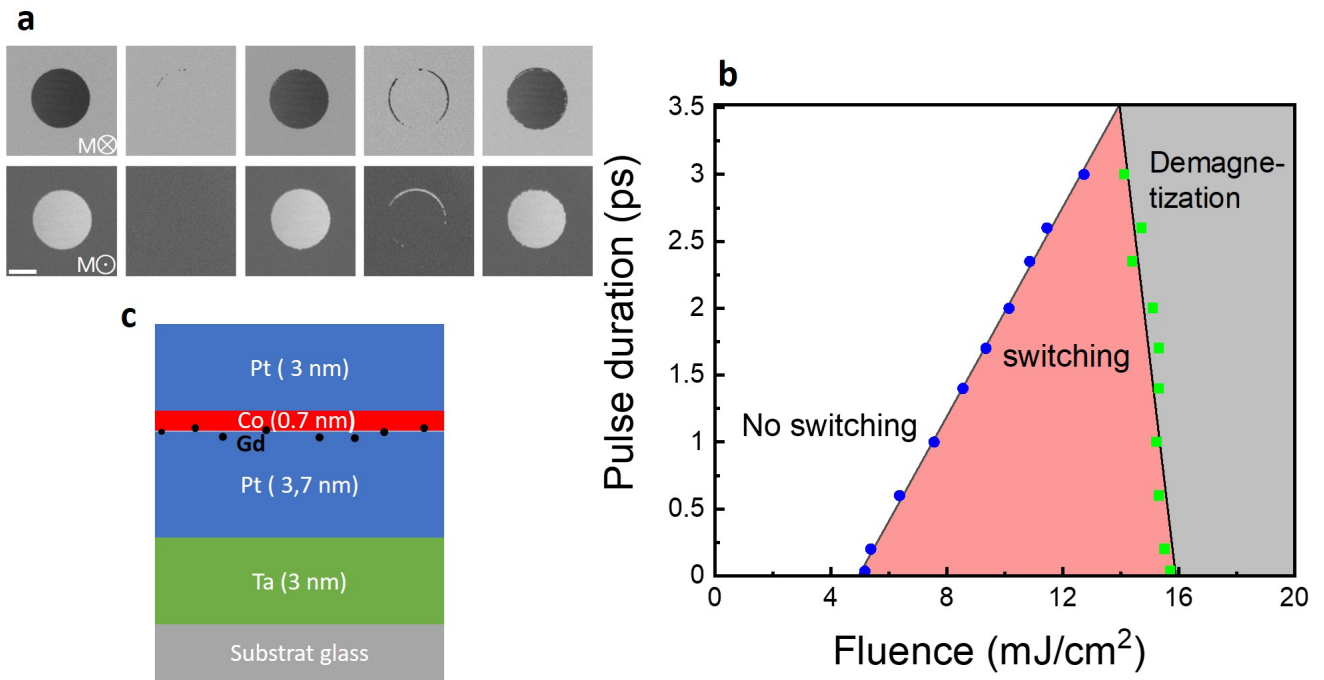


Figure 1: **Principal résultat de ce travail.** a) Images magnéto-optiques du film continu de Pt(3.7 nm)/Gd/Co(0.7 nm)/Pt(3 nm) obtenues après l'action de cinq impulsions laser uniques consécutives de 35 fs. La zone gris foncé (gris clair) représente l'aimantation hors plan du film pointant "vers le haut" ("vers le bas") comme représenté par le point (croix) encerclé. Chaque impulsion femtoseconde unique avec une fluence de 11.9 mJ/cm² illumine la même région circulaire du film et retourne l'aimantation à l'intérieur. b) Diagramme d'état AO-HIS réalisé en faisant varier la fluence et la durée de l'impulsion. Le cercle bleu foncé et le carré vert clair représentent respectivement la fluence seuil de retournement et la fluence de démagnétisation. c) Croquis de l'empilement des couches minces.